Intense heavy ion beam-induced effects in carbon-based stripper foils

Zur Erlangung des Grades eines Doktors der Naturwissenschaften (Dr. rer. nat.)
genehmigte Dissertation von Dipl.-Ing. Katharina Kupka aus Frankfurt am Main
Tag der Einreichung: 24.05.2016, Tag der Prüfung: 07.07.2016
August 2016 — Darmstadt — D 17

1. Gutachten: Prof. Dr. Christina Trautmann
2. Gutachten: Prof. Dr. Wolfgang Ensinger

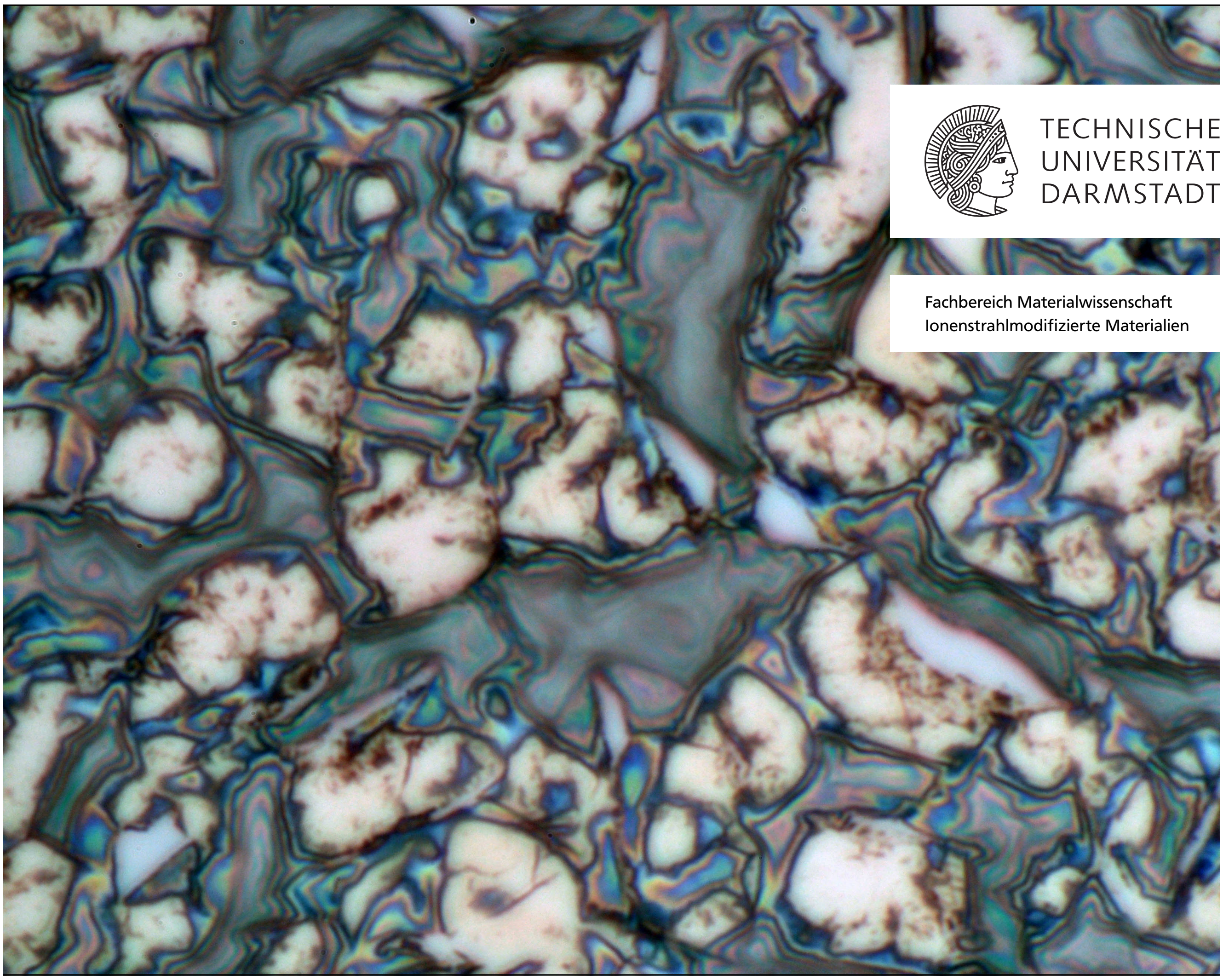

TECHNISCHE
UNIVERSITÄT
DARMSTADT

Fachbereich Materialwissenschaft
Ionenstrahlmodifizierte Materialien

Intense heavy ion beam-induced effects in carbon-based stripper foils

Genehmigte Dissertation von Dipl.-Ing. Katharina Kupka aus Frankfurt am Main

1. Gutachten: Prof. Dr. Christina Trautmann
2. Gutachten: Prof. Dr. Wolfgang Ensinger

Tag der Einreichung: 24.05.2016
Tag der Prüfung: 07.07.2016

Darmstadt — D 17

Bitte zitieren Sie dieses Dokument als:
URN: urn:nbn:de:tuda-tuprints-56116
URL: http://tuprints.ulb.tu-darmstadt.de/5611

Erklärung zur Dissertation

Hiermit versichere ich, die vorliegende Dissertation ohne Hilfe Dritter nur mit den angegebenen Quellen und Hilfsmitteln angefertigt zu haben. Alle Stellen, die aus Quellen entnommen wurden, sind als solche kenntlich gemacht. Diese Arbeit hat in gleicher oder ähnlicher Form noch keiner Prüfungsbehörde vorgelegen.

Darmstadt, den 04.08.2016

(Katharina Kupka)

Abstract

Amorphous carbon or carbon-based stripper foils are commonly applied in accelerator technology for electron stripping of ions. At the planned facility for antiproton and ion research (FAIR) at the Helmholtzzentrum für Schwerionenforschung (GSI), Darmstadt, thin carbon stripper foils provide an option for directly delivering ions of intermediate charge states to the heavy ion synchrotron, SIS 18, in order to mitigate space charge limitations during high-intensity operation. In case of desired high end-energies in the synchrotron, a second stripping process by a thicker carbon foil provides ions of higher charge states for injection into the SIS18. High beam intensities and a pulsed beam structure as foreseen at FAIR pose new challenges to the stripper foils which experience enhanced degradation by radiation damage, thermal effects, and stress waves. In order to ensure reliable accelerator operation, radiation-hard stripper foils are required. This thesis aims to a better understanding of processes leading to degradation of carbon-based thin foils. Special focus is placed on ion-beam induced structure and physical property changes and on the influence of different beam parameters.

Irradiation experiments were performed at the M3-beamline of the universal linear accelerator (UNILAC) at GSI, using swift heavy ion beams with different pulse lengths and repetition rates. Tested carbon foils were standard amorphous carbon stripper foils produced by the GSI target laboratory, as well as commercial amorphous and diamond-like carbon foils and buckypaper foils.

Microstructural changes were investigated with various methods such as optical microscopy, scanning electron microscopy (SEM), profilometry and chromatic aberration measurements. For the investigation of structural changes X-ray photoelectron spectroscopy (XPS), Raman spectroscopy, high resolution transmission electron microscopy (HRTEM), in-situ Fourier-transform infrared spectroscopy (FTIR) and small angle X-ray scattering (SAXS) were used. The changes of physical properties, in particular the electrical resistivity, thermal conductivity and stiffness of the foils were studied by in-situ 4-point probe, laser flash analysis and atomic force microscopy, respectively. A technique for measuring temperature of very thin, semitransparent and free-standing stripper foils during irradiation by means of an infrared (IR) camera was developed and applied.

The experimental investigations were complemented by molecular dynamics simulations of amorphous carbon exposed to different swift heavy ions. The simulations provide information on the structural changes in the tracks at atomic scale. Virtual amorphous carbon cells were created by simulating liquid quenching and plasma deposition, yielding cells with different degrees of clustering of sp^2 and sp^3 bonding. The impacts of swift heavy ions were modeled by an instantaneous energy deposition deduced from inelastic thermal spike model calculations.

Results of experiments and simulations provide evidence for the beam-induced transformation of amorphous carbon to a defected graphitic structure and for clustering of sp^2 and sp^3 bonds. These structural changes result in severe property changes. The electrical and thermal properties of amorphous carbon seem to improve during beam exposure, but the mechanical properties degrade severely. The beam conditions have a strong influence on the evolution of induced structure and property changes.

A better understanding of the response of (amorphous) carbon stripper foils to swift heavy ion beams as revealed by dedicated irradiation and characterization experiments performed within this thesis, provides criteria for material requirements for future stripper foils used in high-power heavy ion accelerators such as FAIR.

Zusammenfassung

Amorphe Kohlenstofffolien oder kohlenstoffbasierte Folien werden typischerweise für das Strippen von Elektronen zur Ladungserhöhung von Ionen in Beschleunigern eingesetzt. In der geplanten Beschleunigeranlage FAIR (Facility for Antiproton and Ion Research) bieten dünne amorphe Stripperfolien eine Möglichkeit, Ionen mit mittleren Ladungszuständen zu erzeugen und direkt in das Schwerionensynchrotron SIS18 zu injizieren, um Raumladungseffekte während des Hochstrombetriebs abzuschwächen. Für hohe Endenergien im Synchrotron liefert eine zweite, dickere Kohlenstofffolie Ionen mit höheren Ladungszuständen für die Injektion ins SIS18. Die bei FAIR geplanten hohen Strahlintensitäten und eine gepulste Strahlstruktur stellen eine Herausforderung für die eingesetzten Stripperfolien dar, die durch Strahlenschäden, thermische Effekte und Spannungswellen eine besondere Schädigung erfahren. Um einen zuverlässigen Beschleunigerbetrieb zu gewährleisten, sind strahlenharte Stripperfolien essentiell. Diese Arbeit hat zum Ziel, ein besseres Verständnis der Prozesse zu erlangen, die zur Stripperfolien-Schädigung führen. Ein Fokus liegt dabei auf ionenstrahlinduzierten Änderungen der Struktur und physikalischen Eigenschaften, sowie auf dem Einfluss der Stahlparameter.

Bestrahlungsexperimente wurden am M3-Strahlzweig des Linearbeschleunigers UNILAC des GSI Helmholtzzentrums für Schwerionenforschung in Darmstadt mit verschiedenen Schwerionenstrahlen, unterschiedlichen Pulslängen und Wiederholraten durchgeführt. Die getesteten Folien beinhalteten amorphe Kohlenstofffolien, die im GSI Targetlabor hergestellt wurden, sowie kommerzielle amorphe und diamantähnliche Kohlenstofffolien und Buckypaper Folien.

Mikrostrukturelle Änderungen wurden mit verschiedenen Methoden untersucht, zu denen optische Mikroskopie, Rasterelektronenmikroskopie (REM), Profilometrie, und chromatische Aberrations-Messungen gehören. Für die Charakterisierung der strukturellen Änderungen wurden Photoelektronenspektroskopie (XPS), Raman Spektroskopie, Hochauflösende Transmissionselektronenmikroskopie (HRTEM), in-situ Fourier-Transform-Infrarotspektroskopie (FTIR) und Röntgen-Kleinwinkelstreuung (SAXS) genutzt. Die Änderung physikalischer Eigenschaften, wie die des elektrischen Widerstandes, der thermischen Diffusivität und der Steifigkeit wurden mittels Vier-Punkt-Methode, Laser Flash Analyse und Rasterkraftmikroskopie (AFM) untersucht. Für die Messung der Temperatur der dünnen, freistehenden und semi-transparenten Stripperfolien während der Bestrahlung wurde eine Kalibierungsmethode für eine Infrarot-Kamera entwickelt.

Die experimentellen Untersuchungen wurden durch molekulardynamische Simulationen von ionenbestrahlten amorphem Kohlenstoff ergänzt. Die Simulationen liefern Informationen über strukturelle Änderungen in der Ionenspur auf atomarer Ebene. Die Simulationszellen wurden mit dem Verfahren des Quenchen aus der flüssigen Phase und mittels Plasmaabscheidung hergestellt. Die resultierenden Zellen besitzen eine unterschiedliche Ausprägung von Clustern aus sp^2 und sp^3 gebundenen Bereichen. Die Schwerionen wurden durch eine instantane Energiedeposition simuliert, die von Berechnungen basierend auf dem inelastischen Thermal Spike Model abgeleitet wurde.

Die Ergebnisse der Experimente und Simulationen zeigen eine Transformation des amorphen Kohlenstoffs in eine defektreiche graphitische Struktur und zeigen die Präsenz von sp^2 und sp^3 gebunden Clustern. Diese Strukturänderungen führen zu erheblichen Eigenschaftsänderungen. Während sich die elektrische und thermische

Leitfähigkeit durch die Bestrahlung verbessert, verschelchtern sich die mechanischen Eigenschaften. Die Strahlparameter zeigen einen starken Einfluss auf den Verlauf der induzierten Struktur- und Eigenschaftsänderungen. Die umfangreichen Ergebnisse dieser Arbeit tragen zu einem besseren Verständnis des Verhaltens von (amorphen) Kohlenstoff-Stripperfolien unter Schwerionenbestrahlung bei und liefern Kriterien für Materialvorgaben für die Anwendung von Stripperfolien in Schwerionen-Beschleunigeranlagen wie FAIR.

Contents

Part I.

Introduction

This part describes the background of the presented experiments and simulations. The discussed contents in chapter 1 to 3 are a collection of the state of the art of the field and are no product of the author's work. Scientific expressions are used according to the cited references.

1 Motivation

The Facility of Antiproton and Ion Research (FAIR) is an international accelerator facility under construction at the GSI Helmholtzzentrum für Schwerionenforschung. This new facility will enable unique experiments with high-energy ions and antiprotons in the area of nuclear structure and nuclear matter physics, atomic and plasma physics, biophysics as well as materials science [1]. The modular start version of FAIR will consist of a ring accelerator (SIS100 heavy ion synchrotron) with a circumference of 1100 meters connected to storage and collector rings and experimental caves (figure 1.0.1) [2]. The current GSI facility will serve as pre-accelerator and injector for the new facility. For this propose, the current universal linear accelerator (UNILAC) (figure 1.0.2) and heavy ion synchrotron SIS18 will be upgraded [2, 3].

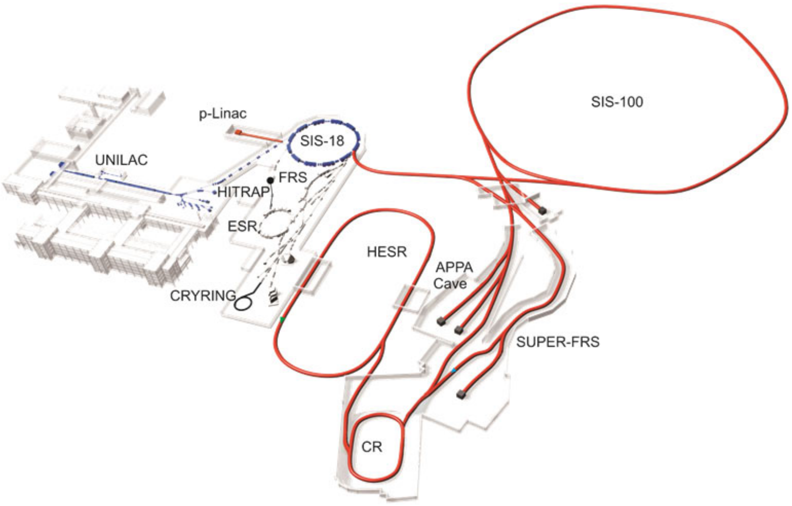

Figure 1.0.1.: Layout of the existing GSI facility (left, in blue) and the planned modular start version (MSV) of the FAIR facility (right, in red) [4].

The UNILAC consists of two injectors, the High Current (HSI) and the High Charge Injector (HLI), delivering all ion species up to uranium. The ion beams used for irradiations in this work were provided by low-current Penning or high-current MEVVA ion sources at the front-end. After extraction from the ion source, the ions are transported into the low energy transport line (LEBT) and accelerated to 1.4 MeV/u. They are stripped by a N_2 jet gas stripper and a magnetic charge separator system selects one charge state for further acceleration. The post-stripper section consists of an ALVAREZ DTL (drift tube linac) of 4 tanks that accelerates the ions up to 11.4 MeV/u. A carbon foil stripper in the transfer channel to the synchrotron SIS18 provides higher charge states for acceleration to energies up to 1 to 2 GeV/u in the synchrotron [5]. To meet FAIR requirements, UNILAC and SIS18 have to provide required beam intensities. For uranium ions for instance, the UNILAC has to deliver 3.3×10^{11} U^{28+} ions per 100 µs to the SIS18 [7].

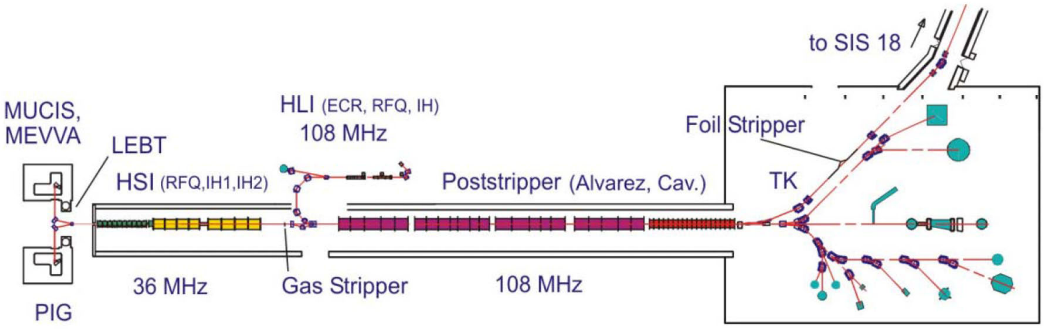

Figure 1.0.2.: Schematic overview of the GSI UNILAC [6].

1.1 Stripper foils for FAIR

In many ion-beam accelerators thin solid foils are used to increase the charge state of the particles by stripping off electrons. As described above, intensities in the UNILAC have to be increased to meet FAIR requirements. A way for increasing the beam intensities is to decrease the charge state of the ions which are injected into SIS18 in order to mitigate space charge limitations. A thin, solid carbon stripper foil at 1.4 MeV/u may therefore provide an option for directly delivering an intermediate charge state to the heavy ion synchrotron during high-intensity operation [5, 7–9]. Solid carbon stripper foils produced by the GSI Target Laboratory of different thicknesses were tested at the 1.4 MeV/u-stripper section [7]. These experiments revealed the capability of 20 μg/cm^2 amorphous carbon foils for delivering U^{39+} ions to SIS18. The foils exhibited an average lifetime of 11±4 h. U^{39+} beam emittance was found to match the SIS-acceptance [7]. Like in the current GSI accelerator, a thicker carbon foil (200 to 600 μg/cm^2) in the transfer channel to SIS18 will provide high charge states for higher end energies in the synchrotron. Due to its low density and excellent thermo-mechanical properties, carbon is the most promising material candidate to withstand highest beam intensities. Regarding the exposure under these extreme conditions, reliably working stripper foils as well as the prediction and increase of their lifetime are of great interest at GSI/FAIR, but also for other emerging high power facilities like SPIRAL2 in France and FRIB in the US and several other accelerator laboratories [10–18]. In order to select the most suitable carbon material and maximize the lifetime of the stripper foils, systematic investigations of the processes leading to failure are needed. Due to this demand, various issues of the different types of carbon foils under heavy ion irradiation are investigated within this work, including beam-induced radiation damage, (micro-)structure and property changes, thermal effects and performance limits.

1.2 Amorphous carbon stripper foils

Thin amorphous carbon foils are of interest because they combine many advantages. This concerns the desired beam parameters after stripping such as low energy straggling, the minimization of multiple scattering and high ion beam transmission [19]. Due to the influence of density, solid state stripper foils provide higher charge states than gas strippers, and carbon as a low-Z material provides higher charges states than materials with high Z [20, 21]. Moreover, carbon is the material with lowest Z that can be fabricated into very thin foils [19]. Amorphous carbon foils can be produced by various methods (chapter 3) and in high quantities. The stability in vacuum at high temperatures and low longterm activation are other practical advantages. However, the application of amorphous carbon stripper foils suffers from their limited lifetime because the foil replacement interrupts beam operation. A reliably working stripper foil as well as the prediction and increase of its lifetime are therefore of great interest and have been investigated mainly experimentally for many years in different accelerator laboratories. The research conducted in this field concentrated mainly on the improvement of preparation methods of free-standing amorphous carbon foils and lifetime monitoring during operation [10, 11, 14, 15, 22–44]. The most common methods for the production of amorphous carbon stripper foils are evaporation [23, 45], laser ablation techniques [26, 33, 38], arc discharge methods [22–24, 36, 37, 46] and sputtering [28–32, 34, 35, 41]. Sugai *et al.* [25, 37] as well as Zeisler *et al.* [47] developed boron doped carbon stripper foils with increased lifetime. Other approaches to increase the lifetime include different mounting techniques [18, 48]: Specifically slackening [45] of the foils to prevent stresses and mounting on rotating stripper wheels to distribute the ion beam over a larger area [10, 49] were found to significantly improve the lifetime. Measurements [16, 37, 50] and calculations [35, 51] of the temperature during irradiation and analysis of the decreased foil thickness [15, 25, 37, 42, 43, 52–55] provided information on the processes limiting the lifetime.

Even though the lifetime increase of the stripper foils is a topic in research for many years, the destruction mechanisms by swift heavy ions are still not properly understood. A reason could be that only few groups have investigated the structural changes in amorphous carbon stripper foils. Sander and Bukow characterized already in 1978 the graphitization in evaporated amorphous carbon foils by light ion (H^+, Li^+, He^+) irradiation and by heating using electron diffraction and scanning electron microscopy [56]. Ranzinger and Maier-Komor proposed a pre-treatment of the amorphous carbon stripper foils by laser light to induce more crystalline structure by graphitization because they expected reduced radiation damage in (single) crystalline carbon foils and therefore an increased lifetime under heavy ion irradiation [57, 58]. Transmission electron microscopy investigations by Dollinger and Maier-Komor [46, 51] showed an anisotropic arrangement of quasi-graphitic nanocrystals in laser-plasma deposited amorphous carbon foils. According to irradiation experiments this random orientation is responsible for longer lifetimes compared to evaporated and glow discharge deposited foils. In the recent years, few more studies [16, 41] focused on structural changes in amorphous carbon stripper foils by transmission and scanning electron microscopy. For a better understanding of the stripper foil degradation, more investigations need to focus on the structural and physical property changes induced by swift heavy ion irradiation. Also the influence of different beam parameters needs to be clarified. For this reason, this thesis investigates the changes of (micro-)structure, as well as thermal, electrical and mechanical properties by various characterization techniques and simulations in different carbon-based stripper foils and for various ion beams of different time-structures.

2 Ion-matter interaction

The term "swift heavy ions" typically relates to ions of high mass and energies in the MeV to GeV range. These energies can be reached in large ion accelerators. When a swift heavy ion penetrates a solid it loses energy along its path until it is stopped at a certain depth. The energy deposition in the material is described by the stopping power $S(E)$ or linear energy loss $\mathrm{d}E/\mathrm{d}x$ which is the average loss of kinetic energy E per unit path length x [59]:

$$S(E) = -\left(\frac{\mathrm{d}E}{\mathrm{d}x}\right) \tag{2.1}$$

The depth in which the ion is stopped is called projected range or penetration depth. The total range X describes the full pathway of the ions and is determined by integrating the inverse energy loss along the ion path [60]:

$$X = \int_0^{E_0} \left(\frac{\mathrm{d}E}{\mathrm{d}x}\right)^{-1} \mathrm{d}E \tag{2.2}$$

where E_0 is the incident kinetic energy of the ion. Two main mechanisms cause dissipation of the energy and the deceleration of the penetrating ion. For high specific energies above about 10^{-2} MeV/u the dominant process is based on inelastic interaction of the projectile with the target electrons causing excitation and ionization of the target atoms (electronic energy loss). As the ion energy decreases towards the end of the ion trajectory elastic collisions with the target nuclei become predominant (nuclear energy loss) resulting in a collision cascade and displacement of target atoms. For ions of relativistic energies also photons are generated (Bremsstrahlung, Cerenkov radiation). Above a threshold energy, called Coulomb barrier, of the projectile, the ion can get close enough to the target nuclei to induce nuclear reactions. For uranium ions bombarding a carbon target, this barrier is at approximately 5.1 MeV/u.

The total stopping power S_{total} is the sum of all these stopping processes. In a good approximation, S_{total} is dominated by the electronic energy loss S_{e} and the nuclear energy loss S_{n} ($S_{\mathrm{total}} = S_{\mathrm{e}} + S_{\mathrm{n}}$). Figure 2.0.1 presents the energy regimes of the electronic and nuclear energy loss in carbon for uranium ions. The different energies for sample irradiations performed within this thesis are indicated. Figure 2.0.2 presents the electronic energy loss for different ions used in this work. The energy loss contributions were calculated by the SRIM-2013 code [59, 61] assuming a carbon target density of 2.253 g/cm^3. For lower densities of the carbon target the overall energy loss would decrease. In the high energy regime, the code has an accuracy of approximately 10 to 20 %.

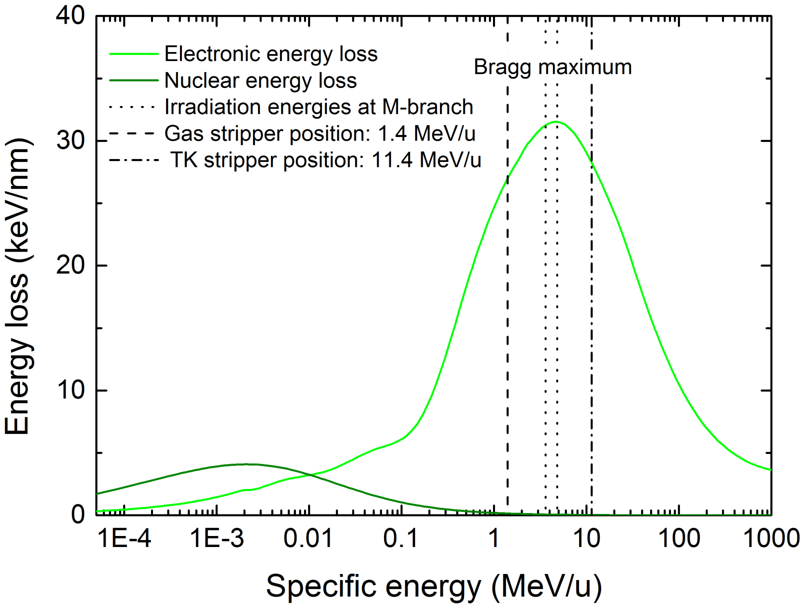

Figure 2.0.1.: Electronic and nuclear energy loss of U ions in carbon (density of 2.253 g/cm^3), calculated with SRIM-2013 [61]. Lines indicate the ion energies for sample irradiations used in this work and stripper positions in the UNILAC accelerator of GSI (compare to figure 1.0.2).

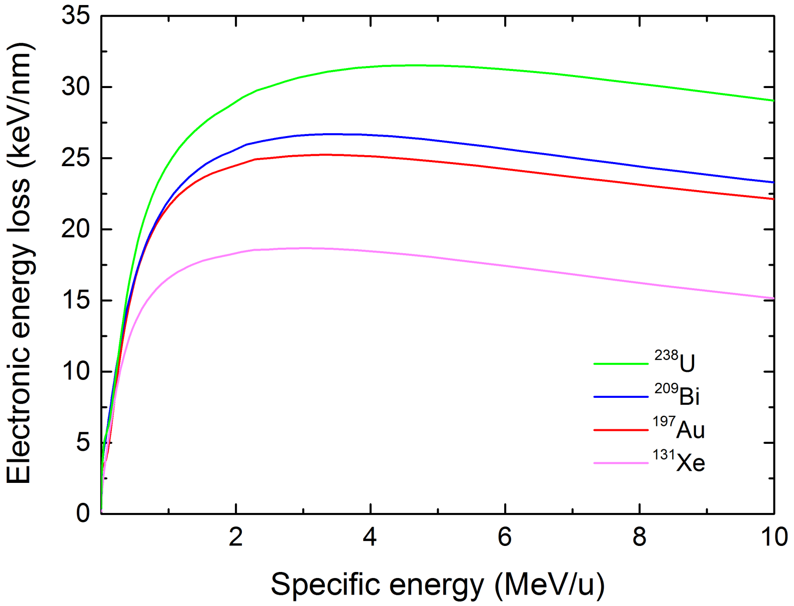

Figure 2.0.2.: Electronic energy loss of different ions in carbon (density of 2.253 g/cm^3), calculated with SRIM-2013 [61].

2.1 Electronic energy loss

For energetic heavy ions in the MeV to GeV range interacting with a material, the electronic energy loss is the dominating process. By inelastic collisions the kinetic energy of the projectile is transferred to the target electrons. In the subsequent electron cascade further target atoms are excited and ionized. Due to the high mass of the heavy ions compared to the electrons, deceleration of the ion occurs in many collisions, each with a small energy transfer over a long distance. The ion trajectory is approximately a straight line. The energy loss in this regime is a function of velocity and effective charge state of the ion. A general concept for the description of the electronic energy loss was developed by Bohr and Bethe [62]. In 1913 Bohr introduced a classical theory of the interaction between a fast heavy charged particle and an electron bound in an harmonic potential [63]. 20 years later, Bethe treated the problem from a quantum-mechanical perspective by using the first Born approximation [64]. Bloch found the bridging formulation between the classical Bohr and the quantum-mechanical Bethe approach for projectiles with a velocity much larger than the velocity of the target electrons [65, 66]. For very high ion velocities, when the projectile velocity approaches the speed of light, a relativistic correction is added to the formula and the Bethe-Bloch relativistic stopping formula describes the electronic energy loss [67, 68]:

$$-\left(\frac{\mathrm{d}E}{\mathrm{d}x}\right)_{\mathrm{e}} = 4\pi e^4 N_{\mathrm{t}} \frac{Z_{\mathrm{p,eff}}^2 Z_{\mathrm{t}}}{m_{\mathrm{e}} v_{\mathrm{p}}^2} \left[\ln\left(\frac{2m_{\mathrm{e}} v_{\mathrm{p}}^2}{I_{\mathrm{t}}}\right) - \ln(1-\beta^2) - \beta^2\right] \tag{2.3}$$

$Z_{\mathrm{p,eff}}$ denotes the effective charge state of the projectile, v_{p} the projectile velocity, Z_{t} the atomic number of the target material, e the charge of an electron, N_{t} the target density, m_{e} the electron mass, I_{t} the effective ionization potential of the target material and β describing the ratio of projectile velocity v_{p} and speed of light c ($\beta = \frac{v_{\mathrm{p}}}{c}$).

The charge state of the projectile depends on the projectile velocity. According to Bohr's stripping theorem, all electrons with orbital velocities v_{e} smaller than the velocity of the ion v_{p} will be stripped-off in the target [69, 70]. Therefore a charge exchange between projectile and target has to be considered [67]. Electron loss due to this stripping process but also electron capture due to the attractive force of the nucleus result in an effective charge $Z_{\mathrm{p,eff}}$ of the projectile which denotes the statistical net charge on the partially neutralized ion [71] and which is smaller than the nuclear charge Z_{p} (atomic number of the projectile). The relation between velocity v_{p} and the effective charge state of the ion in the Bohr concept is described as [67]:

$$Z_{\mathrm{p,eff}} = Z_{\mathrm{p}}\left(1 - \exp\left(-\frac{v_{\mathrm{p}}}{v_0} Z_{\mathrm{p}}^{-\frac{2}{3}}\right)\right) \tag{2.4}$$

with the atomic number of the projectile Z_p, the Bohr velocity $v_0 = \frac{2\pi e}{h} = 2.185 \times 10^8$ cm/s (with the Planck constant h).

After entering the solid, the ion is decelerating and the electronic energy loss of the ion increases with the inverse energy $\frac{1}{E}$ until the maximum of electronic energy loss, called Bragg peak or Bragg maximum, is reached (figure2.0.1). For carbon targets and ions used in this work, the Bragg maximum is between 3 and 5 MeV/u (figure 2.0.1). For further decreasing projectile energies the energy loss decreases with the square root of the energy $\sqrt{E}$ as described in the Lindhard-Scharff-Schiott (LSS) theory [72]. At the low and high energy side of the Bragg peak, the same energy loss occurs, but the ions have different velocities. Even though the magnitude of energy loss is equal, a higher ion velocity leads to a lower energy density, because the energy is deposited into a larger volume. This effect is called velocity effect [73]. For the irradiation of thin amorphous carbon films with energies between 2 and 10 MeV/u, electronic energy loss is predominant (figure 2.0.1).

2.2 Nuclear energy loss

In the energy range of keV to MeV, nuclear energy loss is the dominating process for decelerating the projectile. This is the case for the last hundred nanometer of the projectile range. The ion mainly undergoes elastic collisions with the target atoms (knock-on processes) [67]. If the energy transferred to the target atoms is larger than the displacement energy, the atoms are removed from their lattice positions. If the kinetic energy of the displaced atoms is high enough, they can interact with other target atoms resulting in a collision cascade, generating vacancies and interstitials [67]. The extension of the collision cascade depends on ion energy and mass of the projectile. The displacement energy depends mainly on the structure and composition of the target material. If the energy is smaller than the displacement energy, the energy is transferred to the phononic system, resulting in heating of the target material. Since all experiments in this work are performed around the Bragg peak, the influence of nuclear energy loss is not considered.

2.3 Track formation mechanism

In many materials, mainly insulators, the irradiation with swift heavy ions leads to so-called ion tracks. The radial energy deposition in the material ($\propto \frac{1}{r^2}$ with radius r from the center of ion path [74]) results in cylindrical regions of damaged material in the range of a few nanometers in diameter. The mechanism of track formation is complex and not completely understood. First, the ion transfers its kinetic energy to the electrons of the target atoms, resulting in ionization and generation of energetic electrons (time scale 10^{-17} to 10^{-16} s). These electrons are energetic enough to ionize other atoms, producing an ionization cascade (10^{-15} to 10^{-14} s) [75]. At about 10^{-13} to 10^{-10} s the electronic subsystem couples its energy to the atomic lattice exciting phonon modes. This results in the formation of defects, defect clusters and amorphization. The process in which the energy is transferred from the electrons to the lattice and how the final track is generated is still a topic of research. Coulomb explosion model [76] and thermal spike model are two approaches that try to explain these processes. However, only the thermal spike model, originally proposed by Dressauer [77] and further developed by Toulemonde [78], has been successfully applied for descriptions and predictions of track creation in many different materials [78–84].

2.3.1 Inelastic thermal spike model

In the thermal spike model track formation is described by a rapid heating, melting and subsequent quenching of a molten cylinder along the ion trajectory resulting in defect production and amorphization. The model describes the electrons and lattice atoms as two individual but coupled subsystems. The energy of the ion is first transferred to the electrons (electronic energy loss) yielding a rapid heating of the electron subsystem to a very high temperature T_{e}. This electronic heating expands over the rage of the electron cascade. The energy of the electronic subsystem is then transferred to the cold atomic lattice subsystem via electron-phonon coupling which is expressed by the coupling term $g(T_{\mathrm{e}}-T_{\mathrm{a}})$ with g being the coupling constant and $(T_{\mathrm{e}}-T_{\mathrm{a}})$ the temperature difference between the two subsystems. The strength of electron-phonon coupling defines the temperature of the atomic lattice, and therefore the magnitude of the thermal spike. The heat diffusion in both subsystems is described by classical heat equations with the electronic energy loss as a heat source. Assuming a temperature gradient only in radial direction, electron and lattice temperature can be described in cylindrical coordinates (r denotes the radius from trajectory):

$$C_{\mathrm{e}}(T_{\mathrm{e}})\frac{\partial T_{\mathrm{e}}}{\partial t} = -\frac{1}{r}\frac{\partial}{\partial r}\left(rK_{\mathrm{e}}(T_{\mathrm{e}})\frac{\partial T_{\mathrm{e}}(r,t)}{\partial r}\right) - g(T_{\mathrm{e}}-T_{\mathrm{a}}) + A(r,t), \tag{2.5}$$

$$C_{\mathrm{a}}(T_{\mathrm{a}})\frac{\partial T_{\mathrm{a}}}{\partial t} = -\frac{1}{r}\frac{\partial}{\partial r}\left(rK_{\mathrm{a}}(T_{\mathrm{a}})\frac{\partial T_{\mathrm{a}}(r,t)}{\partial r}\right) + g(T_{\mathrm{e}}-T_{\mathrm{a}}) \tag{2.6}$$

where T denotes the temperatures, C the specific heat coefficients and K the thermal conductivities. The indices e and a indicate the respective electronic and atomic lattice subsystem and t denotes the time [84, 85]. $A(r,t)$ describes the initial spatio-temporal energy deposition transferred from the projectile to the electron subsystem with a Gaussian time distribution and a radial distribution of the electrons $F(r)$ according to Katz model [74, 85]:

$$A(r,t) = b\,S_{\mathrm{e}}(E)\,\exp\left(\frac{-(t-t_0)}{2s^2}\right)F(r) \tag{2.7}$$

s is the half-width of the Gaussian distribution and describes the time needed for the electrons to reach thermal equilibrium. b is a normalization factor to ensure that the integration of $A(r,t)$ equals the electronic energy loss $S_{\mathrm{e}}(E)$. In insulators there are no free electrons, but at high electron temperatures, the electrons can be regarded as hot free electrons in a metal and therefore the specific heat becomes temperature independent [86]. The specific heat for the electronic subsystem C_{e} can be approximated as $1\,\mathrm{J/(cm^3K)}$ and the thermal diffusivity D_{e} as $2\,\mathrm{cm^2/s}$ [86]. The electron-phonon mean free path λ is described by C_{e}, D_{e} and the electron-phonon coupling constant g and can be approximated as $\lambda^2 = \frac{C_e D_e}{g} \approx \frac{2}{g}$ [85]. The numerical solution of the two differential heat equations (equation 2.5 and 2.6) yields the lattice temperature $T_{\mathrm{a}}(r,t)$ as a function of time and radial distance from track center. Within the model, track formation is defined as the radial area around the ion path, where the lattice temperature T_{a} reaches the melting temperature. In the calculation the latent heat for the solid-liquid phase change [86] is taken into account. Melting is followed by rapid quenching, freezing the molten phase. This condition is achieved by a strong electron phonon coupling described by g. The temperature of the atoms T_{a} as a function of radius can be converted into an energy deposition per atom (eV/at). This energy deposition profile can serve as an input for molecular dynamics simulations which provide information on the material structure, coordination and density in and around the track [86, 87].

3 Amorphous carbon materials

Carbon exists in a unique variety of crystalline and non-crystalline forms. Amorphous carbon is a term for a disordered form of carbon with no long-range order. The interatomic distances and interbonding angles deviate from graphite and diamond lattice [88]. The versatile microstructure of carbon originates from its three possible hybridizations sp^3, sp^2 and sp^1. Amorphous carbons consist primarily of sp^2 and sp^3 hybridizations. In the sp^3 (fourfold) bonding configuration, as present in diamond, the carbon atoms form four tetrahedrally oriented sp^3 orbitals that result in four strong σ bonds. In sp^2 (threefold) configuration, as in graphite, three σ bonds and one weaker π bond are formed by three trigonally directed sp^2 orbitals and one π orbital which lies perpendicular to the sp^2 orbital plane. The ratio and clustering of these bonding configurations essentially determines the material properties [89–91]. Due to the strong σ bonds, amorphous carbon with high sp^3 content is more dense than amorphous carbon with high sp^2 content. Depending on the sp^2 to sp^3 ratio, carbon can form structures in a broad range of densities from less than 2 g/cm^3 to more than 3 g/cm^3 [91]. The bonding ratio in amorphous carbon together with the degree and habitus of clustering defines the properties of the final structure. sp^3 bonding gives the amorphous carbon mechanical hardness [92–95], chemical and electrochemical inertness [96] and optical transmittance, whereas the sp^2 bonding provides electrical conductivity [97, 98]. Tailored engineering of the microstructure can therefore access a broad spectrum of properties for special demands. To distinguish the different forms of amorphous carbons, McKenzie[91] suggested to use the term tetrahedral amorphous carbon (t-aC) for disordered carbons with a high sp^3 content and amorphous carbon aC for a predominately sp^2 bonded network. Diamond like carbon (DLC) refers to an amorphous carbon with a "significant" amount of sp^3 and sp^2 bonding [89]. However in literature as well as by manufactures this nomenclature is not always used [99]. According to McKenzie [91], sp^2 rich amorphous carbon materials can be further classified by four criteria: the fraction of minority bonding (sp^3 or sp^1), the relative number of five-, six-, and seven- or higher-membered rings (ring statistics), dimensions, curvature and cross-linking of sp^2 bonded layers by sp^3 sites as well as the arrangement of adjacent sp^2 sheets.

Various methods are used for the deposition of amorphous carbon films (examples for references describing the method in brackets). Arc discharge ([100–102]), laser ablation ([103]), sputtering ([104]) and ion beam deposition ([98, 105]) are believed to produce films with a high degree of sp^3 bonding, whereas evaporated films ([105]) are mainly sp^2 coordinated [89, 91]. The deposition parameters influencing the final carbon film structure are summarized by Lifshitz. For all methods these parameters are the characteristics of the particle (distribution, energy, angle of incidence), the ambient pressure during deposition, the substrate temperature and deposition rate [99]. The structure of amorphous carbons can be identified by direct or indirect bonding characterization methods [106]. However, the short range order is hard to access due to missing analysis methods in terms of resolution and sensitivity [104, 106]. The use of different characterization techniques therefore helps to identify the characteristics of a certain structure from different perspectives [106].

3.1 Structure and properties of amorphous carbon materials

3.1.1 Electronic structure and electronic properties

The existence of σ and π bonds in carbon are the origin of its atypical behavior compared to other group 14 elements like Si or Ge. π bonds can be formed with more than one atom in the neighborhood, giving rise to long range forces and polarizability. This causes an enhancement of π-state matrix elements in infrared and Raman spectroscopy [89]. The interaction between σ and π states is small, since their orbitals lie perpendicular to each other and at different energy levels [107]. Robertson and O'Reilly developed a model [89, 90, 107] to describe the clustering within a mixed sp^2 and sp^3 bonded random network. Their model originates from the long-range attraction of the π states, that form a half-filled band and the energy gain by structural changes that produce a gap at the Fermi level E_F [89, 90]. The cluster model expresses criteria for sp^2 cluster formation in a sp^3 bonded matrix (described in detail in [89, 90, 107]). According to the model, the formed clusters tend to include an even number of π orbitals and to align parallel to each other forming planar sp^2 clusters to maximize the interaction. Delocalization of π electrons over a ring and the arrangement in larger graphitic sheets or clusters releases energy, whereas odd- or eight-membered rings are not favored, because they introduce states near E_F which lower the binding energy. Because the π states lie closer to the Fermi level than the σ states, the alignment of the cluster controls the electronic and optical properties and the matrix (sp^3) controls the mechanical properties. A schematic of the density of states (DOS) is presented in figure 3.1.1. The shape and size of the components vary depending on sp^2 and sp^3 bonding contents in a specific amorphous carbon sample as shown by Chen in [108]. For planar, compact sp^2 bonded clusters the band gap E_G was found to be given by $E_G \approx \frac{2\gamma}{M^{0.5}} \approx \frac{2\gamma}{L_a}$ where γ is an interaction parameter (in eV) describing the nearest neighbor V(ppπ) interaction between π orbitals, M is the number of sixfold rings in the cluster and L_a is the in-plane correlation length [89]. This finding of Robertson relates the size of the gap only to the sp^2 bonded clusters. According to Robertson, the model can explain the band gap of microcrystalline graphite and thermally annealed DLCs, but results in a too large degree of clustering in other amorphous carbons and therefore in bandgaps that are too large [89]. The reason for this is that distorted clusters have smaller band gaps, which means that the distortion of the clusters rather than their size controls the bandgap. In general, this model also applies for amorphous carbon which

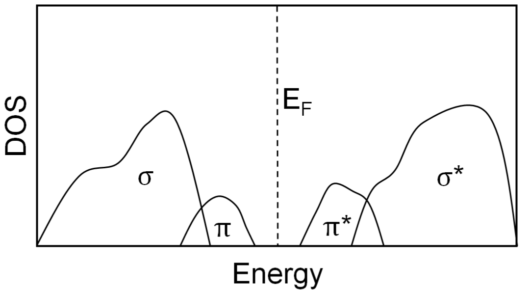

Figure 3.1.1.: Schematic DOS of amorphous carbon. The shape and height of the σ and π components varies depending on the fraction of sp^2 and sp^3 bonding (adapted from a scheme in [107] and calculated data in [89]).

are mainly sp^2 coordinated and will form sp^3 clusters in an sp^2 matrix. The high degree of disorder and defect density in amorphous carbon gives rise to states that lie slightly above the valence band edge or slightly below the conduction band edge.

Amorphous carbon is different in comparison to other amorphous semiconductors like a-Si or a-Ge because its structure possesses a significant amount of sp^2 hybridization. Since the π bonds give rise to a much lower energy gap than σ bonds, the electronic properties of amorphous carbon are controlled by the fraction and clustering of sp^2 coordinated atoms [97]. Amorphous carbon thus shows a different conduction mechanism than other tetrahedrally coordinated amorphous semiconductors. Dasgupta *et al.* [97] present a model that describes the conduction of amorphous carbons to be dependent mainly on the ratio of sp^2 to sp^3 bonding. They find different conduction processes for amorphous carbons with an sp^2 to sp^3 ratio above and below "percolation threshold" and for different temperature regimes. In amorphous carbons consisting of segregated graphitic islands of sp^2 bonded atoms in a sp^3 bonded matrix (DLC or t-aC) they attribute conduction near room temperature to hopping between neighboring sp^2 islands. Electrons are excited into empty states above Fermi level that are spatially located at the boundaries of the graphitic islands. By this, the excited electrons hop through the sp^3 matrix. For higher temperatures (above 500 K) conduction is based on the excitation of electrons to band-tail states of π bonded atoms. Both mechanisms are correlated to the size and average distance between graphitic islands.[97] For a sp^2 to sp^3 ratio above percolation threshold Dagupta *et al.* explain conduction by hopping in band tails for a wide range of temperatures.

3.1.2 Vibrational properties

The vibrational or phonon density of states (VDOS) for amorphous carbon reflects the character of sp^2 and sp^3 bonds. The sp^2 bonds are shorter and stiffer compared to sp^3 bonds, leading to a higher frequency of lattice vibrations. This can be seen also in the VDOS of graphite which has vibrational modes up to 1600 cm^{-1} ([109]), whereas the VDOS in diamond which extends up to 1400 cm^{-1} [91]. Since there is no crystal momentum conservation in amorphous materials, all phonon modes are allowed also in amorphous carbon, and phonons with arbitrary wave vector can participate in inelastic photon collisions [91]. The Raman and infrared spectra of amorphous carbons therefore should reproduce the vibrational density of states [90]. In case of Raman spectroscopy, the VDOS is weighted by a matrix element which enhances certain modes. Because π bonds lie at lower energy and therefore are more polarizable, the matrix element for π bonds is larger than for σ bonds, and sp^2 sites essentially determine the Raman spectrum [89, 110]. sp^3 bonding, even when in majority, therefore only indirectly affects the Raman spectrum by shifting the modes to higher frequencies and influencing the peak shape [91]. For infrared spectroscopy the matrix element does not show a large difference between sp^2 and sp^3 bonds and hereby resembles the VDOS better than a Raman spectrum of amorphous carbon [91].

3.2 Annealing effects and radiation damage in amorphous carbon

Swift-heavy ion irradiation causes structural changes in amorphous carbon by both temperature effects due to beam-induced heating and radiation damage. In literature, mainly annealing and low energy ion effects in the context of ion deposition processes are studied in amorphous carbon. Annealing of amorphous carbon films has been of interest in research motivated by the need of films of larger thickness, which is limited due to high stresses in films with a high sp^3 fraction. Stress can be released by temperature treatment, as reported by several groups. In t-aC films with high sp^3 content a stress relief was observed [111, 112], whereas for DLC films with intermediate sp^3 content an increase in the stress level was reported by Monteiro [113]. In addition, the controlled transformation from a phase with high sp^3 fraction to a high sp^2 fraction is of interest for electronic applications [114]. Electronic and field emission applications also motivate the production of local areas of sp^2 bonded carbon in an sp^3 matrix, for instance by laser patterning [114, 115]. In this context, the main methods for characterization of the induced changes are Raman spectroscopy [111, 113, 114, 116, 117] and electron energy loss spectroscopy (EELS) [112, 118]. All of these studies reveal graphitization when annealing amorphous carbon samples. Most structural changes were found to occur in the temperature range from 400 to 600°C [111, 113] or deposited laser energy density of 200 to 400 mJ/cm^2 [114], varying with the film thickness [115]. Dillon *et al.* [111] attribute the structural changes under annealing to the growth of crystallites in number and size. In addition, they observe a growth of crystallite dimensions above 800°C by a decrease of the I_D/I_G ratio (intensity ratio of the D and the G peak) in Raman spectra.

Only little research is concerned with energetic ion irradiation of amorphous carbons. Interest in radiation damage by energetic ions in amorphous carbon, mainly linked to materials in nuclear industry, or first walls in fusion reactors [119]. Pawlak *et al.* [120, 121] and Paterson *et al.* [122] found graphitization in hydrogenated amorphous carbon after ion bombardment. Rotaru *et al.* [83] studied the effect of electronic energy loss of different ions in deuterated amorphous carbon. They report a nonlinear decrease of sp^3 bonding content and of the deuterium concentration with increasing fluence. By fitting a Poisson law to the experimental data recorded at different fluences, they deduced the damage cross sections and the corresponding track radii (assuming cylindrical geometry). For uranium ions ($S_e = 25$ keV/nm) they find track radii between 4.2 ± 1.0 and 4.7 ± 0.9 nm. Waibliner [123] created conductive tracks in DLC films by swift heavy ion irradiation for the application as field emission cathodes. Inspired by this idea, Krauser, Zollondz and Schwen studied the conductivity [124–128], hillock height and diameter [124, 129], field emission properties [127, 130] and doping dependence [128, 131] of the graphitic ion tracks formed by different ions in t-aC and a-C:H (hydrogenated amorphous carbon) films by means of atomic force microscopy (topology- and current-mappings), transmission electron microscopy and molecular dynamics (MD) simulations.

Part II.

Experimental damage analysis of swift heavy ion irradiated carbon foils

4 Irradiation Conditions

Irradiation experiments were performed at the universal linear accelerator (UNILAC) (figure 1.0.2) at the GSI Helmholtzzentrum für Schwerionenforschung in Darmstadt. In the post-stripper section of the UNILAC, the ion beam can be extracted to the M-branch. Inside the M-branch cave, the beam can be directed to three different experimental beamlines M1, M2 and M3. For all irradiations and in-situ experiments in this work, the M3 beamline was used. After entering M3, the ion beam size and shape are adjusted by slits. The current measured at the slits is used for flux monitoring and control during irradiations and measurements. Calibration of the signal is performed using a Faraday cup located behind the slits. The adjusted beam spot on the sample varied between 1 and 4 cm^2. Three chambers allow experiments with different in-situ equipment (e.g. FTIR spectrometer, IR camera).

The irradiations in this work were performed with heavy ions such as ^{238}U and ^{197}Au. Since the energy loss scales with the square of the projectile atomic number (see Bethe-Bloch equation 2.3), the heavy ions induce maximum radiation damage in the samples. Selected ion energies for the irradiations were 3.6, 4.8 and 5.9 MeV/u. For carbon targets, these energies are in the range of the Bragg peak and the electronic energy loss is therefore at its maximum value (figure 2.0.1). In addition, these specific energies are below (only in case of 5.9 MeV/u slightly above) Coulomb barrier, which is desirable to minimize induced activation of the samples. A first adjustment of beam size and homogeneity is achieved by magnetic defocussing and visualization on a luminescence (Cr-doped Al_2O_3) screen. The samples were mounted on AlMg frames on aluminum holders.

All irradiations were performed at room temperature under normal beam incidence, accumulating fluences up to 10^{15} ions/cm^2 (estimated fluence uncertainty 10 to 20 %). The pulse structure of available beams varied for different experiments (see Table 4.0.1) between repetition rates of 50 and 0.2 Hz and pulse lengths between 4 and 0.1 ms. In the following, repetition rate and pulse length are used to specify beam conditions for certain ions. This large variation is due to different operation modes of ion sources available for beamtimes. The repetition rate slightly varies within the indicated frequency window due to beam sharing between UNILAC, synchrotron (SIS), and storage ring (ESR) experiments. Table 4.0.1 gives an overview of the irradiation conditions. The range of ions in amorphous carbon and graphite is in all cases far larger than the foil thickness.

In addition to the M3-irradiations, some standard samples produced at the GSI target laboratory (aC-TL) were irradiated in 2011 at the gas stripper position of the UNILAC (figure 1.0.2) with an energy of 1.4 MeV/u and a current of 5 mA. The round beamspot had a size of about 2 cm in diameter. The beam intensities at this irradiation facility are much higher (about one order of magnitude) compared to M-branch ion fluxes. The samples irradiated under these conditions provide therefore information on enhanced radiation damage due to lager fluences and larger ion fluxes.

Table 4.0.1.: Beam characteristics of different irradiation conditions. The energy loss dE/dx was calculated with SRIM-2013 code which only provides values for equilibrium charge state [59, 61], and a carbon density of 2.253 g/cm^2.

Ion	Energy (MeV/u)	Energy (MeV)	Pulse length (ms)	Repetition rate (Hz)	dE/dx (keV/nm)	Charge state
^{131}Xe	4.8	629	1.2	5	18.1	25+
^{197}Au	4.8	946	1.2	2	24.9	25+
^{197}Au	3.6	709	4	37	25.3	26+
^{197}Au	4.8	946	4	30 to 47	24.9	25+
^{197}Au	5.9	1162	4	32	24.3	26+
^{209}Bi	4.8	1003	0.5 to 1	3.4	26.4	26+
^{238}U	4.8	1142	0.1 to 0.4	0.2 to 2	31.6	28+, 29+
^{238}U	1.4*	333	0.15	1	27.2	4+

*Irradiation performed at gas stripper position (compare figure 1.0.2).

5 Samples

Carbon foils of different areal density ("thin" ∼20 µg/cm^2, "thick" ∼600 µg/cm^2), structure and origin were tested:

(1) amorphous carbon (aC-TL) foils produced by resistance evaporation at the GSI target laboratory [45],

(2) diamond-like carbon (DLC-MM) foils produced by laser-plasma ablation from MICROMATTER$^{\mathrm{TM}}$ (Canada),

(3) amorphous carbon foils (aC-ACF) produced by arc evaporation in vacuum from ACF-Metals, The Arizona Carbon Foil Co., Inc. (USA),

(4) single-walled carbon-nanotube based (buckypaper) foils (CNT-DN) prepared by vacuum filtration of nanotubes produced by laser ablation from Danubia NanoTech (Slovakia).

Present standard stripper foils at GSI are aC-TL, therefore they also served as a standard material in this study. Freestanding amorphous carbon foils are generally produced by covering a substrate with a soluble intermediate layer. In the case of aC-TL glass substrates are lubricated in a manual process with a betaine-sucrose solution. When drying, the sugar solution crystallizes. Carbon is deposited on the intermediate layer by resistance evaporation in high vacuum. The coated substrate is immersed in water, where the sucrose layer dissolves and releases the carbon foils which can be fished out onto AlMg frames. All thin foils are mounted slackened on the foils to prevent stresses, however wrinkles cannot always be avoided. Thick foils need to be glued to the frames with carbon paste (butylacetate and carbon soot). The foil thickness is given in areal density, because the mass density is not known. The areal density of the ∼600 µg/cm^2 foils was crosschecked by measuring the sample size and weight (microbalance) whereas the areal density of the ∼20 µg/cm^2 aC-TL foils was determined by means of UV-visible spectrometry. Since thickness variations within the thick foils are large, and the exact areal density of 600 µg/cm^2 hardly can produced, the term 600 µg/cm^2 refers to foils with an areal density between 570 and 630µg/cm^2. Thicknesses of the commercial foils were provided by the suppliers. All foils were fixed on identical aluminum frames with a round hole, providing self-supporting foils of 30 or 20 mm in diameter. Figure 5.0.1 and 5.0.2 present photographs of the transparent thin foils (20 µg/cm^2) and the opaque thick foils (∼600 µg/cm^2), respectively. aC-TL foils are less shiny compared to DLC-MM and ACF foils. Thick DLC-MM and aC-ACF foils can have a quite different morphology ranging from a flat and shiny surface to a buckled/wrinkled, and dull surface. Buckling is a common phenomenon observed in DLC foils (e. g. in [132]) and related to internal stresses of the films. Exemplary photographs of different foil morphologies are presented in figure 5.0.2. For off-line measurements small pieces of the irradiated samples were cut and deposited on silicon wafers (figure 5.0.3). Thin foils stick to the wafer by adhesion, thick foils had to be glued at the edges with carbon paste. For sample analysis, attention was paid to cut pieces from similar areas (center) of the beamspot, based on the assumption that the beamspot does not change for a series of irradiations. In addition to these samples for systematical measurements of this work, samples of other materials and thicknesses were irradiated and are presented in chapter 6.

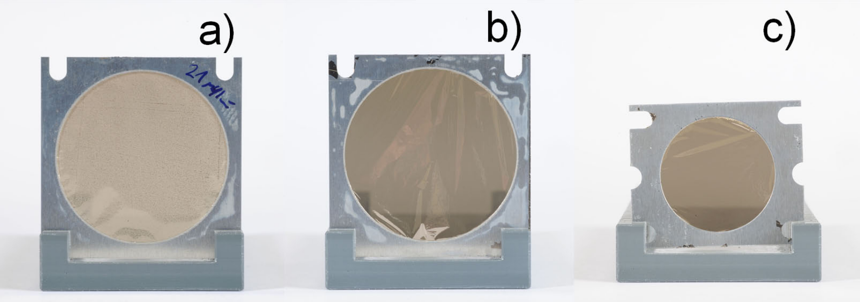

Figure 5.0.1.: Representative photographs of pristine 20 $\mu g/cm^2$ amorphous carbon foils. a): aC-TL (diameter 30 mm), b): DLC-MM (diameter 30 mm) and c): aC-ACF (diameter 20 mm)

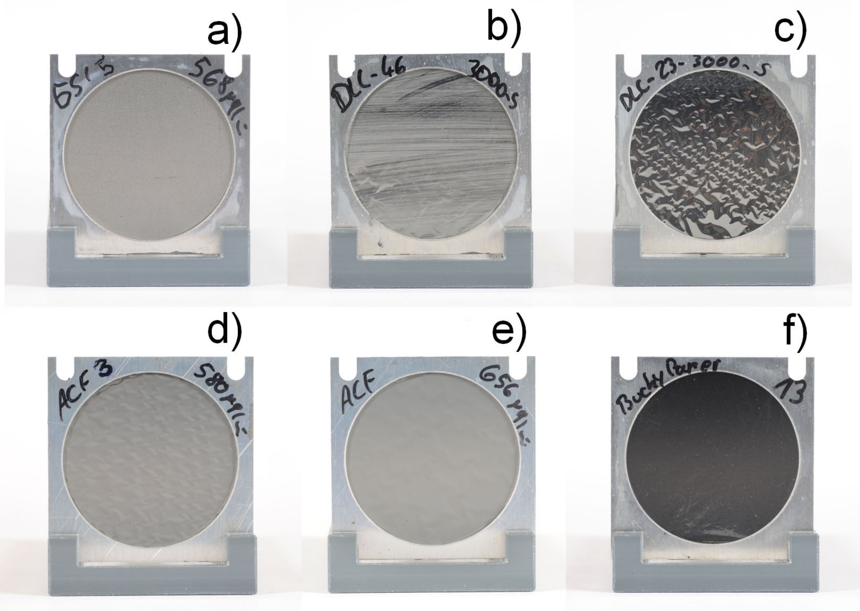

Figure 5.0.2.: Representative photographs of ~600 $\mu g/cm^2$ amorphous carbon foils (diameter 30 mm). a) aC-TL, b) and c) DLC-MM, d) and e) aC-ACF, f) CNT-DN

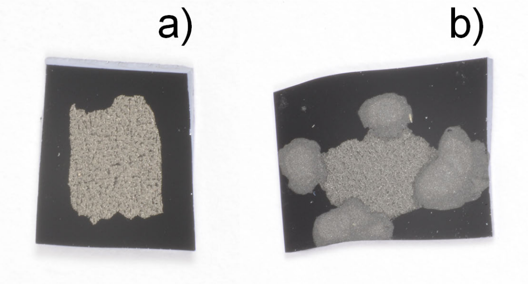

Figure 5.0.3.: Foils deposited on silicon wafers for off-line characterization. a) pristine 20 $\mu g/cm^2$ aC-TL, sticking to wafer by adhesion and b) ~600 $\mu g/cm^2$ aC-TL foil glued with carbon paste. The size of the foils is ~5×5 mm.

6 Visible changes in various carbon-based foils

This chapter presents visible beam-induced changes in various carbon-based stripper foils which yield first indications on the structural changes and factors causing final failure of the foils.

Figure 6.0.1 shows a 20 µg/cm^2 aC-TL foil during irradiation with 3.6 MeV/u Au ions (38 Hz, 4 ms). The images were taken with a camera attached to the beamline and show the evolution of the foil exposed to a square-shaped beamspot of approximately $15 \times 15\,\text{mm}^2$. At 5×10^{11} ions/cm^2 the border of the beamspot is clearly visible. The area outside this visible beamspot was probably irradiated by some secondary ions and is not completely pristine. In the following, this region is called halo (inspired by the term beam halo). The large wrinkles of the foil at low fluence show that the suspended foil experiences some tension due to the mounting on the frame. Up to about 5×10^{13} ions/cm^2 the material in the beamspot develops crinkles, indicating some kind of material modification. At the largest fluence (5×10^{14} ions/cm^2) a typical tensile stress pattern is visible in beamspot, suggesting that the material within the beamspot undergoes compaction. This phenomenon is known and the reason why stripper foils are usually mounted slackened on the frames [45].

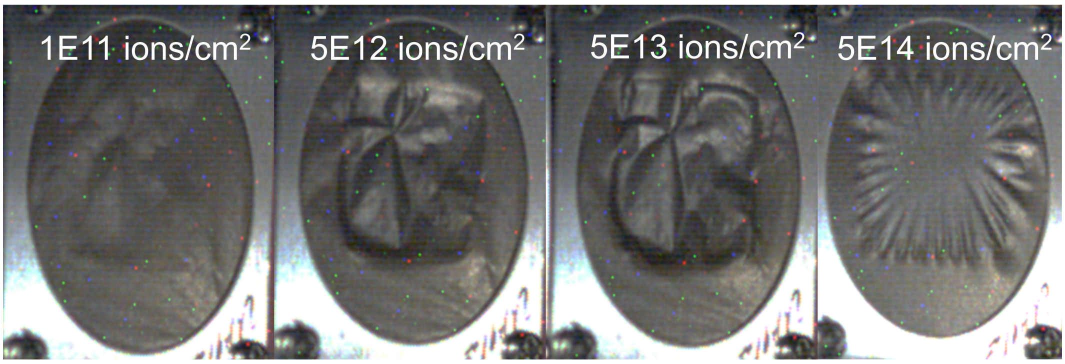

Figure 6.0.1.: Photographs of a 20 µg/cm^2 aC-TL foil (∅ 30 mm) at different fluence steps under irradiation with a 3.6 MeV/u Au ions (38 Hz, 4 ms) showing the material transformation in the beamspot and compaction at high fluence.

Another example is presented in figure 6.0.2, which shows an aC-TL foil irradiated with 4.8 MeV/u U ions of a fluence of 5.7×10^{14} ions/cm^2. The material in the beamspot does not appear as smooth and shiny as the halo area. This image thus also indicates a material transformation. The transformation of ion-irradiated amorphous carbon has been described as a graphitization process already in 1979 by Sander and 1987 by Dollinger [46, 51, 56]. The photographs in figure 6.0.1 and 6.0.2 show the consequences of this graphitization process by compaction and the different material appearance in the beamspot. The graphitization process in aC-TL seems to increase the density, which in turn indicates that pristine aC-TL has a lower density than (nanocrystalline) graphite. Since amorphous carbon films with some fraction

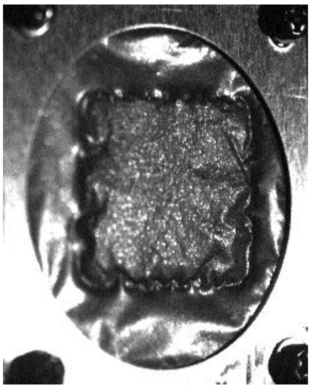

Figure 6.0.2.: Graphitized beamspot (~15×15 mm^2) of 20 µg/cm^2 aC-TL (∅ 30 mm) irradiated with 4.8 MeV/u U ions of a fluence 5.7×10^{14} ions/cm^2.

of sp^3 bonding generally have a higher density (as for example in [107]), the observed compaction gives rise to the assumption that aC-TL holds some degree of porosity. Experimental evidence for this hypothesis is given in the following chapters of this work.

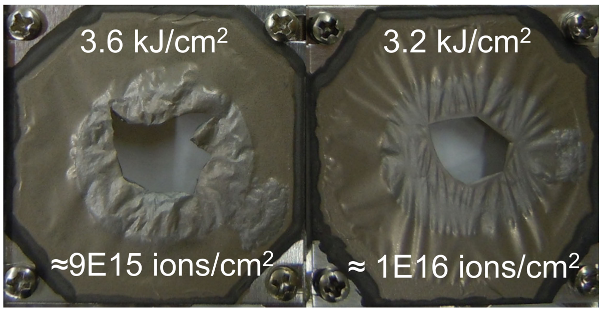

Figure 6.0.3.: Photographs of 20 µg/cm^2 aC-TL foils (∅ 30 mm) irradiated with 1.4 MeV/u U ions (1 Hz, 0.15 ms) showing a colour change of the material and thinning in the beamspot.

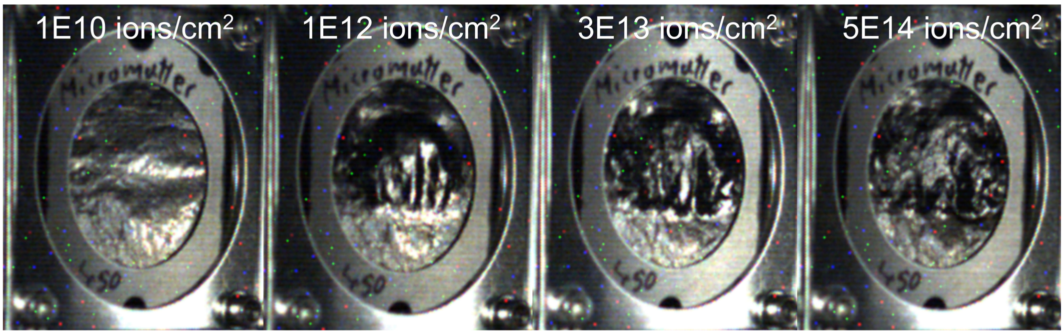

Figure 6.0.4.: Photographs of a ~95 µg/cm^2 DLC-MM foil during irradiation with a 3.6 MeV/u Au beam (38 Hz, 4 ms) showing expansion at high fluence.

Irradiation at the gas stripper position (1.4 MeV/u U ions, 1 Hz, 0.15 ms, see table 4.0.1) results in thinning of the foils, cracking and finally loss of the material in the beamspot center (figure 6.0.3). In this case the beamspot was focused and therefore has a Gaussian intensity distribution. The irradiated area around the center of the beamspot shows wrinkling and a color change. The color change suggests that the graphitization influences the optical properties.

In contrast to beam-induced compaction of aC-TL foils, DLC-MM foils show wrinkles in the beamspot area throughout the irradiation (figure 6.0.4). The evolution of slackening indicates that the material expands and that the density decreases.

Figure 6.0.5 presents photos of various other carbon foils. The response of buckypaper foils[1] ($140\,\mu g/cm^2$), covered with a sputter-deposited $10\,\mu g/cm^2$ carbon layer and irradiated with 3.6 MeV/u Au beam (38 Hz, 4 ms) of a fluence of 8×10^{12} ions/cm^2 and with 4.8 MeV/u U ions (1 Hz, 0.2 ms) of 8×10^{12} ions/cm^2 are shown in figure 6.0.5a and b. A $250\,\mu g/cm^2$ graphene platelet-based foil[2] irradiated with 4.8 MeV/u U ions (1 Hz, 0.2 ms) of a fluence 5×10^{13} ions/cm^2 is presented in figure 6.0.5c. The buckypaper foils show wrinkles in the beamspot related to stresses due to material transformations, which finally cause the foils to fail. The graphene-platelet foil presents a very sharp transition between halo and beamspot, which resulted in the complete loss of the material in the beamspot. Like in the case of aC-TL, this is an indication that the transition area between beamspot and halo plays a critical role for failure. For comparison, an aC-TL foil of $97\,\mu g/cm^2$ irradiated with 4.8 MeV/u U ions (1 Hz, 0.2 ms) at a fluence of 5×10^{13} ions/cm^2 is presented in 6.0.5d. The foil was deposited slackened to avoid stresses due to compaction, showing that aC-TL in contrast to the presented alternative materials in figure 6.0.5a, b and c does not fail in a medium fluence regime.

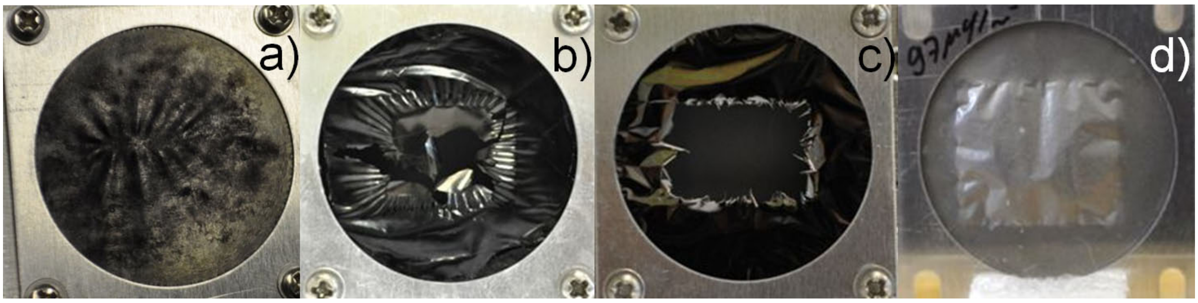

Figure 6.0.5.: a) buckypaper of $140\,\mu g/cm^2$ irradated with 3.6 MeV/u Au ions (38 Hz, 4 ms) of a fluence 8×10^{12} ions/cm^2 and b) irradiated with 4.8 MeV/u U ions (1 Hz, 0.2 ms) to 8×10^{12} ions/cm^2. c) Graphene platelet-based foil $250\,\mu g/cm^2$ irradiated with 4.8 MeV/u U ions (1 Hz, 0.2 ms) of fluence 5×10^{13} ions/cm^2. d) presents a $97\,\mu g/cm^2$ aC-TL foil (deposited slackened to avoid stresses) irradiated with 4.8 MeV/u U ions of fluence 5×10^{13} ions/cm^2.

---

[1] provided by Hiroo Hasebe, RIKEN Nishina Center, Japan.

[2] provided by Applied Nanotech, Inc., USA.

7 Morphological changes

7.1 Optical microscopy

Light-optical microscopy provides a simple tool to visualize surface (micro-)structure of different carbon-based samples. Bright-field illumination generates a contrast based on the absorption of light in the sample and dark-field illumination probes the light scattered by the sample. The combination of these two illumination techniques creates a comprehensive view of the sample microstructures.

Figure 7.1.1 presents representative micrographs in bright-field (a, c, e) and dark field (b, d, f) mode of different magnifications for pristine 20 $\mu g/cm^2$ aC-TL foils. The micrographs are also representative for thick aC-TL foils, because the surface microstructure of 600 $\mu g/cm^2$ aC-TL shows no significant difference compared to thin foils. Even at lowest magnification (7.1.1a, b), a reproduction of betaine-sucrose crystals can be observed. Bright areas in figure 7.1.1a correspond to thin and flat sample areas, in which the sucrose solution did not recrystallize. These areas do not correspond to holes as confirmed by scanning transmission electron microscopy (section 7.2). At larger magnification in figure 7.1.1c and d, the size, shape and distribution of the crystal replica can be identified. The size of the reproduced crystals ranges from a few μm to up to 30 μm and their shape is relatively round, with out sharp edges. Accumulation of small or large crystals can be seen, but also mixed areas. At highest magnification (7.1.1e and f), cracks across the sugar crystal replica become visible. Due to the different heights, not all crystal replica are in focus.

Im comparison to the pristine material, aC-TL irradiated with 4.8 MeV/u U ions (5×10^{14} ions/cm^2) appears similar at low magnification (7.1.2a and b). Higher magnification images show that the sugar crystal replica do not have the round shape and smooth edges as in the pristine material (7.1.2c to f).

An aC-TL foil irradiated at the gas stripper position (1.4 MeV/u) to about 3.8×10^{16} ions/cm^2 seems to be thinner in the area of the beam spot center because this area appears brighter (left part figure 7.1.3a and b). The reproduced morphology of the betaine-sucrose crystals almost disappeared and only small foldings remain (figure 7.1.3 c to f). This causes a flattening of the sample compared to the pristine foil.

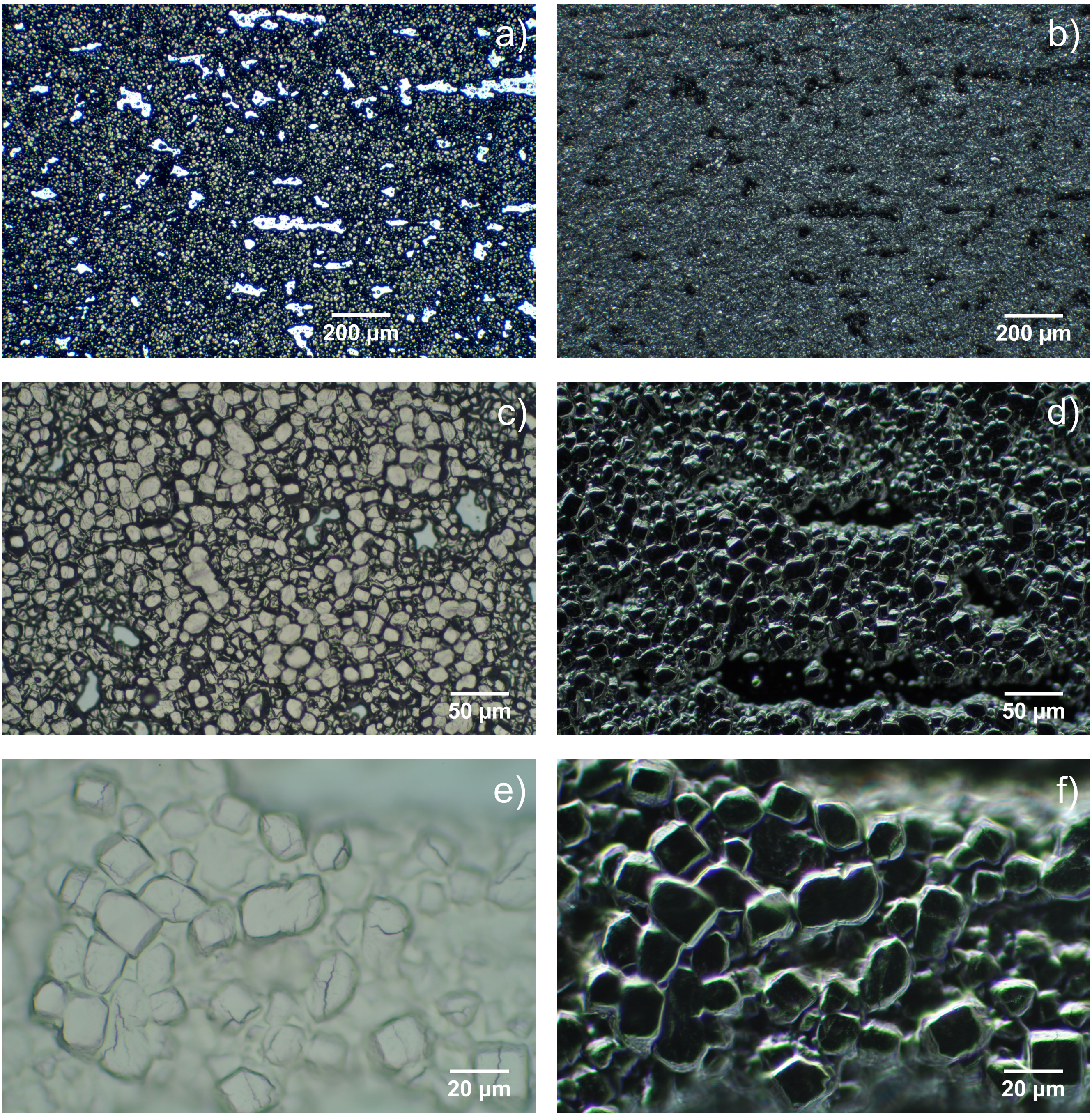

Figure 7.1.1.: Representative light-optical micrographs (bright-field (a, c, e) and dark field (b, d, f)) at different magnifications of pristine 20 μg/cm^2 aC-TL foils. The micrographs are also representative for thick aC-TL foils, because the surface microstructure of 600 μg/cm^2 aC-TL shows no significant difference compared to thin foils.

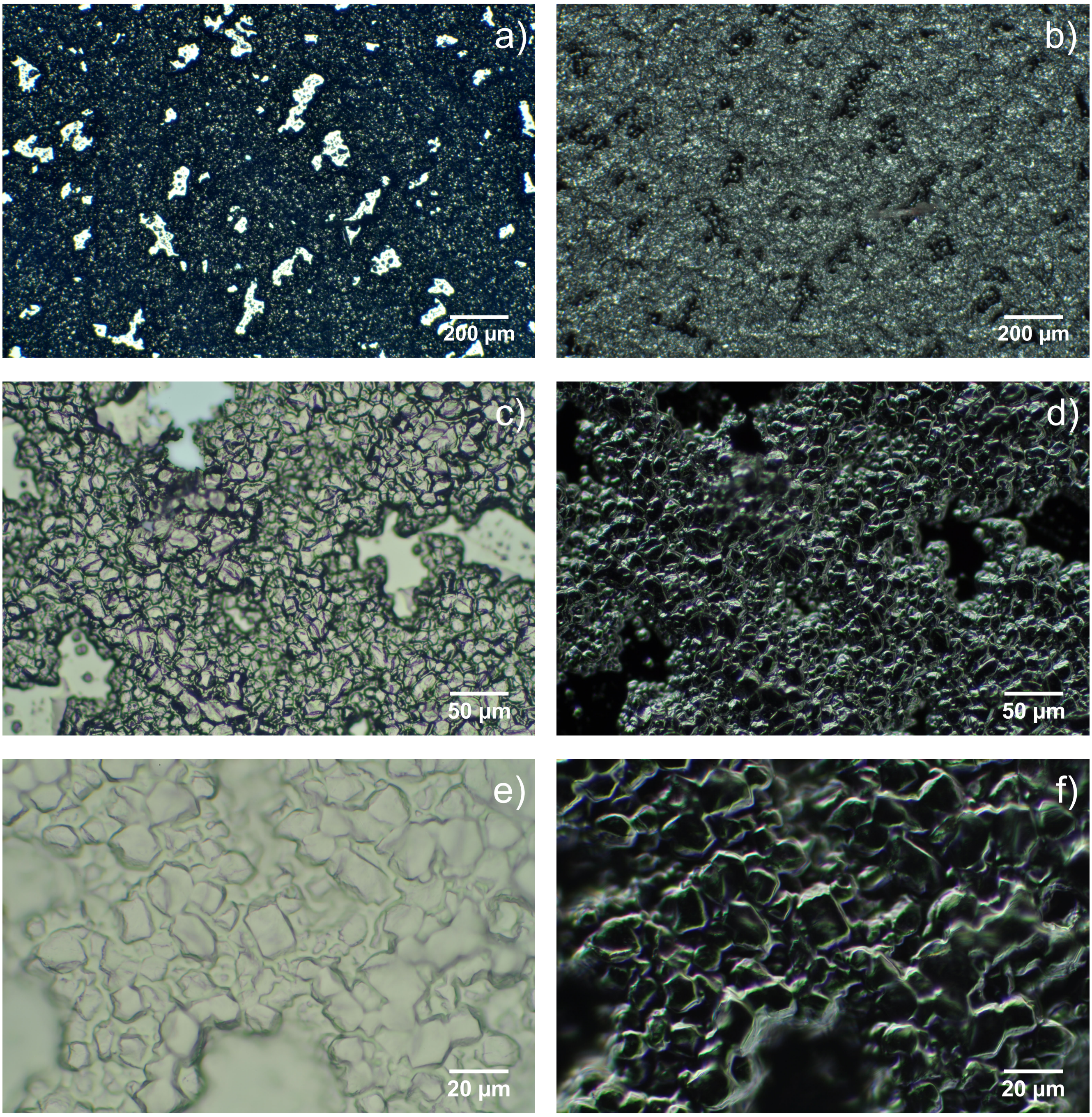

Figure 7.1.2.: Representative light-optical micrographs of 20 and 600 µg/cm^2 aC-TL foils irradiated with 4.8 MeV/u U ions of fluence of 5×10^{14} ions/cm^2.

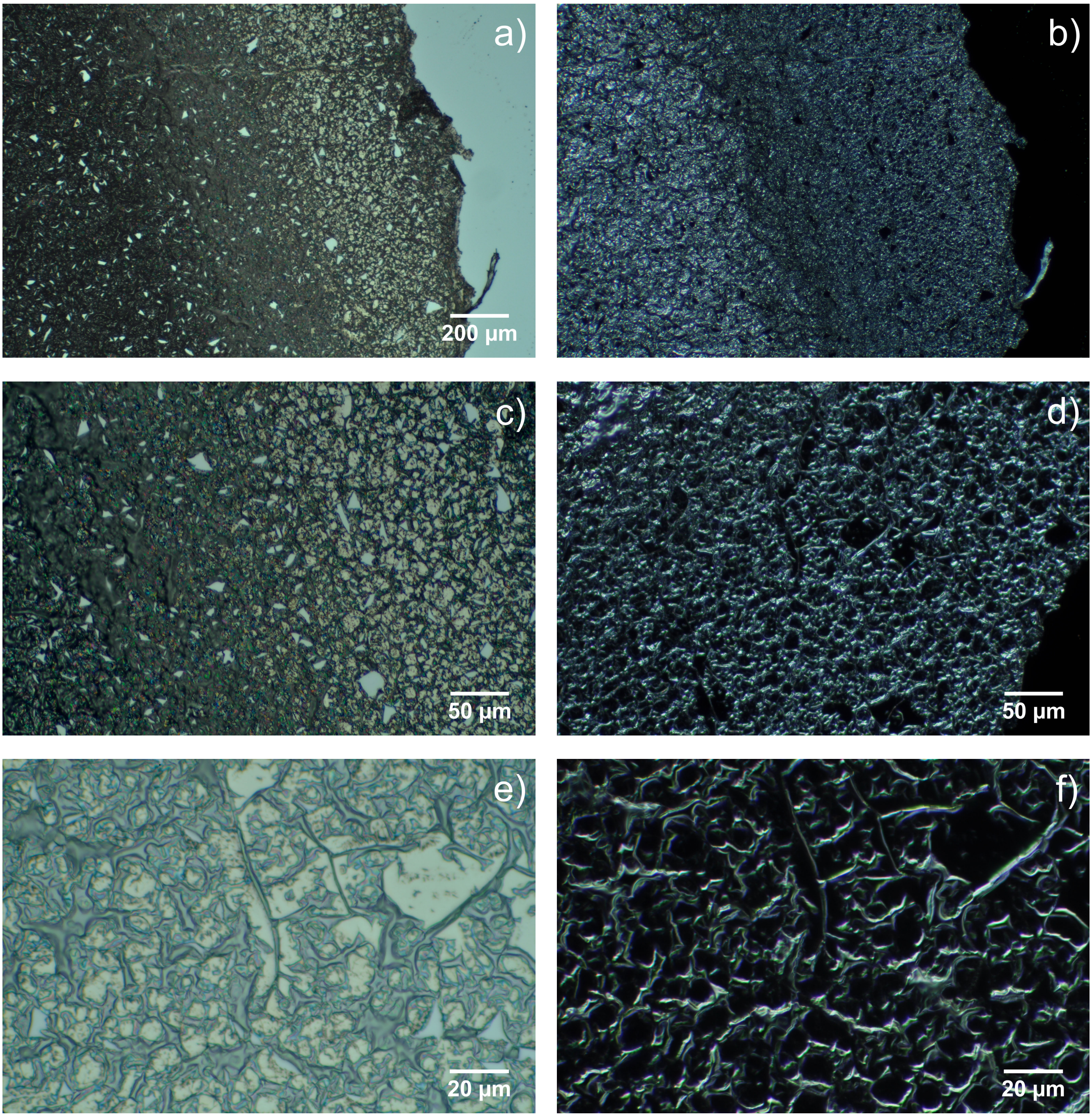

Figure 7.1.3.: Representative light-optical micrographs of 20 μg/cm^2 aC-TL foil irradiated at the gas stripper position with 1.4 MeV/u U ions of fluence $\sim$3.8 × 10^{16} ions/cm^2.

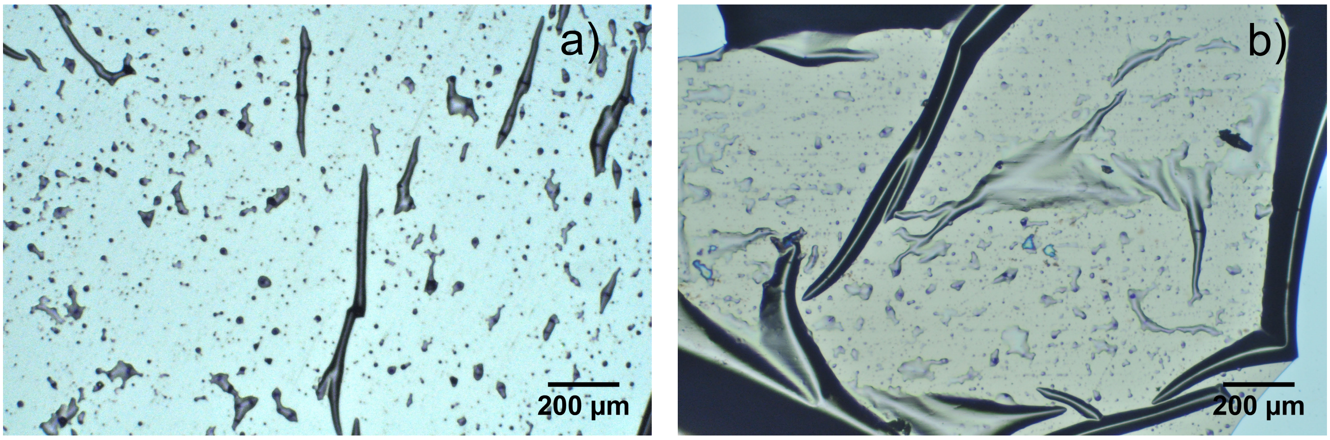

Figure 7.1.4.: Representative light-optical micrographs of 20 µg/cm^2 DLC-MM foils: a) pristine and b) irradiated with 4.8 MeV/u U ions of fluence 5×10^{13} ions/cm^2.

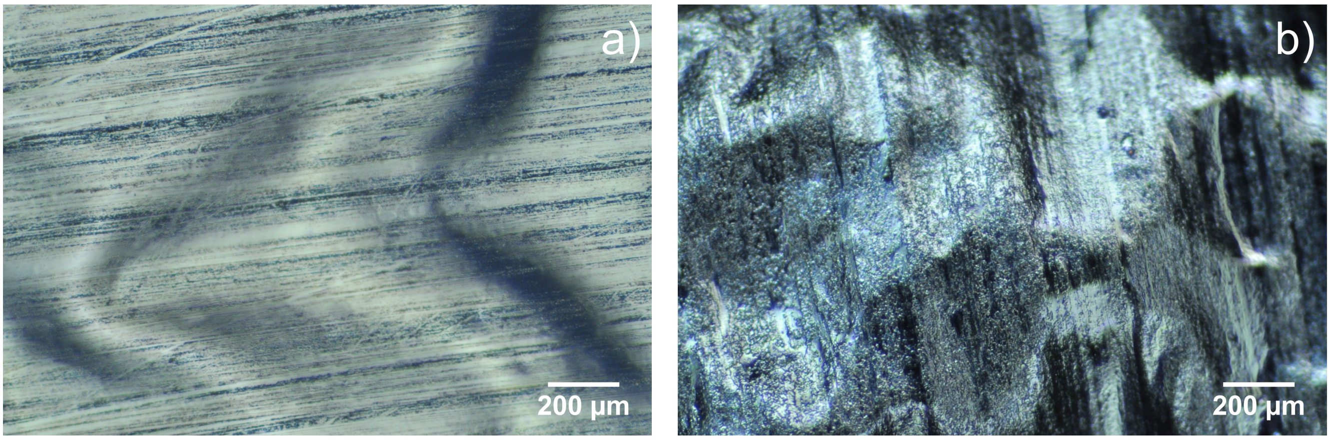

Figure 7.1.5.: Representative light-optical micrographs of ≈600 µg/cm^2 DLC-MM foils: a) pristine and b) irradiated with 4.8 MeV/u Au ions of fluence 5×10^{13} ions/cm^2.

Pristine 20 µg/cm^2 DLC-MM (figure 7.1.4a) shows a very flat surface with some small pinholes or defects. The folded areas originate from the deposition onto a silicon wafer. The surface of DLC-MM irradiated with 4.8 MeV/u U ions of fluence 5×10^{13} ions/cm^2 (figure 7.1.4b) shows no significant difference in microstructure. Because these foils do not exhibit small structures like the crystal replica in case of aC-TL, only images at large magnification are presented (also for the foils in the following). The situation is different in thick 600 µg/cm^2 DLC-MM foils (figure 7.1.5a and b where large and symmetric buckling is visible in the pristine foil figure 7.1.5a, whereas the irradiated material (4.8 MeV/u Au, 5×10^{13} ions/cm^2) in figure 7.1.5b shows wrinkles and buckling, which is not symmetric.

Thin 20 µg/cm^2 aC-ACF in figure 7.1.6 appears very similar in pristine and irradiated (4.8 MeV/u Au, 5×10^{13} ions/cm^2) state. Small defects are visible in both pristine and irradiated material, the foldings and air inclusions originate from deposition onto the silicon wafer. 600 µg/cm^2 aC-ACF foils before and after irradiation (4.8 MeV/u Au, 5×10^{13} ions/cm^2) in figure 7.1.7 and b, respectively, show similar buckling, but irradiation leads to stronger buckling.

The microstructural appearance of pristine and irradiated CNT-DN (4.8 MeV/u Au, 1×10^{12} ions/cm^2) in figure 7.1.8 is not significantly different, both micrographs present a large number of defects.

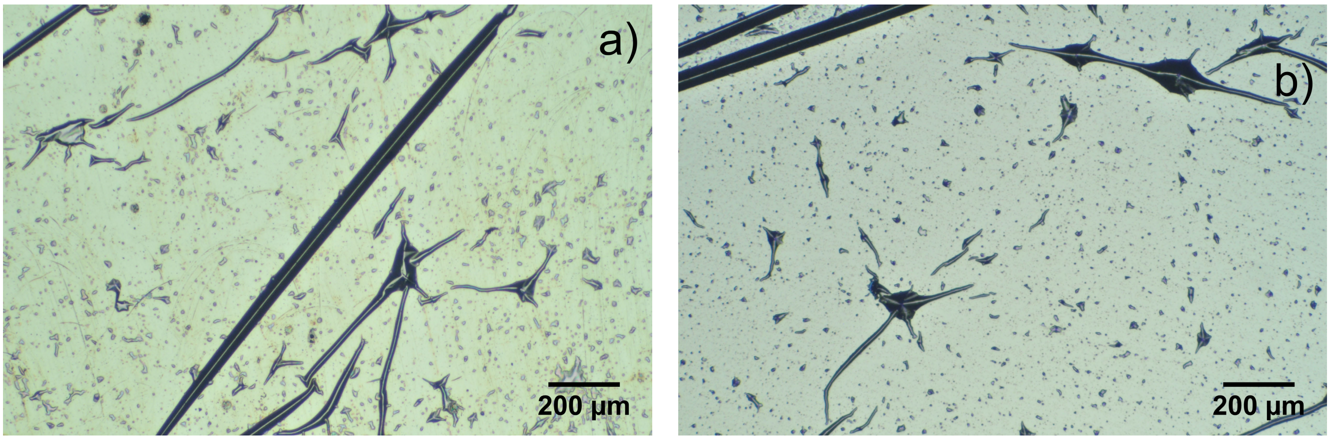

Figure 7.1.6.: Representative light-optical micrographs of 20 µg/cm^2 aC-ACF foils: a) pristine and b) irradiated with 4.8 MeV/u Au ions of fluence 5×10^{13} ions/cm^2.

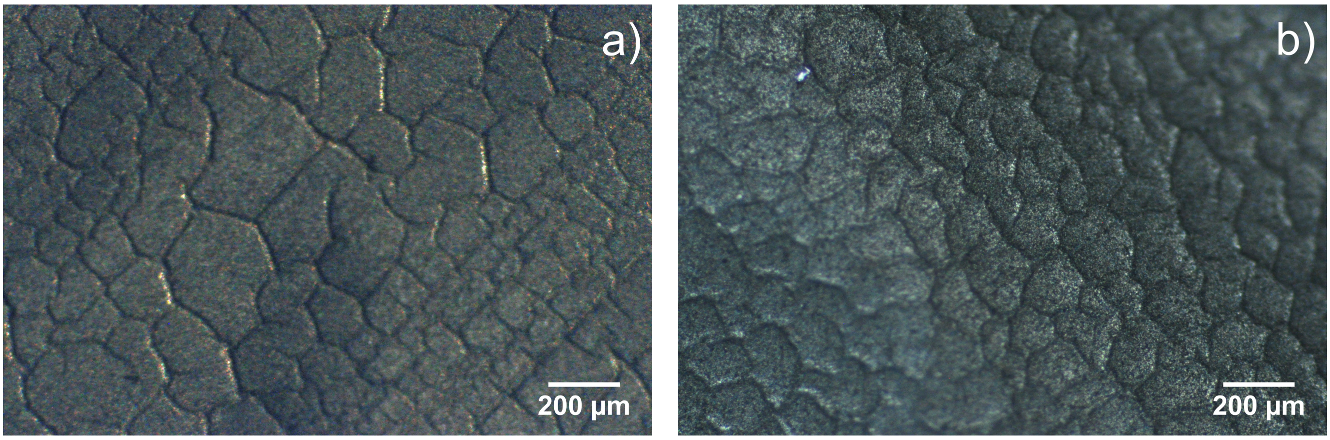

Figure 7.1.7.: Representative light-optical micrographs of 600 µg/cm^2 aC-ACF foils: a) pristine and b) irradiated with 4.8 MeV/u Au ions of fluence 5×10^{13} ions/cm^2.

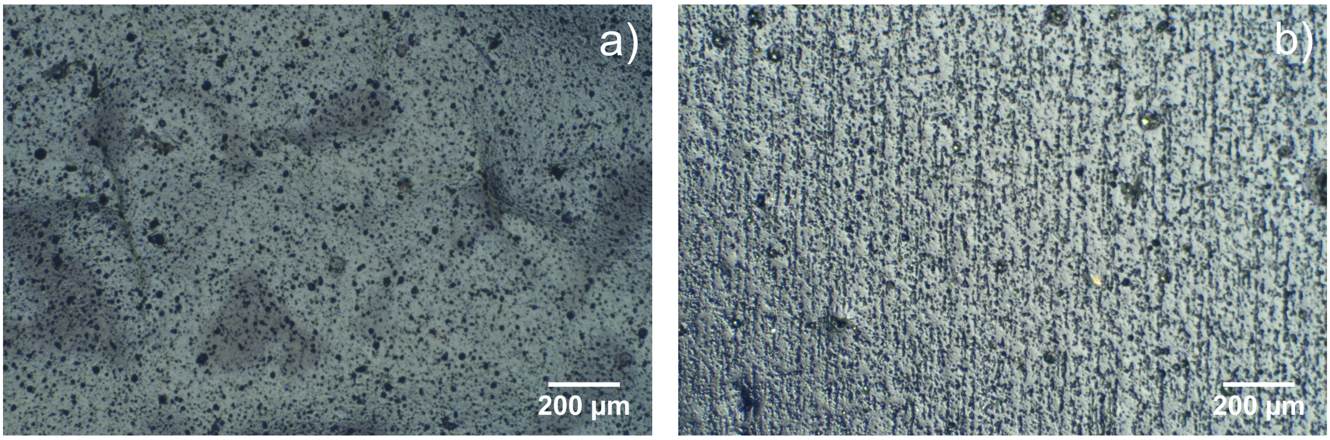

Figure 7.1.8.: Representative light-optical micrographs of 200 µg/cm^2 CNT-DN foils: a) pristine and b) irradiated with 4.8 MeV/u Au ions of fluence 1×10^{12} ions/cm^2.

In conclusion, light-optical micrographs provided a quick and easy access on the microstructure before and after ion irradiation. Only for aC-TL foils exposed to most extreme conditions at 1×10^{14} ions/cm^2 a significant difference was identified. For 600 µg/cm^2 DLC-MM and aC-ACF foils no significant microstructural changes were observed except increased buckling and wrinkles.

7.2 Scanning electron microscopy

Complementary to optical microscopy, scanning electron microscopy (SEM) and scanning transmission electron microscopy (STEM) were used for the investigation of the microstructure of aC-TL samples. Because electrons have a much smaller de Broglie wavelength than visible light, a much higher resolution can be achieved compared to optical microscopy. The beam is focused on a specimen and scanned over the sample in a raster pattern. STEM mode detects the transmitted electrons passing through a thin specimen and therefore combines the principles of transmission electron microscopy and scanning electron microscopy. A JEOL JSM-7401F scanning electron microscope equipped with a transmission electron detector (STEM-in-SEM) at 20 kV and with a working distance of 6 mm was used for the imaging of 20 μg/cm^2 aC-TL foils. For SEM imaging, the aC-TL foils were attached to silicon wafers, while the foils were sandwiched between double copper TEM grids with a diameter of 3.05 mm for STEM mode. Two different secondary electron detectors were used for imaging: the lower detector (LEI) provides some topological information, but usually images are coarser and the upper detector (SEI) which usually provides better resolved images.

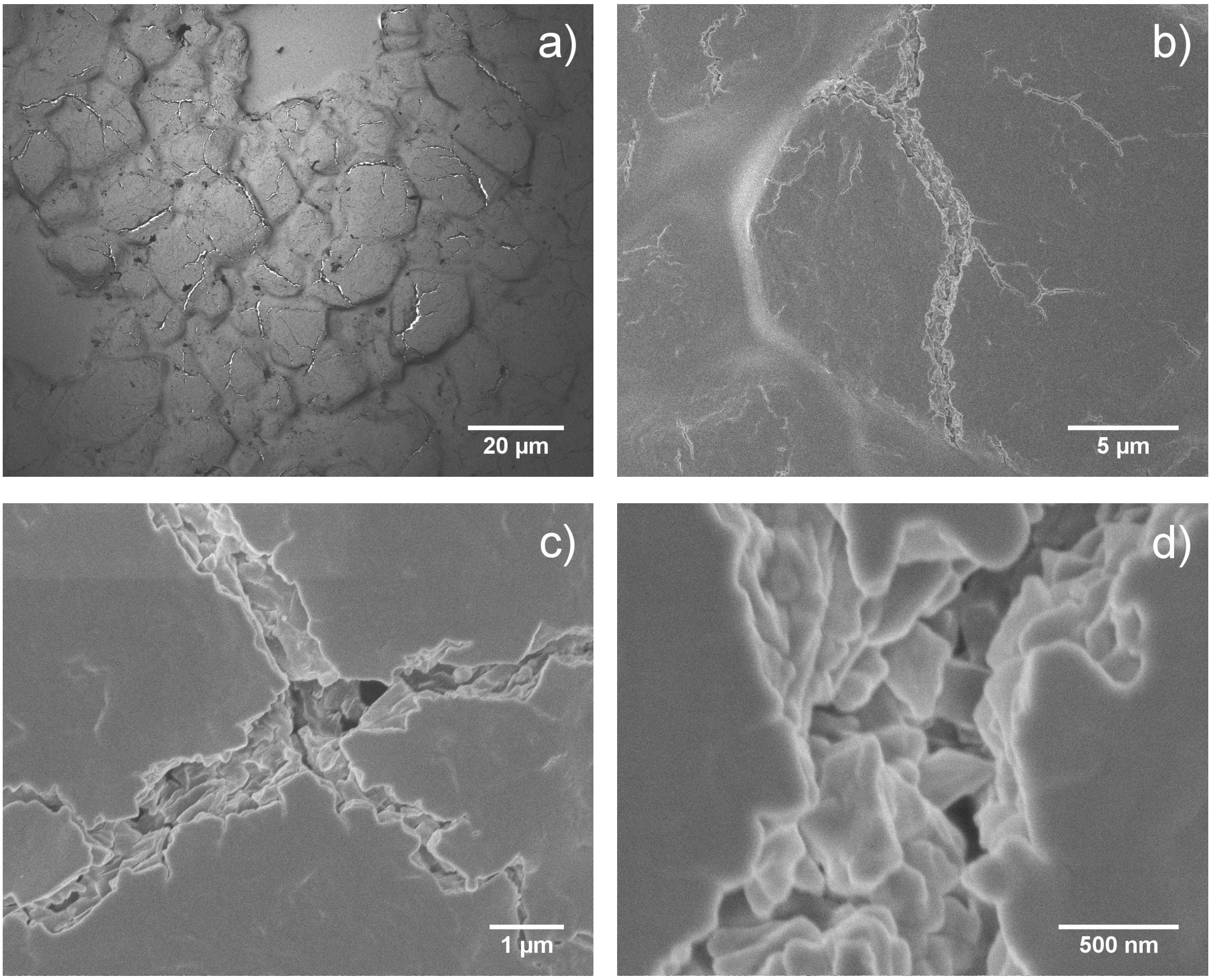

Figure 7.2.1.: SEM images of 20 μg/cm^2 pristine aC-TL. a) STEM and b)-d) SEM mode.

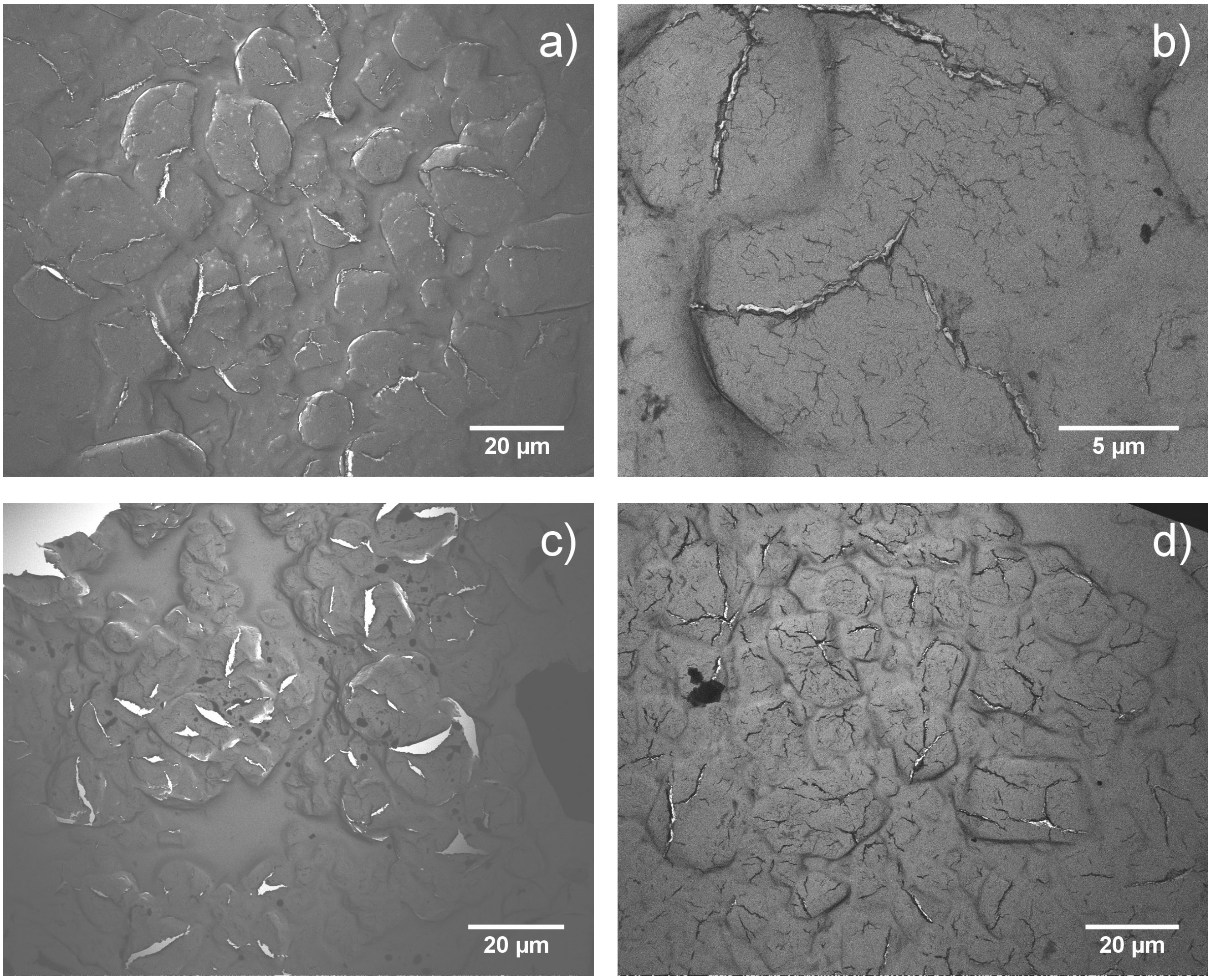

Figure 7.2.2.: STEM images of 20 μg/cm^2 aC-TL irradiated with (a, b) 4.8 MeV/u U ions, fluence of 5.7×10^{14} ions/cm^2 and 1.4 MeV/u U ions, fluence of $\approx 3.8 \times 10^{16}$ ions/cm^2, in the beamspot (c) and halo (d).

Figure 7.2.1 shows images of pristine 20 µg/cm^2 aC-TL foils. Penetrating cracks (white) and surface cracks (black) are visible for pristine material (figure 7.2.1a). Imaging at higher magnification (figure 7.2.1b to 7.2.1d) shows a platelet-structure in the crack, suggesting a porous structure of the sample. A representative STEM image of the beamspot of an aC-TL foil irradiated with 4.8 MeV/u U ions (fluence 5.7×10^{14} ions/cm^2) is presented in figure 7.2.2a. A large number of cracks (white) is visible. The halo region (figure 7.2.2b) shows an increased number of widespread and small surface cracks (black) compared to the pristine material. In the beamspot center of an aC-TL sample irradiated at gas stripper position (1.4 MeV/u U ions, 3.8×10^{16} ions/cm^2) larger cracks appear (figure 7.2.2c). Also the halo region of this sample shows a large number of surface cracks, possibly caused by tensile stresses due to compaction of the material in the beamspot center (figure 7.2.2d). The compaction of aC-TL was also observed for an aC-TL foil irradiated with 4.8 MeV/u Au ions (figure 6.0.1), which showed pronounced buckling in the transition area from irradiated (beamspot) to non-irradiated (halo) area. To clarify the role of the cracks to failure process, penetrating cracks were analyzed in terms of length. For each

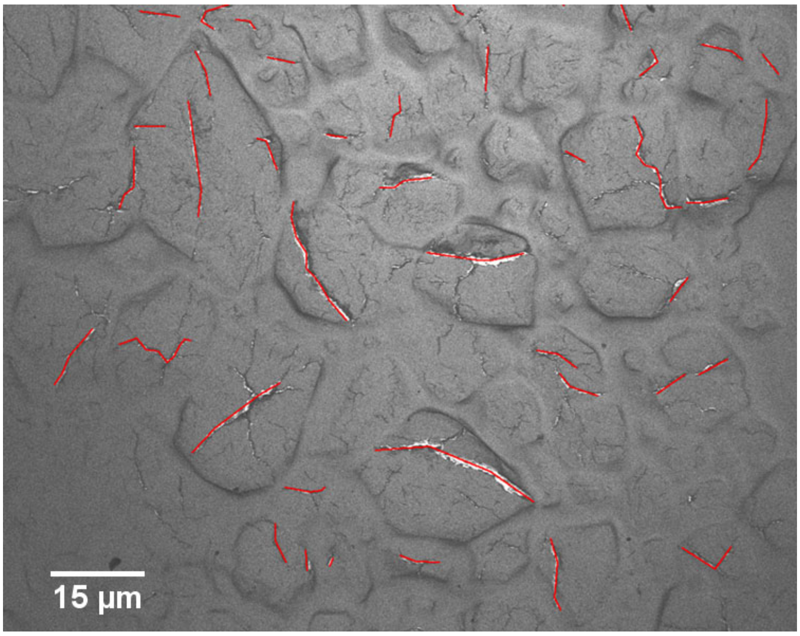

Figure 7.2.3.: STEM images of 20 µg/cm^2 aC-TL irradiated with 4.8 MeV/u U ions of 5.7×10^{14} ions/cm^2 with crack length analysis by segmented lines along penetrating cracks (red).

sample of a given fluence, 15 images recorded in the STEM mode were investigated in halo and beamspot regions. Using the program ImageJ [133], the length of the cracks was measured by defining segmented lines along penetrating cracks (figure 7.2.3). Cracks smaller than 6 µm were disregarded, due to the high chance of omitting some of these cracks.

Histograms in figure 7.2.4 present the number of cracks per mm^2 as a function of crack length, grouped into bins of 2 µm width. Three fluences for 4.8 MeV/u Au and U ions were investigated: A low fluence of 1×10^{11} ions/cm^2 for Au ions and 5×10^{11} ions/cm^2 for U ions (figure 7.2.4a), 5×10^{12} ions/cm^2 for both ions(figure 7.2.4b) and 5×10^{14} ions/cm^2 for Au and 5.7×10^{14} ions/cm^2 for U ions (figure 7.2.4c). The errors of 5 % account for the possibility of missing penetrating cracks, which is larger for small crack sizes. The error of crack length is disregarded, because this uncertainty is thought to be small in comparison to the used bin with of 2 µm.

For low fluences (figure 7.2.4a), the number of cracks is similar or slightly larger for the pristine sample compared to the irradiated samples. Only in the halo region, the number of intermediate cracks with sizes in the range of 12 to 16 µm appear to be slightly increased. An increased number of intermediate cracks (8 to 14 µm) in the halo region is clearly seen for an intermediate fluence 5×10^{12} ions/cm^2 of irradiation with Au ions. The number of small and intermediate cracks (6 to 12µm) in the beamspot is larger compared to the pristine sample. This effect is not seen in the samples irradiated with U ions, indicating an influence of the beam pulse structure on the cracking process. A reason could be the different temperature profiles for different beam structures (details in chapter 10): The high-repetition rate of the Au beam causes a higher mean and base temperature during irradiation, so that the sample material in the beamspot is constantly heated during irradiation. For U irradiation, the temperature rises shortly to high values, followed by cooling after each pulse. A constant heating in the beamspot causes also heating of the halo area and the frame. Stresses might be induced by a different degree of thermal expansion of the AlMg frame and aC-TL (coefficient of thermal expansion (CTE) of Al with

$23.1 \times 10^{-6}K^{-1}$ [134] is about a factor of ten larger compared to aC:H as found by Marques *et al.* [135] with $2-4 \times 10^{-6}K^{-1}$ for aC:H depending on sp^2 fraction.). Also, different temperatures in the beamspot and halo region might cause stresses that finally result in cracks. At high fluences, an increased number of very small (6 to 10 µm) cracks in the beamspot and intermediate to large (8 to 12 and 14 to 22 µm) cracks in the halo region are observed for the irradiation with Au ions. The irradiation with U ions causes an increase of the number of intermediate and large cracks (8 to 22 µm) especially in the beamspot, but also in the halo region. At large fluences the effect of beam-induced material transformation might be larger than effects due to different temperature profiles. As indicated in section 6, aC-TL foils experience compaction, possibly causing an increased number of cracks in both beamspot and halo region. The larger energy loss of U ions in the material could also explain, why this effect is more pronounced for U compared to Au irradiation. A direct comparison of the total number of cracks in figure 7.2.4d shows that the overall number of cracks slightly rises with increasing fluence for both, Au and U irradiation. The total number of cracks is larger in pristine aC-TL than in low- and intermediate fluence material. A reason is, that the number of small cracks has the largest contribution to the total number of cracks and that a large number of small cracks is prominent already in pristine material. Nevertheless the total number of cracks in foils irradiated with U ions is larger than in pristine materials at higher fluences.

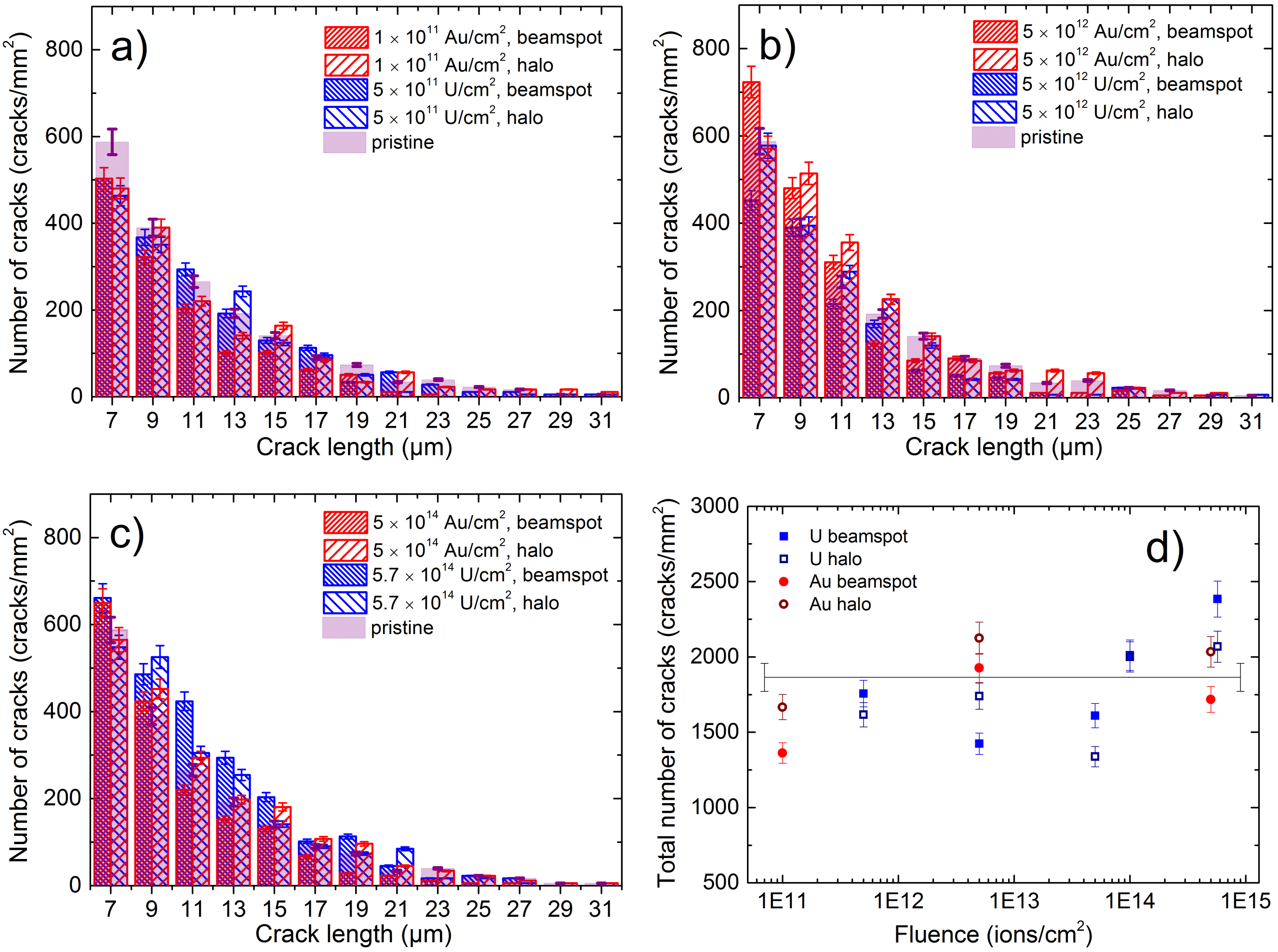

Figure 7.2.4.: Number of cracks per mm^2 as a function of crack length, grouped into bins of 2 µm width. Three fluences for irradiation with 4.8 MeV/u Au and U ions were investigated: a) 1×10^{11} ions/cm^2 for Au ions and 5×10^{11} ions/cm^2 for U ions, b) 5×10^{12} ions/cm^2 for both ions and c) 5×10^{14} ions/cm^2 for Au and 5.7×10^{14} ions/cm^2 for U ions. d) Total number of cracks per mm^2 as a function of fluence.

7.3 Profilometry

As seen from optical microscopy measurements, the microstructure and morphology of amorphous carbon samples from different suppliers is quite different. The characteristics of micro-slackening and buckling can be investigated by profilometry in order to obtain information on topography. The profilometer stylus is in contact with the sample under a defined load or contact force and scans laterally across a specified distance. Scan speed and data signal sampling rate control the horizontal resolution.

A DEKTAK profilometer from Veeco with a tip radius of 12 μm was used for the measurements. Samples were deposited on silicon wafers. The thin foils (20 μg/cm^2) stick to the wafer by adhesion, whereas thick foils (∼600 μg/cm^2) had to be glued at the edges with carbon paste. Scan lengths were in the range of mm with a resolution 0.22 to 0.30 μm.

A comparison of 20 and 600 μg/cm^2 aC-TL, DLC-MM and aC-ACF samples under increasing weight (force) of the stylus is presented in figure 7.3.1. The micro-slackening in aC-TL (figure 7.3.1a and b) corresponds to the replicated structure of the betaine-sucrose crystals and is in the range of 10 to 33 μm. The measured foil height of thin aC-TL decreases clearly for increasing force. Larger forces than 2 mg could not be be measured without moving the foil. The sample expands smoothly over the silicon wafer, however it is not clear if air is confined under the foil in some areas. When applying the stylus, parts of the foil where the material does not stick to the wafer are pressed down. Other regions that stick to the wafer might be compressed. The measured height for aC-TL foils is much higher compared to other thin amorphous carbon foils like DLC-MM and aC-ACF. This might be an indication for a sponge-like structure of thin aC-TL foils, which is also supported by other measurements.

DLC-MM (figure 7.3.1c) and aC-ACF (figure 7.3.1e) samples show a more flat surface with areas of larger height due to small foldings and air inclusions under the foil, which were also seen in the microscopy images in section 7.1 and 7.2. The foldings are pressed down with increasing force for both DLC-MM and aC-ACF. The average thickness under highest load is in the range of 0.15 μm. A foil thickness of 150 nm for a 20 μg/cm^2 foil corresponds to a density of about 1.3 g/cm^3. This density would be much lower than many reported values which are between 2 g/cm^3 and 3 g/cm^3 [91]. However, also in case of these materials it is not clear if for example air is confined under the foil. For this reason profilometry can be used to compare the topography of different sample materials, but determined thicknesses should be treated carefully.

Thick 600 μg/cm^2 foils of these materials show no significant change in height with an increased force (figure 7.3.1b, d, e). Micro-slackening and buckling are preserved, even if the buckling is pronounced like in the case of aC-ACF (figure 7.3.1f). Estimations of the thickness by taking average values of the profiles would yield roughly 10 to 11 μm for aC-TL, 5 to 6 μm for DLC and 5 to 10 μm for aC-ACF (disregarding the large buckling). Due to the micro-slackening and buckling of the foils, a reliable thickness cannot be determined from profilometry measurements. Especially for the 600 μg/cm^2 foils, which do not stick to the silicon wafer by adhesion, uncertainty of profilometer measurements results from parts of the sample being not completely flat on the wafer.

Figure 7.3.2 presents a three dimensional surface plot of 20 μm aC-TL with the dimension 300 × 1000 μm, which consists of 30 scans with a length of 1000 μm. The arithmetic surface roughness R_a (also Arithmetic Average (AA) and Center Line Average (CL)) is a standard roughness parameter

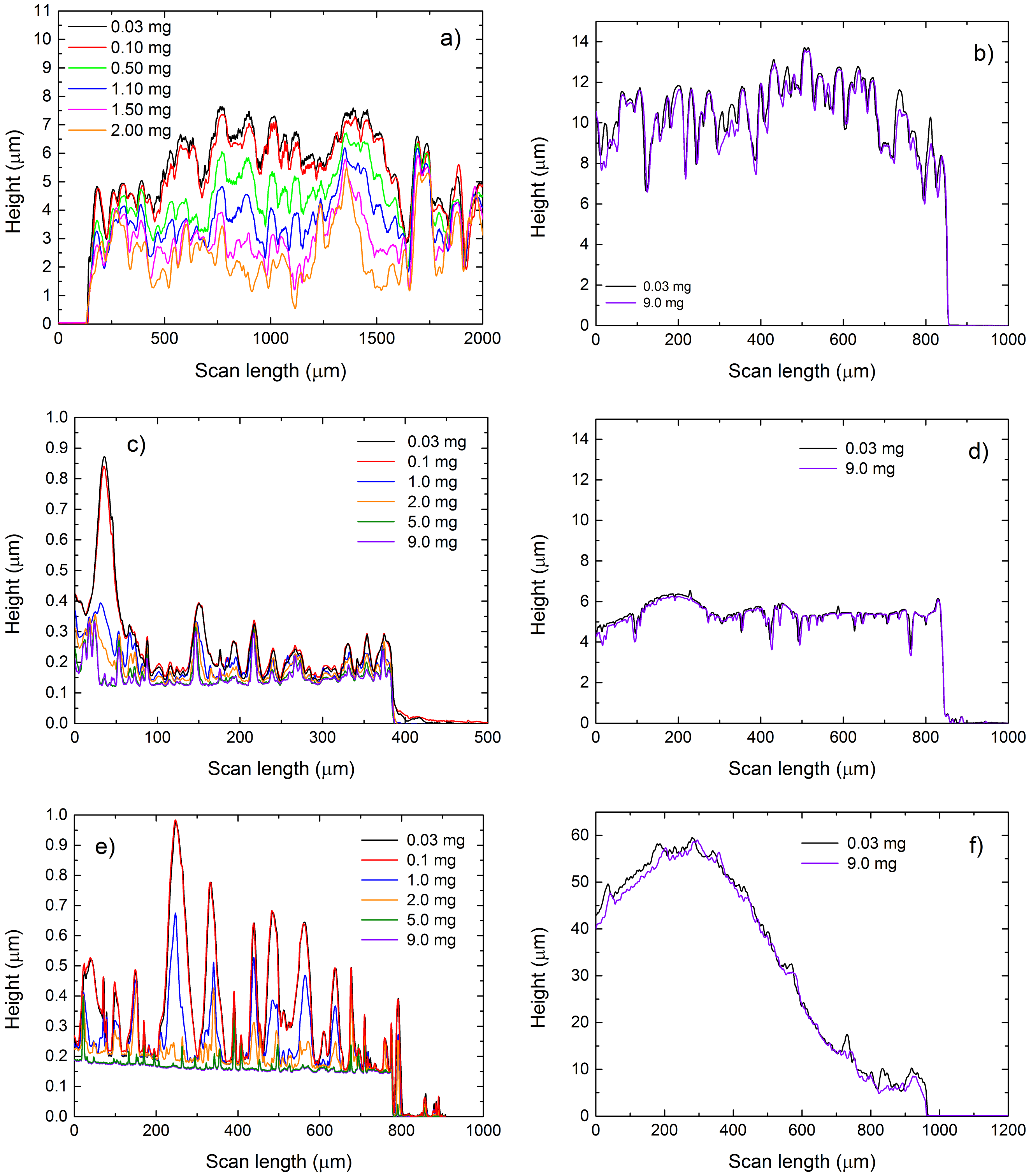

Figure 7.3.1.: Height profiles as a function of scan length of different loads (0.03 to 9 mg) for pristine 20 µg/cm^2 foils (left) and 600 µg/cm^2 foils (right). a) and b) aC-TL , c) and d) DLC-MM, e) and f) aC-ACF samples.

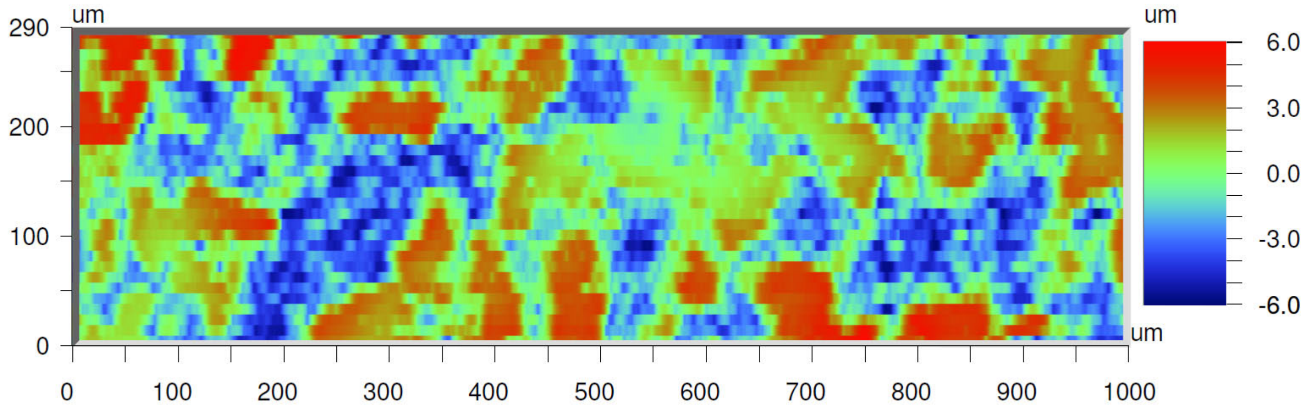

Figure 7.3.2.: Three dimensional surface plot of pristine 20 µm aC-TL with the dimension 300 × 1000 µm (including 30 individual profiles).

and describes the arithmetic average deviation from the mean thickness within the assessment length. The analysis of figure 7.3.2 yields a roughness R_a of 2.2 µm. The plot shows, that the extent of micro-slackening is larger for some regions and that "high" and "low" regions are not homogeneously distributed over the sample. The roughness value R_t presents the maximum peak to minimum valley heights within the assessment length and therefore gives an impression of maximum oscillation of thickness values. The R_t value is 11.6 µm.

Because the micro-slackening depends strongly on the crystallization of the betaine-sucrose solution during manual lubrication, the final roughness values of different samples and measurement in different locations on one sample are quite different. Since only small areas of the sample surface can be mapped, a representative value for the whole sample to describe the change of roughness or micro-slackening induced by irradiation cannot be obtained. Nevertheless, this method provides qualitative information on the degree of micro-slackening and buckling and a rough estimate of the thickness of the different foils.

7.4 Chromatic aberration

Thickness determination of the carbon films by means of profilometry is imprecise, because it measures only one side of the samples. An alternative thickness measurement from both sample sides can be performed by a MicroProf® device (FRT GmbH) which uses chromatic sensors. The measurement is based on chromatic aberration using white light passing a spherical lens with strong chromatic aberration. The light is dispersed due to the wavelength dependence of the refractive index. Different colors therefore have different focuses. When a sample is placed under such a sensor, a certain wavelength is in focus depending on the sample thickness. The thickness of the sample is deduced from the peak position in the intensity-wavelength spectrum.

The method was applied for different pristine foils: 600 μg/cm^2 aC-TL, DLC-MM, aC-ACF and 250 μg/cm^2 pristine CNT-DN. For each sample an image of the thickness distribution and a profile along a horizontal and a vertical line with a resolution of 0.06 mm are presented.

aC-TL samples show a smooth surface (figure 7.4.1a), because micro-slacking due to the betaine-sucrose crystals is at a much smaller scale compared to the sample diameter. The thickness along the vertical and horizontal profiles varies roughly between less than 0.5 and 9 μm.

The DLC-MM foil shows large buckling in the thickness image (7.4.2a) and in the profiles, although the measurement from both sides of the sample should result in a homogeneous thickness. The variations might be due to a tilted sample surface (due to buckling), which would yield a larger sample thickness. The values for the thickness vary between roughly 0.5 and 7 μm.

Buckling in aC-ACF foil has similar compared to DLC-MM (figure 7.4.3). The profile plot (7.4.3b) shows thickness values between 0 and 11 μm.

The CNT-DN sample shows some foldings and small buckling (figure 7.4.4a), but scattering of thickness values in the profile is less compared to the other samples (7.4.4b). The thickness varies between roughly 2 and 5.5 μm (disregarding one large wrinkle).

Table 7.4.1 shows the mean, minimum an maximum thickness values and the standard deviation of measured values for the complete sample set. From the surface density and corresponding thickness values the sample density was calculated. For aC-TL the density is approximately 1.6 g/cm^3, for DLC-MM 1.54 g/cm^3 and for aC-ACF 1.34 g/cm^3. All these values are smaller compared to literature values of bulk graphite density (2.253 g/cm^2) and amorphous carbon films in literature (2 g/cm^3 to 3 g/cm^3 [91]). Since the measured thickness of DLC-MM and aC-ACF is possibly overestimated due to buckling, the density of these samples might be underestimated. The density of CNT-DN is 0.83 g/cm^3 and thus much smaller than for all other foils. This is not unexpected due to the nature of thin foils made of nanotube fabrics.

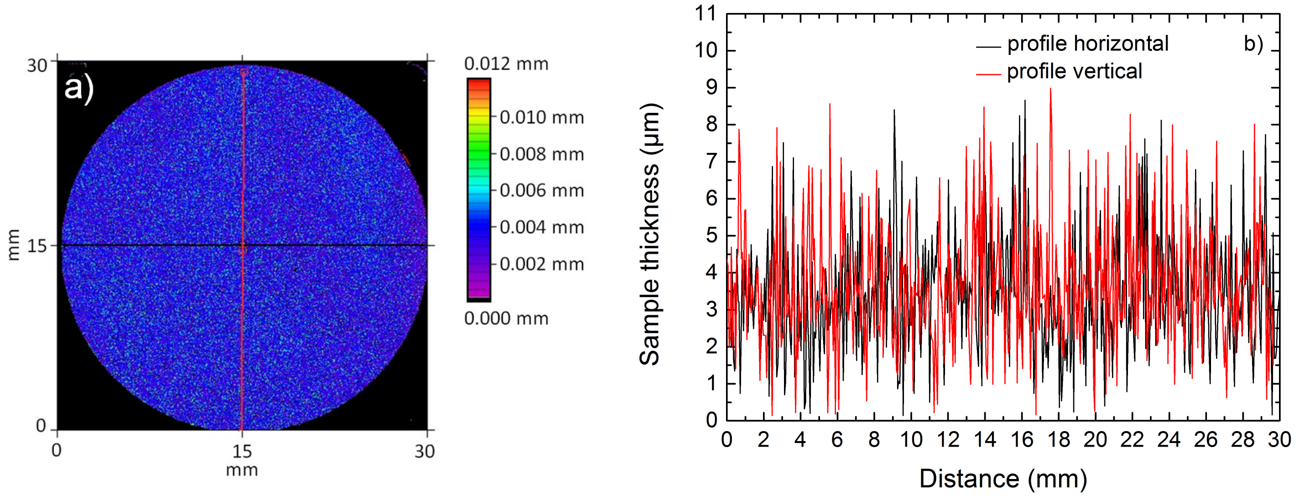

Figure 7.4.1.: Thickness analysis by chromatic aberration. a) Thickness distribution (colors indicate thickness values) and b) profiles along a horizontal (black, in a) and a vertical line (red) for pristine ~600 µg/cm^2 aC-TL.

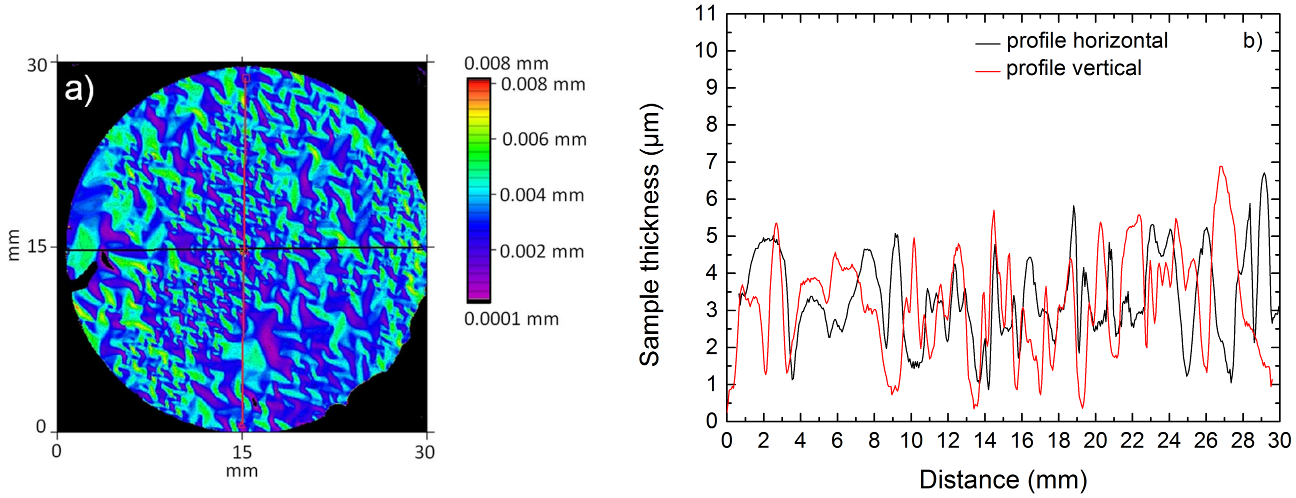

Figure 7.4.2.: Thickness analysis by chromatic aberration. a) Thickness distribution (colors indicate thickness values) and b) profiles along a horizontal (black, in a) and a vertical line (red) for pristine ~600 µg/cm^2 DLC-MM.

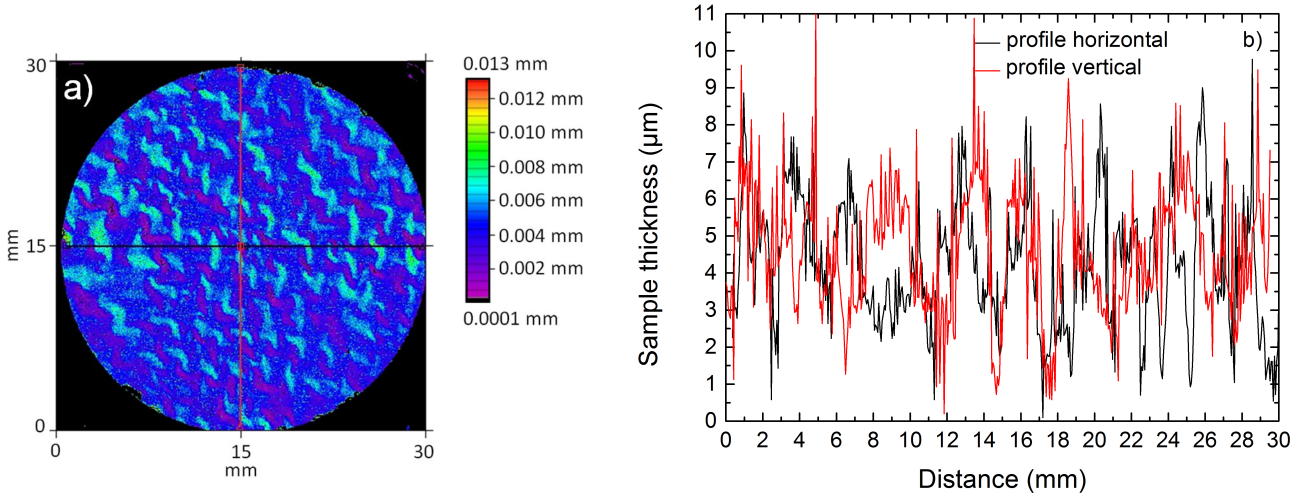

Figure 7.4.3.: Thickness analysis by chromatic aberration. a) Thickness distribution (colors indicate thickness values) and b) profiles along a horizontal (black, in a) and a vertical line (red) for pristine ∼600 µg/cm^2 aC-ACF.

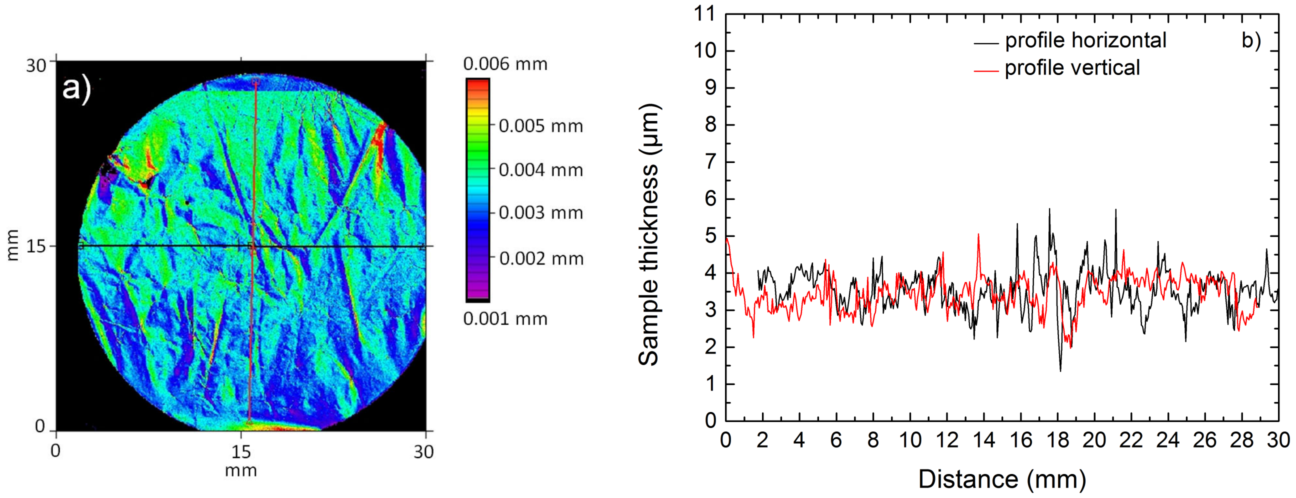

Figure 7.4.4.: Thickness analysis by chromatic aberration. a) Thickness distribution (colors indicate thickness values) and b) profiles along a horizontal (black, in a) and a vertical line (red) for pristine 200 µg/cm^2 CNT-DN.

Table 7.4.1.: Results of thickness measurement by chromatic aberration for different ≈600 µg/cm^2 pristine foils.

Material	Areal density (µg/cm^2)	Mean thickness (µm)	Standard deviation (µm)	Min. thickness (µm)	Max. thickness (µm)	Calculated Density (g/cm^3)
aC-TL	566	3.677	0.729	1.850	16.162	1.54
aC-TL	568	3.407	0.820	0.376	11.836	1.67
aC-TL	664	4.139	0.871	0.296	9.694	1.60
aC-TL	564	3.334	0.937	0.254	10.108	1.69
DLC-MM	600	4.005	1.097	0.420	10.464	1.50
DLC-MM	600	3.916	0.486	1.462	6.023	1.53
DLC-MM	600	3.347	1.210	0.191	9.035	1.79
DLC-MM	600	4.527	3.588	0.637	43.335	1.33
aC-ACF	589	4.396	1.146	0.220	9.512	1.34
aC-ACF	589	4.385	1.314	0.292	10.359	1.34
aC-ACF	580	4.328	1.496	0.191	13.809	1.34
CNT-DN	250	3.432	0.610	0.278	0.610	0.73

8 Structural changes

8.1 X-ray photoelectron spectroscopy

X-ray photoelectron spectroscopy (XPS) is a common technique for the determination of sp^2 and sp^3 contents. Monoenergetic X-rays incident on a sample surface cause electron emission due to the photoelectric and Auger process. The kinetic energy of the emitted photoelectrons E_{kin} is measured and the binding energy of the electron is deduced. E_{kin} is given by the energy of the incident photon $h\nu$, the binding energy E_{b} of the photoelectron emitted from a specific atomic orbital and the work function of the spectrometer W_{s} [106]:

$$E_{\mathrm{kin}} = h\nu - E_{\mathrm{b}} - W_{\mathrm{s}} \tag{8.1}$$

The work function of the spectrometer is constant and can be determined by the measurement of the Fermi energy of a metallic sample. The advantage of this method is that no reference material is needed, since the chemical shifts of the C1s peak due to the configuration of carbon bond, do not show a direct relationship with the matrix [106, 136]. Diaz *et al.* [136] introduced a method for the decomposition of the C1s peak into two contributions for sp^2 and sp^3 hybrids based on the observation that graphite and diamond have slightly different C1s peak positions [137]: graphite at 284.15 eV and diamond at 285.5 eV [106]. The sp^2 component is assigned to a lower binding energy than the sp^3 component. The discrepancy between measured data and fit (deconvolution by a sp^2 and a sp^3 component) at higher binding energies in the range of 286 to 289 eV was attributed to carbon-oxygen bonds [138–140].

XPS measurements were carried out at the DArmstädter Integrated System for BATtery research (DAISY-BAT) at Surface Science department of Technische Universität Darmstadt by Ruben Precht. The system is equipped with a PHI 5000 VersaProbe photoelectron spectrometer, providing a $\mathrm{Al}_{\mathrm{K}_\alpha}$ X-ray beam with a spot of 100 µm in diameter. The XPS spectra where calibrated to the Fermi level and the core level lines of a copper foil which was sputtered with argon ions to remove surface adsorbates. All measurements were carried out in ultra-high vacuum of approximately 10^{-9} mbar. Survey spectra were measured for all samples to ensure the absence of unexpected contaminations. These spectra revealed no other peaks than for oxygen or carbon. XPS detail spectra (C1s) were measured with a step size of 0.05 eV. On each sample two measurements were performed at different positions. In a series of pre-measurements, aC-TL samples were sputtered with 1 to 2 keV argon ions to test if contaminations could be removed from the surface. The asymmetric shape of the C1s peak, influenced by carbon-oxygen bonds in the sample, showed only minor changes. To avoid structural and probably chemical changes of the samples, the final XPS measurements were performed without prior argon-ion sputter cleaning.

A Shirley background [141] was subtracted from the raw data, removing a s-shaped background which is proportional to the intensity of the corresponding peak at a specific electron energy [142]. Voigt profiles were used to fit the different components of the C1s peak. As suggested by Diaz *et al.* [136], the Gaussian component accounts for the chemical disorder and instrumental energy resolution and the Lorentzian component includes the lifetime of the photoionization process. The Lorentzian width was therefore fixed to 0.2 eV [136, 143]. The Gaussian width was fixed to 0.8 eV as in [139], except for the sp^2 component, which was kept in a range between 0.6 and 0.8 eV to achieve a better fit quality. In literature, the sp^2 component is often fitted by a Doniac-Sunjic (DS) funtion, which has an asymmetric shape accounting for the semi-metallic nature of highly oriented pyrolytic graphite (HOPG, pure sp^2) with an asymmetry resulting from screening due to electron-hole pair excitations at the Fermi energy [106, 136, 143, 144]. In this study the use of a DS function did not yield an acceptable fit quality. Jackson *et al.* state that an asymmetric fit is not appropriate for a highly disordered sp^2 phase and electrically insulating amorphous carbon films [145]. In addition, the subtraction of a Shirley background reduces the asymmetric shape of the C1s peak. The sp^2 component was thus fitted with a Voigt function which is also commonly used in literature, e. g. [138, 139]. Three additional Voigt peaks (0.2 eV Lorentzian and 0.8 eV Gaussian width) were fitted to consider oxygen components C−O, C=O and O−C=O (figure 8.1.1) as proposed in [140]. Due to a possibly poor conductance of amorphous carbon films, surface charging could influence the XPS spectra [106]. For this reason the distance between sp^2 and sp^3 component was fixed to 0.9 eV in accordance with the shift of ∼0.9 eV between C1s peaks for diamond and graphite [143]. The shift between the oxygen components was set to 1.1 eV.

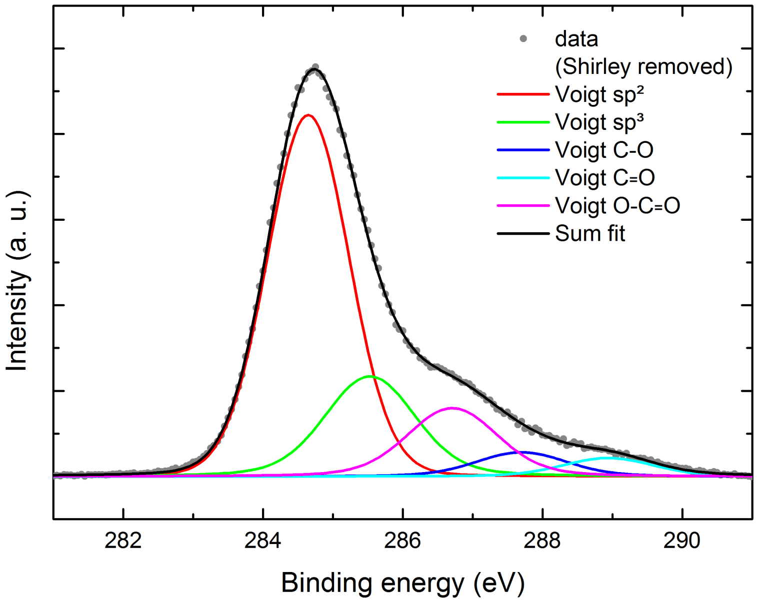

Figure 8.1.1.: Deconvolution of C1s peak of a DLC-MM sample irradiated with 4.8 MeV/u U ions to a fluence of 5×10^{13} ions/cm^2. A Shirley background was subtracted and is not presented. Voigt profiles are shown for the identified contributions to the C1s peak: sp^2, sp^3, C−O, C=O and O−C=O.

Fits to the data were calculated using the software fityk 0.9.8 [146] and Levenberg-Marquard algorithm for least-square optimization. Error bars represent standard deviations for the fitted intensities. In addition to the uncertainties introduced during the measurement, the large number of fitting parameters produce large errors of the binding energies and the intensity. Special attention was therefore paid to physically meaningful parameters as suggested by Haerle [143]. Also, the FWHM (full width at half maximum) of the components should be larger than the resolution of the analyzer [143]. This was the case for all measurements of this work. To get an idea of the errors of the final sp^2 and sp^3 contents, two independent measurements on different locations in the beamspot were performed and are compared in the following graphs. In addition to the errors of the XPS measurement and fitting procedure, also the inhomogeneous distribution of the fluence across the samples plays an important role. The fluence uncertainty is estimated to 15 %, but for better clarity it is not presented in the graphs. Bonding contents were calculated by the intensities of sp^2, sp^3 and O components divided by the sum of all component intensities.

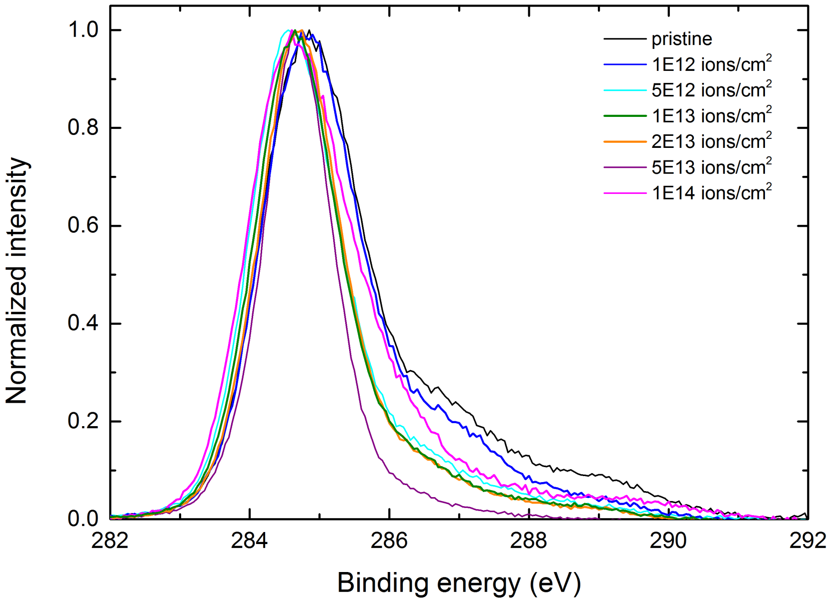

Figure 8.1.2.: XPS spectra for 20 μg/cm^2 aC-TL foils of different fluences irradiated by a 4.8 MeV/u U beam.

XPS spectra of 20 μg/cm^2 aC-TL foils irradiated with 4.8 MeV/u U ions at different fluences are presented in figure 8.1.2. With increasing fluence, the tail intensity towards higher binding energies decreases and the overall peaks appear more narrow, except for the sample at 1×10^{14} ions/cm^2. A small shift of the overall peak maximum to lower binding energies can be observed. Both observations indicate a decrease of sp^3 and oxygen bonding content. The term oxygen bonding content/fraction refers to oxygen bound to carbon in C−O, C=O or O−C=O contributing to the C1s peak.

Bonding content as a function of fluence for different ions and aC-TL, DLC-MM and aC-ACF foils is presented in figure 8.1.3. Oxygen and sp^3 are in a similar range. Therefore oxygen bonding fractions are not presented in 8.1.3 for better visibility of sp^3 bonding contents. Individual graphs for each irradiation condition including oxygen fractions can be found in the appendix A. Lines correspond to measurements on pristine samples. The errors present the uncertainty of bonding content by the fitting procedure using the standard deviation of the fit parameters and considering error propagation. Pristine 20 μg/cm^2 aC-TL foils (a) show an sp^2 content of about 60 % and an sp^3 content of about 15 to 20 %. At low fluences the bonding contents scatter significantly. Above about 5×10^{12} ions/cm^2, the sp^2 contents for all ions are clearly higher than pristine values, sp^3 bonding contents are smaller. The large scattering of the derived bonding contents might be related to an inhomogeneous beam spot during heavy-ion irradiation, but also clustering of sp^2 and sp^3 hybridized atoms already in pristine samples cannot be excluded (as discussed in section 3). In case of irradiation with U ions a decrease of sp^2 contents is seen for fluences of 1×10^{14} and 5.7×10^{14} ions/cm^2. sp^3 contents increase less in comparison, since measured oxygen contents increase for these samples. In addition to the Uranium fluence series, crosses represent bonding contents derived for a sample irradiated with 1.4 MeV/u U ions of fluence 3.8×10^{17} ions/cm^2. This sample shows a higher sp^2 content compared to the highest fluence (1×10^{14} ions/cm^2), but a lower sp^2 content than the maximum fraction observed at 5×10^{13} ions/cm^2 of the irradiations with 4.8 MeV/u U ions. Comparable sp^3 contents indicate a smaller oxygen content. In 20 µg/cm^2 DLC-MM foils the scattering seems less pronounced. sp^2 values for the pristine foils are comparable to aC-TL foils, derived sp^3 are larger. This would yield a smaller oxygen content in the DLC-MM samples. Irradiation increases sp^2 and decreases sp^3 values already at small fluences. 20 µg/cm^2 aC-ACF foils show slightly smaller sp^2 content in the range of 50 to 55 % and sp^3 bonding content in the range of 35 % comparable to the sp^3 content in DLC-MM foils and larger compared to aC-TL foils. Like in DLC-MM no clear increase of sp^2 bonding content with increasing fluence is obvious, since all irradiated aC-ACF samples show an increased sp^2 and a decreased sp^3 content.

Concluding the XPS measurements, it has to be taken into account that this method only provides information of the surface region of a sample. The information depth is related to the mean free path of the photo-electrons and is usually in the range of a few atomic layers. The amorphous carbon samples irradiated in this work do not exhibit clean surfaces, since they are produced with help of water or different organic solvents and are stored in air. Oxygen and carbon might therefore be part of contaminations and falsify the derived bonding content of the amorphous carbon material itself. In addition, surface atoms are expected to preferably be sp^2 coordinated to reduce present stresses due to their reduced number of neighbors. Despite these side effects, this study provides indications of an increase of sp^2 bonding content and a decrease of sp^3 bonding in aC-TL, DLC-MM and aC-ACF amorphous carbon foils under the irradiation of swift-heavy ions. However, due to a large scattering of the values for measurements on different positions on the same sample as observed also for other off-line characterization methods like Raman Spectroscopy, a comparison of different ions seems to be problematic.

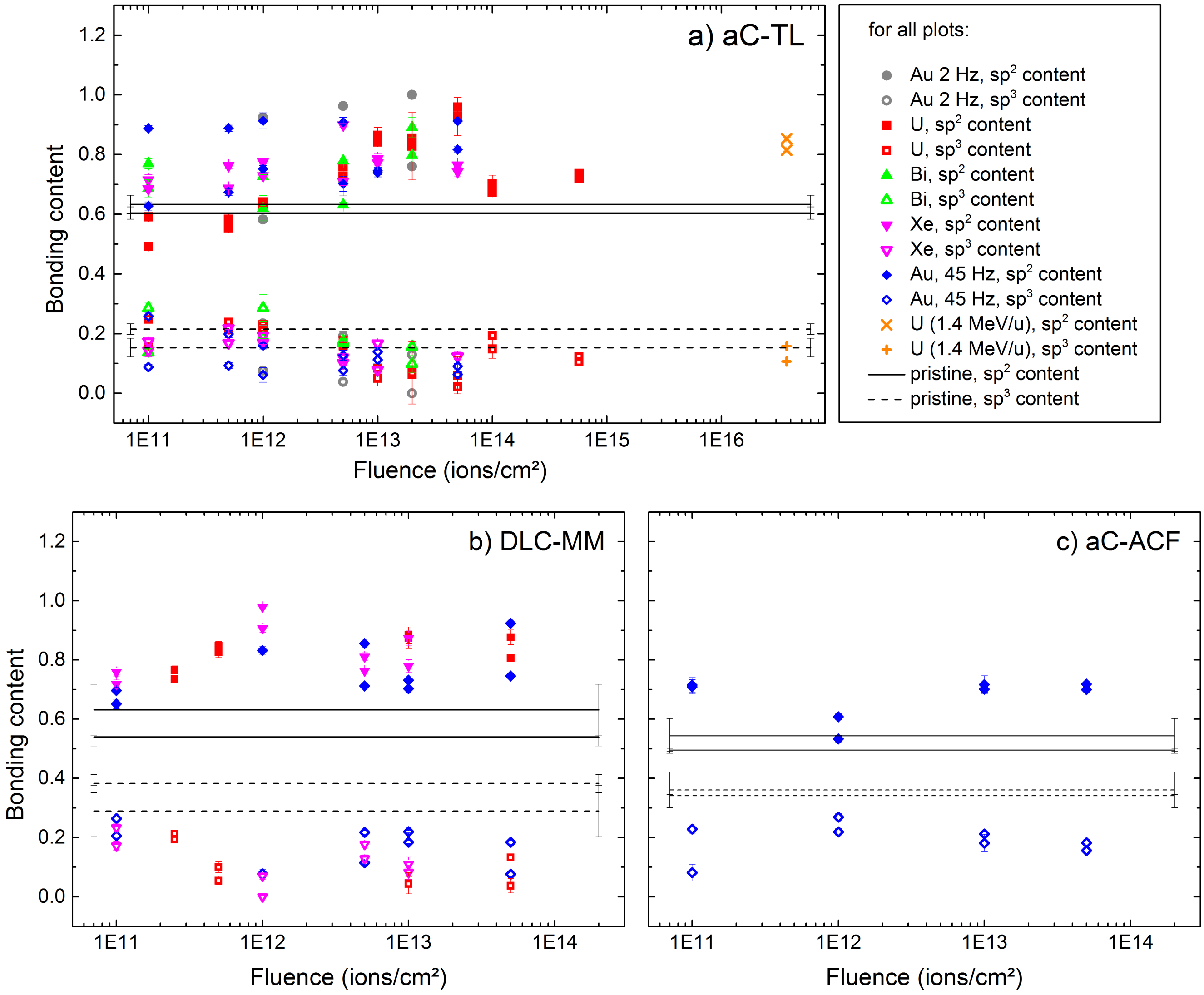

Figure 8.1.3.: sp^2 and sp^3 contents determined from XPS measurements in a) aC-TL, b) DLC-MM, c) aC-ACF irradiated with different ions and beam conditions. The solid line denotes the sp^2 content and the dotted line the sp^3 content of the pristine samples. Two measurements taken in different locations of the beamspot are presented for each fluence.

8.2 Raman spectroscopy

Raman spectroscopy is a nondestructive method for the structural characterization of carbon films based on the analysis of inelastically scattered light. When the energy of incident light matches the energy of an electronic transition, the energy is absorbed and an electron can be raised to an excited state. This process is used in Infrared Spectroscopy. If the energy of incident light does not match the energy of an electronic transition, elastic or inelastic scattering can occur. The highest probability has the elastic process in which the electron cloud in a material or molecule is distorted and the induced dipole moment causes re-emission of light with the same energy. This process is called Rayleigh scattering and is stronger for higher frequencies of the incident light. This is why lasers with shorter wavelength produce stronger Raman signals. Raman scattering describes the process when energy is transferred between the incoming light and the material or molecule, resulting in an energy change of the scattered light. This inelastic process involves quasi-particles like phonons in solids or vibrations in molecules. An incident photon can transfer a certain amount of energy to a material, thereby exciting the matter to a virtual intermediate state. This virtual state is a deformation of the electron cloud around a bond or molecule by interaction with the electromagnetic radiation (laser light), creating a phonon or vibrations. Relaxation results in an inelastically scattered photon that has less energy than the incident one (Stokes shift). Excitation of matter which is already in an vibrational state can transfer energy to the incoming photon by destroying a phonon. Relaxation to the ground state emits a photon with higher energy (anti-Stokes). Because at ambient temperature much more atoms are in the (vibrational) ground state than in an vibrational excited state, Stokes Raman intensity is always larger than anti-Stokes Raman intensity. Raman spectroscopy measures the transferred energy in this inelastic Raman scattering process which is weak in comparison to Rayleigh scattering (10^{-5} to 10^{-8} of the incident beam intensity [147]).

Raman spectra of (amorphous) carbon materials reveal information about bonding type, domain size and stresses [106]. The first order Raman spectrum of diamond has a single band at $1332\,\mathrm{cm}^{-1}$, which is related to a zone center mode of T_{2g} symmetry [89]. Single crystalline graphite shows a band at $1580\,\mathrm{cm}^{-1}$ of E_{2g} ("G-peak"), which is not dependent on the orientation towards the laser beam [106]. In polycrystalline graphite an additional mode of A_{1g} symmetry appears at $1350\,\mathrm{cm}^{-1}$, called "D-peak" (with "D" for disorder). In amorphous and nanocrystalline carbons both G- and D-peak are present around $1550\,\mathrm{cm}^{-1}$ and $1360\,\mathrm{cm}^{-1}$, respectively [106]. Because the crystal momentum is not conserved in amorphous materials, all phonons should be allowed and produce a smooth Raman spectrum without intense bands. Ferrari and Robertson [89, 110, 148] suggest that the presence of the G and D mode is mainly due to sp^2 sites. The π bonds have a lower energy and are therefore more polarizable, causing the matrix element for π bonds to be larger than for σ bonds. Thus, sp^2 sites essentially determine the Raman spectrum [89, 110]. In their model, bond stretching of all sp^2 sites (both rings and chains) cause the G-peak. The G mode therefore does not require sixfold rings [110]. The D-peak is due to breathing vibrations of sixfold rings (A_{1g} symmetry), involving phonons at the K zone boundary [89, 110, 149].

In carbon-nanotubes several additional features appear for first order Raman modes in the spectra. A radial breathing mode (RBM) due to radial bond-stretching of the nanotube is located at the low frequency end of the Raman spectrum, usually between 100 and $500\,\mathrm{cm}^{-1}$ [150]. Its exact frequency depends on the nanotube diameter [150]. The G band has a double-peak structure, a G^{-} at $\sim 1570\,\mathrm{cm}^{-1}$ and G^{+} at

~1590 cm^{-1}. G^- is due to vibrations of the atoms along the nanotube and G^+ results from vibrations along a circular path around the nanotube [150]. For large nanotube diameters the two features combine to a similar G band like in graphite [150].

Raman measurements in this study were performed with a commercial HORIBA Jobin Yvon$_{\text{TM}}$ (HR800) Raman spectrometer with 180° geometry (incoming and scattered light has the same optical path). A continuous wave diode pumped solid state laser (λ = 473 nm) with a power of 25 mW was used for the experiments. An edge filter is used for discrimination of the Rayleigh signal. A monochromator with a grating of 1800 lines/mm separates the light into its spectral contributions and a cooled CCD detector records the signal. The built-in microscope allows measurements at high magnification. Due to the low signal of amorphous films, the aperture hole was enlarged to 1073 µm and measurements were performed with the highest magnification objective (×100). To prevent altering of the sample by the laser beam, a filter was used to attenuate the laser to 1 % of its original power. A set of pre-measurements showed no modification by the laser beam with these settings. Long exposure time of 150 to 200 s were needed to achieve a signal in this configuration. In order to increase signal to noise ratio, 2 or 4 cycles were recorded. For each sample, single measurements of 5 spots were superimposed to create a mean spectrum. Raman spectra of amorphous carbon films do not show any second order peaks. Measurements were therefore restricted to Raman shifts from 800 to 1900 cm^{-1}.

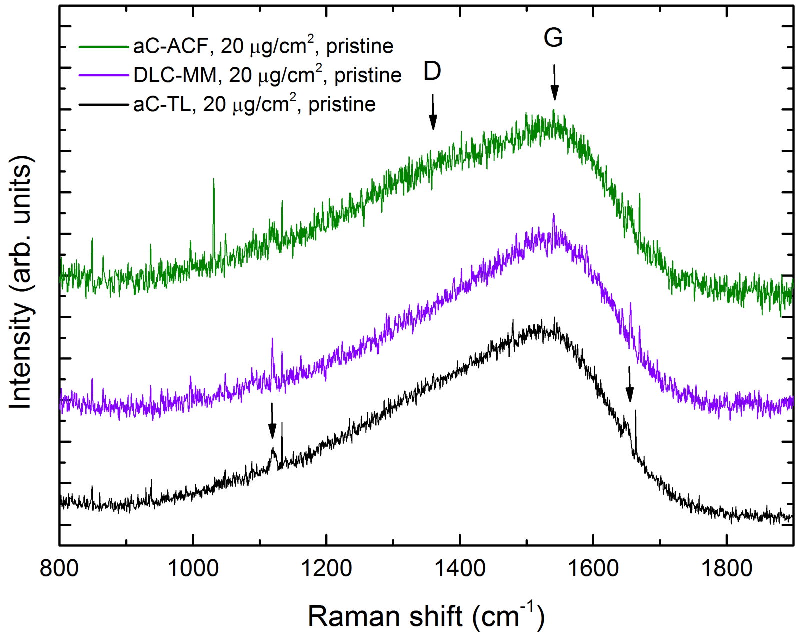

Figure 8.2.1.: Raman spectra of pristine 20 µg/cm^2 aC-TL (black), DLC-MM (purple) and aC-ACF (green). The broad band consists of D and G peak, the arrows indicate small additional peaks which appear in some samples.

Spectra of the different amorphous carbon films (aC-TL, DLC-MM, aC-ACF) investigated in this study are presented in figure 8.2.1. Since spectra of 20 and 600 µg/cm^2 samples are very similar, results are representative for both thicknesses. The tree different foils show a broad peak, which consists of a convolution of the D-peak and G-peak. The shape is very similar for all materials, with only slight differences in the height of D-peaks. In addition to the D and G peak, a small peak at 1120 to 1150 cm^{-1} appears

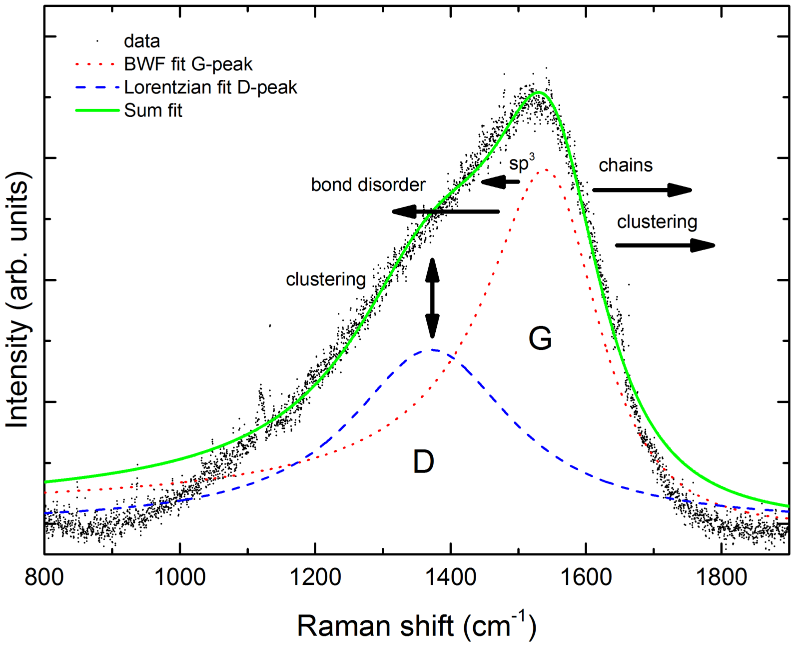

Figure 8.2.2.: Deconvolution of Raman spectrum of pristine 20 µg/cm^2 aC-TL with Lorentzian shape for the D-peak (dashed, blue line) and a Breit-Wigner-Fano (BWF) lineshape for the G-peak (dotted, red line). The green line shows the overall fit. Arrows indicate influences to peak positions and intensities based on the decription by Ferrari et al. in [110].

for some of the samples. In literature the origin of this peak is still under discussion. Some research groups attribute it to nanocrystalline diamond [106, 117, 151] or carbon-hydrogen bonds present at grain boundaries of nanocrystalline diamond [152], even though it is not always observed in nanocrystalline diamond films [117]. Also vibrations of sp^3-hybridized C−C bonds have been proposed [153]. However other groups (e.g. [154, 155]) follow the suggestion of Ferrari and Robertson [148] to assign this peak to trans-polyacetylene chains at grain boundaries and surfaces in hydrogen containing amorphous carbon foils or to structures of a mixed sp^2-sp^3 nature [156]. In both cases annealing causes this peak to disappear [148, 151]. In the present study an additional very small peak at ∼1660 cm^{-1} appears for some samples. Since both peaks are not consistently found for a certain material or correlated to fluence, it is assumed that these peaks relate to contaminations, for instance from remains of intermediate layers during deposition. It may also play a role that the samples were deposited on silicon wafers with the use of isopropanol and in some cases fixed with carbon glue (butyl acetate and carbon soot). In addition, the samples are stored in air.

Figure 8.2.2 presents the deconvolution of the spectra as performed for all amorphous carbon-based materials in this study (aC-TL, DLC-MM and aC-ACF). Fitting was done with a Breit-Wigner-Fano (BWF) line shape for the G peak and a Lorentzian line shape for the D peak as proposed by McCulloch and Ferrari [110, 157, 158]. In literature also two Gaussian functions are common [110, 159]. The use of the asymmetric BWF function is motivated by the asymmetry of the vibrational density of states (VDOS) of graphite and amorphous carbon towards lower wavenumber [159] and the coupling of a discrete mode to continuum [110]. A linear background was subtracted between 900 to 1800 cm^{-1} prior to the deconvolution. The use of this fitting method significantly increased fit quality and was used for all different amorphous carbon materials of this study. The small additional peaks at 1120 to 1150 cm^{-1} and

$\sim$1660 cm^{-1} do not influence the fit of the D-peak and G-peak due to their very small intensity and are therefore not included in the overall fit.

In case of the CNT-DN samples, after subtracting a linear background in the same range, a Lorentzian shape for the D and the G^{+} bands, and a BWF function for the G^{-} band were used for deconvolution. An asymmetric (BWF) line shape of the G^{-} feature indicates a metallic nature of the single-walled carbon-nanotubes [150]. The BWF line shape is expressed by [110, 159]:

$$I(\omega) = \frac{I_0\left[1 + \frac{2(\omega-\omega_0)}{Q\Gamma}\right]^2}{1 + \left[\frac{2(\omega-\omega_0)}{\Gamma}\right]^2} \tag{8.2}$$

$I(\omega)$ is the Raman intensity at a wavenumber ω, ω_0 is the peak position, I_0 is the peak intensity at ω_0, Γ the full width at half maximum (FWHM) and $1/Q$ the BWF coupling coefficient. For Q approaching zero, a Lorentzian line shape is recovered. Due to the asymmetry of this function, the maximum of the G peak (BWF line) is located at lower wavenumber than the peak position ω_0. The G peak position therefore corresponds to the corrected position ω_{max} [110]:

$$\omega_{\text{max}} = \omega_0 + \frac{\Gamma}{2Q} \tag{8.3}$$

Fits were obtained with the software fityk 0.9.8 [146] and Levenberg-Marquard algorithm for lest-square optimization. Error bars represent uncertainties calculated by Gaussian propagation of error method using the standard deviation for the fitted parameters. In addition to these uncertainties by the fitting procedure, errors are introduced by the irradiation conditions, the fluence measurement and an inhomogeneous distribution of the fluence over the samples. This fluence uncertainty is estimated to be ±15 %. To make the graphs more accessible, this uncertainty is not presented as an error bar. Special care was taken that the global minimum during least-squares optimization was found and that initial values did not influence the final fit results. The disagreement of the fit for outer area of the overall peak ($<$1000 cm^{-1} and $>$1700 cm^{-1}) is a result of linear background subtraction between 900 to 1800 cm^{-1}. However, a high fit quality for the main part of the peak could only be achieved accepting this deviation in the outer region.

The main parameters that are typically used to characterize (amorphous) carbon films are the intensity ratio of D to G peak ($I_{\text{D}}/I_{\text{G}}$), G peak position (corrected by formula 8.3) and peak width. Tuinstra and Koenig [149] found that $I_{\text{D}}/I_{\text{G}}$ is inversely proportional to the in-plane correlation length or grain/cluster size L_{a} (for the laser excitation wavelength 514.5 nm):

$$\frac{I_{\text{D}}}{I_{\text{G}}} = \frac{44\mathring{A}}{L_{\text{a}}} \tag{8.4}$$

Ferrari suggested, that this relationship does not apply to small cluster sizes [110]. For cluster smaller than 2 nm he proposed another relation:

$$\frac{I_\mathrm{D}}{I_\mathrm{G}} = 0.0055 \mathring{A} \cdot L_\mathrm{a}^2 \tag{8.5}$$

The constants for both equations have been obtained from X-ray diffraction in several studies [89, 106, 110, 149]. Ferrari [110] developed a model to describe all amorphous carbons by a phenomenological three stage model in which disorder is introduced to an infinite graphite sheet (neglecting the hydrogen content). In this model different competing factors define the shape of Raman spectra. These are clustering of sp^2 phase, bond disorder, the presence of sp^2 rings or chains, and sp^2/sp^3 ratio. Their influence on the Raman spectra is indicated in figure 8.2.2. An "amorphization trajectory" [160] describes the three stages from graphite to tetragonal amorphous carbon [110]:
(1) perfect graphite to nanocrystalline graphite
(2) nanocrystalline graphite to aC (mainly sp^2)
(3) aC to t-aC (≈100 % sp^3).
Stage 1 describes the reduction of grain size in graphite following equation 8.4. The structure still consists of graphitic rings. With decreasing L_a phonon confinement allows higher frequency modes. The G peak shifts upwards from ∼1580 to ∼1600 cm^{-1} and $I_\mathrm{D}/I_\mathrm{G}$ ratio increases due to formation of a D peak. An example for the transition from stage 1 to stage 2 is ion irradiation of graphite as described by Mc Culloch *et al.* [157]. Stage 2 corresponds to disordering of the graphitic structure and damage of six-fold rings, being still mainly three-fold coordinated. This causes the phonon modes to soften lowering the VDOS in comparison to graphite [89]. The G peak position decreases from ∼1600 to ∼1510 cm^{-1} [110]. Tuinstra Koenig equation (8.4) is not valid anymore. $I_\mathrm{D}/I_\mathrm{G}$ is proportional to the cluster size and therefore decreases. The final configuration of stage 2 is found for instance in sputtered aC [110]. In stage 3 the sp^3 content increases, developing a structure of short chains. Because the bond length in chains is shorter compared to rings, their vibrational frequency is higher and the G peak shifts upwards again [89]. In addition, the line shape of the G peak becomes more symmetric with increasing sp^3 content. $I_\mathrm{D}/I_\mathrm{G}$ decreases further to zero [110]. The width of the G peak is connected with the cluster size, a FWHM larger than 50 cm^{-1} corresponds to L_a smaller than 1 nm [89]. Ferrari also provides a detailed description of the transition in reverse direction, the "ordering trajectory" or "hysteresis cycle" [110]. Examples are high energy deposition, ion implantation of t-aC or annealing, which result in a lower temperature regime for the process of sp^2 clustering than sp^3 to sp^2 conversion. Depending on the starting sp^3 fraction, $I_\mathrm{D}/I_\mathrm{G}$ ratio and G peak position therefore follow a different path of increase towards values corresponding to a nanocrystalline graphite structure [110]. In conclusion this model illustrates the importance of distinguishing between graphite and amorphous carbon: The growth of a D peak corresponds to the introduction of disorder in graphite, but also to an ordering process in amorphous carbon.

Figure 8.2.3 presents Raman spectra of pristine and 4.8 MeV/u U irradiated aC-TL foils. With increasing fluence a D-peak develops around 1360 cm^{-1}. This effect is even more pronounced in samples irradiated at the gas stripper position with 1.4 MeV/u U ions of higher intensities and corresponding larger energy deposition (figure 8.2.6a). The spectrum of an aC-TL sample irradiated with 7.4×10^{13} U-ions/cm^2 (in the range of M-branch accessible fluences), shows a broad peak with visible D and G contributions. For higher fluences in the range of 10^{16} ions/cm^2, the width of both peaks decreases significantly, and D and G peak clearly separate.

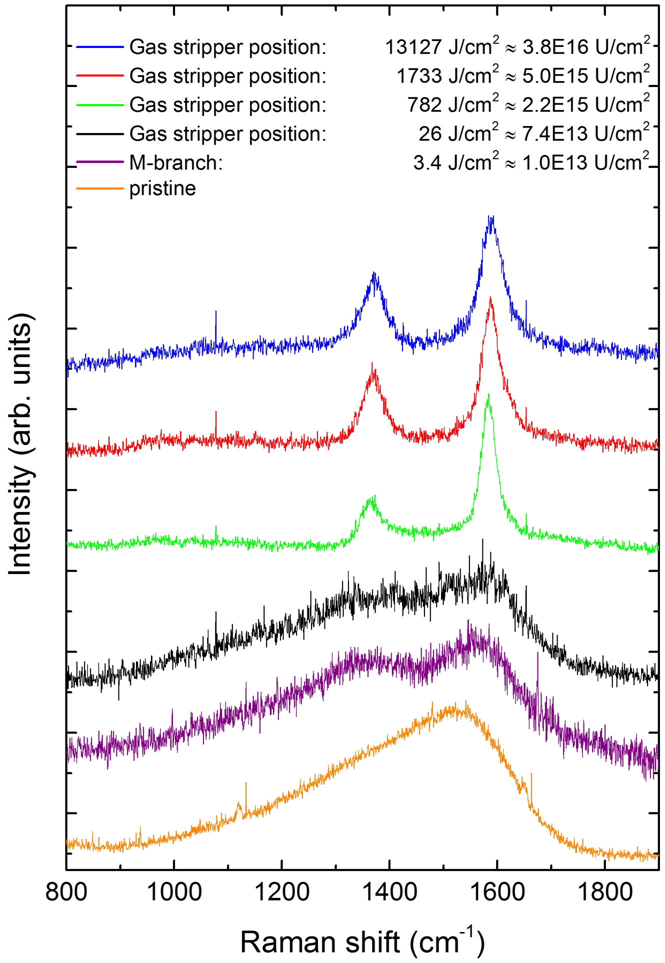

Figure 8.2.3.: Raman spectra of pristine (orange) and irradiated 20 µg/cm^2 aC-TL foils at M-branch (4.8 MeV/u U, 0.6 Hz, 0.2 ms, purple) and gas stripper position (1.4 MeV/u U, 1 Hz, 0.15 ms). Fluences (ions/cm^2) and deposited energy (J/cm^2) are given in the legend.

The D peak in the pristine CNT sample is small in comparison to the G peak. The D peak increases in height and width with increasing fluence under irradiation of 4.8 MeV/u Au ions (figure 8.2.4). The radial breathing mode (RBM), G$^-$ and G' peak show no significant changes, which indicates that the carbon nanotube structure is still preserves. Unfortunately no fluences above 7×10^{11} ions/cm^2 could be investigated, because the samples failed.

I_D/I_G ratio and G line position were analyzed to get more detailed information on the material transformations. Figure 8.2.5 presents I_D/I_G and G position as a function of fluence for aC-TL (a), DLC-MM (b) and aC-ACF (c) and irradiated with different ion beams. Pristine values are the mean of 5 measurements, the error corresponds to the standard deviation of the individual measured values. A general increase of the I_D/I_G ratio with increasing fluence is observed for all ions in aC-TL. The G positions seem to slightly shift to larger values compared to the pristine spectrum, but stay constant with increasing fluence for irradiations with different ions. Generally an upward shift of the G position indicates an ordering of sp^2 sites [90] and decrease of bond-angle disorder [157]. The same applies for the D-peak intensity increase and therefore I_D/I_G ratio increase. However, U and Au irradiated samples show a decrease of I_D/I_G ratio for fluences higher than 3×10^{13} ions/cm^2. Further information on this behavior was obtained from the I_D/I_G investigation of higher fluences in aC-TL foils irradiated at gas stripper position of the UNILAC.

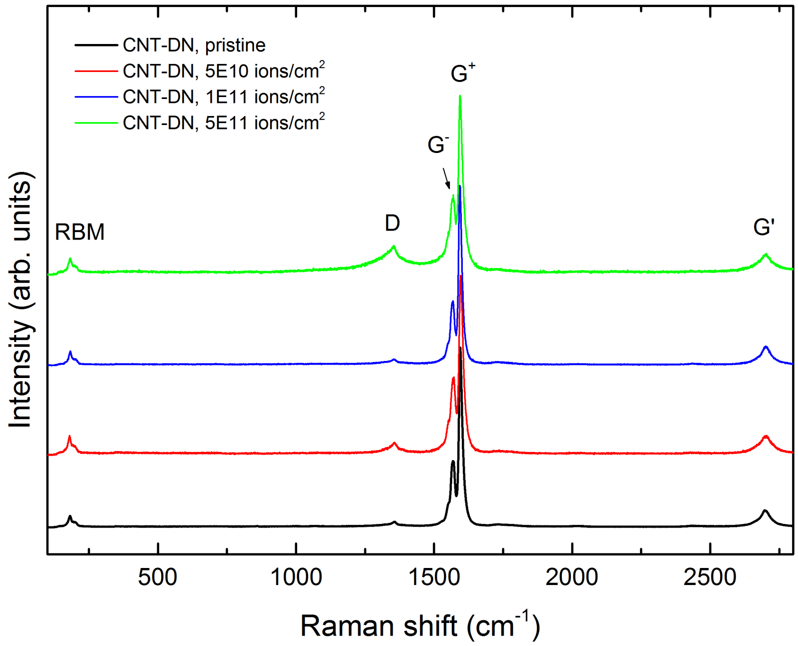

Figure 8.2.4.: Raman spectra of pristine (black) and irradiated 600 μg/cm^2 CNT-DN foils with 4.8 MeV/u Au ions (45 Hz). Fluences (ions/cm^2) are given in the legend.

Figure 8.2.3a shows the corresponding graph. Samples with higher fluences follow the trend of samples irradiated at the M-branch up to 1×10^{14} ions/cm^2 with I_D/I_G ratios being smaller than the peak value at around 1×10^{13} ions/cm^2. This decrease has been observed in literature by Dillon *et al.* in 1984 [111] for annealing of amorphous carbon foils deposited by radio-frequency-discharge. They observed an increase up to 800°C followed by a decrease in I_D/I_G ratio for higher temperatures. According to Robertson [90], the initial increase can be explained with an increase in short-range order, connected to a reduction of bond-angle disorder. The decrease is interpreted as an increase of crystallite dimensions [90]. McCulloch *et al.* [157, 158] found a similar effect for 320 keV Xe implanted glassy carbon and explained their observation with an increasing disorder in the transformation process from micro-crystalline graphite to amorphous carbon. 5 years later, Ferrari found a proportionality of I_D/I_G and cluster size in amorphous carbons (equation 8.5), which relates a decrease in D peak intensity to a decrease in cluster size [110]. DLC-MM (8.2.5b) shows an increase of I_D/I_G with increasing fluence and a slight decrease for samples irradiated with U and Xe ions of 5×10^{13} ions/cm^2 and 1×10^{13} ions/cm^2, respectively. G positions in DLC-MM scatter around the pristine value. A slight decrease of G position is seen for irradiation with U ions above a fluence of 5×10^{13} ions/cm^2. I_D/I_G and G position in aC-ACF (8.2.5 c) show a similar evolution as a function of fluence for the irradiation with Au ions. A slight increase is observed around 1×10^{13} ions/cm^2, the other values are close to the pristine value. The CNT samples show much lower I_D/I_G values and much higher values for the G peak position in both pristine and irradiated material. An increase of I_D/I_G ratio is observed, like also reported by Hulman *et al.* for the γ-ray irradiation of single-walled carbon-nanotubes [161]. The increase of the D peak intensity in the CNT-DN is similar to the D peak growth in graphite by the formation of defects under ion irradiation. Nevertheless, the presence of all modes for the highest fluence (7×10^{11} ions/cm^2) indicated that the CNT-structure was preserved. I_D/I_G ratios of irradiated samples which are smaller than of the pristine material might indicate that the clustering in amorphous carbons is very localized in pristine samples and for small fluences.

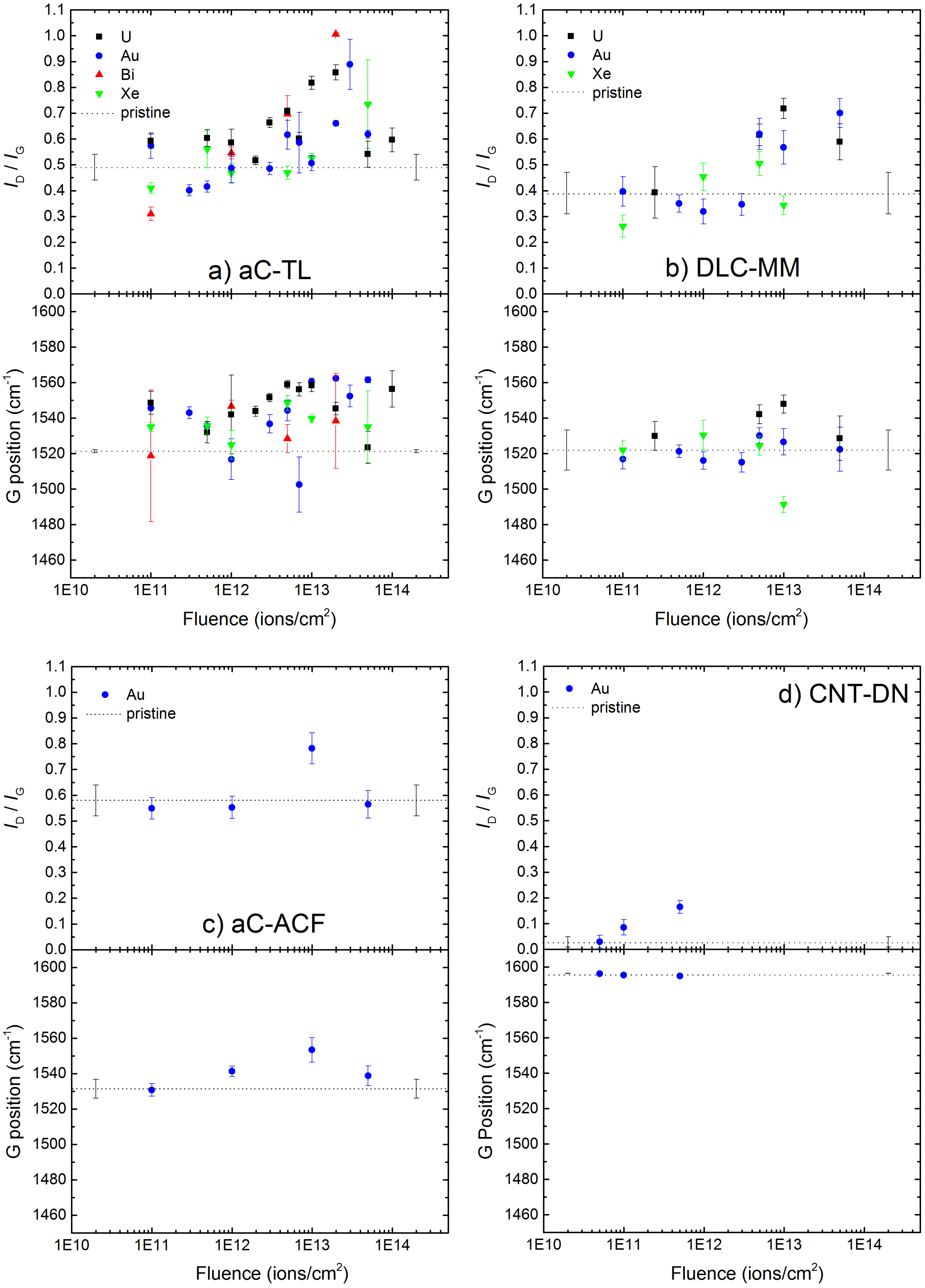

Figure 8.2.5.: $I_\mathrm{D}/I_\mathrm{G}$ and G line position as a function of fluence for different materials: a) aC-TL, b) DLC-MM, c) aC-ACF, d) CNT-DN irradiated with different beams: 4.8 MeV/u U (0.6 Hz, 0.2 ms; black squares), Au (045 Hz, 4 ms; blue circles), Bi (3.4 Hz, 1.2 ms; red up-triangles), Xe (5 Hz, 10.2 ms; green down-triangles). Pristine values are indicated by the dotted line.

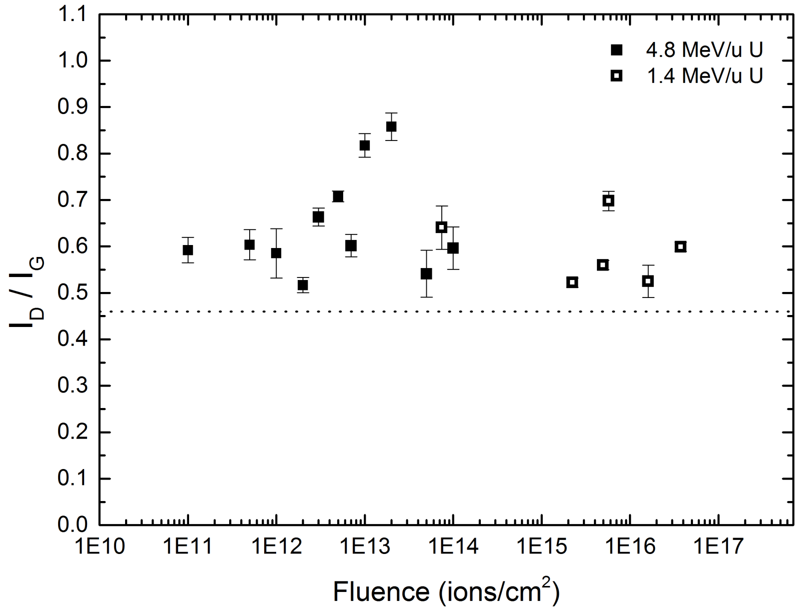

Figure 8.2.6.: $I_\mathrm{D}/I_\mathrm{G}$ as a fuction of fluence for aC-TL irradiated with 4.8 MeV/u U ions at M-branch (closed symbols, same data as in 8.2.5a) and 1.4 MeV/u U ions at gas stripper position (open symbols).

Cluster sizes were calculated for the measurements presented above by formula 8.5 of Ferrari [110]. The corresponding values are shown in figure 8.2.7 as a function of fluence and sp^2 content as determined by X-ray photoelectron spectroscopy (XPS). sp^2 contents are a mean of two individual measurements at different sample spots. Due to the proportionality of cluster size L_a and $I_\mathrm{D}/I_\mathrm{G}$, the evolution of cluster size L_a as a function of fluence is very similar to the evolution of $I_\mathrm{D}/I_\mathrm{G}$ in figure 8.2.5. Less values are presented in the sp^2 fraction graphs, since not all samples could be analyzed by XPS. In aC-TL cluster sizes increase up to 14 as a function of fluence. Cluster sizes as a function of sp^2 content do not show a clear trend with increasing sp^2 fraction. This might be caused by the scattering of values of sp^2 fraction for measurements performed in different spots. As for XPS, this effect might be related to clustering of sp^2 and sp^3 sites and also by inhomogeneous irradiation. For U irradiation a decrease of cluster size for high sp^2 content (corresponding to a large fluence) is observed. DLC-MM foils also show a general increase of cluster size with fluence and sp^2 fraction, and also a decrease of L_a as a function of fluence in the case of U irradiation. For aC-ACF foils no clear trend of L_a with fluence or sp^2 fraction can be observed. Since the XPS measurements did not show an increasing sp^2 fraction with fluence, the plot of cluster size versus sp^2 content does not yield a similar evolution versus fluence.

Based on the observed trends of cluster sizes verses irradiation in aC-TL and DLC-MM, a model for structure evolution can be developed.

In this view, which is based on equation 8.5, the increase of $I_\mathrm{D}/I_\mathrm{G}$ is related to an increase of cluster size with increasing fluence. Observed cluster sizes are in agreement with values reported by other groups, e.g. Abrasonis *et al.* [162] or Wada *et al.* [116]. The decrease of $I_\mathrm{D}/I_\mathrm{G}$ ratio in the case of irradiation with U ions is therefore assigned to a decrease of cluster sizes. This reduction of cluster sizes observed for fluences above 3×10^{13} ions/cm^2 (8.2.7) could be related to the process of track overlapping in this fluence range. According to a single-impact model [163, 164] the fluence for a certain percentage of track coverage can be calculated. For tracks with a radius of 5 nm, the fluence for 99 % track coverage

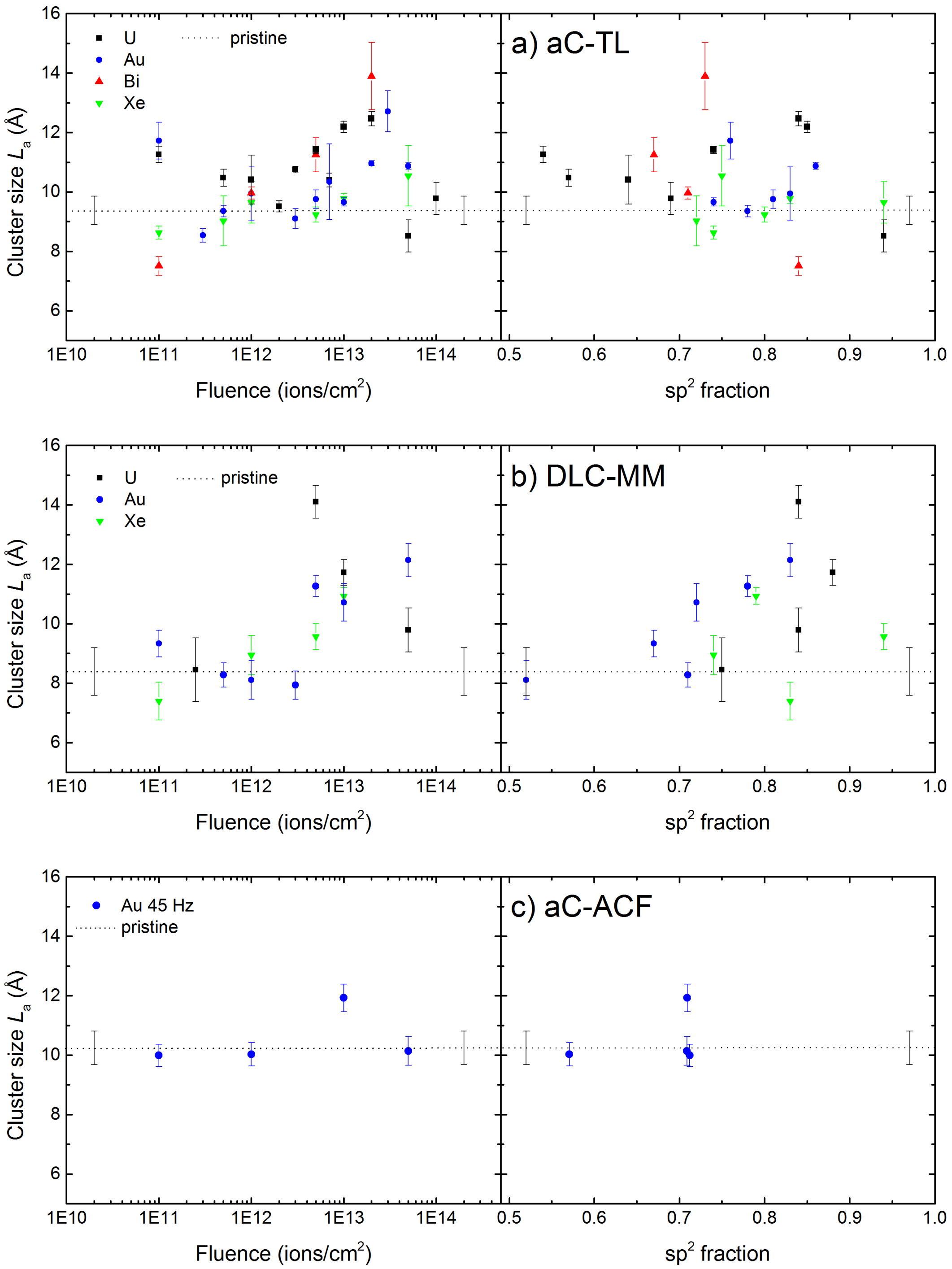

Figure 8.2.7.: Cluster size L_a determined from eq. 8.5 as a function of fluence and sp^2 content (mean values from XPS measurements) for different materials: a) aC-TL, b) DLC-MM and c) aC-ACF and irradiation with different ions: 4.8 MeV/u U (black squares), Au (blue circles), Bi (red up-triangles), Xe (green down-triangles). Pristine values are indicated by the dotted lines.

would be about 6×10^{12} ions/cm^2, for a radius of 3 nm at a fluence of approximately 2×10^{13} ions/cm^2. The fluence steps of our samples are too large to estimate track radii. After an increase of order due to growing clusters, the formation of rings and reduced bond angle disorder, the second ion hits could induce new defects. That this trend is only observed for U ions might be due to the fact, that U has the highest energy loss and therefore is expected to lead to larger tracks. The trend of lager tracks for

U compared to Au or other ions is also observed in other studies of this work, for example, by fitting infrared transmittance data or small angle X-ray scattering (SAXS) measurements. Errors of cluster sizes were determined by the Gaussian error propagation method using the errors for I_D/I_G shown in figure 8.2.5. Uncertainties for fluence and sp^2 content were estimated to be 15 % and 10 %, respectively. The constant used in formula 8.5 was determined for a laser excitation wavelength of 514 nm [110], whereas this study used a laser with a wavelength of 473 nm. Cluster sizes are therefore not precise, nevertheless the excitation wavelengths are close enough to provide an idea of cluster sizes.

8.3 On-line Infrared spectroscopy

The interaction of matter with radiation in the infrared (IR) region is associated with an absorption process which involves the change of the electric dipole moments. The absorption of energy in the region from 4000 to 400 cm^{-1} (2.5 to 25 µm, commonly referred to as mid-IR region) induces an excitation of vibrations of the atoms in molecules. Infrared spectroscopy measures the radiation transmitted by the sample as a function of frequency.

In an absorption process, the energy in the system has to be conserved. The total incident energy is partly absorbed, reflected and transmitted (for non-opaque objects):

$$\alpha_{\lambda,\Theta,T} + \rho_{\lambda,\Theta,T} + \tau_{\lambda,\Theta,T} = 1 \tag{8.6}$$

$\alpha_{\lambda,\Theta,T}$ is the absorptivity , $\rho_{\lambda,\Theta,T}$ the reflectivity and $\tau_{\lambda,\Theta,T}$ the transmittivity of a material as a function of wavelength λ, incident angle Θ and temperature T. Absorbance, reflectance and transmittance depend on sample properties like shape, thickness, surface roughness and oxidation state.

In order to stay in thermal equilibrium, a real body emits the same amount of radiation that was absorbed. This relation of absorptivity and emissivity $\epsilon_{\lambda,\Theta,T}$ of a real body in thermal equilibrium is described by Kichhoff's law of thermal radiation [165]:

$$\epsilon_{\lambda,\Theta,T} = \alpha_{\lambda,\Theta,T} \tag{8.7}$$

The emissivity describes the ratio of thermal radiation from a real material compared to an ideal black body at the same temperature as given by Stefan-Boltzmann law and is a function of wavelength and temperature. Emissivity is a material property, whereas the term emittance refers to a specific sample. In the following the terms emittance and transmittance describe experimentally determined values.

In diamond, infrared absorption is not allowed due to its symmetry, whereas in graphite two infrared-active modes exist at 1585 cm^{-1} (E_{1u}) and 868 cm^{-1} (A_{2u}) [166]. In amorphous solids, the selection rules for crystalline solids are relaxed, that means there is no crystal momentum conservation. This allows all modes, including the one-phonon absorption, which is forbidden in diamond [167]. In this sense, a similarity between infrared spectra and Raman spectra could be expected, but their intensity is modulated by different matrix elements leading to different spectra (see section 3.1.2).

The infrared spectrum of evaporated amorphous carbon measured by Knoll and Geiger [168] shows no sharp transitions and no strong absorption bands, but humps at 702, 1233 and 1465 cm^{-1}. In the presence of hydrogen, several C-H stretching and bending modes appear in the spectrum [107]. IR spectroscopy is therefore a common method for studying the H content in aC samples. Wei *et al.* [169] propose three contributions to the emittance spectrum of DLC. In the mid-infrared region up to wavenumber of 4000 cm^{-1} they find mainly phonons and free carriers to determine the emittance and transmittance spectra.

Under ion irradiation, the transmittance of the foils changes as a function of fluence. To monitor this process, transmission spectra were recorded with an in-situ Nicolet 6700 FTIR spectrometer attached to the M3-beamline (figure 8.3.1). The infrared source and the detector of the spectrometer are placed outside of the irradiation chamber. The infrared beam passes in and out of the vacuum chamber through 4-mm thick ZnSe windows, which have a transmission of 93 %. The absorption edge of ZnSe limits the measurement to the wavenumber range 4000 to 650 cm^{-1} (2.5 to 15.4 µm). FTIR spectra are taken during beam stops by rotating the target from irradiation position 1 (normal to the ion beam) to FTIR measurement position 2 (normal to the infrared beam). Due to the relatively large FTIR beamspot of 7 mm in diameter, a large area of the beamspot contributes to the measurement, reducing errors by beamspot inhomogeneities. Background spectra were recorded before each fluence step to correct for contributions from residual gas, the entrance windows (ZnSe) and air outside the chamber.

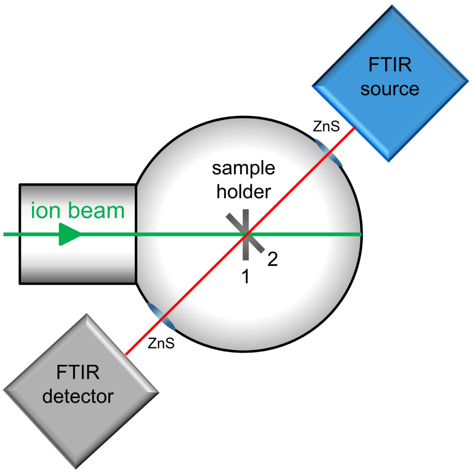

Figure 8.3.1.: Scheme of in-situ FTIR spectroscopy setup at the M3-beamline of the GSI UNILAC accelerator. The infrared source and detector of the spectrometer are placed outside of the irradiation chamber equipped with two ZnSe windows, enabling entrance and exit of the IR beam. The sample holder can rotate in order to move the sample from the ion irradiation position (1) to the FTIR measurement position (2) [170].

Recorded spectra are presented for the irradiation of 20 $\mu\text{g/cm}^2$ aC-TL foils with 4.8 MeV/u U ions in figure 8.3.2. No sharp transitions and no absorption bands are visible, except a slight hump at about 1600 cm^{-1}. This is an indication, that the amorphous carbon film is not hydrogenated. The hump could be related to the maximum of the phonon density of states of graphite in this region. Rodil *et al.* [171] found a broad absorption band at ≈1240 cm^{-1} in sputtered amorphous carbon. In the aC-TL foils a very broad absorption feature could be identified in the region of 1000 to 1600 cm^{-1}. Rodil *et al.* attribute the IR adsorption at ≈1240 cm^{-1} to the presence of sp^2 clusters of conjugated chains or rings. In their model, an enhanced electron-phonon interaction in these large conjugated systems is responsible for the enhancement of the IR absorption in this region analogous to the fingerprint region in organic molecules. Raman (section 8.2) and XPS (section 8.1) measurements indicate a large fraction of sp^2 bonding and clustering already in pristine amorphous carbon films.

The transmittance of the pristine foil increases with decreasing wavenumber from about 0.45 to 0.85. Throughout irradiation, the transmittance shifts to lower values. Additionally, the rise towards lower wavenumbers is less distinct for high fluences. For the largest fluence of 1×10^{14} ions/cm^2 the transmittance increases from 0.15 to 0.20 with decreasing wavenumbers. The vibrational density of states

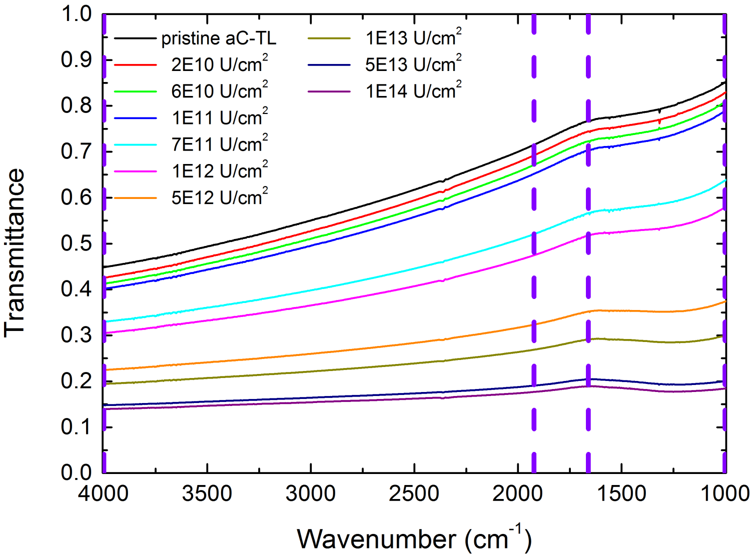

Figure 8.3.2.: In-situ infrared transmittance spectra of a 20 µg/cm^2 aC-TL foil irradiated with 4.8 MeV/u U ions recorded at various fluence steps during irradiation. Vertical dashed lines represent the wavenumbers at which transmittance values were extracted.

of diamond has its main features in the range of 1300 and 900 cm^{-1} and a plateau between 800 and 600 cm^{-1}, whereas graphite has no strong features in this region. A flattening of the spectrum may therefore be explained by the decrease in sp^3 bonding content induced by the ion irradiation. Since the selection rules of the amorphous state are relaxed, a broad spectrum is expected. The decrease of overall transmittance in the mid-IR region could therefore be attributed to the conversion of sp^3 to sp^2 bonding. The formation of defects by the ion irradiation may also contribute.

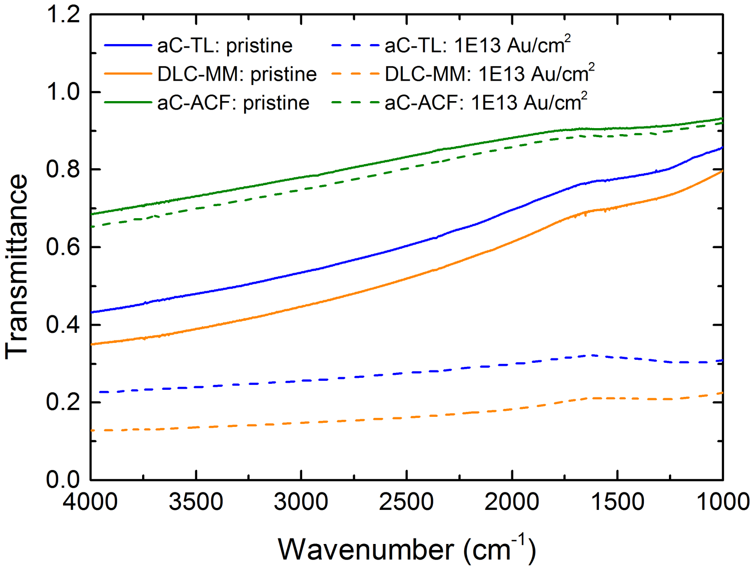

Figure 8.3.3.: Infrared transmittance spectra for 20 µg/cm^2 aC-TL, DLC-MM and aC-ACF foils pristine (line) and irradiated with 4.8 MeV/u Au ions to a fluence of 1×10^{13} ions/cm^2 (dashed).

A comparison of transmittance spectra for the three different types of foils (figure 8.3.3), pristine and irradiated to a fluence of 1×10^{13} Au/cm^2, shows that the shape of the spectra is very similar. DLC-MM and aC-ACF also have no sharp transitions and no absorption bands. The hump at about 1600 cm^{-1} is

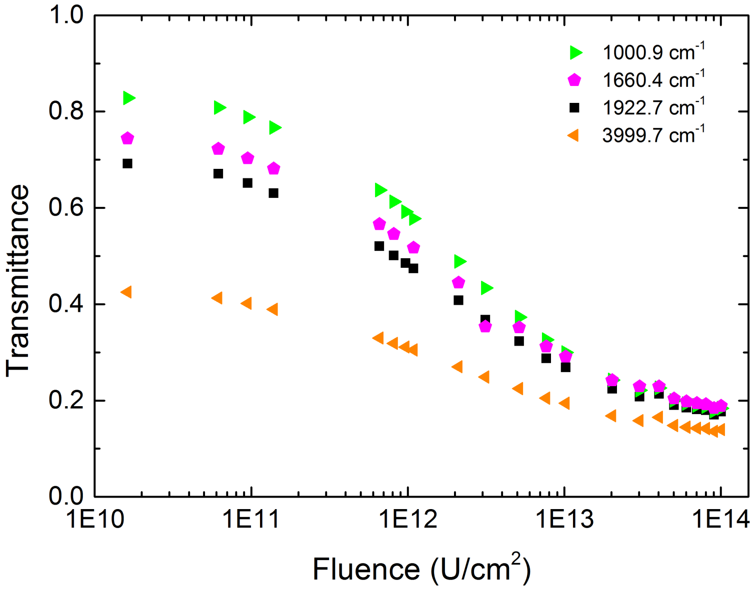

Figure 8.3.4.: Transmittance as a function of fluence extracted from infrared spectra at different wavenumbers for 20 µg/cm^2 aC-TL irradiated with 4.8 MeV/u U ions (2Hz, 0.6 ms), as indicated in figure 8.3.2.

visible, but less distinct in aC-ACF. Also, the spectra of aC-ACF are more flat and only decrease from about 0.93 to 0.69 with increasing wavenumbers. XPS measurements (section 8.1) indicate a higher fraction of sp^3 bonding in pristine aC-ACF films. A higher sp^3 content could explain the overall higher transmittance (for the same areal density as for DLC-MM and aC-TL) and flat spectra in this type of amorphous carbon.

For better visualization of the changes induced by ion irradiation, four transmittance values at different wavenumbers were extracted and plotted as a function of fluence (figure 8.3.4). The transmittance decreases exponentially for all extracted wavenumbers, starting at low fluences of about 1×10^{11} ions/cm^2. At high fluence the transmittance saturated at 0.2 to 0.15 for all wavelengths. At lower wavenumbers (1000.9 cm^{-1}) the decrease is larger than at higher wavenumbers (3999.7 cm^1). In order to study different samples, ions and beam conditions, the transmittance at 1922.7 cm^{-1} was selected for further analysis and as an input for thermographic measurements (chapter 10).

Figure 8.3.5 presents the relative transmittance change $(\tau - \tau_0)/\tau_0$ with τ_0 being the initial transmittance before irradiation in aC-TL, DLC-MM and aC-ACF for different ions and beam conditions represented by the repetition rate and pulse length (detailed beam parameters are presented in table 4.0.1). For low-repetition rates of short pulsed U and Au beams (2 Hz) the onset of transmittance decrease is shifted to lower fluences compared to aC-TL irradiated at high repetition rate (Au 45 Hz). This may indicate that short intensive pulses are more efficient in converting sp^3 to sp^2 bonds. In case of irradiation with Xe ions, the onset of transmittance decrease is shifted to higher fluences, which might be an effect of the smaller energy loss compared to Au and U ions of the same specific energy.

For the DLC-MM foil irradiated with the same beam conditions (Au 45 Hz, 4 ms) as aC-TL, the transmittance decreases at lower fluences, indicating that DLC-MM is more sensitive to ion irradiation. In contrast to the DLC-MM foil, the transmittance decrease in the aC-ACF foil is comparably small. This might be a sign of a lower sensitivity to the heavy ion beam.

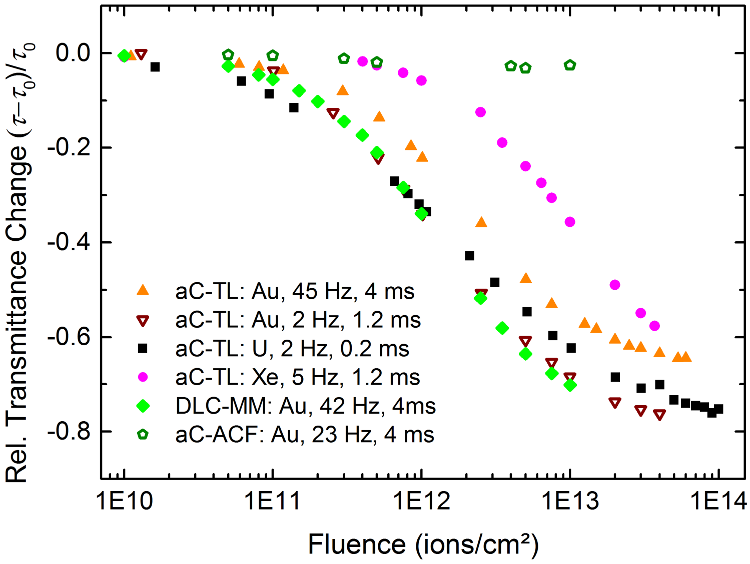

Figure 8.3.5.: Relative transmittance change $(\tau - \tau_0)/\tau_0$ of 20 µg/cm^2 aC-TL foil at 1922.7 cm^{-1} for different ions and beam parameters. The energy for all irradiations was 4.8 MeV/u.

The exponential decrease of the transmittance as a function of ion fluence (figure 8.3.5) plotted in non-logarithmic scale can be described by the Poisson equation, based on a single hit process of the ions [163, 164]:

$$\tau(\phi) = \tau_f + a \exp(-\sigma\phi) \tag{8.8}$$

where τ denotes the transmittance extracted from a certain wavenumber at a given fluence ϕ, σ is the cross section of structural change, τ_f the minimum transmittance at high fluences and a is a fitting parameter. Using the cross section and assuming cylindrical track symmetry ($\sigma = \pi r^2$), the corresponding track radius can be calculated. An example for a fit with this equation is presented in figure 8.3.6 (blue) for aC-TL irradiated with 4.8 MeV/u U ions and transmittance values extracted at 1922.7 cm^{-1}. The errors were estimated to be 15 % for the fluence and 0.02 absolute error in transmittance, accounting for uncertainties during irradiation and transmittance measurement (background subtraction etc.). The fit with the Poisson law does not have a good quality for fluences between 5×10^{12} and 3×10^{13} ions/cm^2. The track radius determined from this fit is 3.4 ± 0.2 nm (error determined from the fit). Because the data shows a slight linear decrease for fluences larger than 2×10^{13} ions/cm^2, the saturation of the fit does not reproduces the data well. This slight decrease towards large fluences might be an indication for an additional effect occurring after about 2×10^{13} ions/cm^2. To account for this additional influence, a linear term $(+b\phi)$ was added to the Poisson equation (green fit) yielding a track radius of 4.2±0.2 nm. Also this fit does not reproduce the data in the fluence range from 5×10^{12} and 2×10^{13} ions/cm^2. Fits based on a double hit process [163, 164] did not yield good fits either. For this reason, the fit was restricted to a maximum fluence of 1×10^{13}ions/cm^2 (red), yielding a track radius of 4.6 ± 0.2 nm. The fit quality is much better, however the fit saturates at higher transmittance, causing an overestimation of the determined track radius. For this reason errors of the tracks are estimated to be larger (0.5 nm) than the values determined from the fits.

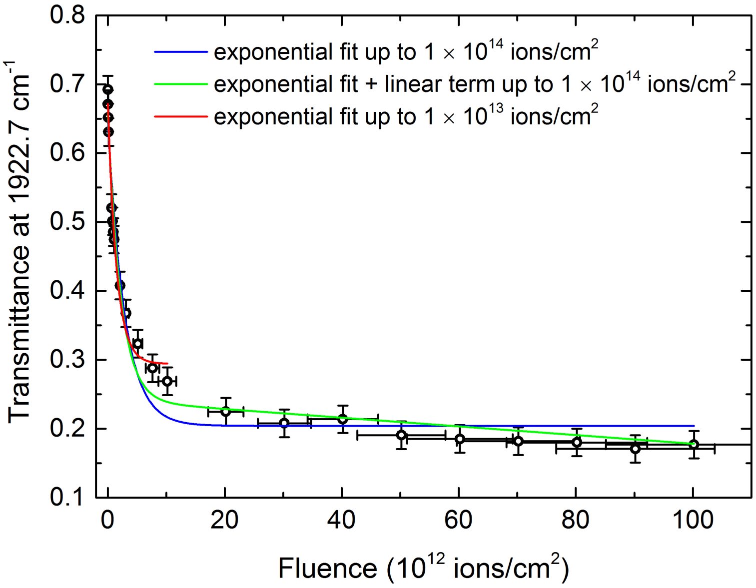

Figure 8.3.6.: Transmittance of 20 μg/cm^2 aC-TL at 1922.7 cm^{-1} irradiated with 4.8 MeV/u U ions with exponential fits according to equation 8.8. Errors were estimated to be ±0.02 for the transmittance and ±15 % for the fluence.

In order to understand the influence of the position (wavenumber) for transmittance value extraction on the cross section and track radius, fits were performed for all positions presented in figure 8.3.4. According to the discussion above, the maximum fluence for the fit was chosen to be 1×10^{13} U ions/cm^2.

Table 8.3.1.: Cross sections and track radii in 20 μg/cm^2 aC-TL irradiated with 4.8 MeV/u U ions extracted from fits of transmittance decrease as a function of fluence, extracted at different wavenumbers from the IR spectra in figure 8.3.4.

wavenumber (cm^{-1})	σ (nm^2)	r (nm)
1000.9	57.8 ± 13	4.3 ± 0.5
1660.4	60.6 ± 13	4.4 ± 0.5
1922.7	66.7± 13	4.6 ± 0.5
3999.7	58.2 ± 13	4.3 ± 0.5

Cross sections vary between approximately 58 and 67 ± 13 nm^2 (table 8.3.1). Derived track radii are in the range of 4.3 ± 0.5 nm and 4.6 ± 0.5 nm. The errors include the error of the absolute cross sections/tracks due to a smaller saturation value of the fit. The small difference between the absolute track radii shows that all wavenumbers could be used for the calculation of track radii. Since the values derived from the transmittance at 1922.7 cm^{-1} are an input for thermographic measurements (chapter 10), they are also used for a comparison of different ion irradiations and with a DLC-MM foil (table 8.3.2). However, since track values are slightly larger for this wavenumber compared to the values at other wavenumbers in the spectrum (table 8.3.1), the absolute tracks sizes are possibly slightly overestimated. The transmittance decrease of Au ions (45 and 2 Hz beams) in aC-TL and DLC-MM were fitted with the procedure described for U irradiation up to a fluence of 1×10^{13} ions/cm^2. In the case of Xe ions the fit was extended to 4×10^{13}ions/cm^2, because the transmittance decrease is shifted to higher fluences compared to the other ions. Irradiation with U ions shows the largest radius together with the low-repetition rate Au beam (2 Hz). Rotaru *et al.* [83] found radii of comparable size (4.2 to 4.7 nm) in DLC irradiated with U ions. The high repetition rate Au beam (45 Hz) creates a smaller radius than the beams with low repetition rate (and shorter pulse length). This agrees well with the interpretation of figure 8.3.5. Xenon irradiation results in a much smaller radius, probably related to the smaller $\mathrm{d}E/\mathrm{d}x$. The tracks formed by irradiation of a DLC-MM foil by a 45 Hz Au beam is larger than for the corresponding irradiation of aC-TL. This observations supports the statement, that DLC-MM is more sensitive to ion irradiation than aC-TL. In case of aC-ACF, no tracks are presented due to a low fit quality, resulting from very small changes of the transmittance.

Table 8.3.2.: Track radii calculated from the cross sections of the fits for the data shown in figure 8.3.5 (transmittance values extracted at 1922.7 cm^{-1} as a function of fluence for different ion irradiation and 20 μg/cm^2 aC-TL and DLC-MM).

aC-TL **U (2 Hz)** (nm)	**aC-TL** **Au (45 Hz)** (nm)	**aC-TL** **Au (2 Hz)** (nm)	**aC-TL** **Xe (5 Hz)** (nm)	**DLC-MM** **Au (45 Hz)** (nm)
4.6 ± 0.5	3.7 ± 0.5	4.6 ± 0.5	1.8 ± 0.5	4.5 ± 0.5

The observation of different track radii for different beam conditions, however, rises the question if also other processes are involved in the decrease of the transmittance, because the track radius is expected to mainly depend on the energy loss of the ion. The main difference between the U beam with low repetition rate and very short pulse length in comparison to a Au beam of high repetition rate, is the intensity of the individual pulses (pulse intensity). The different pulse intensity causes a higher maximum (peak) temperature during one pulse in the beamspot (measured by IR thermography, figure 10.2.2) and more intense stress waves in the case of the U beam. Since the origin of the transmittance decrease is not conclusively clarified, further experiments need to investigate the additional effects influencing the size of the tracks.

8.4 Transmission electron microscopy

Transmission electron microscopy (TEM) provides a valuable technique for the morphological, compositional and crystallographic characterization of materials. Since electrons have a much smaller de Broglie wavelength than visible light, a much higher resolution down to atomic scale can be achieved. The microscope is usually composed of an electron source, a system of condenser lenses for focusing the beam on the sample and an objective lens for forming an image with the electrons that interacted with the sample. Additional lenses magnify the image and project it on a screen. As the electron beam is transmitted through the very thin sample, the electrons are scattered elastically and inelastically. Elastically scattered electrons in forward direction are used to form images or diffractions patterns, whereas the energy loss of inelastically scattered electrons is detected in electron energy loss spectrometry (EELS).

Using elastically scattered electrons, two different imaging modes are possible which utilize the direct or the diffracted beam. The bright field imaging mode (BF) forms an image with unscattered electrons transmitted through the specimen. Contrast is formed by thickness and density variations (mass-thickness contrast) and diffraction for crystalline materials, when the angle of lattice planes to the electron beam fulfills Bragg condition ($2d \sin\theta = n\lambda$) with interplanar distance d, scattering angle 2θ, wavelength λ and an integer n). In both cases, bright regions result from weak diffraction. Dark field mode (DF) selects a single diffracted beam for imaging. Bright areas are caused by atomic planes which are in Bragg condition and which produce the selected diffracted beam. The DF method allows to visually differentiate crystal phases.

Diffraction patterns are formed on the back focal plane of the objective lens and provide information on the crystal structure and orientation of different crystal phases and crystallite sizes. The use of an aperture produces a diffraction pattern of a specific area on the specimen and is called selected area electron diffraction (SAED).

In high resolution imaging (HRTEM) diffracted and transmitted beam are superimposed to enhance the contrast along lattice lines, providing lattice parameter directly from the images. TEM of thin amorphous carbon show a homogeneous image without structural features due to the lack of long-range order of the amorphous state. Diffraction patterns show one or two diffuse rings with no discrete reflections. Therefore TEM investigation of amorphous carbon is commonly used to detect areas which show some degree of ordering like turbostratic or nanocrystalline carbon. In the case of amorphous carbon stripper foils, TEM investigations revealed ion-beam induced graphitization [27, 41, 46] as described in chapter 1.2.

Pristine and irradiated 20 $\mu g/cm^2$ aC-TL foils were investigated in a JEM-2100F and a ARM-200F microscope at the Materials and Earth Sciences Department of Technische Universität Darmstadt. Measurements were conducted by Stephan Lauterbach and Leopoldo Molina-Luna. Small pieces were cut from the foils and fixed (clamped) in a double-copper grid. An acceleration voltage of 200 kV was used for the measurements and special attention was paid to avoid damage or modification of the specimen by the electron beam.

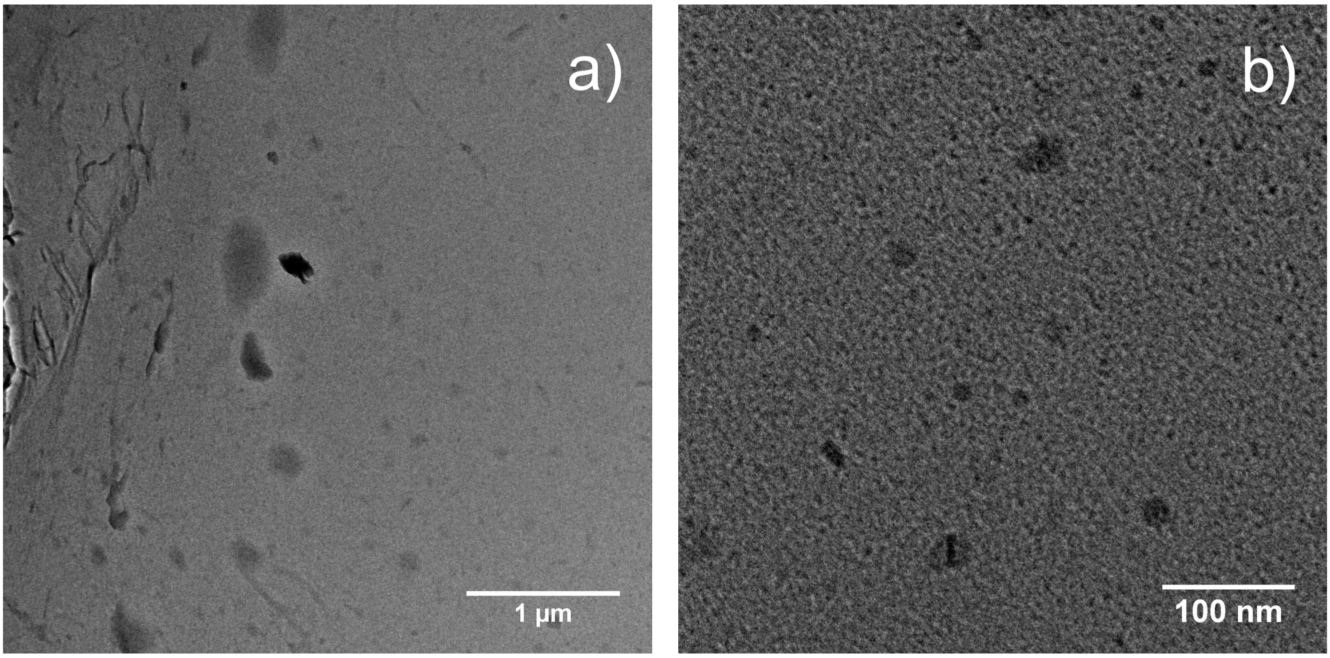

Figure 8.4.1.: TEM images of pristine aC-TL at different magnifications.

Figure 8.4.1a and b present images of a pristine aC-TL sample. They show a homogeneous structure typical for amorphous materials. A few black spots are visible, which might be related to contaminations or density variations. In comparison, a sample irradiated with 4.8 MeV/u U ions to a fluence of 5.7×10^{14} ions/cm^2 is presented in figure 8.4.2. Short-range ordering is visible in the form of turbostractic carbon and is indicated by arrows (figure 8.4.2b). Grey value profiles of four lines (figure 8.4.2c) were used to determine the spacing between the fringes. The distance between the fringes was determined by counting the peaks of grey value over a certain distance and divide the length of the line by this number. The interlayer distance found for these three line are between 0.34 and 0.37 nm and are slightly larger than the interlayer spacing of graphite: 0.335 nm. A list of interlayer distances for graphite and diamond and corresponding hkl are presented in table 8.4.1. An example for a grey value profile of one of the lines (2) is presented in figure 8.4.2d. The SAED pattern shows the typical diffuse rings for amorphous carbon. Determination of interlayer spacings from the radii of the rings in the SEAD pattern (8.4.7c) shows interlayer distances of 0.21 nm and 0.12 nm. A ring for the (002) planes in graphite with a lattice spacing of 0.34 nm is absent. The measurement accuracy due to the resolution of the TEM images and spacing determination by grey value peaks was estimated to be ±0.02 nm.

A fast Fourier transformation image (FFT) of the indicated area (blue square) in 8.4.2a shows two bright spots with a distance of approximately 0.35 nm from the center (figure 8.4.2c). To investigate changes at higher fluences, a sample irradiated with 1.4 MeV/u U ions of fluence 3.8×10^{16} ions/cm^2 (deposited energy about 13 kW/cm^2) was analyzed. At low magnification, dark areas are visible (figure 8.4.3 a and b), which are not seen in TEM images of pristine samples (figure 8.4.1). At higher magnification these darker areas show to be an agglomeration of smaller dark areas (figure 8.4.3 c - e). These dark spots have a round shape and are of the size of 3 to 10 nm. EDX (energy-dispersive X-ray spectroscopy) measurements proved that they consist only of carbon. Lattice fringes are visible at high magnification.

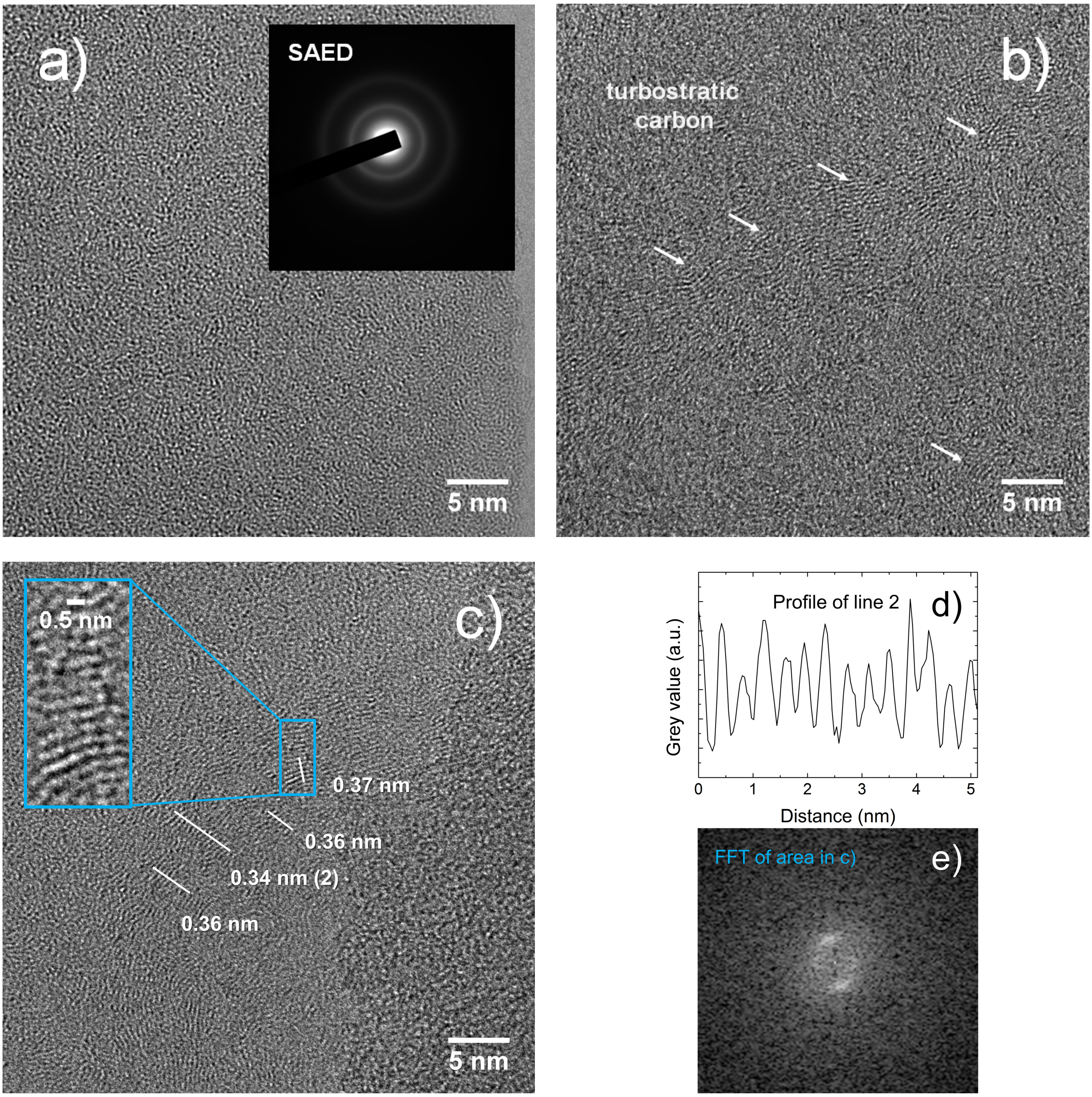

Figure 8.4.2.: HRTEM images (a, b, c) and SAED pattern (in a) of aC-TL irradiated with 4.8 MeV/u U ions to a fluence of 5.7×10^{14} ions/cm^2. Turbostratic carbon (in b) is indicated by arrows. The given values (in c) are the interplanar distance determined from the grey value line profiles, which are indicated by lines. d) presents an exemplary profile for line 2 (in c). e) shows the FFT image of the blue, enlarged area indicated in c).

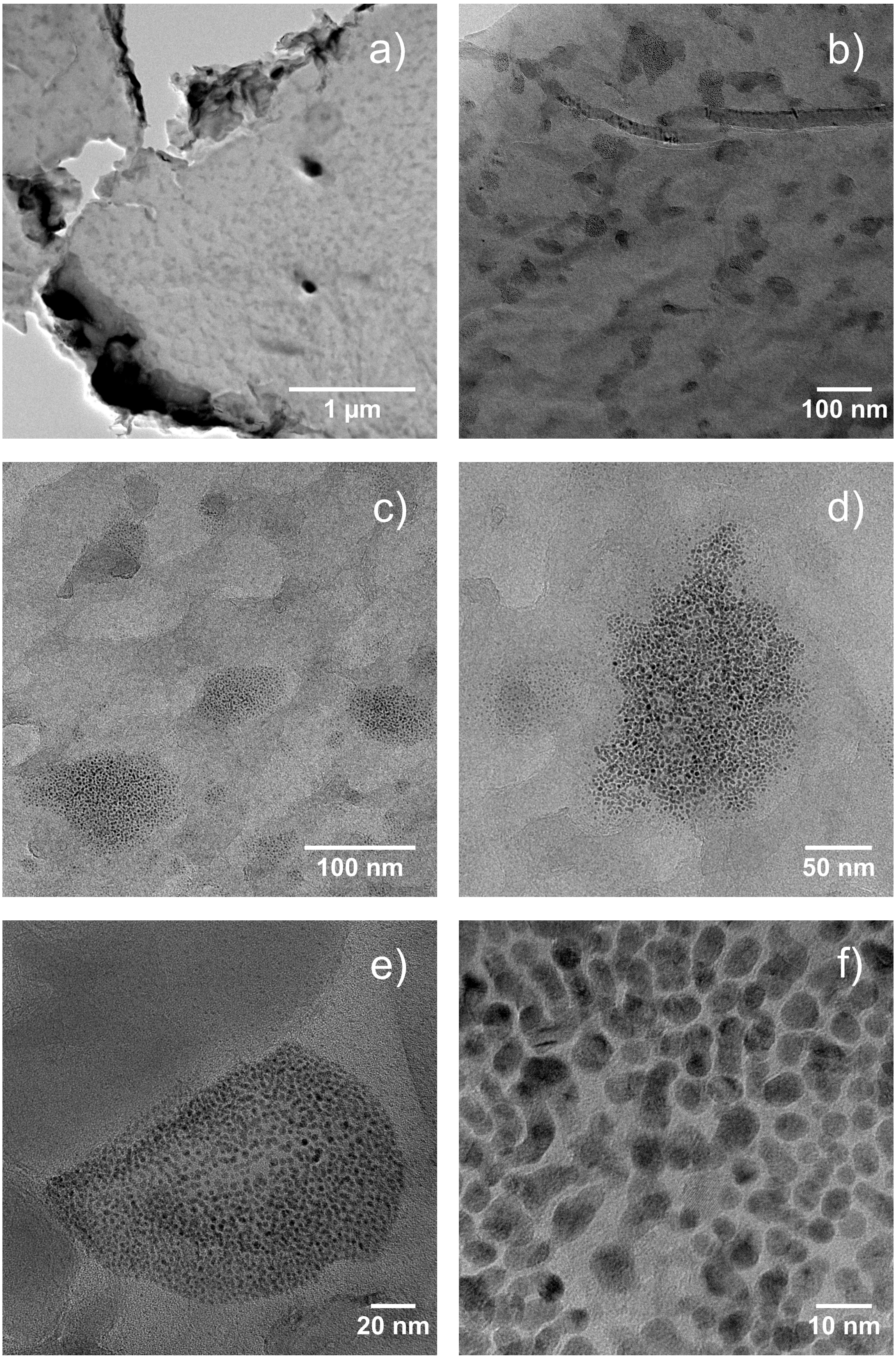

Figure 8.4.3.: HRTEM images at different magnifications of aC-TL irradiated with U ions at the gas stripper position of fluence 3.8×10^{16} ions/cm^2 (deposited energy about 13 kW/cm^2).

Figure 8.4.4 presents determined interlayer spacings of different line profiles. In addition to spacings in the range of 0.34 to 0.36 nm as found in the sample irradiated with 4.8 MeV/u U ions of 5.7×10^{14} ions/cm^2 (figure 8.4.2), smaller lattice plane spacings in the range of 0.21 to 0.22 nm are detected in the dark areas. These interlayer spacings match spacings of the (111) planes of cubic diamond (0.206 nm) or (100) (0.218 nm) and (002) (0.206 nm) planes in hexagonal diamond. However, also (100) and (101) plane interplanar distances in graphite are 0.213 nm and 0.203 nm respectively. A FFT of image 8.4.4c shows spots with a radius of 0.21 nm from the center, indicating a polycrystalline structure. Calculated interplanar spacings and corresponding planes are presented in table 8.4.1.

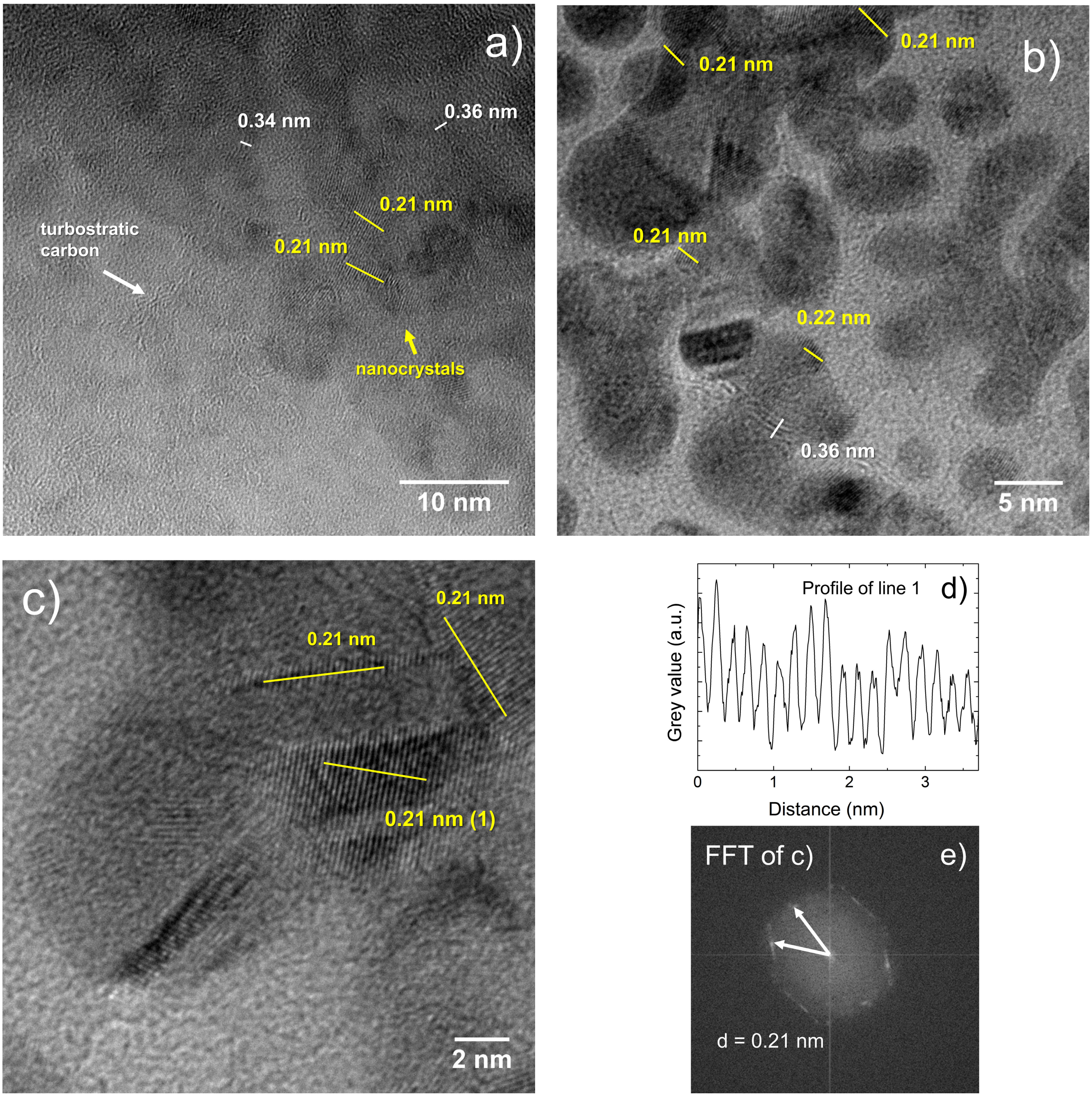

Figure 8.4.4.: HRTEM images of aC-TL irradiated with U ions of fluence 3.8×10^{16} ions/cm^2. Indicated lines present grey value profiles. d) shows the profile of line 1 (in c), e) the FFT image of c).

Table 8.4.1.: Interplanar distances and corresponding hkl, calculated for graphite and diamond.

	h	k	l	d (nm)		h	k	l	d (nm)
Graphite	0	0	2	0.335	**Diamond**	1	1	1	0.206
(hexagonal)	1	0	0	0.213	**(cubic)**	2	2	0	0.126
	1	0	1	0.203		3	1	1	0.108
	1	0	2	0.180	**Diamond**	1	0	0	0.218
	1	0	2	0.167	**(hexagonal)**	0	0	2	0.206
	1	0	2	0.154		1	0	1	0.193
	1	0	2	0.123		1	0	2	0.150
	1	0	2	0.116		1	1	0	0.126
	1	0	2	0.114		1	0	3	0.116
	1	0	2	0.112					

A conversion of graphitic areas to nano-diamond could be possibly caused by the rapid deposition of very high energy densities creating high pressures in the short pulses. There are many publications that describe the transformation of graphite by ion irradiation [172–176] and a amorphous carbon to diamond conversion by nanosecond laser pulses [177]. Other authors, like Dollinger *et al.* [27] attribute interlayer spacings of 0.21 nm found in annealed amorphous carbon foils to graphite nanocrystals, based on the assumption that all (002) planes lie parallel to the surface and corresponding (002) rings are therefore not visible in the SAED pattern. SAED pattern from different regions of the sample are presented in figure 8.4.5. The ring pattern corresponding to area 1 shows two rings, which correspond to interlayer distances 0.21 nm and 0.12 nm. The SAED pattern of the dark area 2 presents an asymmetric shape and an additional ring which includes also bright spots and corresponds to a lattice plane spacing of 0.34. The diffraction pattern from area 3 shows many bright spots that form different rings. Calculated interlayer spacings from these rings are (inside to outside): 0.29, 0.23, 0.19, 0.17, 0.12, 0.10 nm. Most of these spacings can be attributed to either graphite planes or diamond planes. However in the case that the nanocrystals are of diamond phase, the SAED pattern most probably would be a superposition of graphite and diamond reflections. A clear identification based on these data is therefore not possible. Nevertheless, some details in the images support the identification of diamond nanocrystals. A few of the observed nanocrystals show bright areas and lines in the dark field image in figure 8.4.6. The bright areas in which Bragg condition is fulfilled prove the presence of nanocrystals and bright lines suggest that some of the nanocrystals are twinned. Twinning along (111) planes in diamond is commonly reported in literature [173, 178], because the twin interface is one of the lowest energy defects in diamond [172]. Combined with the round appearance of the nanocrystals, the presence of twinning might support the assumption of nano-diamond formation.

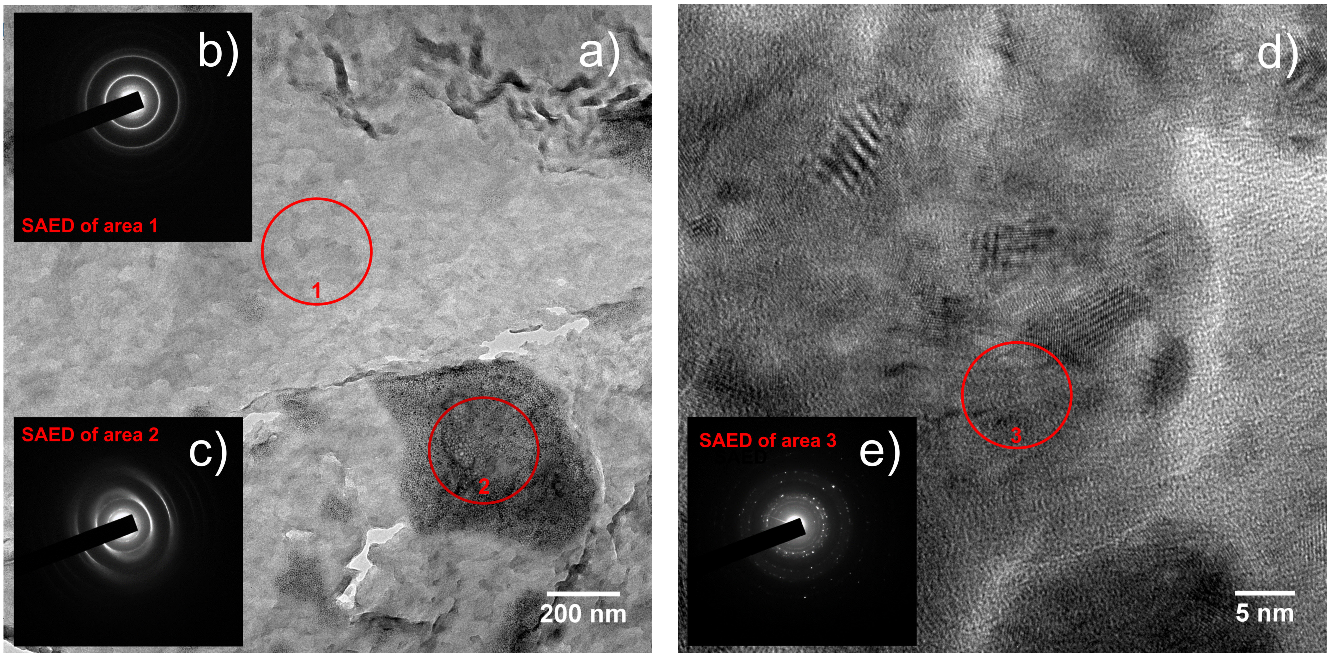

Figure 8.4.5.: HRTEM images (a, b) of aC-TL irradiated with U ions of fluence 3.8×10^{16} ions/cm^2 and SAED pattern of indicated area 1 (b), 2(c), 3 (e).

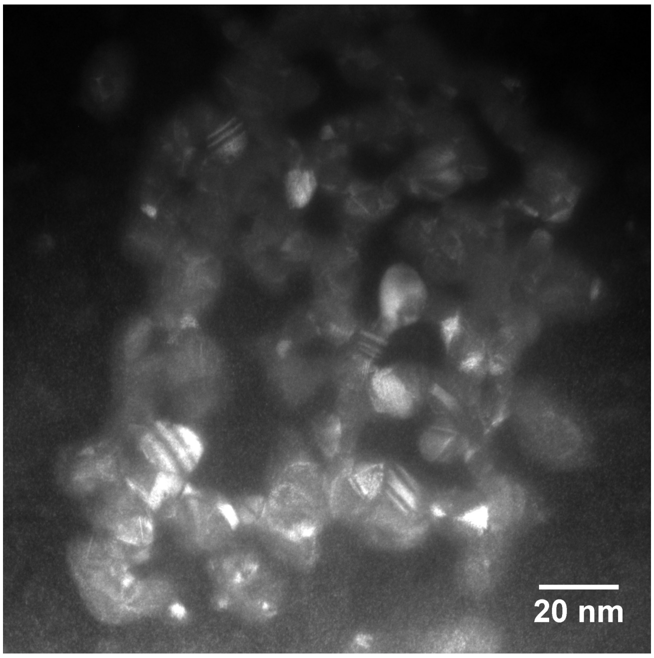

Figure 8.4.6.: Dark field TEM image of aC-TL irradiated with 1.4 MeV/u U ions of fluence of about 3.8×10^{16} ions/cm^2. Bright areas show the presence of nanocrystals.

In addition, the effect of temperature in comparison to ion irradiation, which involves both heating and radiation damage, was investigated with an annealed (1000°C, 1 hour) aC-TL sample. The annealing temperature was chosen to be larger than the temperature of about maximum 250°C during irradiation with a U beam at M-branch conditions (measured by an IR camera, chapter 10). Temperatures during irradiation at the gas stripper position might be much higher, since the ion flux is one order of magnitude larger. Figure 8.4.7a and 8.4.7b show cracks. Their shape appears to be a result of material compaction. The large crack in figure 8.4.7b indicates delamination of very thin layers at the edges. These observations support the view of aC-TL being a layered material with some extend of porosity. Larger magnification (8.4.7c and 8.4.7d) presents some areas of turbostratic carbon, however the most regions only present incipient ordering. This indicates that the structural changes induced by ion irradiation are larger compared to the effect of temperature alone. Further studies should investigate these differences. Interestingly, the SEAD pattern in 8.4.7c shows rings which correspond to interlayer distances of 0.21 nm and 0.12 nm, as it was also found for the samples irradiated with 4.8 MeV/u U ions in 8.4.2c. A ring corresponding to the (002) planes of graphite is not visible, like in the case of the sample with lower fluence (4.8 MeV/u U, 5.7×10^{14} ions/cm^2). These observations provide support for the model of Dollinger *et al.* [27], in which the nanocrystals consist of graphite but the (002) planes lie parallel to the electron beam. Further studies with high resolution are needed to finally identify the nanocrystals found in this sample. It would be interesting, if a similar phase could be found also for high repetition rate beams, for which the effect of stress waves are expected to be weaker.

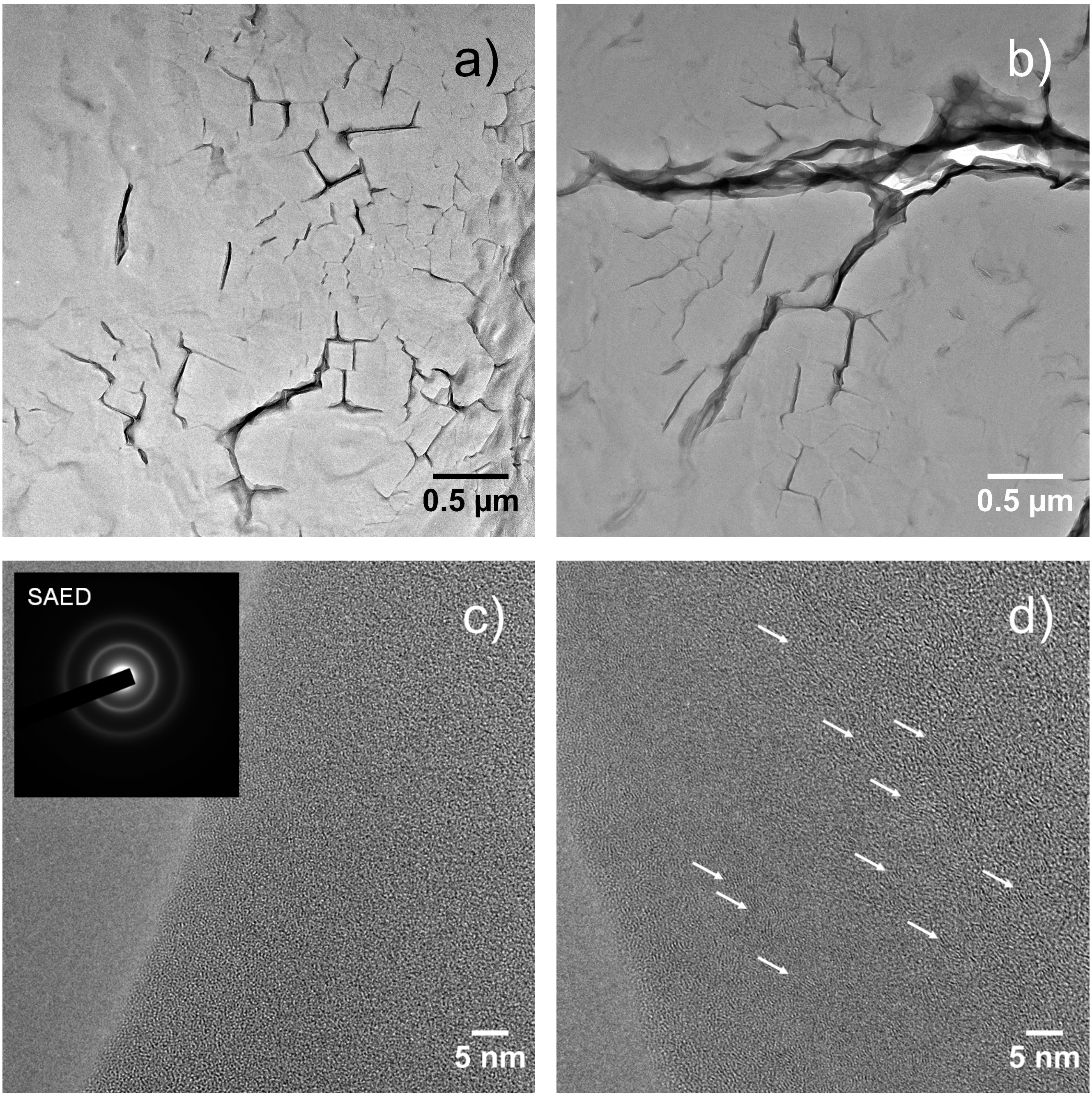

Figure 8.4.7.: HRTEM images and SAED pattern of aC-TL annealed for one hour at 1000°C. a and b: Low magnification images showing cracks. c and d) HRTEM images and SAED pattern (of c). Turbostratic carbon is indicated by arrows (in d).

8.4.1 Electron energy loss spectroscopy

Electron energy loss spectroscopy (EELS) uses inelastically scattered electrons that lose energy and are deflected from their original path when passing through a thin sample. The energy loss depends on the electron arrangement of the target material. Electron energy loss spectra therefore provide information about the local electronic structure and bonding [179] . In case of amorphous carbon, EELS is a common method to quantitatively characterize sp^2 and sp^3 fractions. The analysis of the scattered electron beam can be performed in a transmission electron microscope (TEM), but there exist also other techniques. Typical EEL spectra cover energies in the range of 0 to 2 keV including three regions [106]: (1) The zero-loss peak formed by elastically scattered and unscattered electrons. (2) The low-loss region from 0 to ∼100 eV [180]. For carbon this region usually extends up to 40 eV and losses are due to excitation of electronic transitions in the valence band and bulk plasmons [106]. (3) The high-loss region formed by excitation of deeper core levels. In carbon, transitions from 1s level to empty states in 2p energy level denote the carbon K-edge [180]. This spectral feature is a direct representation of the empty density of states [180]. The K-edge is usually in the range of 285 eV and larger and has two main peaks. For graphite a small pre-peak appears at 285 eV due to the excitation of π^* states from sp^2 hybridized carbon atoms based on the assumption that there is no significant amount of sp bonding [106]. The 285 eV peak is absent in diamond EELS. The larger peak around 290 eV is visible in both diamond and graphite and is caused by σ^* excitation from sp^3 for diamond and sp^2 for graphite. In amorphous carbon both peaks are present because it has both sp^2 and sp^3 bonds.

EELS measurements were performed by Leopoldo Molina-Luna in the same TEM as used for imaging (previous section 8.4) and 200 kV acceleration voltage. Spectra were recorded with 1 s exposure time. The spectral energy resolution was deduced from the width of the zero-loss peak to about 1.5 eV. For each measurement spot 100 single spectra were superimposed to achieve one final spectrum. Spectral treatment was performed using open-source Cornell Spectrum Imager [181]. The background was considered by power law fitted in the range from 150 to 269 eV (tail extending from zero-loss to the K-edge). The resulting normalized spectra are presented in figure 8.4.8. A common method proposed by Berger and McKenzie [182] was used for quantification of sp^2 and sp^3 bonding contents. This method is based on the ratio of the area (integrated intensity) of the pre-peak at 285 eV to the total area of the spectrum in an energy window ΔE. This value is compared to a reference of 100 % sp^2. In this study a polycrystalline graphite sample is used as a reference (figure 8.4.8). Robertson [89] emphasized the importance of eliminating the orientation dependence of single-crystalline graphite by using a randomly oriented micro-crystalline graphite sample. Alexandrou [183] proposed C_{60} as a reference alternative. By assuming that the intensity of the π^* pre-peak is directly proportional to π bonding in the amorphous carbon material, the sp^2 fraction f can be calculated by the following formula [182]:

$$f = \frac{I_{g\pi^*}}{I_{aC\pi^*}} \frac{I_g(\Delta E)}{I_{aC}(\Delta E)} \tag{8.9}$$

$I_{g\pi^*}$ and $I_{aC\pi^*}$ are the integrated intensities of the π^* pre-peak of the graphite reference sample and the amorphous carbon foil, respectively. $I_g(\Delta E)$ and $I_{aC}(\Delta E)$ are the integrated intensities of the whole spectrum in an energy window ΔE. For the π^* pre-peak the integration was performed from the edge of

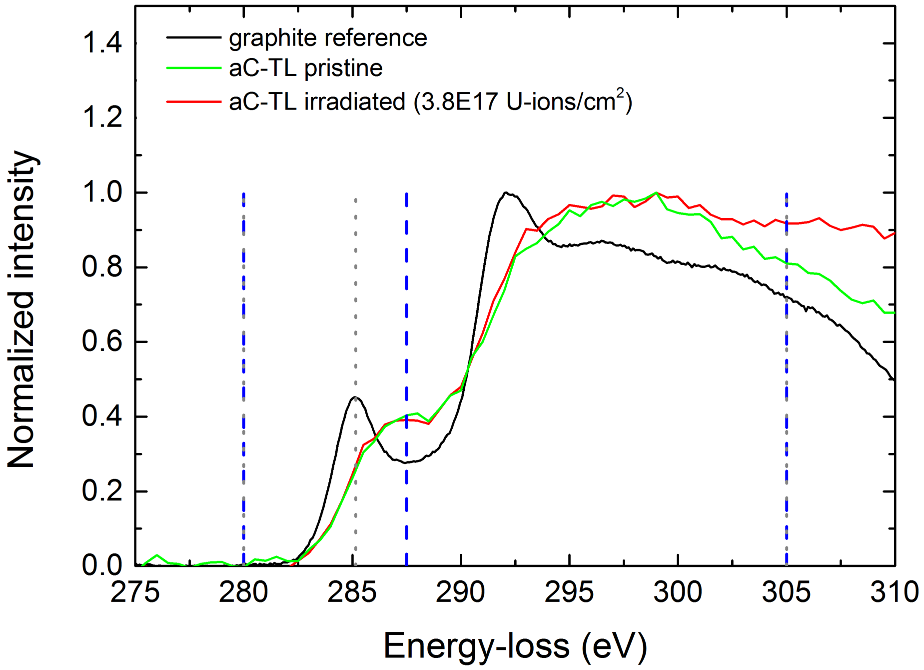

Figure 8.4.8.: EELS spectra for graphite, pristine aC-TL and irradiated aC-TL with 1.4 MeV/u U ions of fluence of 3.8×10^{16} ions/cm^2. The dashed and dotted vertical lines indicate the borders of the energy windows.

rise (280 eV) to the peak maximum (285.2 eV for $I_{g\pi^*}$ and 287.5 eV for $I_{aC\pi^*}$) of the pristine and irradiated aC-TL sample spectra. A small energy window ΔE of 25 eV (280 to 305 eV) was used to reduce the effect of plural scattering towards higher energy losses. The borders of the energy windows are indicated by dotted and dashed lines in figure 8.4.8. Plural scattering is indicated by the flat appearance of the spectrum towards higher energy losses and might result from the samples being too thick. Having an areal density of 20 µg/cm^2, the thickness of aC-TL samples used in this study is larger than the usual thickness of TEM-samples. Mean sp^2 fractions for a pristine and an irradiated (3.8×10^{16} U-ions/cm^2) aC-TL sample were calculated from measurements in 5 different spots on each sample. The irradiated sample was the same specimen as used for TEM imaging (previous section 8.4). Calculated mean sp^2 fractions of pristine and irradiated aC-TL are 0.54 and 0.65, respectively. The standard deviation of the values is about ±0.07, however the absolute values are influenced by the choice of energy windows and integration boundaries [106] as well as by plural scattering due to the large thickness of the samples which has the effect of reducing the determined sp^2 fraction [182]. The estimated uncertainty due to differences in analysis is about ±0.1. An interesting observation is, that values of the pristine and irradiated foils differ only little (taking into account the large standard deviation). Comparing the sp^2 fractions of aC-TL determined by EELS (pristine 0.54, irradiated 0.65) and deduced from XPS (pristine 0.6, irradiated 0.83), the bonding content for pristine aC-TL derived with EELS is only slightly smaller. In case of the irradiated sample the difference is larger. Assuming that XPS overestimates sp^2 fractions (as discussed in section 8.1), the real values might therefore lie in between. In case the nanocrystals which were observed in HRTEM images are of diamond phase, their presence could explain why the sp^2 fractions for the irradiated samples are not higher. In conclusion, EELS measurements provide support for our XPS measurements described in section 8.1, however for an extensive EELS study more samples should be investigated. Improvement of the analysis could be achieved by using other evaluation techniques which are not based on integration of energy windows but for example on graphite DOS functions as proposed in [184].

8.5 Small angle X-ray scattering

Small angle X-ray scattering (SAXS) is a technique that measures elastic scattering of X-rays at very low angles, typically between 0.1 to 10° [185]. At these angles scattering results from density fluctuations on the nanometer scale, because length scales in the sample and the scattering angle are inversely proportional (Bragg condition $2d\sin\theta = n\lambda$ with lattice constant d, scattering angle 2θ, wavelength λ and an integer n), the scattering angle decreases for increasing object size. This allows for the investigation of size, shape and spatial orientation of nanometer sized objects, such as ion tracks. For this reason SAXS has been used to characterize the structure and morphology of ion tracks in various materials. Comparison of the results to molecular dynamics simulations have often shown a good agreement of simulation and experiment [87, 186–189].

SAXS measurements and data analysis were performed by Patrick Kluth at the SAXS beamline at the Australian Synchrotron in Melbourne, Australia. The energy of the X-ray beam with a spot size of about $0.04\,\text{mm}^2$ was 11 keV. Measurements were conducted in transmission mode, with the ion tracks tilted 5° with respect to the X-ray beam. The scattered beam was recorded at 1.6 m distance from the sample using a Pilatus 1 M detector with exposure times of 2 s. Background correction of the individual measurements was performed by subtracting the signal of a pristine aC-TL and DLC-MM sample, respectively. Figure 8.5.1 presents scattering images of aC-TL samples of approximately $600\,\mu\text{g/cm}^2$ irradiated with 4.8 MeV U to a fluence of 1.5×10^{11} ions/cm^2 (a) and Au ions to fluences of 1×10^{11} and 3×10^{11} ions/cm^2 (b and c, respectively). A DLC-MM sample of approximately $600\,\mu\text{g/cm}^2$ irradiated with Au ions to fluences of 5×10^{11} ions/cm^2 is shown in figure 8.5.1d. Colors depict the scattering intensity in q-space (with $q = 4\pi\sin(\theta)/\lambda$ being the scattering vector), with the color scale from bright to dark corresponding to increasing intensity. Under normal beam incidence (beam parallel to the ion tracks), the scattering pattern would appear radially symmetrical. A small tilt (5°) with respect to the X-ray beam leads to highly anisotropic scattering, visible in form of streaks in figure 8.5.1. These streaks are caused by the high aspect ratio of the ion tracks which are a few nm in diameter, but have a length in the range of µm corresponding to the sample thickness.

The scattered intensity I within the streaks is analyzed as a function of the scattering vector q yielding information about radial electron energy density distribution and morphology within the track [189]. Figure 8.5.2 shows the oscillating scattering intensities as a function of q along the streaks for aC-TL irradiated with different ions (beams). The I(q) data was fitted using a cylinder model that assumes a constant density difference in the track compared to the matrix. The scattering intensity is described by the scattering amplitude $f(q)$ [189]:

$$f(q) = 2\pi l\, r \Delta\rho\, \frac{J_1(rq)}{q} \tag{8.10}$$

q is the scattering vector, l is the length of the ion track and therefore the thickness of the sample, r is the track radius, $\Delta\rho$ the difference in electronic density between amorphous ion track and matrix material and $J_1(rq)$ the Bessel function of first order [186, 187, 189]. The ion track radius is convoluted with a narrow Gaussian distribution to account for a variation of the radius with depth within the sample and deviation from perfectly abrupt track boundaries [186, 187]. The scattering intensity I is then propor-

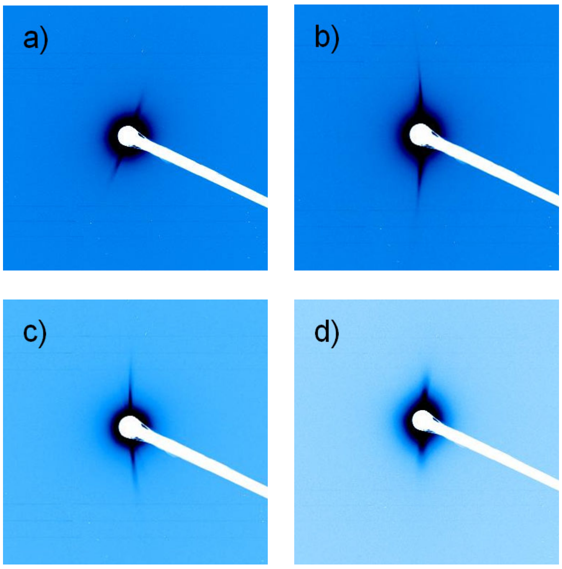

Figure 8.5.1.: SAXS images for irradiated ~600 µg/cm^2 (4.8 MeV/u): aC-TL of a) 1.5 × 10^{11} U-ions/cm^2, b) 1 × 10^{11} Au-ions/cm^2, c) 3 × 10^{11} Au-ions/cm^2; d) DLC-MM of 5 × 10^{11} Au-ions/cm^2.

tional to $| f(q) |^2$. Fits obtained by least square algorithm are presented in figure 8.5.2. For an aC-TL sample irradiated by a 4.8 MeV/u U ions to a fluence of 1.5×10^{11} ions/cm^2 a track radius of 4.4 ± 0.2 nm was obtained. Track radii for aC-TL samples irradiated with 4.8 MeV/u Au ions of 3×10^{11} ions/cm^2 are slightly smaller: 4.1 ± 0.1 nm (for 1×10^{11} ions/cm^2) and 3.9 ± 0.2 nm (3×10^{11} ions/cm^2). The width of the distribution is approximately 20% of the track radii in all cases. Even though streaks are visible for the DLC-MM sample presented in figure 8.5.1, which indicate the presence of tracks, $I(q)$ data could not be fitted with acceptable quality. The observed track radii agree well with radii found by IR spectroscopy in section 8.3 where a larger radius of 5.2 ± 0.2 nm was found for U and a similar radius of 4.0 ± 0.1 nm for Au irradiation with similar beam conditions.

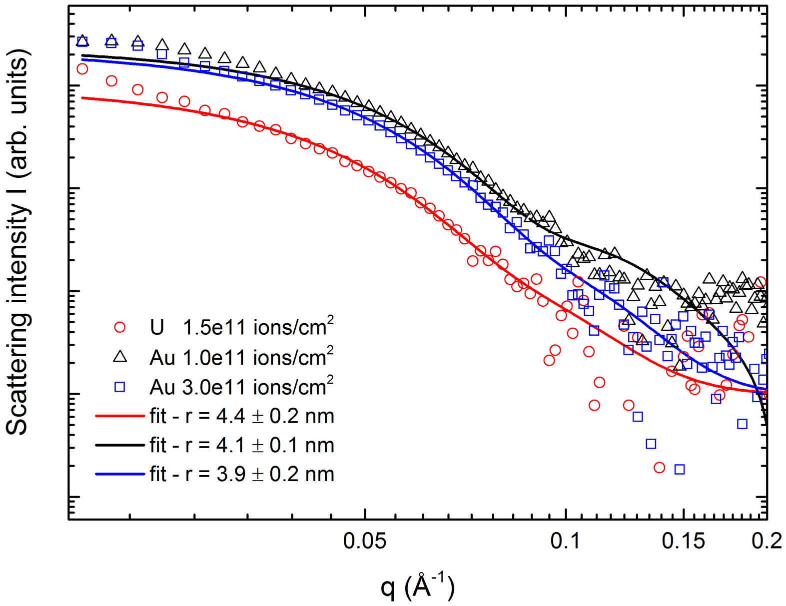

Figure 8.5.2.: Small angle X-ray scattering data for 4.8 MeV/u Au and U irradiation of 20 µg/cm^2 aC-TL foils and corresponding fits.

9 Physical properties changes

9.1 On-line electrical resistivity

The measurement of electrical resistivity is an important way to characterize the electronic structure and properties of amorphous carbon films [89]. In this study, the resistance of a thick amorphous carbon film (aC-TL, approximately 550 µg/cm^2) was measured as a function of fluence using a four-point probe setup presented in figure 9.1.1. This setup was developed and tested ([190]) for the characterization of heavy-ion induced radiation damage in isotropic graphite. The sample with geometry of $10 \times 30\,\mathrm{mm}^2$ was mounted on a PEEK back plate and fixed by the four electrodes (figure 9.1.1). Irradiation was performed with a 5.9 MeV/u Au beam (32 Hz, 4 ms) with a flux of 5×10^9 ions/(cm^{2}s). At this energy the range of the ions in carbon (2.253 g/cm^3) is ∼53 µm and thus much larger than the aC-TL sample thickness.

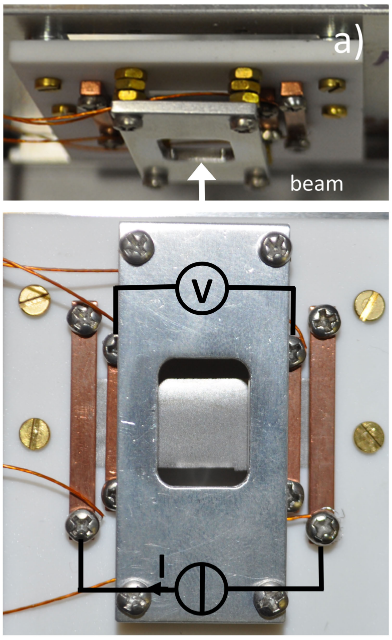

Figure 9.1.1.: Four-point probe setup for electrical resistivity measurements. a) presents the holder and the direction of the ion beam in top view. b) frontal view of the 550 µg/cm^2 aC-TL sample mounted on the back plate and the four Cu electrodes for current application and voltage measurement. The size of the irradiated area is defined by a mask.

Current and voltage were measured and controlled by a Keithley 2450 SourceMeter, with a data acquisition rate of 1 Hz. A constant current of 1 mA was applied. By measuring the voltage throughout the irradiation, the resistance of the sample can be calculated by the relation

$$R_{\mathrm{sample}} = \frac{U}{I} \tag{9.1}$$

where R denotes the resistance of the sample, I the applied current and U the measured voltage.

As visible in figure 9.1.1 the sample was covered by a mask to define the size of irradiated area and to protect the electrodes from irradiation. The sketch in figure 9.1.2 illustrates the geometry of the irradiated and pristine area of the sample and the corresponding resistors R_ϕ and R_{pristine}.

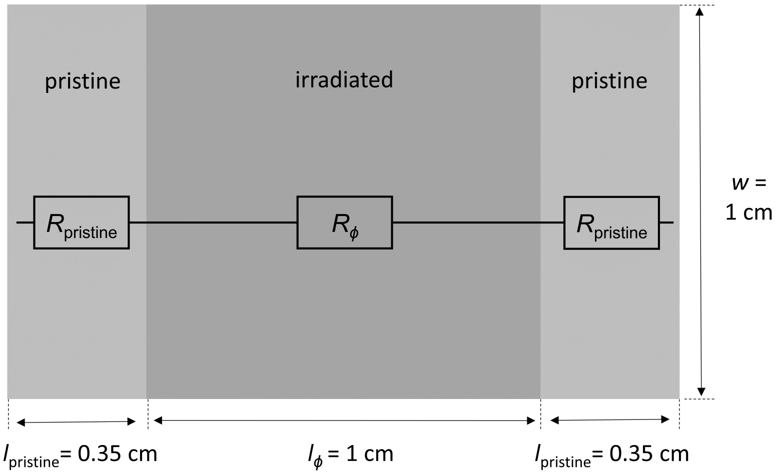

Figure 9.1.2.: Sketch of the sample geometry for resitivity measurements (top view) with the irradiated part in the middle and pristine areas left and right. The corresponding resistors in series are indicated.

The overall measured resistance for one sample R_{sample} is therefore described by a series of these resistors:

$$R_{\text{sample}} = R_\phi + 2R_{\text{pristine}} \tag{9.2}$$

Assuming that the sample size does not change by irradiation, R_{pristine} can be calculated using the initial resistance R_0 measured before starting irradiation:

$$R_{\text{pristine}} = \frac{R_0 l_{\text{pristine}}}{l_\phi + 2l_{\text{pristine}}} = \frac{R_0 0.7\,\text{cm}}{1.7\,\text{cm}} \tag{9.3}$$

l_ϕ is the length of the irradiated area and l_{pristine} the length of the non-irradiated areas (covered by the mask), as illustrated in figure 9.1.2. The resistivity of the irradiated material results in:

$$\rho_{\text{irr}} = \frac{A_\phi (R_{\text{sample}} - 2R_{\text{pristine}})}{l_\phi} \tag{9.4}$$

where A_ϕ is the irradiated cross-sectional area calculated using the width $w = 1\,\text{cm}$ and thickness of the sample h_ϕ which are assumed to be constant during the complete irradiation (The change of length, width and thickness by heating or structural changes are small enough not to be taken into account).

The relative resistivity change $(\rho_{\mathrm{irr}}-\rho_0)/\rho_0$ with ρ_0 being the initial resistivity before irradiation as a function for 550 µg/cm^2 aC-TL up to a maximum fluence of about 3×10^{13} ions/cm^2 is presented in figure 9.1.3. The resistivity decreases and seems to saturate at about 30 % of the initial value. Since sp^2 fraction is the crucial parameter defining the electrical conductivity [97], the decrease of resistivity and therefore increase of conductivity is in line with the observation of sp^2 content increase by other methods in this work.

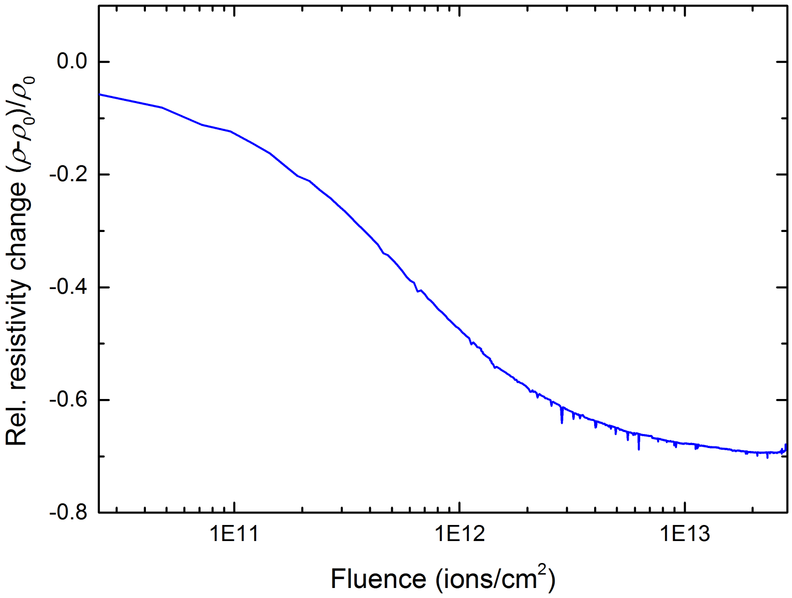

Figure 9.1.3.: Relative resistivity change $(\rho_{\mathrm{irr}}-\rho_0)/\rho_0$ in 550 µg/cm^2 aC-TL as a function of fluence for irradiation with 5.9 MeV/u Au ions (32 Hz, 4 ms) with a flux of 5×10^9 ions/(cm^{2}s).

During the irradiation experiment, the temperature during irradiation was monitored with an infrared camera. Depending on flux and pulse intensity, the temperature varied in a range from room temperature (without beam) to 250°C. Heating by the heavy ion beam caused a resistivity change of about 5 % as deduced from a test in which the beam was turned off during irradiation (figure 9.1.4). This finding agrees well will beam-induced heating in isotropic graphite in similar experiments [190].

The exponential decrease of resistivity was fitted by the Poisson equation according to the single impact model [163, 164] as used for the infrared transmittance data in section 8.3:

$$\rho_{\mathrm{rel}}(\phi)=\rho_{\mathrm{f}}+a\exp(-\sigma\phi) \tag{9.5}$$

$\rho_{\mathrm{rel}}(\phi)$ denotes the relative resistivity change $(\rho_{\mathrm{irr}}-\rho_0)/\rho_0$ at a given fluence ϕ, σ is the cross section of the induced material change, ρ_{f} is the final resistivity and a the fitting parameter. The resulting fit is presented in figure 9.1.5. As in the transmittance measurements, the data was fitted to a maximum fluence of 1×10^{12} ions/cm^2, which allows a direct comparison of the determined values. Assuming cylindrical track symmetry, the corresponding track radius can be calculated from the cross section ($\sigma=\pi r^2$). The derived track radii for a fit up to 1×10^{13} Au ions/cm^2 is 5.7 ± 0.5 nm (the error was estimated from the investigation of different fits in section 8.3). This value is larger compared to the track radius calculated from the transmittance decrease of the Au irradiated aC-TL sample in chapter 8.3 (3.7±0.5 nm). Larger tracks determined from on-line resistivity measurements compared to other techniques have been ob-

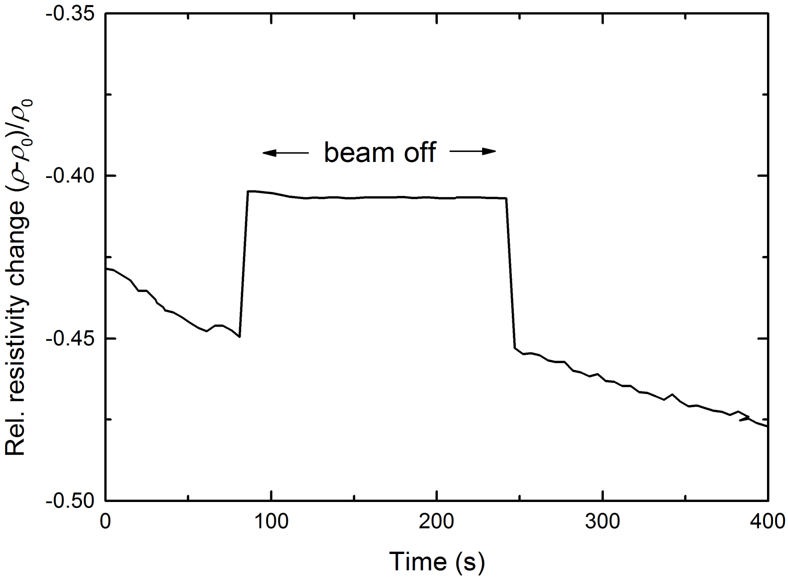

Figure 9.1.4.: Relative resistivity change as a function of irradiation time for irradiation with 5.9 MeV/u Au ions (32 Hz, 4 ms). Stopping the beam during irradiation causes a resistivity increase of approximately 5 %.

served also in graphite [191]. A reason might be structural modification within the halo region around the track core that might also contribute to the measured resistivity drop, causing the determined track radius from the resistivity decrease to be larger than for other methods.

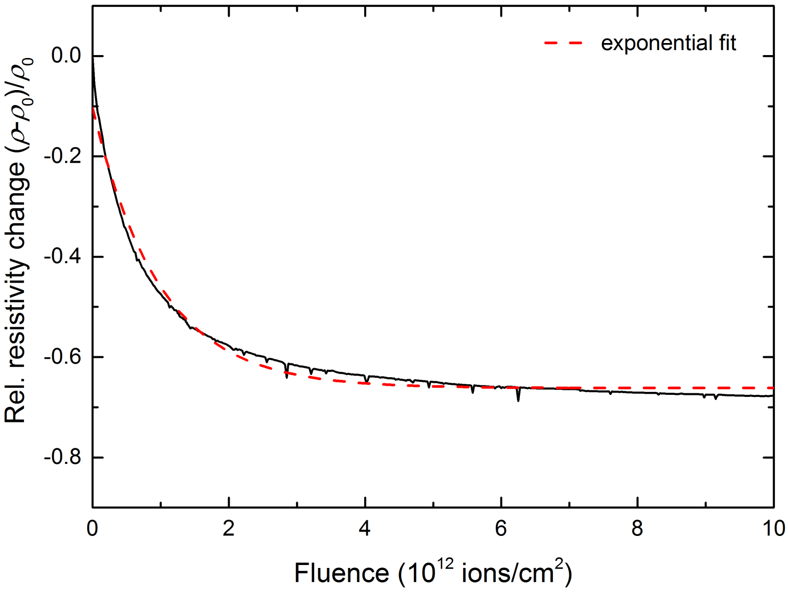

Figure 9.1.5.: Relative resistivity change $(\rho_{irr}-\rho_0)/\rho_0$ of a 550 µg/cm^2 aC-TL sample as a function of fluence for irradiation with 5.9 MeV/u Au ions (32 Hz, 4 ms). The dotted line is an exponential fit to the data based on equation 9.5.

9.2 Laser flash analysis

Ion beam-induced heating of material is one of the factors influencing the final failure of stripper foils. Pulsed beams induce short temperature rises. The resistance to thermal shocks depends on the fracture strength and thermal properties of the material. The investigation of the thermal conductivity and its changes during ion irradiation is therefore crucial for the investigation of stripper foil lifetime and performance. The one-dimensional heat flux in x direction q_x is defined by the the thermal conductivity K and the temperature gradient (Fourier's law):

$$q_x = -K \frac{\mathrm{d}T}{\mathrm{d}x} \tag{9.6}$$

The thermal conductivity in solids is associated with two mechanisms: phonon and free electron transport. Since disordered carbon materials usually have a low number of free charge carriers, heat conduction is dominated by phonons. The thermal conductivity is determined by the mean free path of the phonons, limited by scattering at defects and boundaries or on other phonons. The disorder in amorphous carbon therefore reduces the thermal conductivity due to increased phonon scattering. The thermal conductivity K for steady heat transport is strongly dependent on the temperature. K is a function of the thermal diffusivity a, which characterizes the reaction (time-wise) to a temperature change, the heat capacity c_p and the density ρ:

$$K(T) = a(T)\, c_p(T)\, \rho(T) \tag{9.7}$$

Laser flash analysis is a fast, versatile and precise absolute method for measuring the thermal diffusivity of various samples in a wide temperature range. In transmission geometry, a laser irradiates the front surface of a specimen. An infrared detector measures the relative temperature rise on the rear surface as a function of time. In an adiabatic case the thermal diffusivity can be calculated from the sample thickness h and the half-time rise temperature $t_{0.5}$, which is defined as the time between the energy deposition and the time when 50 % of the maximum temperature at the rear surface is reached [192]:

$$a = 0.1388 \frac{h^2}{t_{0.5}} \tag{9.8}$$

The origin of this equation is the temperature history of the front and rear surface, derived from a one-dimensional solution of Fourier's law of heat conduction (equation 9.6) as proposed by Parker *et al.* [192]. Cowan [193] and Cape and Lehman [194] revised the mathematical model adding corrections for finite-pulse-time effects and for heat losses by radiation and convection on the surfaces. The finite pulse width is important especially for thin samples, because the half-time $\mathrm{t}_{0.5}$ is shorter, whereas heat losses decrease. For conductivity measurements, a LFA 472 Laser Flash device was used. It is equipped with a laser of 1.064 µm and an InSb IR-detector with a detection range from 1 to 5 µm. Measurements were performed at 20°C and 1 bar. Samples of 10 mm in diameter were cut out of the beamspot center of the irradiated foils. Due to the low sample thickness of approximately 600 $\mu\mathrm{g/cm^2}$, the carbon foils were mounted between two sapphire plates, which have a transmission of ~85 %. To ensure that the sample is not graphitized by the laser, a filter was used, which attenuates the laser intensity to 10 %.

Due to the low thickness of the samples, several error sources had to be considered. Because of the small thickness, the rise of the rear surface temperature is very fast (about 2 ms). Because the thickness is estimated by the areal density of the samples, errors in the thickness directly influence the rise of temperature and therefore the half-times. The sapphire plates were tested for their effect on the diffusivity by a reference measurement on a 1.9 mm thick graphite sample. In this case the effect was negligible, however the effect for the thin samples could be larger. Also, some of the irradiated foils showed a macroscopic delamination, indicating the presence of macroscopic layers in the material. These layers might be caused by the cyclic deposition of the foils. The thermal resistance that results from the heat transfer at the interfaces could change the thermal diffusivity. Due to these problems, the absolute thermal diffusivity values should be treated critically and cannot be compared to literature values. The measurement of thermal diffusivity before and after irradiation is meant to account for these errors in the absolute diffusivity values. The measurement nevertheless provides relative information on the influence of ion irradiation on thermal diffusivity. Data were fitted with Cowan model [193] including pulse correction. Obtained thermal diffusivity values are a mean of 30 individual measurements. Errors represent the standard deviation of these measurements.

Figure 9.2.1 presents the relative thermal diffusivity for different 600 μg/cm^2 amorphous carbon foils irradiated with 4.8 MeV/u U ions as a function of fluence. A clear increase is visible for aC-TL foils over the whole fluence range up to 3×10^{13} ions/cm^2. DLC-MM and aC-ACF foils show the highest values for 1×10^{13} ions/cm^2 and 5×10^{12} ions/cm^2, respectively, followed by a diffusivity decrease for higher fluences. Shamsa *et al.* [195] concluded from their comparison of diamond and fully amorphous sp^3

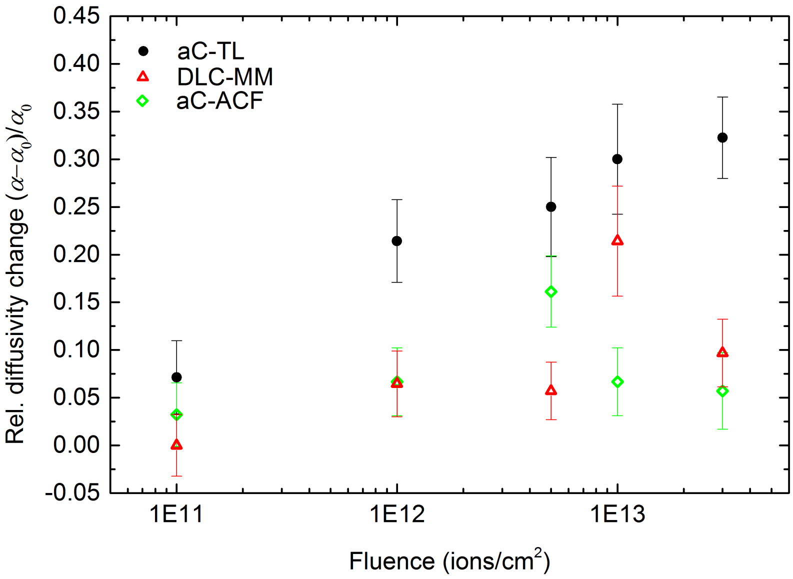

Figure 9.2.1.: Releative change of thermal diffuctivity as a function of fluence for 600 μg/cm^2 aC-TL, DLC-MM and aC-ACF foils irradiated with 4.8 MeV/u U ions.

material, that the conductivity is highly dependent on the ordering of sp^3 and sp^2 phase. In their view an ordering of sp^2 phase into graphitic regions would cause an increase of the thermal conductivity [195, 196]. The increase of diffusivity for DLC-MM and aC-ACF could therefore be attributed to an ordering of sp^2 sites and increase of cluster size. The decrease would then be related to a decrease of cluster sizes. This observed reduction of cluster sizes could be due to track overlapping processes, introducing disorder to the formerly graphitized regions. Using a single-impact model [163, 164] and assuming tracks of a 6 nm radius, the fluence for a 99 % track coverage is about 4×10^{12} ions/cm^2. Smaller tracks would result in a larger fluence required for track overlapping. The overall lower increase of thermal diffusivity in DLC-MM and aC-ACF materials in comparison to aC-TL could be attributed to their supposed larger sp^3 content, which would result in smaller and less sp^2 clusters. Therefore more sp^3 content would be converted into an sp^2 phase and limit the thermal conductivity by phonon scattering on the smaller clusters. This interpretation is supported by Raman spectroscopy in chapter 8.2, which indicated a decrease of cluster size for fluences in similar regimes and both DLC-MM and aC-ACF foils. In the case of aC-TL the decrease of cluster sizes in Raman spectroscopic measurements was observed for fluences larger than 2×10^{13} ions/cm^2. This shift to higher fluences could explain why no decrease is observed in the thermal diffusivity with a maximum fluence of 3×10^{13} ions/cm^2. In general the increase of thermal conductivity for all irradiated foils is helping in dissipating the heat deposited by the beam away from the beam spot and in reducing the amplitude of the stress waves generated by the induced thermal expansion. However, the observed decrease of thermal diffusivity and therefore conductivity at high fluences would limit this positive effect. Further investigations focusing on higher fluences would be needed for an extrapolation to FAIR beam conditions.

9.3 Stiffness measured by atomic force microscopy

Atomic force microscopy (AFM) was used to investigate the elastic properties of pristine and irradiated aC-TL foils. AFM uses a cantilever with a small tip which is scanned over a sample surface. The cantilever deflection caused by the surface structure is measured commonly by the optical lever technique. A laser beam is focused on the backside of the cantilever and a photo diode detects the reflected beam as a function of position [197]. Force-distance curves are frequently used to study the mechanical properties of materials. They plot the force between sample surface and cantilever tip against their distance. By ramping the sample or tip along vertical direction, the deflection δ_c of the cantilever can be detected. Knowing the spring constant k_c, the force between cantilever tip and sample can be calculated by Hooke's law [197]:

$$F = -k_c \delta_c \tag{9.9}$$

The tip-sample distance z depends on the deflection of the cantilever and the deformation of the sample D. Force-distance curves are therefore determined by

$$z = \delta_c + D - Z \tag{9.10}$$

in which Z describes the distance between sample surface and rest position of the cantilever [197]. In the contact regime, the cantilever tip and sample surface are in contact (distance $z = 0$). The elastic deformation of the sample can provide information on mechanical properties like the Young's modulus. The force-distance curve are therefore transferred (equation 9.10 for $z = 0$) to deformation displacement curves, which plot the deformation of the sample surface as a function of cantilever deflection.

Measurements and evaluation were carried out by Andreas Plog from materials science department of Technische Universität Darmstadt. A MFP 3D from Asylum Research microscope with a cantilever (Buget Sensors, spring constant of 36 N/m) and a tip radius of 50 nm was used to measure force-distance curves. These force curves were transferred to deformation-deflection curves. An exemplary curve for pristine aC-TL is presented in figure 9.3.1. Fits of the force curve according to Hertz theory [198] for determination of the elastic modulus (red) did not yield acceptable fit quality. However the slope of these curves is proportional to the stiffness of the material. A $20 \times 20\,\mu\text{m}^2$ square area of $20\,\mu\text{g/cm}^2$ aC-TL samples were investigated. Figure 9.3.2 presents the stiffness of 900 force curves and the corresponding Gaussian fits for pristine (red) and irradiated with 4.8 MeV/u U ions of fluence 5.7×10^{14} ions/cm^2 (blue). The expected value of the Gaussian fit of the pristine sample is at $5.1 \pm 0.8\,\mu\text{V/nm}$ (the error is the standard deviation of the fit) and of the irradiated sample at $2.0 \pm 0.4\,\mu\text{V/nm}$. The material stiffness increased more than factor 2 and the standard deviation decreased by factor two for the irradiated foil. This suggests that the irradiated material is more homogeneous than the pristine.

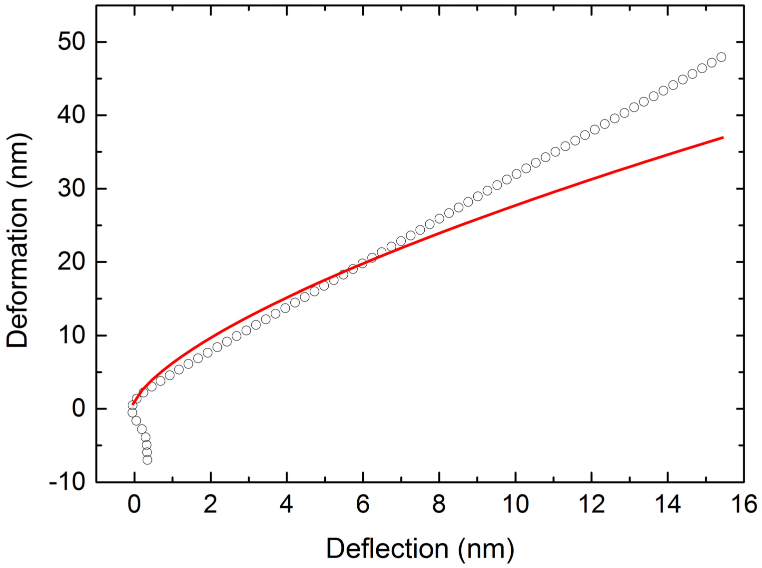

Figure 9.3.1.: Deformation of sample surface as a function of cantilever deflection (force curve) measured by atomic force microscopy for pristine 20 μg/cm^2 aC-TL. The fit (red) corresponds to Hertz model [198] for elastic modulus determination.

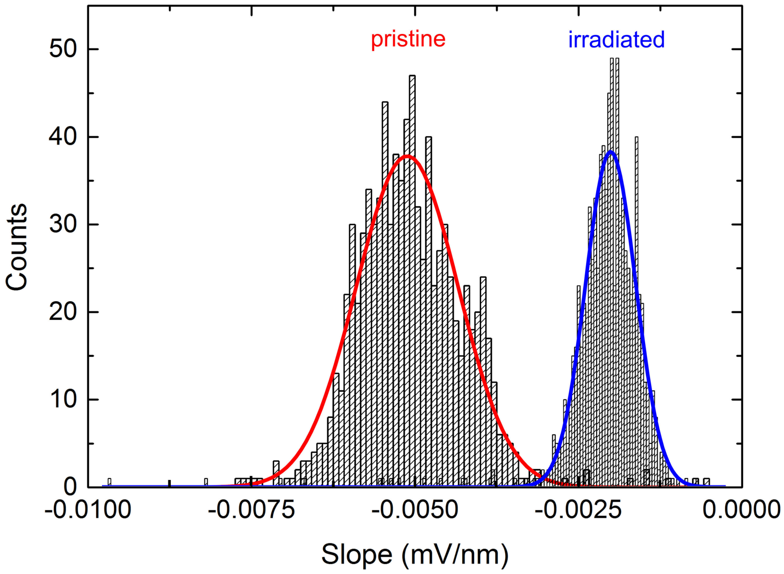

Figure 9.3.2.: Distribution of stiffness and corresponding Gaussian fit for 20 μg/cm^2 pristine (red) and irradiated aC-TL with 4.8 MeV/u U ions of fluence 5.7 × 10^{14} ions/cm^2 (blue).

10 Temperature evolution during beam exposure

Different factors influence the changes and final failure of carbon-based stripper foils. The temperature rise during irradiation is one of these factors. Annealing studies by different authors [111–114, 114–117] showed that temperature treatment by heating, or laser exposure causes structural modification and graphitization of (amorphous) carbon films. Dillon and Monteiro found that significant structural changes in amorphous carbon start in the temperature range between 400 and 600°C [111, 113]. Few measurements [16, 37, 50] and calculations [9, 35, 51] study the temperature evolution of carbon-based stripper foils during ion irradiation. Numerical simulations of beam heating in amorphous carbon foils for U beams of currents and pulse lengths foreseen at FAIR [3] by Tahir *et al.* [9] predict critical temperatures above the sublimation temperature of carbon in vacuum causing severe damage of the stripper foils. The model assumes graphite density for the amorphous carbon foils. A lower density, which is indicated by profilometry measurements, would result in lower peak temperatures. The experimental determination of temperatures during irradiation are therefore needed to complement simulation results. However, the measurement of the absolute temperature of stripper foils during irradiation is not straight-forward, because they are usually thin, freestanding and mounted in vacuum chambers for irradiation. In this study we monitored the carbon foils under beam exposure by means of an infrared camera. To convert the IR signal into temperature, the emissivity of the foils is needed. Due to the semi-transparency of the thin carbon foils and lack of literature values, a method for measuring the emissivity and the influence of the background as well as their change during irradiation was developed. The infrared camera and emissivity data are calibrated by transmittance measurements recorded by off-line and on-line Fourier transform infrared spectroscopy (FTIR). Temperature measurements for thin and thick foils and for different ion fluxes and pulse intensities are presented and provide a benchmark of temperatures induced by irradiation with swift heavy ions.

10.1 Emittance determination

The evolution of the target temperature during irradiation was recorded with an infrared camera (SC7500 FLIR Systems) equipped with a InSb detector operating in the mid-infrared regime (2.5 to 5.2 µm). Within specification environment, the producer gives a measurement accuracy of ±2°C or ±2 % of reading. The integration time of the camera signal is adjustable within 20 ms and 1 µs. The camera was mounted close to a CaF_2 window of the irradiation chamber at a distance of about 10 cm. A calibration process yields the emittance and takes into account background contributions such as reflections from other surfaces. The emittance ϵ, i.e. the effectiveness in emitting energy as thermal

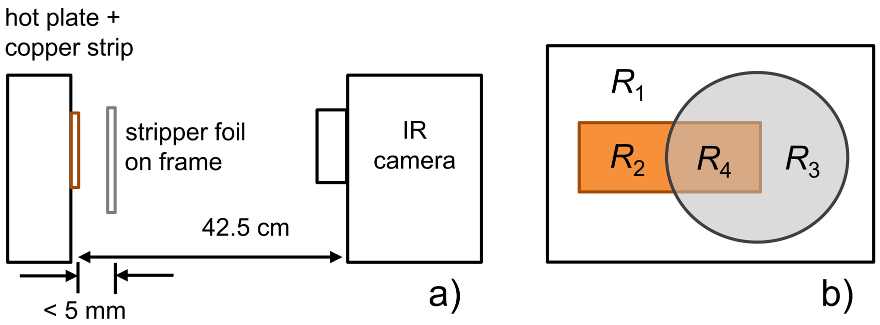

Figure 10.1.1.: Schematic setup for transmittance measurement with the IR camera in (a) side and (b) front view. The different positions of radiance measurements are indicated: R_1 (black sprayed hot plate), R_2 (copper strip), R_3 (graphite foil with hot plate as background), and R_4 (graphite foil with copper as background).

radiation, depends on the wavelength λ, incident angle Θ and temperature T, and can be deduced from the following formula:

$$1 = \epsilon_{\lambda,\Theta,T} + \rho_{\lambda,\Theta,T} + \tau_{\lambda,\Theta,T} \tag{10.1}$$

where ρ denotes the reflectance and τ the transmittance of the foil. To calculate the emittance, the transmittance was experimentally determined for various foil and beam parameters. Given the poor reflectance of all foils, ρ was assumed to be 0.04 for the whole temperature, wavelength and fluence range based on the values for isotropic graphite [199]. A deviation from this value has no strong influence on the temperature calculation; e.g., for a 600 μg/cm^2 thick foil, a reflectance difference of 0.10 would cause a change in temperature by 0.5°C. A similar concept as the standard method for measuring window transmittance [200] was used to determine the transmittance of the semitransparent foils. A scheme of our setup is shown in figure 10.1.1, consisting of a hot plate (R_1) sprayed with graphite to simulate a black body. Measurements of this plate yielded an emittance value of 0.96 ± 0.02. In order to provide a background material with high isothermal contrast, a copper strip (R_2) with a measured emittance of 0.1 was clamped onto the hotplate. The amorphous carbon foil was placed 5 mm in front of the hot plate. The thermal camera was focused onto the foil from a distance of 42.5 cm. For the measurement, the hot plate was heated to a temperature of 80°C. To compensate temperature instabilities of the hot plate, recordings by the camera were collected over a time span of 120 s, with a frame rate of 25 Hz and an integration time of 420 µs. For evaluation of the camera data, the mean radiance, which is the radiant flux per unit solid angle per unit area, were determined from area R_1, R_2, R_3, and R_4 (see 10.1.1b). The difference between the radiances R_1 from the black sprayed hot plate and R_2 from the copper strip serves as a background function B_f. Radiance R_3 is the sum of the radiances R_f from the carbon foil and R_1 reduced by the transmittance τ of the foil:

$$R_3 = \tau R_1 + R_\mathrm{f} \tag{10.2}$$

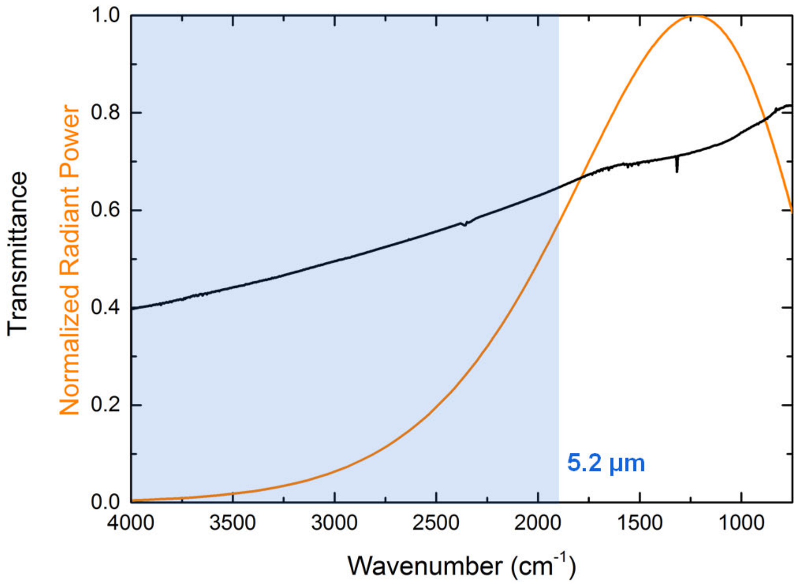

Figure 10.1.2.: Transmission FTIR spectrum of a 20 µg/cm^2 pristine amorphous carbon foil (aC-TL) and normalized black-body radient power for a temperature of 80°C with a maximum at 8.2 µm (orange). The shaded regime indicates the operation regime and the upper detection limit (5.2 µm/ 1923 cm^{-1}) of the IR camera.

R_4 corresponds to the sum of the radiances from the foil and from the copper strip reduced by the foil transmittance:

$$R_4 = \tau R_2 + R_\mathrm{f} \tag{10.3}$$

The difference of R_3 and R_4 defines the difference function D_f. The ratio of D_f and background function B_f yields the transmittance τ of the carbon foil:

$$\tau = \frac{D_\mathrm{f}}{B_\mathrm{f}} = \frac{R_3 - R_4}{R_1 - R_2} = \frac{\tau R_1 + R_f - (\tau R_2 + R_\mathrm{f})}{R_1 - R_2} \tag{10.4}$$

It is noted that the radiance from the environment and the reflection from the carbon foil were not considered here for the sake of simplicity. Values obtained for the transmittance of the carbon foils are a temporal and spatial mean over the recording time and the measured foil area.

Complementing measurements were performed by means of infrared spectroscopy on a FTIR Spectrometer (Nicolet Magna-IR 550, ThermoFisher Scientific) equipped with a dTGS/KBr detector. The spectrum was recorded in the wavelength range from 2.5 to 25 µm (4000 to 400 cm^{-1}). According to Wien's displacement law, the intensity of the black-body thermal emission (radiant power) at the hot plate temperature of 80°C has a maximum at 8.2 µm [201] (figure 10.1.2). The infrared camera records radiance data in the operation regime of 2.5 to 5.2 µm and is thus not taken at the wavelength of maximum emission. When comparing data from both techniques, we therefore used transmittance values at 5.2 µm (1922.7 cm^{-1}) as indicated in figure 10.1.2. The transmittance values deduced from the measurements with the infrared camera are thus expected to be slightly lower than the FTIR spectroscopy results.

As discussed in chapter 8.3, the emittance of the foils changes as a function of fluence under ion irradia-

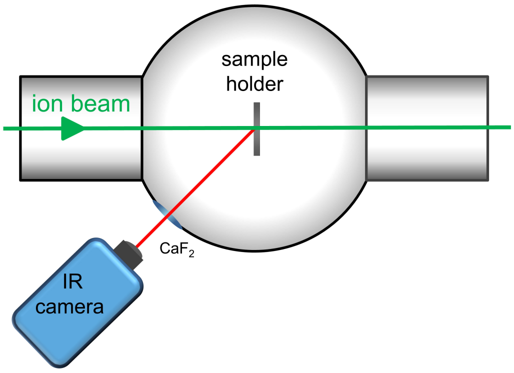

Figure 10.1.3.: Setup for temperature measurements by means of infrared thermography. The IR camera is placed outside in 45° to the irradiation chamber in a distance of 10 cm to a CaF$_2$ window.

tion. Transmittance spectra were recorded with an in-situ Nicolet 6700 FTIR spectrometer during beam stops by rotating the target from irradiation position 1 (normal to the ion beam) to FTIR measurement position 2 (normal to the infrared beam). The evolution of the temperature of different carbon-based stripper foils during irradiation was recorded with the infrared camera mounted at a different irradiation chamber (figure 10.1.3) with a CaF$_2$ window (transmission of 93 %) and similar settings as the one shown in figure 8.3.1. The absorption edge of the CaF$_2$ window at 800 cm^{-1} does not limit the operation regime of the IR camera. All parts of the sample holder were coated with graphite spray to reduce the influence of unwanted reflections at the aluminum frame and holder.

The transmittance values for amorphous carbon foils of different thicknesses measured by the IR camera and deduced from the intensity of FTIR spectra at 5.2 µm are presented in figure 10.1.4. For both methods, the transmittance decreases exponentially in good accordance with the Lambert-Beer law [202, 203]. The results obtained by the two methods follow the same trend. The FTIR data are slightly higher as the spectral transmittance by FTIR spectrometry is measured at 5.2 µm, while the camera measures transmittances over the whole detector range from 1.5 to 5.2 µm. The transmittance decreases from 0.56 (IR camera) (respective 0.62 (FTIR spectrometer)) for a 20 µg/cm^2 foil to 0.08 (IR camera) (respective 0.10 (FTIR spectrometer)) for a 100 µm/cm^2 foil. The transmittance of a 600 µm/cm^2 foil was extrapolated to be 0.04 (emittance 0.96). The uncertainties of the transmittance measurements were estimated to be ±0.05 (IR camera) and ±0.02 (IR spectrometer). These values are fixed absolute errors for all samples. The error for thickness of the aC foils was estimated to be 10 %. The data gives clear evidence that the foil thickness has a direct effect on the emittance. Moreover, when determining the emittance of very thin foils, it is important to take into account contributions of the material behind the foil. This means that no other thermal radiation sources (e.g. beam heated targets behind the foils) should be inside the irradiation chamber during temperature measurement with the IR camera.

The fluence dependence of the foil emittance (or transmittance) was investigated with 4.8 MeV/u beams of different time structure: (1) Au beam of repetition rate 45 Hz and pulse length 4 ms and (2) Au beam of 2 Hz and pulse length 1.2 ms, (3) U beam of 2 Hz and pulse length 0.2 ms, (4) Xe beam of 5 Hz and pulse length 1.2 ms. Fluences up to 6×10^{14} ions/cm^2 were applied.

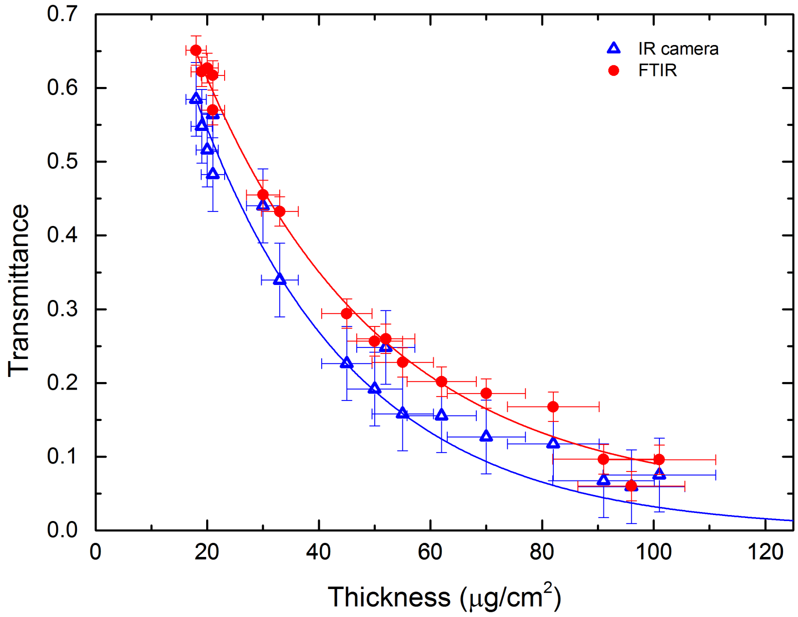

Figure 10.1.4.: Transmittance for amorphous carbon foils (aC-TL) of different thicknesses measured with the IR camera (black squares) and FTIR spectrometer (red circles). Solid lines are exponential fits according to the Beer-Lambert law [202, 203].

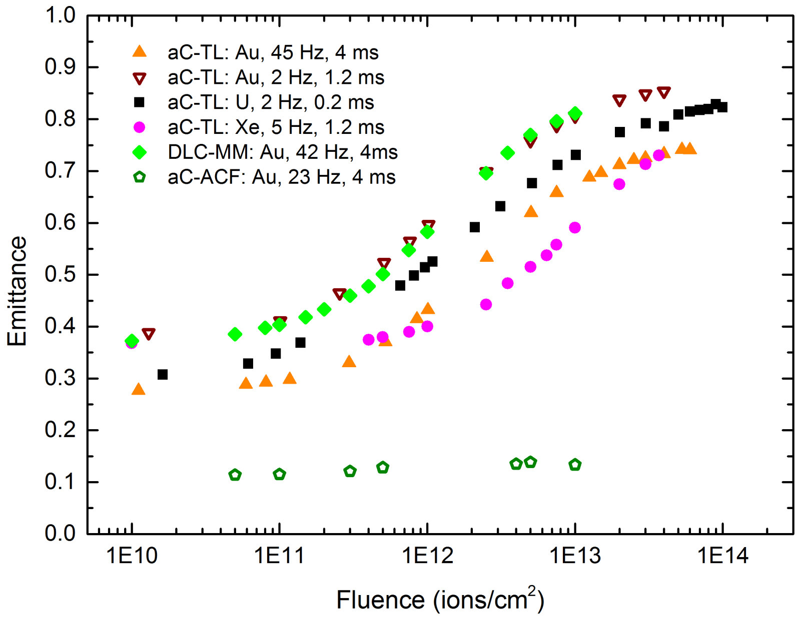

Figure 10.1.5.: Emittance data deduced from on-line FTIR spectroscopy as a function of fluence for the irradiation of 20 μg/cm^2 aC-TL, DLC-MM and aC-ACF foils with different ions and beam parameters (compare table 4.0.1 of irradiation parameters) as indicated by the repetition rates in the legend. The energy for all irradiation was 4.8 MeV/u. Values of the lowest fluence are very close to the values of the respective non-irradiated foils. Pristine values are therefore not presented. Estimated errors of ±0.08 over the whole fluence regime account for the different pristine emittance values of the foils.

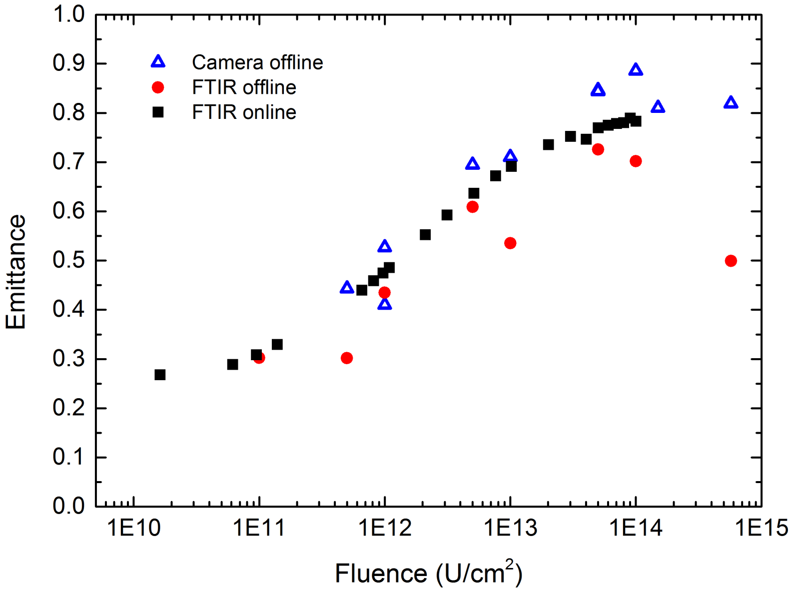

Figure 10.1.6.: Emissivity data for 20 μg/cm^2 aC-TL foils from off-line measurements with the IR camera (blue triangles) and FTIR spectrometer (red circles) as well as on-line FTIR measurements at the beamline (black squares, same data as in figure 10.1.5). The irradiations were performed with 4.8 MeV/u U ions (repetition rate 0.2 to 2 Hz, pulse length 0.1 to 0.4 ms).

Figure 10.1.5 shows the emittance calculated from transmittance values measured by on-line FTIR spectroscopy in sample position 2 (sample 45° to ion beam, figure 8.3.1) for 20 μg/cm^2 amorphous carbon foils. Due to errors of the transmittance measurement, reflectance estimation and sample inhomogeneities, the overall uncertainty is estimated to be ±0.08. Since this is a fixed absolute error for the entire fluence regime, the emittance errors are not presented in the graph. Under all beam conditions the emittance of 20 μg/cm^2 aC-TL foils becomes larger with increasing fluence saturating at about 0.7 (Au ions, 45 Hz), 0.85 (U ions) and 0.85 (Au ions, 2 Hz). Au (45 Hz) irradiation of a 20 μg/cm^2 DLC-MM foil shows a starting saturation at 0.85, whereas 20 μg/cm^2 aC-ACF foil emittance has low values and does not significantly change with fluence. Pristine values are very close to the value at the first fluence step (about 1×10^{10} ions/cm^2) and are therefore not presented in the graphs. Transmittance and therefore emittance starting values are different for the investigated foils, as obvious in figure 10.1.5. The comparison of relative transmittance changes is presented in chapter 8.3. The estimated error of ±0.08 accounts for different transmittance values of pristine foils of a given material.

Figure 10.1.6 presents the emittance data from various transmittance measurements for 20 μg/cm^2 aC-TL foils irradiated with U ions (0.4 to 2 Hz, 0.1 to 0.4 ms pulse length) including data from off-line measurements performed with the IR camera and FTIR spectrometer as well as in situ transmittance measurement at the beamline. Emittance values were calculated from FTIR transmittance values measured in sample position 2 (sample 45° to ion beam, see figure 8.3.1) were used for the comparison with the IR-camera values. It is noted that the on-line data are from one given sample, stepwise irradiated to the maximum fluence, while the off-line measurements originate from different foils exposed to the corresponding fluences. The emittance increase with increasing fluence is confirmed by all measurements. The rather large scattering of the off-line data is partly ascribed to slightly different thicknesses of the different samples (18 to 23 μg/cm^2). Moreover, some of the foils were analyzed beforehand by other techniques and thus the irradiated area remaining for FTIR spectroscopy was slightly smaller than the beamspot of the infrared source.

The results of the on-line FTIR spectroscopy show good agreement with off-line characterization. Consequently recording the transmittance change during irradiation by on-line FTIR measurements is a reliable approach for semitransparent thin foils. The obtained transmittance data thus serve as input parameter to calculate the temperature of the foils from IR camera monitoring during beam exposure. Since the IR camera was mounted under an angle of 45° with respect to the incoming ion beam, the transmittance values were additionally measured in sample position 1 (sample normal to ion beam, compare figure 8.3.1). The values slightly deviate from position 2 yielding a difference in emittance of about 0.06. For this reason, the on-line FTIR transmittance values measured in position 1 were used for the evaluation of the foil temperature during irradiation.

10.2 On-line measurement of foil temperature

On-line temperature measurements were carried out for different types of carbon materials, foil thicknesses, ion parameters, irradiation fluxes, and other beam conditions. The temperature was deduced from emissivity data provided by on-line FTIR spectroscopy including the fluence effect. Temperatures presented in the following depict mean values over the beamspot area. Special care was taken to minimize the effect of fluence by recording short captures and thereby keeping the accumulated fluence low. Figure 10.2.1 shows the temperature evolution of approximately 600 $\mu g/cm^2$ aC-TL foils exposed to ion beams of different repetition rates, pulse lengths, and pulse intensities (indicated in the legend). The horizontal lines "mean peak" and "mean base" denote respective maximum and minimum temperatures averaged over all pulses during beam on target. The temperature maxima fluctuate from pulse to pulse reflecting usual beam instabilities. In the case of the low repetition rate of the U beam (figure 10.2.1a), the time between individual pulses is sufficiently long so the temperature can drop almost to the temperature of the foil without beam. With increasing pulse frequency and pulse length, the mean base temperature becomes larger. This can be seen in figure 10.2.1b, 10.2.1c, 10.2.1d for Au (2 Hz), Bi (3.4 Hz) and Xe (5 Hz) beams, respectively. For the Au beam (47 Hz, 4 ms), the temperature between two pulses drops only by a few degrees. The enlarged part of figure 10.2.1e shows the temperature increase by single Au pulses. The increase from the mean base value to mean peak value within 0.4 ms is related to missing pulses which were delivered to other experiments. For the comparison of beams with different repetition rates and pulse structures two different units are considered: (1) the pulse intensity (ions/(cm^2pulse)) given by the number of ions per area unit and per pulse and (2) the flux (ions/($cm^2 \mu s$)) providing information on the temperature rise in a very short time interval, which helps to compare very short and longer beams pulses.

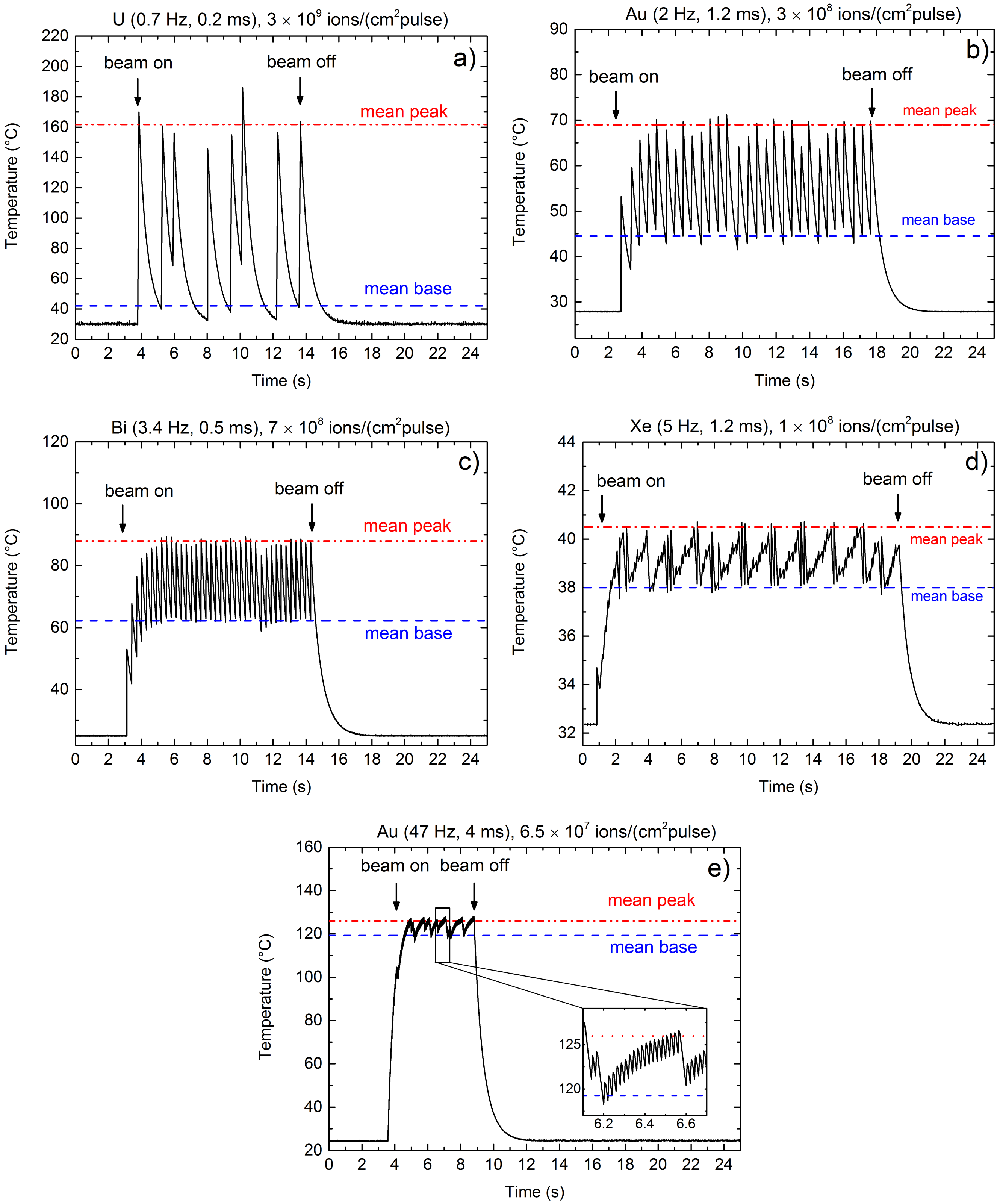

Figure 10.2.1.: Temperature profiles monitored by IR thermography for approximately 600 μg/cm^2 thick amorphous carbon foils (aC-TL) exposed to differently pulsed ion beams (energy 4.8 MeV/u) for selected pulse intensities. The horizontal lines represent averaged values of base and peak temperatures. (a) U beam 0.7 Hz repetition rate, 0.2 ms pulse length; (b) Au beam 2 Hz, 1.2 ms; (c) Bi beam 3.4 Hz, 0.5 ms; (d) Xe 5 Hz, 1.2 ms; (e) Au beam 47 Hz, 4 ms.

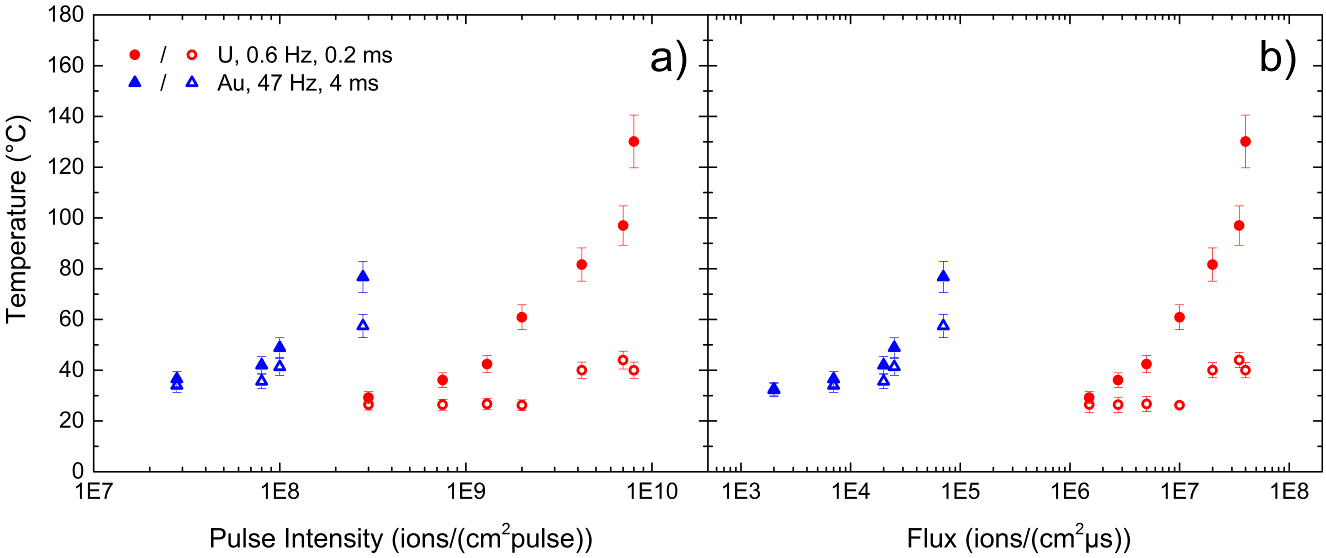

Figure 10.2.2.: Comparison of foil temperature as a function of pulse intensity and flux for 20 µg/cm^2 aC-TL samples using Au ions (47 Hz, 4 ms, blue triangles) and U ions (0.6 Hz, 0.2 ms, red circles). Closed symbols are mean peak temperatures, open symbols correspond to mean base temperatures. The maximum tested pulse intensities or fluxes are due to limits given by the operation mode of the accelerator.

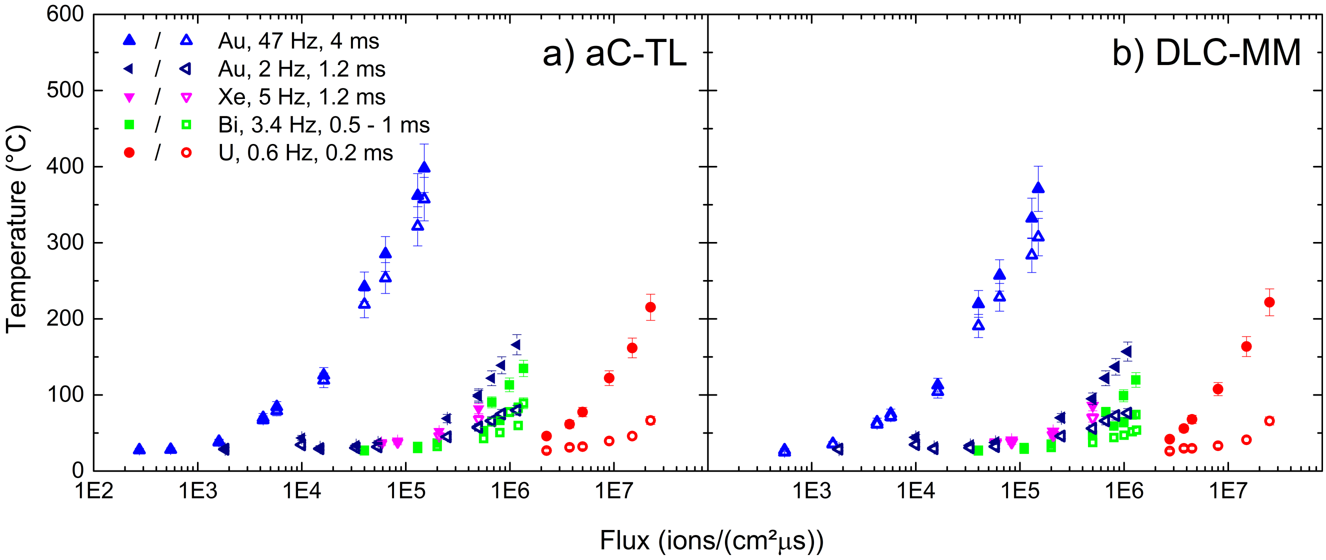

Figure 10.2.3.: Temperature evolution for thick (∼600 µg/cm^2) a) aC-TL in and b) DLC-MM foils as a function of ion flux. The different experiments were performed with an Au beam (47 Hz, 4 ms, blue up-triangles), Au beam (2 Hz, 1.2 ms, dark-blue left-triangles), Bi beam (3.4 Hz, 0.5-1 ms, green squares), Xe beam (5 Hz, 1.2 ms, magenta down-triangles), and U beam (0.6 Hz, 0.2 ms, red circles). Closed symbols correspond to mean peak temperatures, open symbols are mean base temperatures.

Depending on the beam conditions, the base and peak temperatures increase with the pulse intensity (ions/(cm^{2}pulse)) in both thin and thick foils as illustrated in figure 10.2.2 and 10.2.3. Error bars of ±8 % represent uncertainties of the temperature calibration due to systematic errors during transmittance measurement and reflectance estimation. Additional, unavoidable pulse to pulse fluctuations of the beam result in a large scattering of the recorded peak temperatures especially in the case of the U beam. The pulse intensities and fluxes represent mean values deduced from beam current measurements recorded during irradiation. A comparison of pulse intensity and flux as a function of fluence is presented in figure 10.2.2 for 20 µg/cm^2 aC-TL foils. The highest pulse temperature is reached with the U beam (0.6 Hz, 0.2 ms) for 8×10^9 ions/(cm^{2}pulse) or 4×10^7 ions/(cm^{2}µs). Higher pulse intensities/fluxes could not be tested due to limits given by the operation mode of the accelerator. Given by the low repetition rate, the sample cools down between different pulses, thus the mean base temperature remained low. The situation is different for the Au beam (47 Hz, 4 ms) where the high repetition rate results in a significant increase of the base and peak temperature although the pulse intensity was one order of magnitude lower compared to the U beam.

Similar tests were performed for thicker carbon foils (616 to 640 µg/cm^2). The emittance of these foils used for temperature calibration was supposed to be constant at 0.96 for the whole fluence range in all materials, based on the assumption that the reflectivity is not changing drastically. The evolution of the temperature as a function of fluence is presented for ~600 µg/cm^2 aC-TL and DLC-MM (figure 10.2.3a and b). The highest temperature of almost 400°C was reached for Au ions at a flux of 1.5×10^5 ions/(cm^{2}µs). Even though the U beam (0.6 Hz, 0.2 ms) achieves much higher ion fluxes than the Au beam, the maximum temperature is lower in ~600 µg/cm^2 foils. An explanation could be that the surface to volume ratio is smaller in thick foils, the contribution of radiative heat loss is therefore smaller compared to thinner foils. Au (2 Hz, 1.2 ms), Bi (3.4 Hz, 0.5 to1 ms) and Xe (5 Hz, 1.2 ms) beams reach intermediate fluxes and maximum temperatures up to 200°C.

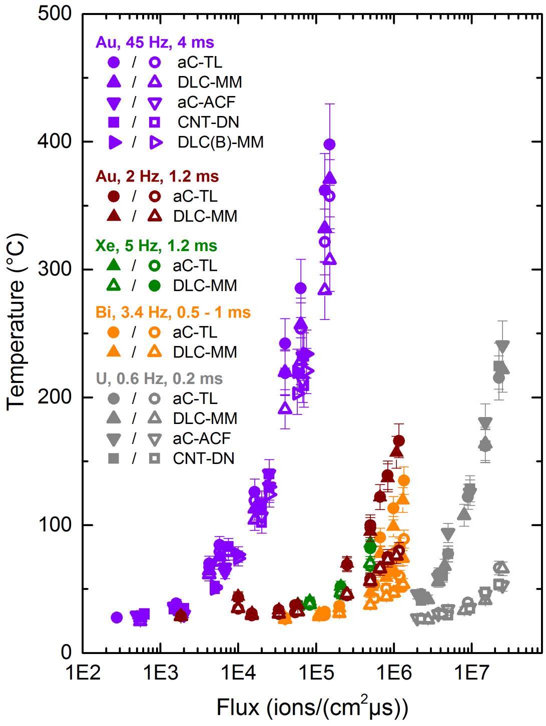

Figure 10.2.4.: Temperature evolution as a function of flux of different beams: Au (45 Hz, 4 ms, purple), Au (2 Hz, 1.2 ms, dark-red), Bi (3.4 Hz, 0.5-1 ms, orange), Xe (5 Hz, 1.2 ms, green), and U (0.6 Hz, 0.2 ms, grey) for different ~600 µg/cm^2 carbon foils: aC-TL (circles), DLC-MM (up-triangles), aC-ACF (down-triangles) and CNT-DN (squares). Closed symbols correspond to mean peak temperatures, open symbols are mean base temperatures.

Figure 10.2.4 summarizes the temperature evolution as a function of flux of different beams and different approximately 600 µg/cm^2 thick carbon foils. For temperature calibration we used the same emittance value of 0.96 as for the aC-TL foils. It is interesting to see that within the uncertainties, all four materials reach the same temperatures and show a similar trend with increasing flux for certain beams.

Beside the dependence of temperature on carbon materials, ion species and pulse structure, also a dependence on fluence could be expected due to the structural changes induced by the ion beams. Figure 10.2.5 presents a temperature measurement in which a beam spike (a very intensive pulse) occurred during the irradiation (at a pulse intensity of 4×10^9 ions/(cm^{2}pulse)) in comparison to the data for the U beam presented in figure 10.2.3a. A beam spike is a very intensive pulse, occasionally occurring during swift heavy ion irradiations. The temperature as a function of pulse intensity (figure 10.2.5a) rises exponentially for the irradiation without a beam spike (red), whereas the temperatures after the occurrence of the spike seem to be lower. The beamspot during the irradiation without a spike shows a confined, squared beamspot and a smaller area in which the heat is distributes (figure 10.2.5b). After the spike, throughout further irradiation the IR camera image in figure 10.2.5c shows that beam heating of the foil is longer not restricted to the square beamspot, but distributes over the hole sample. This observation is an indication that the aC-TL foil was graphitized by the spike, leading to better conductivity.

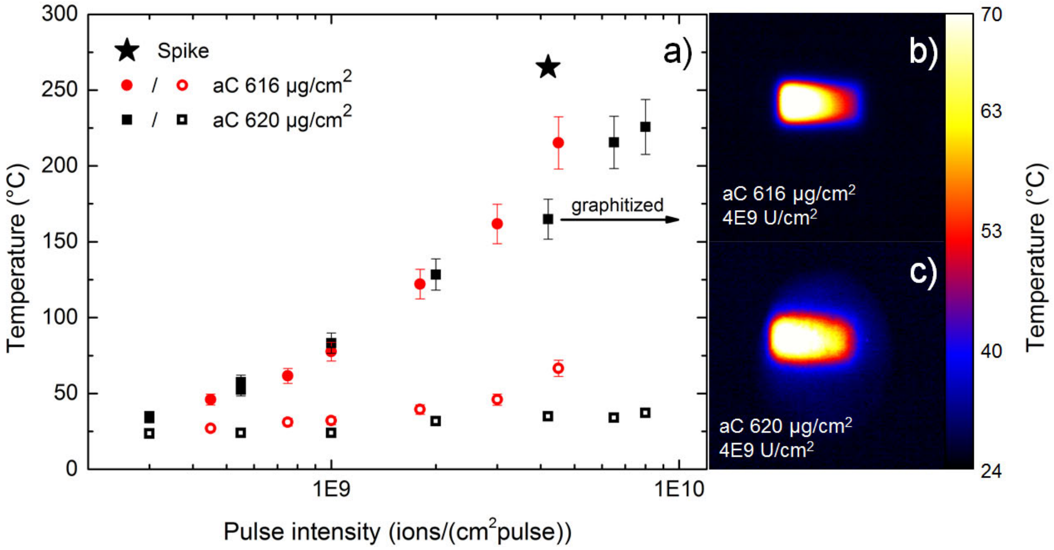

Figure 10.2.5.: a)Temperature evolution as a function of pulse intensity for a U beam (0.6 Hz, 0.2 ms) in 20 µg/cm^2 aC-TL. During one measurement (black squares), a beam spike (a very intensive pulse) occurred during the irradiation step at a pulse intensity at 4×10^9 ions/(cm^{2}pulse) (indicated by the black star). Thermographic images of the beamspot for two irradiations with the same flux without a beam spike (b) and after the beam spike (c). Closed symbols correspond to mean peak temperatures, open symbols are mean base temperatures.

To investigate the effect of graphitization on the evolution of the temperature with increasing fluence, temperature measurements were performed before and after accumulation of a certain fluence. It should be noted, that the measurements before and after irradiation were performed in the same beamtime with nominal identical beam conditions in order to enable a direct comparison. For this reason, part of the the data is similar to data in figure 10.2.2, 10.2.4 and 10.2.3, but was measured during an

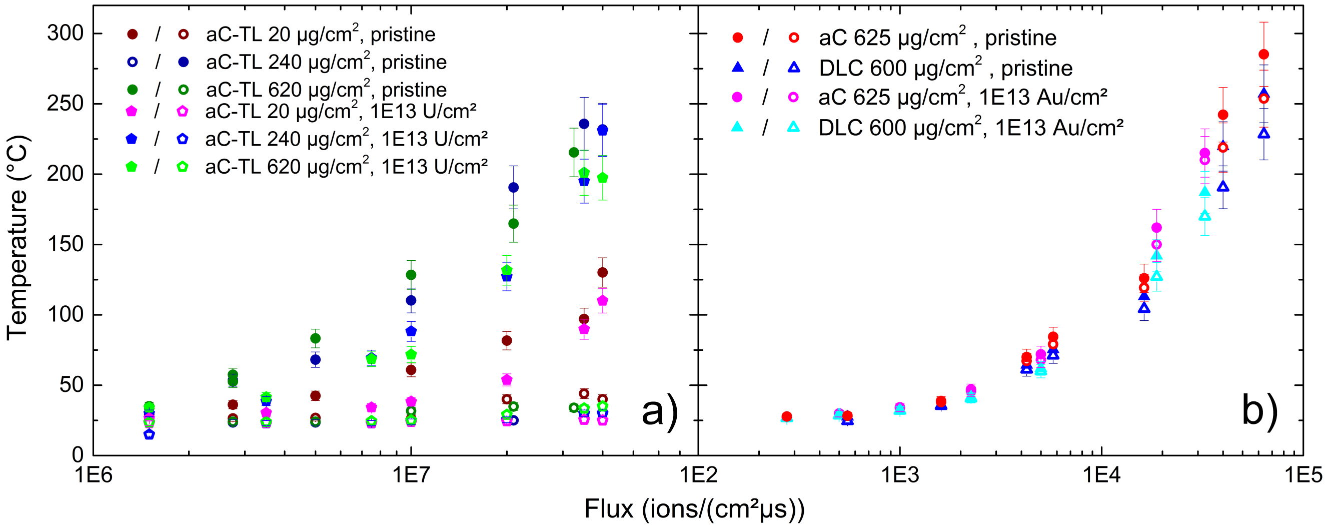

Figure 10.2.6.: a) Temperature evolution as a function of flux for a U beam (0.6 Hz, 0.2 ms) in quasi-pristine and irradiated (1×10^{13} ions/cm^2) aC-TL foils of different thickness. b) Temperature evolution as a function of flux for a Au beam (45 Hz, 4 ms) in pristine and irradiated (1×10^{13} ions/cm^2) ~600 µg/cm^2 thick aC-TL and DLC-MM foils. Closed symbols correspond to mean peak temperatures, open symbols are mean base temperatures.

additional experiment. Figure 10.2.6a shows aC-TL samples of different thicknesses irradiated with U ions (0.6 Hz, 0.2 ms). A temperature measurement for different fluxes was performed, at small fluences. Subsequently the samples were irradiated to a fluence of 1×10^{13} ions/cm^2 and another temperature measurement was performed. Temperatures of the irradiated foils of all thicknesses are slightly smaller than at the initial irradiation stage. Applying the same procedure to approximately 600 µg/cm^2 aC-TL and DLC-foils 10.2.6b, no significant difference between quasi-pristine and foils irradiated to a fluence of 1×10^{13} ions/cm^2 can be detected. The tested fluence of 1×10^{13} ions/cm^2 therefore may not be enough to show changes in the temperature. Further tests with samples of larger fluences would be needed to confirm these observations.

Temperature profiles in figure 10.2.1 illustrate the dependence of the temperature on the beam structure. The repetition rate essentially influences the temperature evolution (figure 10.2.1). Figure 10.2.7 presents temperatures in different 600 µg/cm^2 foils measured for a U beam with a flux of approximately 2×10^7 ions/(cm^{2}µs) and different repetition rates. Error bars for the lowest repetition rate (0.5 Hz) are larger than for higher repetition rate, because the flux was unstable during this measurement. The data indicates, that the temperature increases with higher repetition rates of the same flux (and the same ion). Already for low-repetition rate beams an increase in repetition rates therefore seems to cause a temperature increase.

In contrast to the rather similar temperature characteristics of the different foils over a large range of pulse intensities, their overall stability varied significantly. The CNT foils exhibited the shortest lifetime and fractured after an accumulated fluence of 1×10^{12} ions/cm^2 where all other materials were still intact within accessible fluences in this study. The beam induced structural changes and the response to thermal stress have probably a stronger impact on the foil lifetime than the temperature. The final failure of stripper foils during irradiation might not only be due to the temperature increase of the foils, but also due to heating of the aluminum frame. While Al has a thermal expansion coefficient of 23×10^{-6} K^{-1}

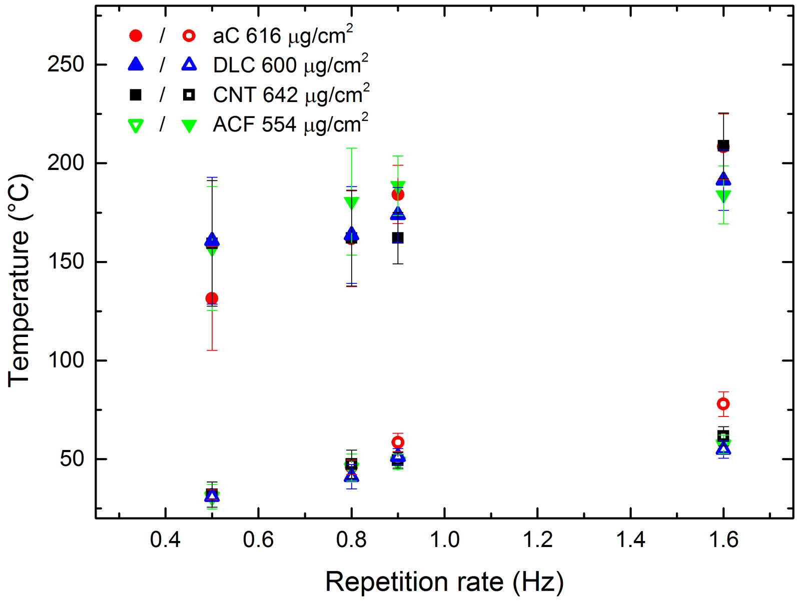

Figure 10.2.7.: Temperature evolution for thick (~600 µg/cm^2) foils: aC-TL (red circles), DLC-MM (blue up-triangles), CNT-DN (black squares), aC-ACF (green down-triangles) as a function of U ion beam repetition rate (0.2 ms pulse length). Closed symbols correspond to mean peak temperatures, open symbols are mean base temperatures.

[204], amorphous carbon shows a much smaller value in the range of 1 to $4 \times 10^{-6}\,\mathrm{K}^{-1}$ depending on the sp^2 fraction [135]. This large difference in expansion may cause additional stresses contributing to failure.

In conclusion, the temperature measurements presented in this chapter provide knowledge on the magnitude of the temperature increase during irradiation for different beams and materials. The beam structure, represented by repetition rate and pulse length, have a large influence on the temperature profile and maximum temperatures. The structure of the tested amorphous carbon and CNT materials seems to have a subordinate effect on the beam-induced temperature increase. However, systematic errors in the temperature measurement lie in the estimation of reflectance and require caution concerning absolute temperature values. Additional measurements to determine the reflectance could increase the accuracy of deduced temperatures from the IR-camera signal. Especially in the case of DLC-MM, which is very shiny already in the visible range, the assumption of a graphite reflectivity might not be right. Calculations or simulations of the temperatures occurring at typical UNILAC beam conditions are needed to verify the results.

Part III.

Model calculation of swift heavy ion impacts

11 Molecular dynamics simulations

Atomistic simulations provide complementary information to experiments on material modifications at a smaller scale and follow track formation on the atomic scale right after the energy was deposited by the ions.

Previous MD simulations on tetrahedral amorphous carbon films with a high fraction of sp^3 hybridization show that the irradiation with swift heavy ions significantly changes the density and bonding content [129, 130, 205].

This work concentrates on the effects of swift heavy ion impacts in amorphous carbon films with 60 % sp^2 content. Simulation cells were produced by simulating liquid quenching and plasma deposition, forming cells with a different degree of clustering. Swift heavy ion impacts are mimicked by an instantaneous energy deposition calculated from the inelastic thermal spike model [206], similar to the simulation setup used to model track formation in silica [186]. In addition to the investigation of changes in density and bonding content, an analysis of the number and size of carbon rings is presented, providing a deeper insight into structural changes of ion tracks in amorphous carbon. Calculated track radii are compared to the experimentally observed cross- sections and track radii in chapter 8.3 and 9.1.

11.1 Simulation setup

Molecular dynamics (MD) simulations offer atomistic insights into structural changes during swift heavy ion irradiation. The movement of atoms is simulated by calculating the force on the atoms from an interatomic potential function. This method enables us to study material modifications induced by swift heavy ions at the atomistic scale. The simulations were performed with the classical MD code PARCAS [207], [208]. Two kinds of simulations were performed: (i) initial sets of simulations to prepare amorphous carbon cells (carried out in 2 different approaches, as described in detail in section 11.3), and (ii) a set which simulated the energy deposition from swift heavy ions in the prepared cells. The temperature and pressure of the simulated amorphous carbon structure was controlled by applying the Berendsen [209] thermostat with the time scaling factor $\tau_T = 50$ fs and barostat with the time constant $\tau_p = 1000$ fs. We also applied the Berendsen temperature control in narrow regions (3 and 4 Å in the DLC films deposition simulations) near the lateral borders of the cell in ion irradiation simulations to minimize the artifacts of temperature control. The empirical Brenner-Beardmore potential [210] as an implementation of the original Brenner potential [211], [212] with extended cut-off parameters ($R = 1.95$ Å, $S = 2.25$ Å) [213] was used for calculation of C−C interactions. Periodic boundaries were applied to simulate bulk material. A time step of 0.26 fs was used for the preparation calculations, ensuring energy conservation in the system. Because some atoms have initially fairly high energies around 10 eV after ion energy deposition, an adaptive time step designed to be able to handle strong collisions was used [214]. The maximum time step used at the end of the simulations was the same value of 0.26 fs.

11.2 Analysis of simulation cells

Visualization of the simulation cells was performed with the open visualization tool OVITO [215]. The obtained simulation data was analyzed in terms of temperature, coordination number, density, as well as size and number of carbon rings as a function of radius from the center of the ion track .

The temperature was calculated from the velocities of the atoms. We analyzed the coordination environment of every atom within the cut-off 1.9 Å. This cut-off was chosen at the minimum position between the first and second peak in the pair distribution function. The atoms with coordination number $n \leq 3$ were defined as atoms with sp^2 hybridization, while atoms with $n \geq 4$ were counted as atoms with sp^3 hybridization. Radial analysis of temperature, coordination number and density was performed by dividing the simulation cell into concentric cylindrical shells of equal width. The optimal width, with respect to obtaining statistically significant results while not losing too much spatial resolution, of each shell was found to be 10 Å.

Within each shell, density $\rho(\mathrm{r})$ was evaluated according to

$$\rho(r) = \frac{N m_\mathrm{c}}{\sum_i^N V_i} \tag{11.1}$$

where N is the number of atoms in the shell and m_c the mass of carbon. The denominator describes the sum over atomic volumes V_i within the shell. The atomic volumes were evaluated using the Voro++ library [216].

The track radii were calculated by applying a fitting function to the density distribution in the final frame after the deposited energy was relaxed and the structure was cooled to 300 K. The fitting function f has the form of a Fermi distribution where $\mathrm{r_t}$ describes the radius for the half-density which is assumed to equal the track radius:

$$f = \frac{\rho_{min} - \rho_0}{\exp \frac{r - r_t}{r_{\rho_0}} + 1} + \rho_0 \tag{11.2}$$

here ρ_min is the minimum density at the track center, ρ_0 is the bulk density outside the track and r_{ρ_0} denotes the width of the transition from the track density to the bulk density ρ_0.

To characterize the number and size of the prime carbon rings (rings without a short-cut) [217], the simulation cell was divided into cylindrical shells of 5 Å in width. The number of shortest rings (the shortest prime rings for each atom) of a certain length was normalized to the total number of shortest rings in the corresponding shell. Since there is only one shortest ring for each atom, the total number of shortest rings corresponds to the total number of atoms in a certain shell.

11.3 Preparation of amorphous carbon structure

Amorphous carbon simulation cells with a sp^2 fraction of about 60 % sp^2 were created by two different types of simulations: (i) Quenching from melt and (ii) plasma deposition. Such a structure is comparable to the measured one for the stripper foils applied in the GSI accelerator in terms of sp^2 fraction. The two different methods for the creation of the amorphous carbon cells result in different degree of clustering of sp^2 and sp^3 bonded atoms (figure 11.3.1). However, the density of the cells is slightly higher than the density expected for amorphous carbons with high sp^2 content. This might be an artifact of the used Brenner potential, which has been previously reported regarding the density relationship between diamond and graphite and therefore produce high density amorphous carbons with unrealistic high sp^2 content [213, 218]. The reason for this behavior is probably related to the short range nature of the potential [218]. The cutoff-extension by Jäger and Albe was shown to solve this problem [213], however in the produced amorphous carbon structures in this study the density is still slightly higher than expected. It has to be taken into account, that this deviation diminishes the thermodynamic driving force volume which potentially favors the sp^3 phase [218].

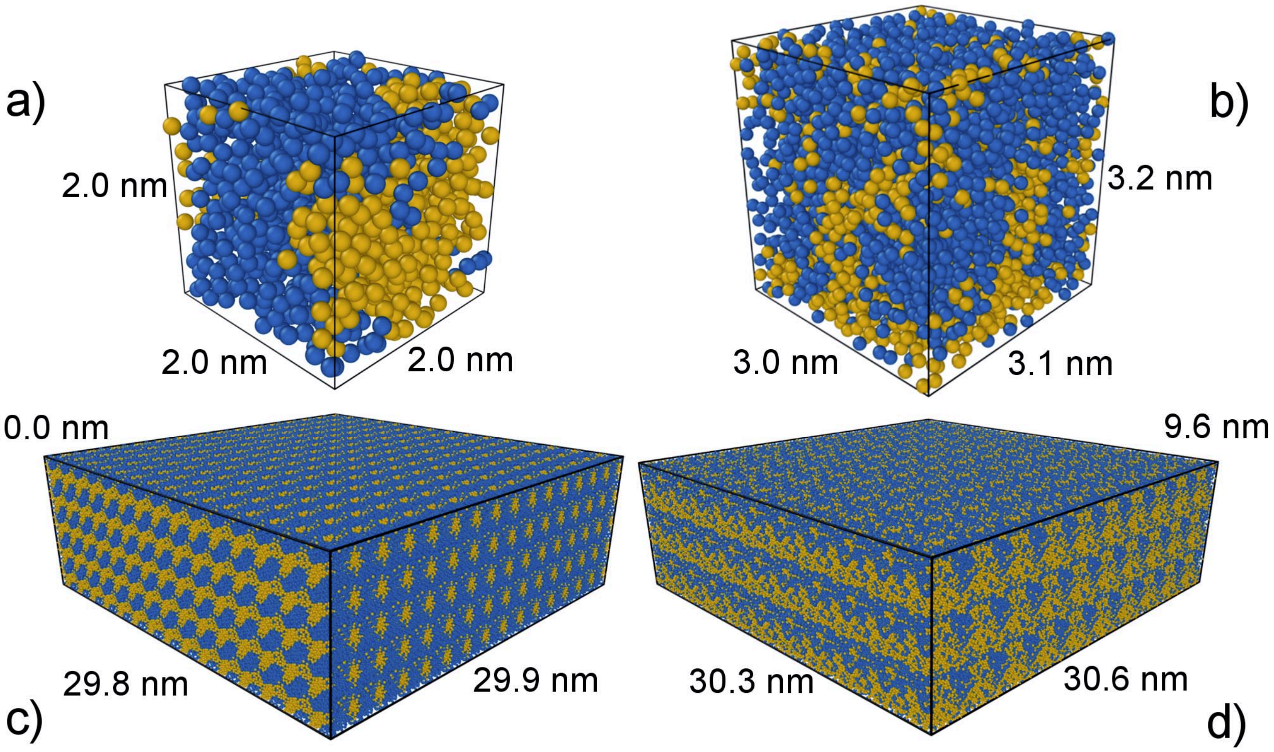

Figure 11.3.1.: Seed cells prepared by liquid quenching (a) and plasma deposition (b). Blue coloured atoms represent 3-fold coordinated atoms (sp^2) and orange coloured atoms are 4-fold coordinated atoms (sp^3). (c) and (d) present the corresponding final large cells for the ion irradiation consisting of multiple units shown in (a) and (b), respectively.

11.3.1 Quenching from Melt

Preparation of the amorphous carbon cell by quenching from melt method consisted of several steps: First, carbon atoms were inserted randomly to the inital cell ($20 \times 20 \times 20\,\text{Å}^3$ in size). The number of the atoms needed for 60 % sp^2 amorphous carbon was roughly estimated by a linear interpolation between the densities of graphite and diamond. In the next step, the sample was cooled down from high temperature (2000 - 6000 K) to 300 K during 100 ps with different cooling rates, searching for the desired sp^2 fraction and minimum potential energy configuration. Stresses in the cell were allowed to relax by applying the Berendsen pressure control (see section 11.1). The best structure was obtained for 1200 atoms, quenched from 5000 to 300 K with a cooling rate of 0.1 K/fs, resulting in a sp^2 content of 58 % (figure 11.3.1 a)). However, the density of this amorphous carbon sample was approximately $3.0\,\text{g/cm}^3$ and therefore slightly higher than the density of $2.7\,\text{g/cm}^3$ deduced by linear interpolation. Tensile stresses of about -10 kbar were relaxed by slightly adjusting the cell size.

A larger cell of adequate size (1350000 atoms, $297.5 \times 299.1 \times 100.2\,\text{Å}^3$) for the ion irradiation was obtained by replication of the small cell over periodic boundaries 3 times in depth direction (z) and 10 times in the lateral directions (x and y). The velocities were randomized by simulating the atom movements at 1000 K followed by slow cooling to 300 K. The resulting structure showed inclusions of sp^3 hybridized atoms in a sp^2 matrix as presented in figure 11.3.1 c). The overall sp^2 content was calculated to remain 58 %.

11.3.2 Plasma Deposition

In addition to the cell created by the quenching method, two cells were obtained by plasma deposition and further treatment, leading to two slightly different structures. The plasma deposition simulation was performed by Wei Ren at the University of Helsinki. In this simulation, the parameters were slightly different from those used for other simulations presented in this study. The amorphous carbon film was grown on a (111)-oriented diamond substrate of about $30 \times 30 \times 20\,\text{Å}^3$ size. Carbon atoms were deposited from normal incidence with an initial energy of 30 eV. Two atomic layers were fixed at the substrate surface to prevent the entire system from moving during the irradiations. Each bombardment was simulated within the time scale of 10 ps, followed by a relaxation time of 3 ps linearly cooling down the entire system to 300 K between subsequent impacts. The analytic bond-order potential of Brenner [212] with extended cut-off parameters was used to model the C-C interactions. By extending the cut-off parameters ($R = 1.95$ Å, $S = 2.25$ Å) a much higher fraction of sp^3 hybridizations could be formed as reported by Jaeger and Albe [213]. A small cell with the dimensions $30.29 \times 30.59 \times 32.00$ Å was cut from the inner part of the obtained DLC film. By this, the sp^2 rich surface layer as well as the DLC layer on top of the diamond substrate were removed. The obtained a simulation cell has periodic lateral boundaries, but is non-periodic in the z direction. The simulations of swift heavy ion impacts require periodic conditions in all three dimensions. However, the attempt to apply periodic boundaries on the sides of the new structure will lead to the overlap of positions of atoms on the adjacent sides of the initial cube, causing an artificial burst of potential energy in those positions. To avoid this problem, these atoms were treated in two different ways. For one cell, an additional empty layer of 1 Å was added on top of the simulation cell in z-direction. Subsequently the whole cell was shrunk in this direction to the former height of the cell. For the other cell, atoms with a distance to a neighboring atom shorter than 1.1 Å were removed. Both cells were then heated to 1000 K and subsequently cooled down to 300 K with the rate of 0.1 K/fs. The resulting cells showed a more homogeneous distribution of atoms with sp^3 hybridization in comparison to the cell obtained by quenching from the melt (figure 11.3.1 b)). The overall sp^2 fraction was calculated to be 60 % for both cells. Large cells of adequate size ($302.9 \times 305.9 \times 96.0$ Å^3, 1333800 atoms for method 1 (figure 11.3.1 d)) and 1331100 atoms for method 2) for the ion irradiation were obtained by multiplication of the small cells and randomization of velocities by simulating the atom movements at 1000 K and slowly cooling to 300 K (0.1 K/fs). The density of both cells was calculated to be 3 g/cm^3 with a similar distribution of sp^3 hybridized atoms in the sp^2 matrix. All cells were checked for having an adequate size, i.e. allowing heat and pressure wave dissipation. For each method, three different seeds were used to allow for statistical variation, however, the produced results were identical within the accuracy of the analysis method. In the following, the results obtained for the plasma deposited amorphous carbon will be given only for the cell obtained with the first method (adding an empty layer and shrinking by 1 Å with subsequent relaxation over periodic boundaries in z direction). The results for the cells prepared the other way are very similar and hence are not presented in detail in this chapter, but can be found in the appendix. Only the extracted track radii are presented.

11.4 Swift heavy ion energy deposition

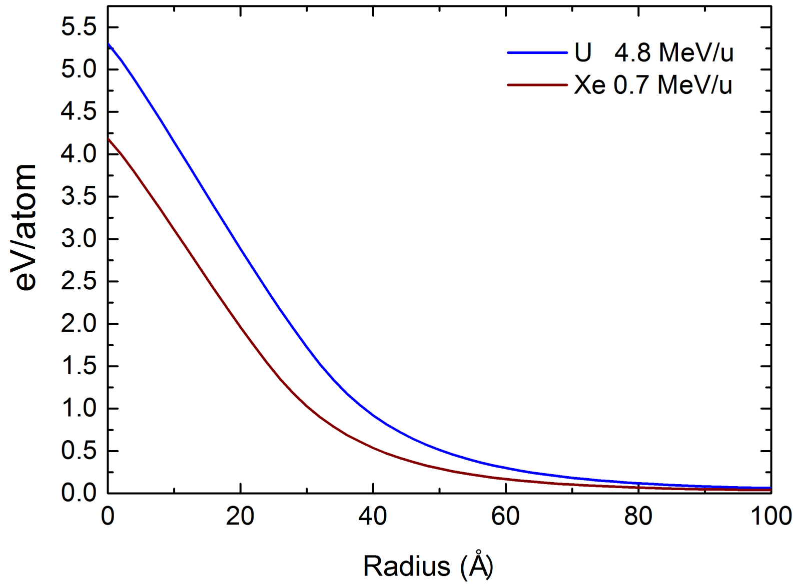

Figure 11.4.1.: Kinetic energy deposition profile for 0.7 MeV/u Xe and 4.8 MeV/u U ions as deduced from the i-TS model by Toulemonde [206].

To mimic the effect of swift heavy ions, random velocities are given to the atoms at the beginning of the simulation in accordance with the radial kinetic energy distribution profile for 0.7 MeV/u Xe (energy loss of 20 keV/nm for 3 g/cm^3 aC) and 4.8 MeV/u U (energy loss of 42 keV/nm for 3 g/cm^3 aC) that was calculated by Marcel Toulemonde (University of Caen Normandy) using the inelastic thermal spike (i-TS) model [206] (figure 11.4.1). The i-TS model is a widely used phenomenological model that consists of a coupled set of heat diffusion equations, describing heat transport in the electronic and atomic subsystems (see chapter 2.3.1). The kinetic energy profile used in MD simulations corresponds to the temperature profile in the atomic subsystem at about 10 fs, when the temperature of the atomic system has reached the maximum in the i-TS calculation. A value of 2.5×10^{14} J/(sKcm^3) was used as the electron-phonon coupling constant determined by Rotaru *et al.* [83] from the measurement of the electron phonon mean free path in DLC equal to 0.9 nm and an amorphous carbon density of 3.0 g/cm^3.

11.5 Results and discussion

Cross sections of the final simulation cells after the ion passage are presented in figure 11.5.1. The formation of a track in the center of the simulation cells is well visible by the increase of sp^2 bonded atoms (blue).

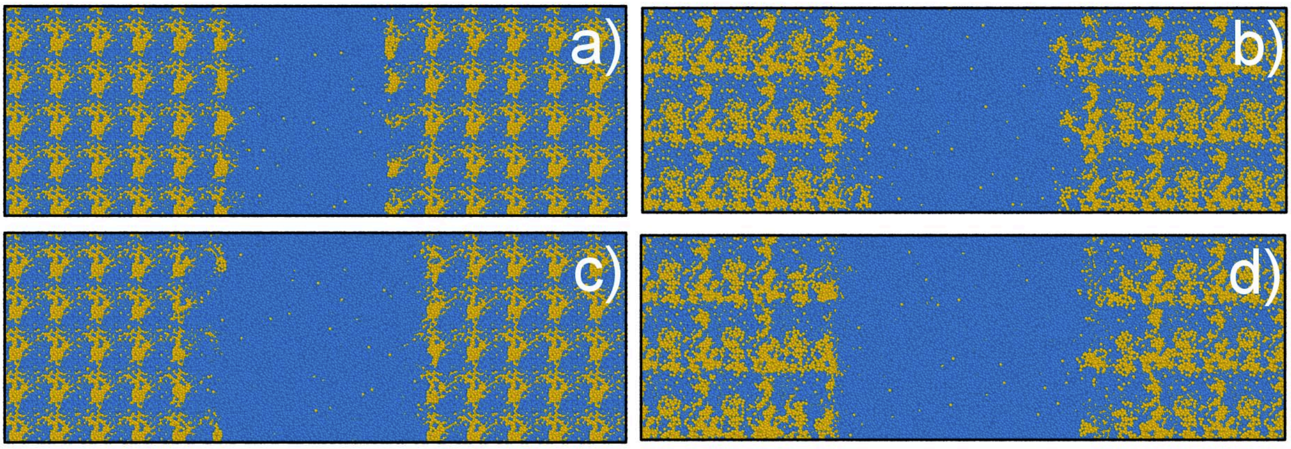

Figure 11.5.1.: Cross sections of the final simulation cells prepared by liquid quenching (left) and plasma deposition (right) after Xe (0.7 MeV/u; a, b) and U (4.8 MeV/u; c, d) ion passage. The ion tracks in the center of the cells are characterized by ane increase of sp^2 bonded atoms (blue), surrounded by atoms correspond to sp^3bonded atoms (orange).

Time evolution of the temperature as a function of radial distance from the track center for both quenched and plasma deposited cells and Xe and U ion impact is shown in figure 11.5.2. Immediately after energy deposition (0.1 ps), a rapid temperature increase in the core of the track is observed in all cells. The temperature rises up to ~8300 K for the liquid quenched cell (figure 11.5.2 a) and up to 9327 K for the plasma deposited cell under Xe irradiation (figure 11.5.2 b). For the irradiation with U ions, the maximum temperature after energy deposition is higher: ~12010 K for the liquid quenched cell (figure 11.5.2 c) and ~12771 K for the plasma deposited cell (figure 11.5.2 d). The temperature decreases radially from the track center, reaching 700 1000 K at the borders of the simulation cells. Since this temperature is considerably below the melting point of carbon (estimated from simulation of carbon [219] with the same potential to be above 3000 K), we assume that the simulation cell is of adequate size for studying the ion impact. Throughout the simulation, the temperature decreases until reaching the initial temperature (≈300 K) at the end of the simulation (100 ps) for all cells. For both ions, the decrease of temperature in time is similar (figure 11.5.3).

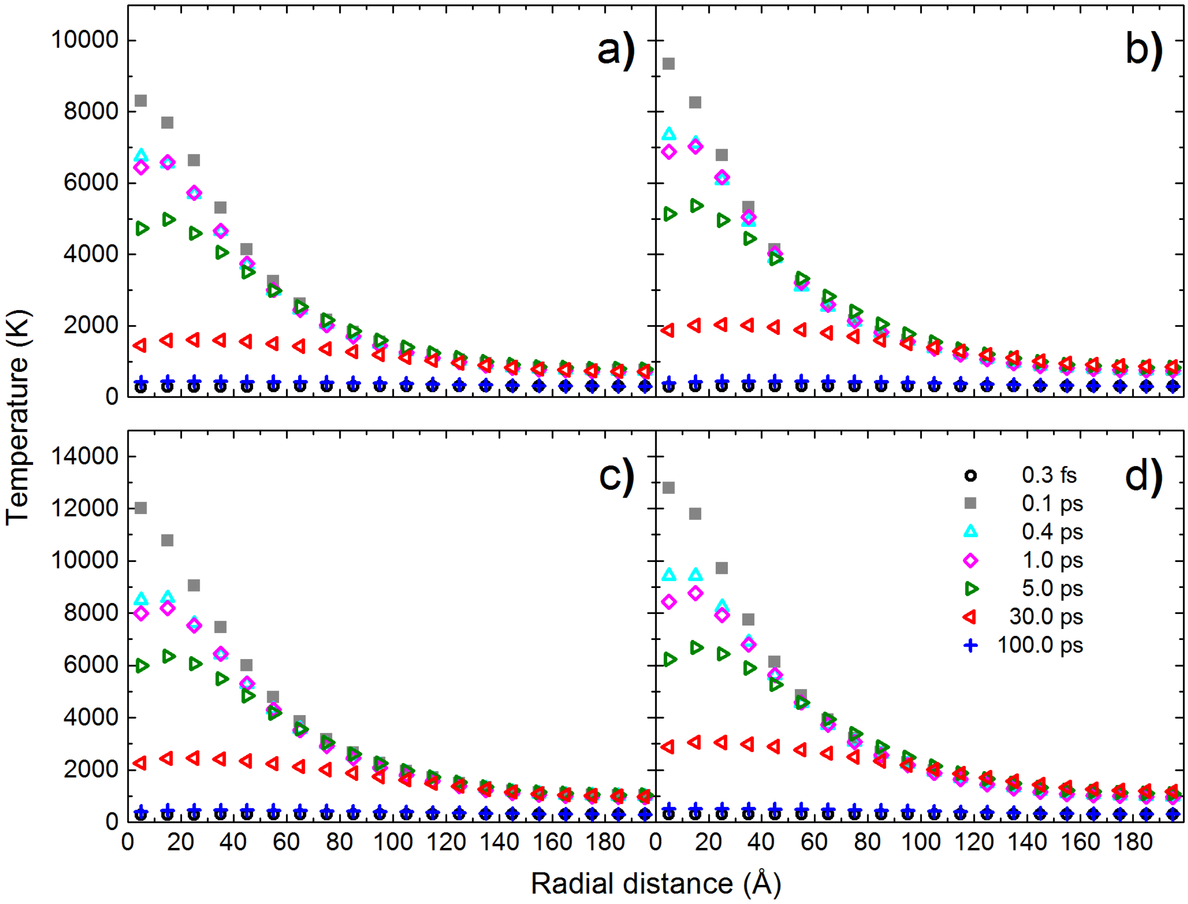

Figure 11.5.2.: Time evolution of temperature as a function of the radial distance from the track center in the quenched (a) and the plasma (b) deposited cell for 0.7 MeV/u Xe ion and in the quenched (c) and the plasma (d) deposited cell for 4.8 MeV/u U ions.

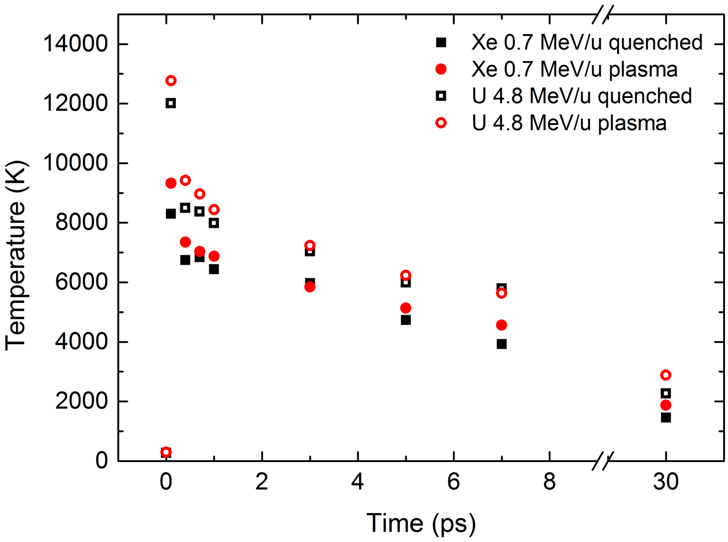

Figure 11.5.3.: Temperature as a function of simulation time in the track center (0 to 5 Å) of the quenched (red circles) and the plasma (black squares) deposited cell for 0.7 MeV/u Xe (closed symbols) and 4.8 MeV/u U ions (open symbols).

Coordination number analysis is presented by the fraction of sp^2 bonded atoms as a function of the radial distance from the track center. The sp^2 fraction in the track core increases gradually with simulation time (figure 11.5.4). For both ions, Xe and U, the respective maximum values of 96 % and 99 % for the quenched and plasma deposited cells are reached at the end of the simulations (after 100 ps). This graphitization is confined to a region of about 50 Å radial distance from the track center. Outside this area, the sp^2 fraction is at the initial level of 60 %.

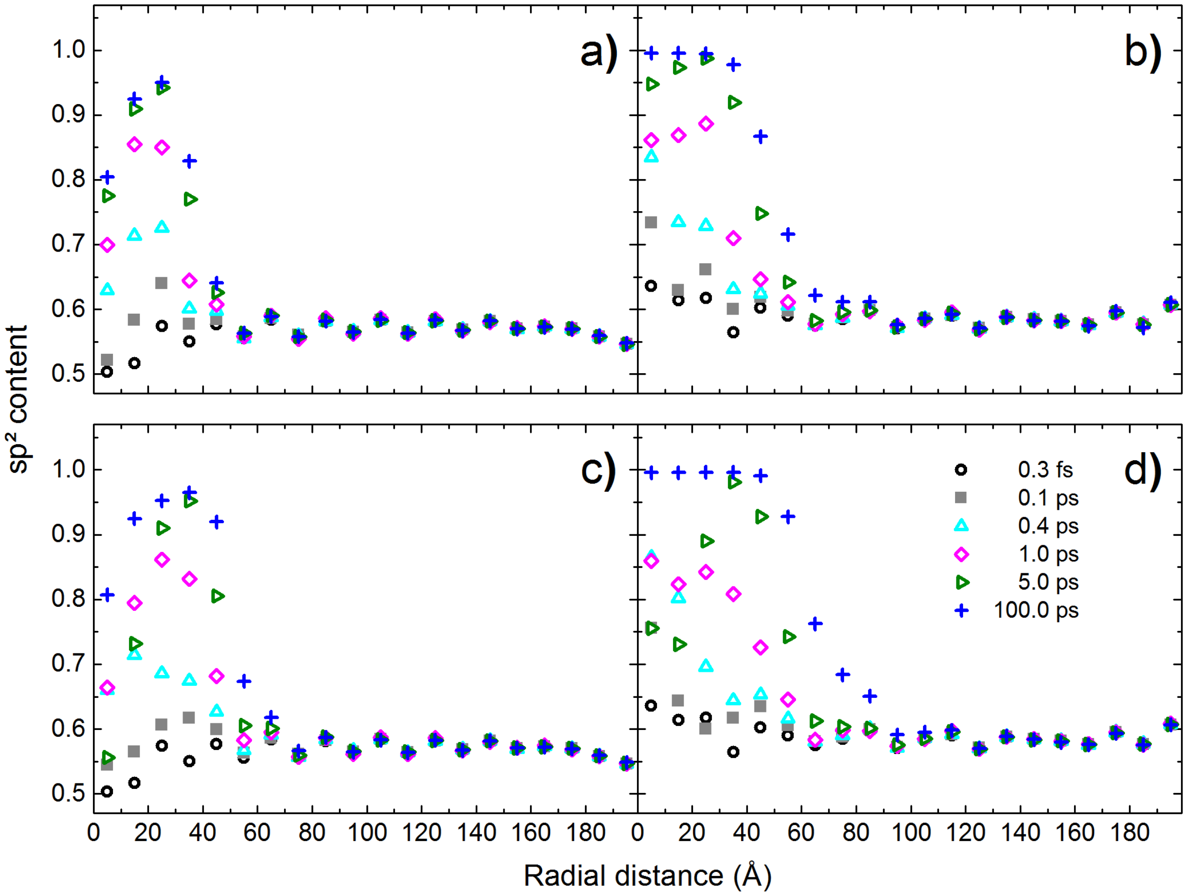

Figure 11.5.4.: Time evolution of sp^2 content as a function of the radial distance from the track center in the quenched (a) and the plasma (b) deposited cell for 0.7 MeV/u Xe and in the quenched (c) and plasma (d) deposited cell for 4.8 MeV/u U ions.

The density profiles presented in figure 11.5.5 show a rapid expansion of the material in the track after energy deposition by Xe and U ions resulting in an non-equilibrium underdensed structure of about 2.4 g/cm^3 (Xe) and 2.2 g/cm^3 (U) for the quenched cell and 2.5 g/cm^3 (Xe) and 2.3 g/cm^3 (U) for the plasma deposited cell. Relaxation towards the end of the simulation forms a structure of respectively 2.7 and 2.8 g/cm^3 density in the track. The density fluctuation outside the track is due to the segregation of 4-fold coordinated atoms and is therefore stronger for the quenched cell. The track radii were calculated by fitting a Fermi function (equation 11.2) to the density data of the relaxed simulation cell after 100 ps (fit shown in figure 11.5.5). Xe irradiation yields a track radius of 28.9 ± 0.5 Å for the quenched cell and 35.1 ± 0.8 Å for the plasma deposited cell prepared with the first method (adding an empty layer and shrinking by 1 Å with subsequent relaxation over periodic boundaries in z direction). The second plasma deposited cell (removal of too close neighboring atoms) gives a radius of 36.0 ± 0.8 Å. For U ions, the track radii are 40.5 ± 0.5 Å for the quenched and 48.6 ± 0.7 Å for the plasma deposited cell prepared with the first method and 50.8 ± 0.6 Å for the second method (compare section 11.3.2). The track radii by U ions are therefore larger than the values found for Xe, which can be attributed to the larger energy loss. For both ions the track radii are smaller for the liquid quenched cell which have a higher degree of sp^3 clustering compared to plasma deposited cells. Even though the evolution in temperature, sp^2 fraction, density and ring analysis as a function of radius from the track center is similar for the two plasma deposited cells, the second cell treatment causes a larger radii. These observations evidence the importance of clustering and atomic arrangement on the track radius.

With the obtained track radii, a rough estimate of the total graphitization fluence without considering overlap of tracks can be calculated using the single-impact model [163, 164]. With a track radius of 4.5 nm 99 % track coverage requires a fluence of about 7×10^{12} ions/cm^2 . These values are within the fluence regime in which experimentally observed saturation of microstructural changes starts (compare section 8). Experimentally determined track radii for 4.8 MeV/u U irradiated aC-TL by SAXS (section 8.5) and on-line FTIR spectroscopy (section 8.3) are 4.4 ± 0.2 nm and 4.6 ± 0.5 nm, respectively. Considering that the extend of clustering and the density are not accurately known for "real" aC-TL, experimental and simulated track radii are well in accordance.

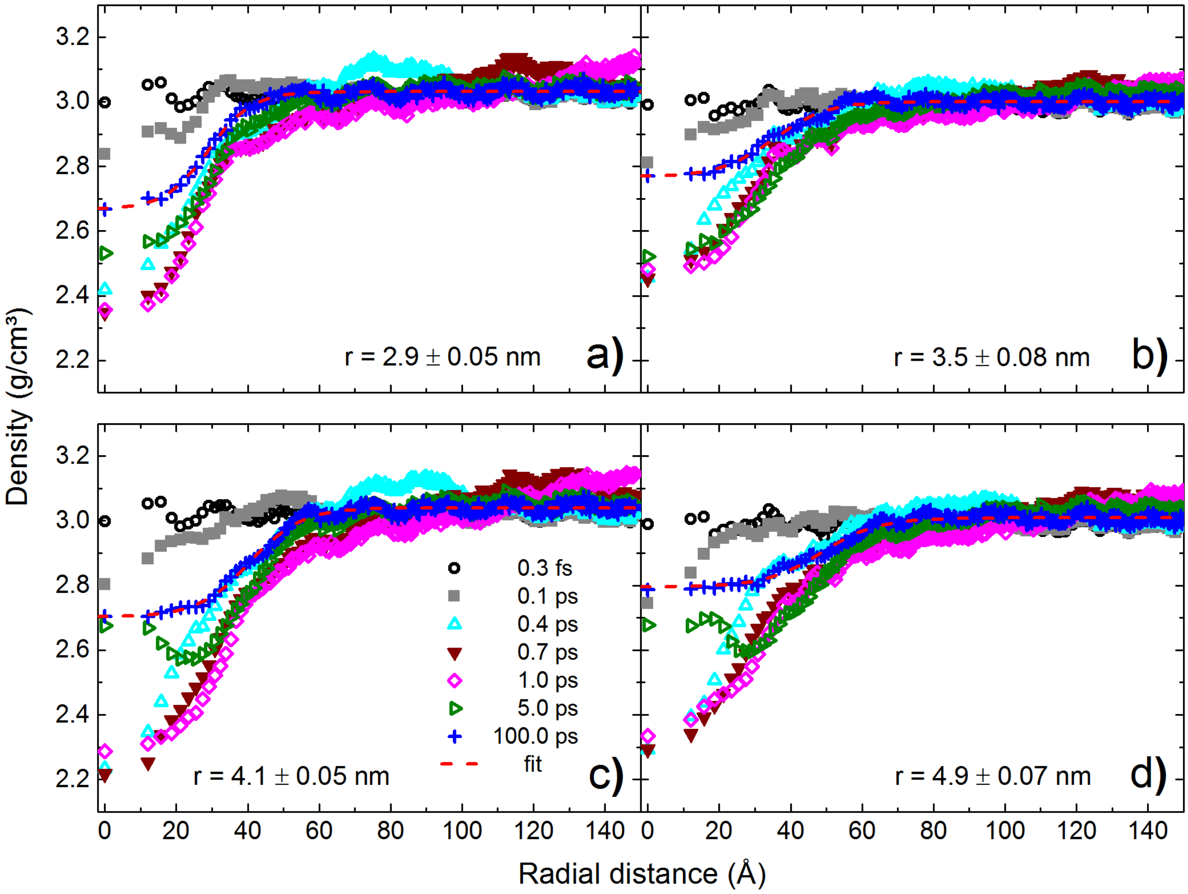

Figure 11.5.5.: Time evolution of density as a function of the radial distance from the track center in the quenched (a) and the plasma (b) deposited cell for 0.7 MeV/u Xe and in the quenched (c) and plasma (d) deposited cell for 4.8 MeV/u U ions. Track radii are derived from the Fermi function (eq. 11.2) fits (dashed lines).

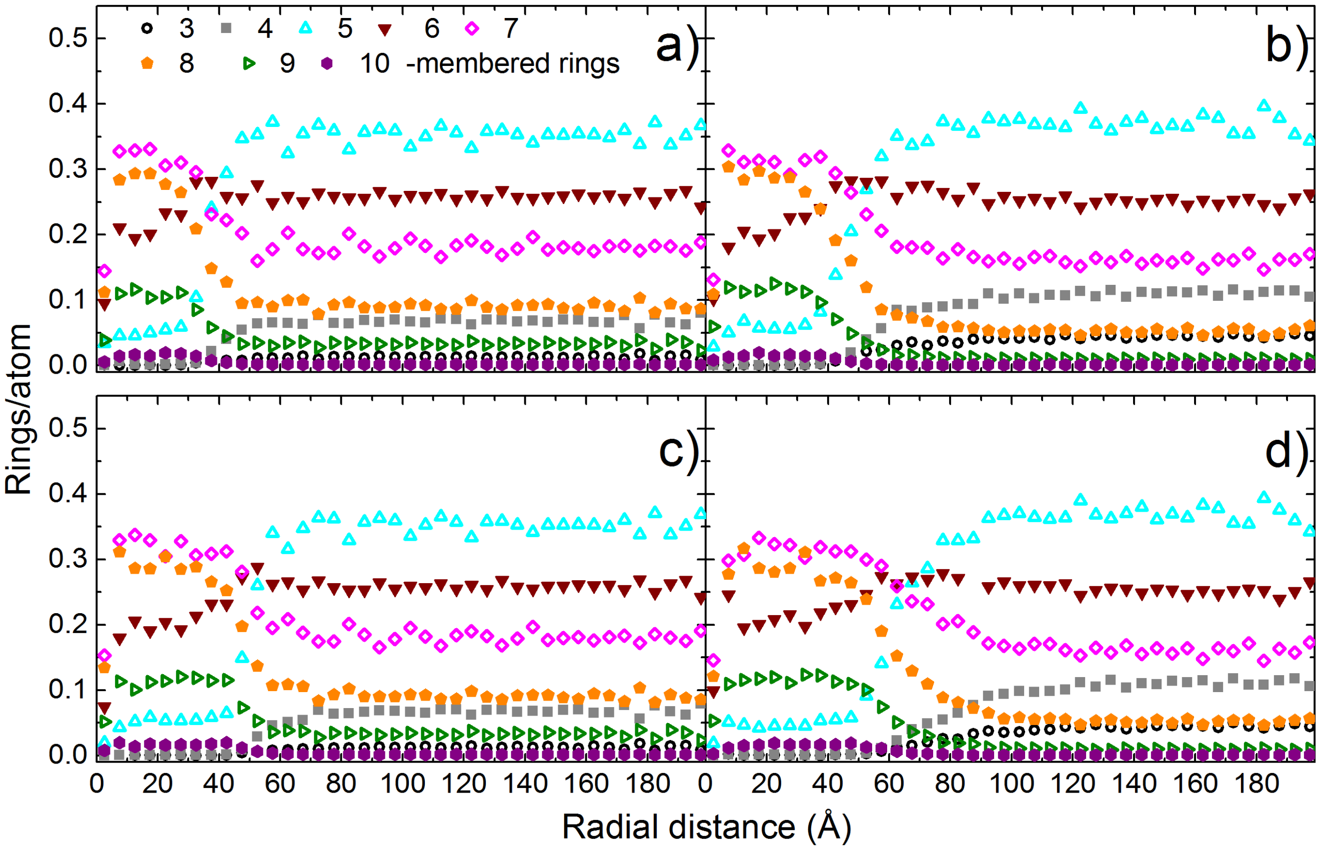

Figure 11.5.6.: Rings per atom as a function of radial distance from track center in the relaxed (100 ps) quenched (a) and plasma deposited (b) cell for Xe 0.7 MeV/u and in the relaxed quenched (c) and plasma (d) deposited cell for U 4.8 MeV/u ions. The term "rings per atom" denotes the number of shortest rings of a certain size normalized to the total number of shortest rings (atoms) in the corresponding shell.

Ring analysis for the relaxed simulation cell (100 ps) is presented in figure 11.5.12. For both quenched and plasma deposited cells, the number of rings per atom for ring sizes smaller than six decreases in the area of the track, whereas the number of rings per atom increases for the 7-membered rings or larger. The ratio of the rings per atom of final relaxed cell and the cell before energy deposition for the 6- and 8-membered rings is presented in figure 11.5.13a and b, respectively. 6-membered rings are abundant in graphite and diamond, whereas 8-membered rings are specific to a defected graphite structure (divacancies), but not to diamond structure. The decreased number of the 6-membered rings in the core of the track and a slight increase of this number in the outer part of the track constitute a core-shell structure of the track with a disordered core and a more ordered shell region. An increase of the 8-membered rings confirms graphitization, or more precisely, the formation of a damaged graphitic structure in the track, since no 8-membered rings are expected in defected diamond. This is in good accordance with positron annihilation experiments on pristine and swift heavy ion-irradiated HOPG which show the presence of twofold to fourfold (chain) vacancy clusters [220].

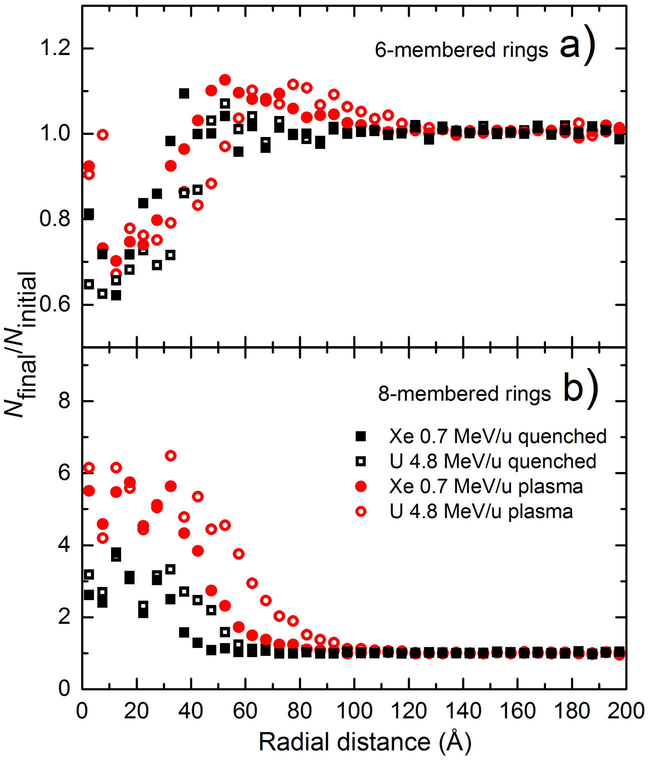

Figure 11.5.7.: Change in the number of occurrences of 6-membered (a) and 8-membered (b) rings per atom as a function of radial distance from the track center for 0.7 MeV/u Xe and 4.8 MeV/u U ion impact. The value is given as the ratio of occurrences in the final simulation frame N_{final} to the initial frame N_{inital} and calculated using 3 different simulation cells (cell fabrication methods are given in the legend).

In conclusion, the results show beam-induced graphitization characterized by the increase of the sp^2 fraction and a density decrease within a cylinder radius in amorphous carbon. Extracted radii for 4.8 MeV/u U irradiation are well in accordance with experiments. The study of amorphous carbon cells with different degree of clustering indicate the strong influence of the local atomic arrangement on the track size. Further experiments are needed to completely understand the influence of the atomic structure on the track formation in amorphous carbons.

Part IV.

Conclusions and Outlook

Application of carbon as a stripper foil material in high-power accelerators requires a better understanding of the induced degradation by radiation damage, thermal effects, and stress waves. A comprehensive knowledge of the carbon stripper foil structure and its changes under extreme beam exposure is needed to develop long-lasting stripper foils for certain beam conditions and environments. This thesis investigates the response of amorphous carbon and carbon-based foils to swift-heavy ion irradiation, with special focus on beam-induced changes of the (micro-)structure and thermal, electrical and mechanical properties by various characterization techniques and molecular dynamics simulations. The influence of different beam time-structures on the induced changes and on beam-heating of the foils is specified.

This thesis concentrated predominantly on the study of amorphous carbon foils produced by the GSI target laboratory (aC-TL), but also other amorphous carbon (DLC-MM, aC-ACF) and buckypaper (CNT-DN) foils purchased from different suppliers were investigated for comparison.
Qualitative analysis by light-optical microscopy illustrates the severe changes of irradiated amorphous stripper foils, including graphitization, compaction of the material in the beamspot and stresses in the transition between beamspot and surrounding non-irradiated area. In contrast, diamond-like carbon foils (DLC-MM) seem to expand in the beamspot during irradiation. For carbon nanotube-based stripper foils (CNT-DN), damage and failure seem mainly related to stresses in the beamspot-halo transition area.
Optical microscopy, scanning electron microscopy, profilometry and chromatic aberration measurements were used to study the microstructure of the standard material aC-TL. Such aC-TL foils are produced by evaporation on a betaine-sucrose intermediate layer. The topography of these crystals is replicated in the carbon film showing pronounced micro-slackening. This micro-slackened morphology is found to flatten during irradiation and seems to be advantageous for the lifetime of the stripper foils. In comparison, other amorphous carbon stripper foils (DLC-MM and aC-ACF) show a initially smooth surface with large-scale buckling of the thick (600 $\mu g/cm^2$) foils, which is enhanced with irradiation. Buckypaper CNT-DN foils show no changes in microstructure until final failure.
Scanning electron microscopy (SEM) measurements on aC-TL samples provide evidence that many mainly small cracks are present in the pristine material. The investigation of these cracks at high magnification revealed a platelet-like structure. Initial cracks close at small fluences. Many small cracks in the halo region and in the beamspot appear under the irradiation with Au ions at medium fluences. For high fluences the number of larger cracks increases, especially for irradiation with U ions. These results indicate that ion beams with short intensive pulses (e.g. U, 2 Hz, 0.2 ms) are more critical

for the failure of the stripper foils than beams with longer pulses (e.g. Au, 45 Hz, 4ms).
Profilometry and chromatic aberration measurements are strongly influenced by the morphology of the foils. The estimated thickness of thin (20 μg/cm^2) aC-TL foils under profilometer load is in the range of 1 to 2 μm. The other 20 μg/cm^2 amorphous carbon foils appear significantly thinner, with thicknesses in the range of 100 to 200 nm. Together with SEM investigations, these observations suggest that the aC-TL material is less dense with some degree of porosity related to a layered or platelet-built structure. Chromatic aberration provides density estimates for the 600 μg/cm^2 foils in the range of 1.3 to 1.8 g/cm^3, lower than the density of graphite (2.25 g/cm^3).

Beam-induced structural modifications were investigated for different irradiation conditions. High resolution transmission electron microscopy (HRTEM) confirms the amorphous structure of the standard aC-TL material. U irradiation at high fluence results in the formation of turbostractic carbon in some areas. A similar pattern is observed for aC-TL foils annealed at 1000°C, which is a much larger than the maximum temperature due to beam heating. In aC-TL irradiated with high intensity and short pulses at very large fluence (3.8×10^{16} ions/cm^2) the formation of nanocrystals is observed.
X-ray photoelectron spectroscopy (XPS) reveals an increase of the sp^2 bonding fraction already at small fluences for all beams. The sp^2 content in the standard aC-TL material increases from about 60 % sp^2 (20 % sp^3, 20 % carbon-oxygen-bonds) to maximum 95 % sp^2 for U irradiation (fluence of 5×10^{13} ions/cm^2). At higher fluences, the measured sp^2 fractions are smaller (about 70 %). sp^2 fractions determined from electron energy loss spectroscopy measurements are 54 % (pristine) and 65 % for a sample exposed to a large fluence (3.8×10^{16} ions/cm^2). The EELS values are larger compared to the values obtained from XPS, but assuming that XPS overestimates sp^2 fractions, and considering the limitations of EELS, the real values might lie in between. For DLC-MM the sp^2 fractions are comparable to aC-TL, even though the measured sp^3 fraction is larger (less oxygen-carbon bonds). For aC-ACF the measured maximum sp^2 fraction stays below 80 % for increasing fluence and the measured sp^3 content is larger compared to aC-TL (similar amount of oxygen-carbon bonds content).
Raman spectroscopy indicates an increase in short-range order and reduction of bond-angle disorder by an increase of I_D/I_G ratio with fluence for aC-TL and DLC-MM foils. According to the model by Ferrari *et al.* the evolution of the intensity ratio corresponds to the growth of in-plane sp^2 clusters in the range of 0.6 to 1.4 nm. CNT-DN foils show an increase of I_D/I_G ratio by the formation of defects, but the overall CNT structure is preserved.
For fluences between about 2 and 5×10^{13} ions/cm^2 a decrease of the sp^2 fraction or cluster size (intensity ratio) is observed for both XPS and Raman measurements. Because overlapping of the ion tracks occurs in this fluence regime, this observation provides an indication that double hit events introduce additional defects or disorder to the graphitized and ordered structure.
In-situ Fourier transform infrared spectroscopy was used to characterize the transmittance decrease during irradiation with different beams in 20 μg/cm^2 aC-TL and DLC-MM samples. The transmittance values are an important input for thermographic measurements, but also provide information on the evolution of structural changes during irradiation. Based on the conclusions from XPS, EELS and Raman measurements, the transmittance decrease seems to be related to the sp^2 content increase and possibly compaction. Xe as a comparatively light ion shows the transmittance decrease at higher fluences compared to heavier Au or U ions. A high repetition rate Au beam (45 Hz, 4 ms) shifts the transmittance

decrease to larger fluences compared to an intensive, low repetition rate, short-pulsed U beam (2 Hz, 0.2 ms). This indicates that the evolution of material transformation depends not only on the ion species (energy loss), but also on beam intensity, repetition rate, pulse length. For U ions the transmittance saturates at approximately 25 % of the initial value. Damage cross sections and track radii can be determined from Poisson fits to the transmittance versus fluence data based on a single-impact model. However, fits based on this model do not reproduce our data at large fluences. This observation suggests that other effects influence the evolution of transmittance, which are presently not included in the model. The fluence range of the fits was therefore limited, accepting an uncertainty of the derive track radii. Largest track radii are observed for short-pulsed U ions (4.6 ± 0.5 nm), and low repetition rate Au ions (4.6 ± 0.5 nm) followed by high repetition rate Au ions (3.7 ± 0.5 nm). The smallest radius is found for Xe ions (1.8 ± 0.5 nm) in agreement with the general observation that the size of ion tracks scales with the electronic energy loss. The track radius determined for a DLC-MM sample (4.5 ± 0.5 nm) is larger compared to aC-TL (3.7 ± 0.5 nm) for similar irradiation conditions, suggesting that this material is more sensitive to ion irradiation.
The size of the tracks is comparable to radii determined by small angle X-ray scattering (SAXS) measurements, which show a slightly smaller radius of 4.4 ± 0.2 nm for irradiation with short-pulsed U ions and slightly larger radii of 4.1 ± 0.1 nm and 3.9 ± 0.2 nm for irradiation with high-repetition rate Au ions.

For a comprehensive understanding of the material transformations during swift heavy ion irradiation, also the changes of the electrical and thermal conductivity, as well as mechanical properties are important. For this reason, measurements of the electrical resistivity (in-situ four-point probe), the thermal diffusivity (laser flash analysis LFA) and atomic force microscopy (AFM) were performed.
The electrical resistivity decreases exponentially with irradiation and saturates at 35 % of the initial value. The track radius determined from a Poisson fit is 5.7 ± 0.5 nm and thus larger compared to valued obtained from FTIR or SAXS measurements. Probably defects in the halo region of tracks contribute to the electrical resistivity yielding larger tracks compared to other methods.
The thermal diffusivity measured by laser flash analysis (LFA) technique increases up to 32 % for aC-TL samples exposed to medium fluence. DLC-MM and aC-ACF foils show a smaller increase and a decrease of values in the track-overlapping regime, as for XPS and Raman measurements. Deformation-deflection curves measured by atomic force microscopy showed a stiffness increase by a factor two for an U irradiated sample of high fluence and an increased homogeneity by less scattering of the stiffness values.

The experimental measurement of temperatures during irradiation is needed to complement simulation results and to define design parameters for future stripper foils. Temperatures were monitored with an infrared camera. The infrared camera data was calibrated by the emittance values calculated from transmittance measurements (on-line FTIR). Measured temperatures increase up to 135°C for the irradiation with U ions (2 Hz, 0.2 ms) of 20 $\mu g/cm^2$ foils and and up to 130°C for irradiation with Au ions (45 Hz, 4 ms) of 600 $\mu g/cm^2$ foils for maximum achievable ion fluxes or pulse intensities. These values provide a benchmark of temperatures occurring during swift heavy ion irradiation. The structure of the (amorphous) carbon materials seems to have only a small effect on beam-induced heating.

To study the structural changes in the tracks, molecular dynamics simulations of ion impacts in amorphous carbon films with 60 % sp^2 content were performed. The ion impacts were mimicked by an

instantaneous energy deposition calculated from the inelastic thermal spike model.
Virtual cells were produced by simulating liquid quenching and plasma deposition and yielded amorphous carbon with a different degree of clustering of sp^2 and sp^3 bonds. The results show that swift heavy ions induce graphitization, which is characterized by the increase of the sp^2 fraction and a density decrease within the track radius. Ring analysis shows that the tracks have a defected graphitic structure with an increased number of 8-membered rings. A larger number of 6-membered rings around the center of the tracks confirms a core-shell like structure. Extracted radii for irradiation with 4.8 MeV/u U ions are larger compared to 0.7 MeV/u Xe ions and well in accordance with experiments. The simulations for U ions provided track radii between 4.0 ± 0.1 nm and 5.1 ± 0.1 nm for the different cells, which are in the range of experimentally determined track radii. Testing of differently produced simulation cells indicates the strong influence of the local atomic arrangement on the track size, in agreement with the influence of clustering indicated by XPS and Raman measurements.

The observed trends in this study lead to suggestions for the development of future carbon stripper foils. In general, short intensive U-ion pulses seem to be more critical than beams with longer pulse length, less intensity and higher repetition rate, like for example Au with 45 Hz and 4 ms. The graphitization process starts already at low fluences, leading to a structure with high sp^2 content, a higher degree of short-range order and less bond-angle disorder. In-plane sp^2 clusters, which seem to be present already in the pristine materials, grow during the beam-induced graphitization process. These structural changes lead to an increase of the electrical and thermal conductivity as well as the stiffness of the amorphous carbon material. High electrical and thermal conductivity are advantageous for the stability of the foils during beam exposure. A high stiffness might limit the stability of stripper foils during irradiation with short, intensive beam pulses, because the amplification of the induced stress waves may cause severe damage. As a consequence, foils with a high sp^3 content like diamond-like or tetragonal amorphous carbon are expected to have poor mechanical characteristics regarding this short-pulsed beam condition. For further clarification additional tests should focus on the mechanical properties of the different stripper foil materials.
However, our experiments clearly show that no ideal stripper material exists for all beam conditions. Amorphous carbon, aC-TL, seems to be the best option for intensive, short pulsed beams, but is pushed to its limits at extreme intensities. Regarding the installation of the stripper foils at the present gas stripper position (1.4 MeV/u), or in the transfer channel (11.4 MeV/u), the radiation damage is expected to be less critical compared to the M-branch (3—6 MeV/u, Bragg maximum). At lower or higher energies (1.4 or 11.4 MeV/u), the lower energy loss of the ions results in smaller track radii and thus less radiation damage. Since also the intensities are lower in the transfer channel compared to the gas stripper position and M-branch, amorphous carbon foils will provide a suitable option for stripping at this location.
Further development of amorphous carbon foils for extreme beam conditions should focus on foils with a graphitic structure. A graphitic structure has the advantage that it has a lower density than diamond-like carbon or tetragonal carbon, resulting in a lower energy deposition of the ion. In addition, the critical transition between the graphitized beamspot and the non-graphitized region outside the beamspot can be avoided by using a graphitic or pre-graphitized foil. The operation at high temperature might increase the stability of a graphitic carbon foil by defect annealing and should be tested in future experiments. Also other material options could provide the discussed properties, for instance graphene-platelet-based

foils, nanotube foils at high temperature or glassy carbon foils.
Since the intensities which are planned at FAIR were not available for the experiments at this work, future lifetime studies should clarify the beam stability of the developed carbon stripper foils under certain beam conditions once the GSI accelerator is upgraded and higher beam intensities are available.

Appendix A: XPS

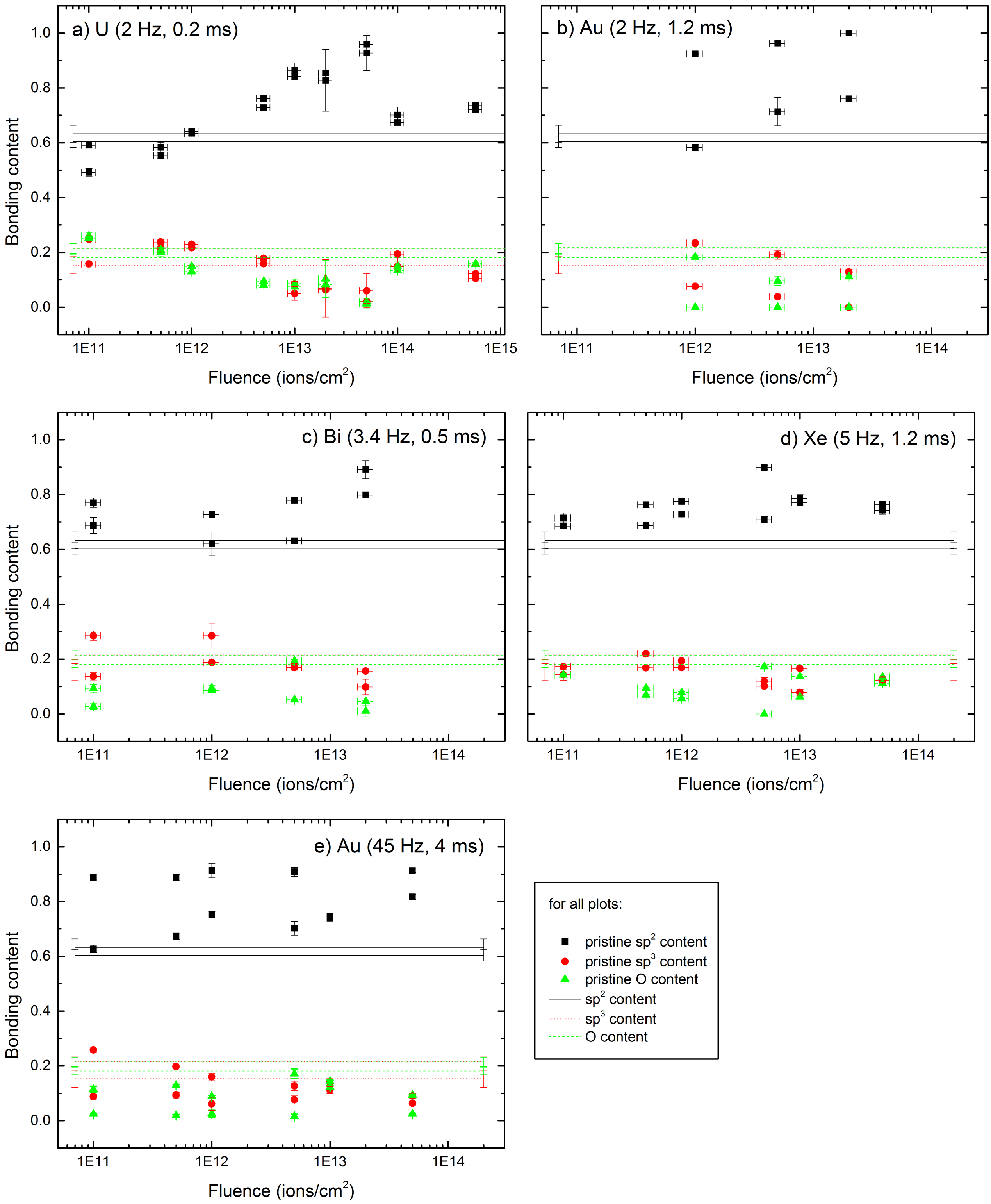

Figure 11.5.8.: sp^2, sp^3 and oxygen (O) bonding content as a function of fluence for 20 µg/cm^2 aC-TL foils irradiated by different ion beams. O bonding content only refers to oxygen bound to carbon in C−O, C=O or O−C=O.

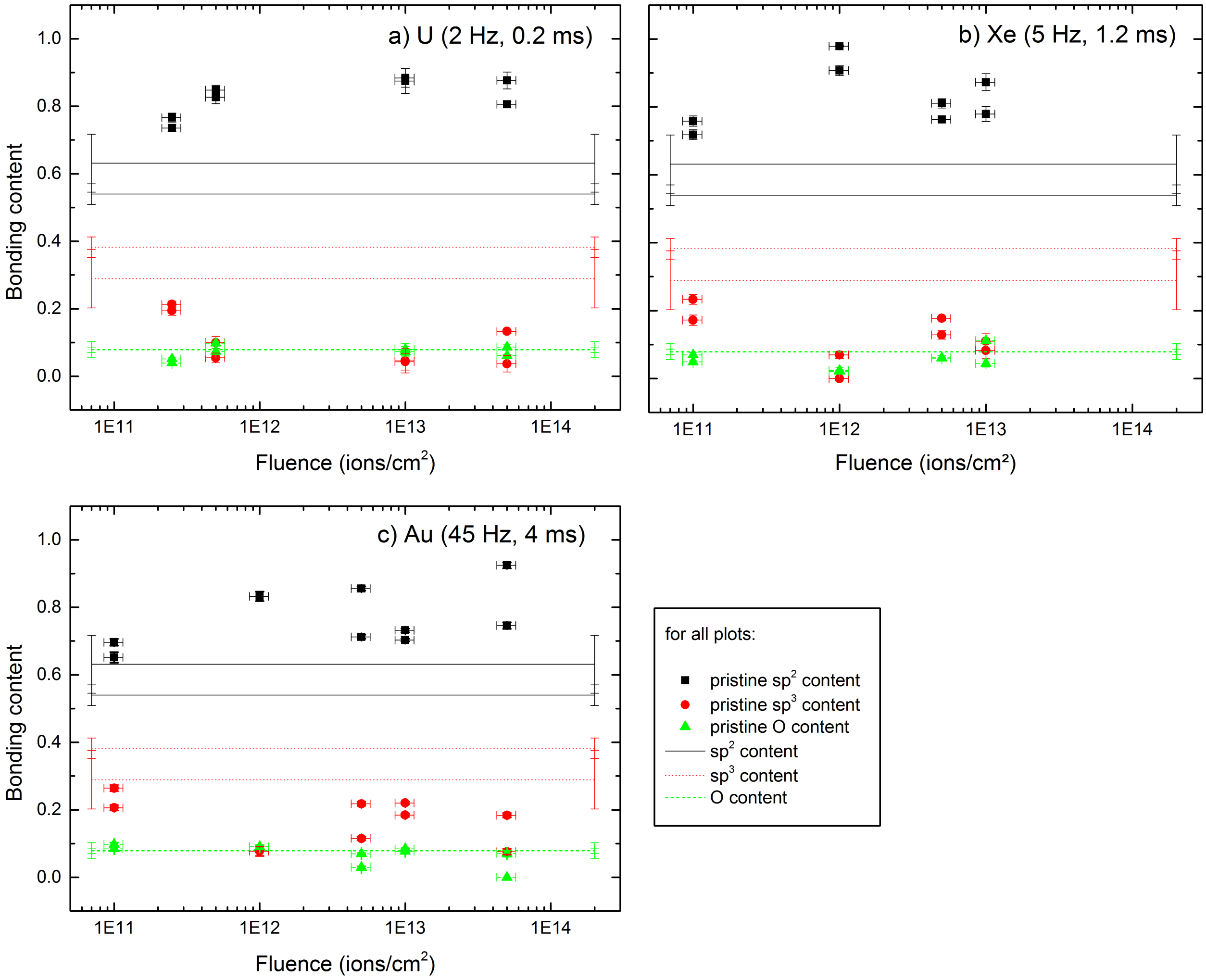

Figure 11.5.9.: sp^2, sp^3 and oxygen (O) bonding content as a function of fluence for 20 μg/cm^2 DLC-MM foils irradiated by different ion beams. O bonding content only refers to oxygen bound to carbon in C−O, C=O or O−C=O.

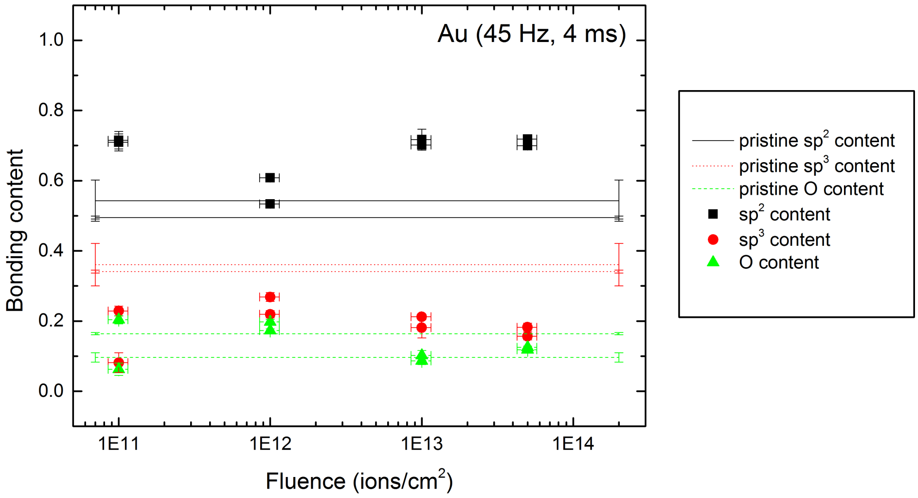

Figure 11.5.10.: sp^2, sp^3 and oxygen (O) bonding content as a function of fluence for 20 μg/cm^2 aC-ACF foils irradiated by 4.8 MeV/u Au beam with 45 Hz. O bonding content only refers to oxygen bound to carbon in C−O, C=O or O−C=O.

Appendix B: MD

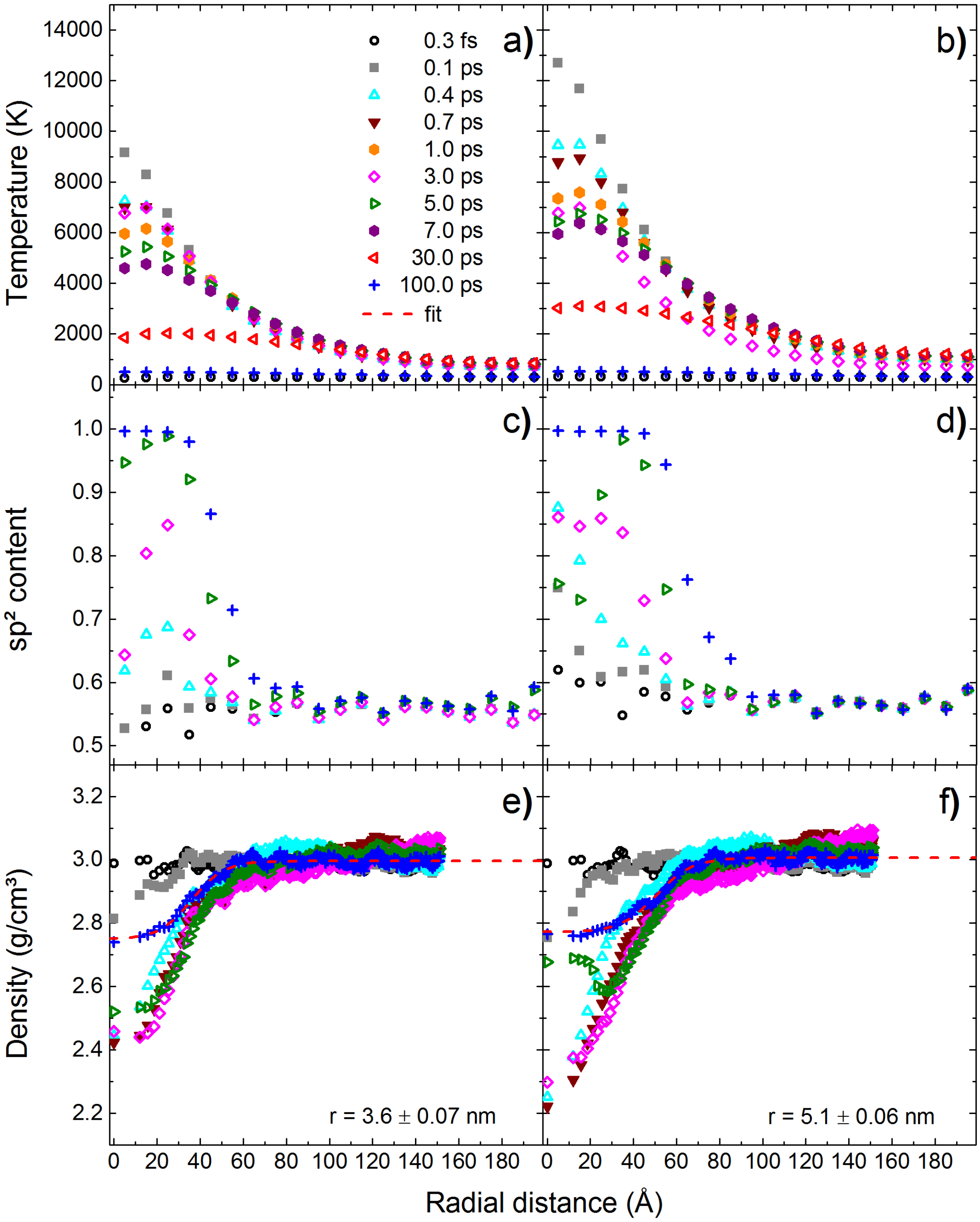

Figure 11.5.11.: Time evolution of temperature, sp^2 content, density as a function of the radial distance from the track center in the plasma deposited amorphous carbon cell produced by the second method (removal of too close neighboring atoms) for 0.7 MeV/u Xe (left: a, c, d) and 4.8 MeV/u U (right: b, d, f) ion impact. Track radii calculated from equation 11.2 are given in e and f.

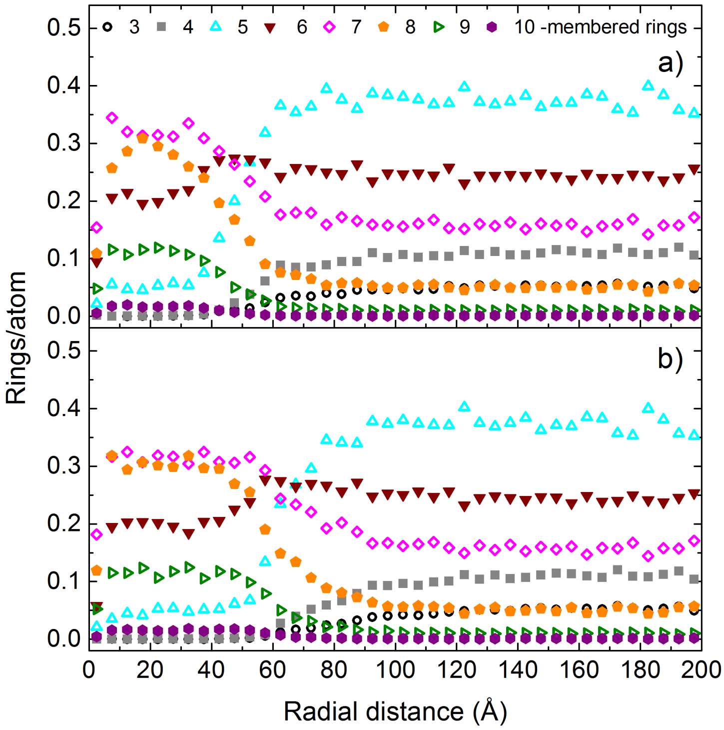

Figure 11.5.12.: Rings per atom as a function of radial distance from track center for the relaxed (100 ps) plasma deposited cell produced by the second method (removal of too close neighboring atoms) for a) 0.7 MeV/u Xe and b) 4.8 MeV/u U ion impact. The term "rings per atom" denotes to the number of shortest rings of a certain size normalized to the total number of shortest rings (atoms) in the corresponding shell.

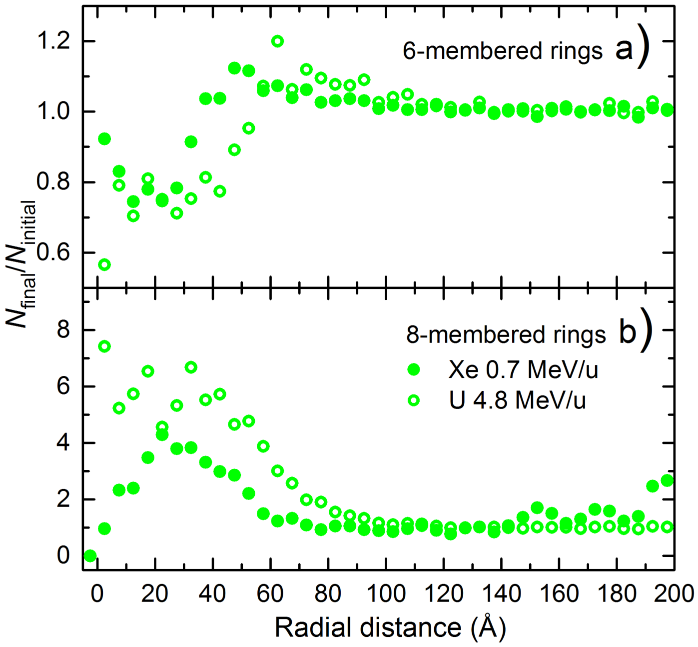

Figure 11.5.13.: Change in the number of occurrences of 6-membered (a) and 8-membered (b) rings per atom as a function of radial distance from the track center in the plasma deposited cell prepared by the second method (removal of too close neighboring atoms). The value is given as the ratio of occurrences in the final simulation frame N_{final} to the initial frame N_{inital}.

Abbrevations

aC	amorphous carbon
aC-TL	amorphous carbon produced at GSI target laboratory
aC-ACF	amorphous carbon from The Arizona Carbon Foil Co., Inc.
AFM	atomic force microscopy
BEI	backscattered electron detector in SEM
BF	bright field
BWF	Breit-Wigner-Fano (function)
CNT	carbon nanotube
CNT-DN	buckypaper foils from Danubia Nanotech
DF	dark-field
DLC	diamond-like carbon
DLC-MM	diamond-like carbon from MICROMATTER^{TM}
DOS	density of states
EDX	energy-dispersive X-ray spectroscopy
EELS	electron energy loss spectroscopy
FAIR	Facility for Antiproton and Ion Research
FFT	fast Fourier transformation
FTIR	Fourier-transform infrared spectroscopy
FWHM	full width at half maximum
GSI	Helmholtz Center for Heavy Ion Research
HOPG	highly oriented pyrolytic graphite
HRTEM	high resolution transmission electron microscopy
IR	infrared
i-TS	inelastic thermal spike
LEI	lower secondary electron detector in SEM
MD	molecular dynamics
mid-IR	mid-wave infrared
RBM	radial breathing mode
SAXS	small angle X-ray scattering

SAED	selected area diffraction
SEI	upper secondary electron detector in SEM
SEM	scanning electron microscopy
SIS100	FAIR heavy ion synchrotron
SIS18	(existing) GSI heavy ion synchrotron
STEM	scanning transmission electron microscopy
SWCNT	single-walled carbon nanotube
t-aC	tetrahedral amorphous carbon
TEM	transmission electron microscopy
UNILAC	Universal Linear Accelerator
VDOS	vibrational density of states
XPS	X-ray photoelectron spectroscopy

List of Figures

List of Tables

Bibliography

[1] GSI Helmholtzzentrum für Schwerionenforschung GmbH Website. https://www.gsi.de/en/start/fair/forschung_an_fair.htm. Accessed 22.05.2016.

[2] Facility for Antiproton and Ion Research in Europe GmbH Website. http://www.fair-center.eu/en/public/what-is-fair/accelerators.html. Accessed 30.11.2015.

[3] H. H. Gutbrot. FAIR baseline technical report. *Gesellschaft für Schwerionenforschung GmbH*, 2006.

[4] APPA Collaboration. Modular start version of the FAIR facility, 17.05.2016.

[5] B. Schlitt, H. Vormann, W. Barth, G. Clemente, L. Groening, M. S. Kaiser, B. Lommel, M. Maier, S. Mickat, and J. Steiner. Charge stripping tests of high current uranium ion beams with methane and hydrogen gas strippers and carbon foils at the GSI UNILAC. *Proceedings of International Particle Accelerator Conference IPAC2013* 3779–3781, 2013.

[6] GSI Helmholtzzentrum für Schwerionenforschung GmbH Website. UNILAC Overview. https://www.gsi.de/work/ fairgsi/linac_operations/linac/unilac/gasstripper.htm. Accessed 22.05.2016.

[7] W. Barth, G. Clemente, L. Dahl, L. Groening, B. Lommel, M. S. Kaiser, M. Maier, S. Mickat, W. Vinzenz, and H. Vormann. High current design U^{40+}-operation in the GSI-UNILAC. *Proceedings of Linear Accelerator Conference LINAC2010*, MOP044:154–156, 2010.

[8] W. Barth, M. S. Kaiser, B. Lommel, M. Maier, S. Mickat, B. Schlitt, J. Steiner, M. Tomut, and H. Vormann. Carbon stripper foils for high current heavy ion operation. *Journal of Radioanalytical and Nuclear Chemistry*, 299(2):1047–1053, 2014.

[9] N. A. Tahir, V. Kim, B. Schlitt, W. Barth, L. Groening, I. V. Lomonosov, A. R. Piriz, T. Stöhlker, and H. Vormann. Three-dimensional thermal simulations of thin solid carbon foils for charge stripping of high current uranium ion beams at a proposed new heavy-ion linac at GSI. *Physical Review Special Topics - Accelerators and Beams*, 17(4):41003, 2014.

[10] H. Hasebe, H. Okuno, H. Kuboki, H. Ryuto, N. Fukunishi, O. Kamigaito, A. Goto, M. Kase, and Y. Yano. Development of long-life carbon stripper foils for uranium ion beams. *Nuclear Instruments and Methods in Physics Research Section A: Accelerators, Spectrometers, Detectors and Associated Equipment*, 613(3):453–456, 2010.

[11] H. Hasebe, H. Kuboki, H. Okuno, I. Yamane, H. Imao, N. Fukunishi, M. Kase, and O. Kamigaito. Development of a new foil compounded from carbon nanotubes and sputter-deposition carbon. *Journal of Radioanalytical and Nuclear Chemistry*, 299(2):1013–1018, 2014.

[12] H. Kuboki, H. Okuno, H. Hasebe, S. Yokouchi, N. Fukunishi, Y. Higurashi, J. Ohnishi, T. Nakagawa, H. Imao, O. Kamigaito, A. Goto, M. Kase, and Y. Yano. Charge-state distribution of ^{238}U in nitrogen gas and carbon foil at 14 and 15 MeV/nucleon. *Physical Review Special Topics - Accelerators and Beams*, 14(5), 2011.

[13] H. Okuno, N. Fukunishi, H. Hasebe, H. Imao, O. Kamigaito, M. Kase, and H. Kuboki. Charge strippers for Radioisotope Beam Factory at RIKEN. *Journal of Radioanalytical and Nuclear Chemistry*, 299(2):945–949, 2014.

[14] I. Sugai, M. Oyaizu, Y. Takeda, H. Kawakami, H. Hattori, and K. Kawasaki. Influence of carbon material and sputtering angle on stripper foil lifetime. *Nuclear Instruments and Methods in Physics Research Section A*, 613(3):448–452, 2010.

[15] I. Sugai, M. Oyaizu, Y. Takeda, H. Kawakami, K. Kawasaki, T. Hattori, and T. Kadono. Lifetime dependence of nitrided carbon stripper foils on sputter angle during N^+ ion beam sputtering. *Nuclear Instruments and Methods in Physics Research Section B: Beam Interactions with Materials and Atoms*, 358:263–270, 2015.

[16] F. Marti, S. Hitchcock, O. K. Kester, and J. C. Oliva. A carbon stripper foil for FRIB. *Proceedings of Linear Accelerator Conference LINAC2010*, TUP105:659–661, 2010.

[17] F. Marti. Heavy ion strippers. *Proceedings of Linear Accelerator Conference LINAC2012*, FR1A01:1050–1054, 2012.

[18] M. A. Plum, S. M. Cousineau, J. Galambos, S. H. Kim, P. Ladd, C. F. Luck, C. C. Peters, Y. Polsky, R. W. Shaw, R. J. Macek, and D. Raparia. Stripper foil failure modes and cures at the Oak Ridge Spallation Neutron Source. *Physical Review Special Topics - Accelerators and Beams*, 14(3), 2011.

[19] V. K. Liechtenstein. Carbon Stripper Foils — Preparation and Quality. In R. Hellborg (ed.), *Electrostatic Accelerators*, Particle Acceleration and Detection 187–191. Springer Berlin Heidelberg, 2005.

[20] H. Okuno, N. Fukunishi, A. Goto, H. Hasebe, H. Imao, O. Kamigaito, M. Kase, H. Kuboki, Y. Yano, S. Yokouchi, and A. Hershcovitch. Low- Z gas stripper as an alternative to carbon foils for the acceleration of high-power uranium beams. *Physical Review Special Topics - Accelerators and Beams*, 14(3), 2011.

[21] H. Okuno. Experience with stripping heavy ion beams. *Proceedings of the 54th ICFA Advanced Beam Dynamics Workshop on High-Intensity, High Brightness and High Power Hadron Beams*, THO1AB02:340–344, 2014.

[22] R. L. Auble, J. K. Bair, D. M. Galbraith, C. M. Jones, P. H. Stelson, and D. C. Weisser. Evaluation of carbon stripper foils for heavy-ion accelerators. *Nuclear Instruments and Methods*, 177(2-3):289–294, 1980.

[23] C. Sofield, L. Bridwell, N. E. B. Cowern, N. R. S. Tait, and D. W. L. Tolfree. The uniformity of carbon stripper foils. *Nuclear Instruments and Methods in Physics Research*, 186(3):505–511, 1981.

[24] D. W. L. Tolfree. A review of recent development work and measurements on carbon stripper foils. *Nuclear Instruments and Methods in Physics Research*, 200(1):15–18, 1982.

[25] I. Sugai, T. Hattori, H. Muto, Y. Takahashi, H. Kato, and K. Yamazaki. Hybrid-type long-lived carbon stripper foils. *Nuclear Instruments and Methods in Physics Research Section A*, 282(1):164–168, 1989.

[26] G. Dollinger and P. Maier-Komor. Carbon stripper foils with isotropic structure for optimum strength against irradiation damage. *Nuclear Instruments and Methods in Physics Research Section B: Beam Interactions with Materials and Atoms*, 53(3):352–354, 1991.

[27] G. Dollinger, P. Maier-Komor, and A. Mitwalsky. Structure investigations of thin carbon foils. *Nuclear Instruments and Methods in Physics Research Section A: Accelerators, Spectrometers, Detectors and Associated Equipment*, 303(1):79–87, 1991.

[28] I. Sugai, M. Oyaizu, T. Hattori, K. Kawasaki, T. Yano, H. Muto, Y. Takahashi, Y. Ishii, F. Hirata, M. Okamura, M. Aratani, M. Yanokura, and K. Yamazaki. Development of heavy ion beam sputtering method for long-lived carbon stripper foils. *Nuclear Instruments and Methods in Physics Research Section A: Accelerators, Spectrometers, Detectors and Associated Equipment*, 320(1-2):15–21, 1992.

[29] H. Muto, M. Oyaizu, I. Sugai, K. Kawasaki, Y. Takahashi, Y. Ishii, Hirata T., and H. Hattori. Development of a highly reproducible mixed ion beam sputtering method for long-lived carbon stripper foils. *Nuclear Instruments and Methods in Physics Research Section B*, 83(1-2):291–294, 1993.

[30] H. Muto, M. Oyaizu, K. Kawasaki, Y. Takahashi, K. Takeuchi, I. Sugai, and T. Hattori. Behaviour of carbon stripper foils prepared by a mixed ion beam sputtering method. *Nuclear Instruments and Methods in Physics Research Section B*, 103(2):249–251, 1995.

[31] V. K. Liechtenstein, T. M. Ivkova, E. D. Olshanski, I. Feigenbaum, R. DiNardo, and M. Döbeli. Preparation and evaluation of thin diamond-like carbon foils for heavy-ion tandem accelerators and time-of-flight spectrometers. *Nuclear Instruments and Methods in Physics Research Section A*, 397(1):140–145, 1997.

[32] V. K. Liechtenstein, T. M. Ivkova, E. D. Olshanski, A. M. Baranov, R. Repnow, R. Hellborg, R. A. Weller, and H. L. Wirth. Preparation and comparative testing of advanced diamond-like carbon foils for tandem accelerators and time-of-flight spectrometers. *Nuclear Instruments and Methods in Physics Research Section A*, 438(1):79–85, 1999.

[33] V. K. Liechtenstein, T. M. Ivkova, E. D. Olshanski, R. Repnow, J. Levin, R. Hellborg, P. Persson, and T. Schenkel. Advances in targetry with thin diamond-like carbon foils. *Nuclear Instruments and Methods in Physics Research Section A*, 480(1):185–190, 2002.

[34] I. Sugai, Y. Takeda, M. Oyaizu, H. Kawakami, Y. Hattori, K. Kawasaki, K. Yoshida, and A. Itoh. Lifetime improvement of nitrided carbon stripper foils by ion-beam sputtering with a binary gas mixture. *Nuclear Instruments and Methods in Physics Research Section A: Accelerators, Spectrometers, Detectors and Associated Equipment*, 521(1):187–191, 2004.

[35] H. Muto. Surface behavior of thin carbon stripper foils under ion beam bombardment. *Revista mexicana de fisica*, 47(3):242–244, 2001.

[36] I. Sugai, Y. Takeda, M. Oyaizu, H. Kawakami, Y. Hattori, K. Kawasaki, and N. Hayashizaki. Test preparation and lifetime measurement of very thin carbon stripper foils made by a controlled DC arc-discharge method. *Nuclear Instruments and Methods in Physics Research Section A*, 480(1):191–193, 2002.

[37] I. Sugai, Y. Takeda, M. Oyaizu, H. Kawakami, Y. Irie, Y. Arakida, K. Hara, H. Hattori, K. Kawasaki, J. Kamiya, M. Kinsho, and K. Kuramochi. Development of thick hybrid-type carbon stripper foils with high durability at 1800K for RCS of J-PARC. *Nuclear Instruments and Methods in Physics Research Section A: Accelerators, Spectrometers, Detectors and Associated Equipment*, 561(1):16–23, 2006.

[38] P. Maier-Komor, G. Dollinger, and R. Krücken. Preparation and investigation of thick carbon foils prepared by laser plasma ablation deposition. *Nuclear Instruments and Methods in Physics Research Section A: Accelerators, Spectrometers, Detectors and Associated Equipment*, 561(1):4–10, 2006.

[39] K. v. Reden, M. Zhang, M. Meigs, E. Sichel, S. Fang, and R. H. Baughman. Carbon nanotube foils for electron stripping in tandem accelerators. *Nuclear Instruments and Methods in Physics Research Section B*, 261(1-2):44–48, 2007.

[40] H. Hasebe, H. Ryuto, N. Fukunishi, A. Goto, M. Kase, and Y. Yano. Polymer coating method developed for carbon stripper foils. *Nuclear Instruments and Methods in Physics Research Section A: Accelerators, Spectrometers, Detectors and Associated Equipment*, 590(1-3):13–17, 2008.

[41] I. Sugai, M. Oyaizu, Y. Takeda, H. Kawakami, T. Hattori, and K. Kawasaki. Measurement of carbon sputtering yield by N+ ion beam and lifetime dependence of resulting foils on thickness. *Nuclear Instruments and Methods in Physics Research Section A: Accelerators, Spectrometers, Detectors and Associated Equipment*, 590(1-3):37–42, 2008.

[42] I. Sugai, M. Oyaizu, Y. Takeda, H. Kawakami, T. Hattori, and K. Kawasaki. Suppression of carbon buildup and lifetime improvement by heating carbon stripper foils. *Nuclear Instruments and Methods in Physics Research Section B: Beam Interactions with Materials and Atoms*, 269(3):223–228, 2011.

[43] I. Sugai, M. Oyaizu, Y. Takeda, H. Kawakami, K. Kawasaki, T. Hattori, and T. Kadono. Sputtering angle effects by Kr mixing in N+ ion beam on the lifetime of nitrided carbon stripper foils. *Journal of Radioanalytical and Nuclear Chemistry*, 299(2):1023–1028, 2014.

[44] Y. Yamazaki, M. Yoshimoto, P. K. Saha, M. Kinsho, T. Taguchi, S. Yamamoto, and I. Sugai. Analyses and the effect of impurities contained in charge stripper foils for the 3-GeV RCS of J-PARC. *Journal of Radioanalytical and Nuclear Chemistry*, 305(3):859–864, 2015.

[45] B. Lommel, W. Hartmann, B. Kindler, J. Klemm, and J. Steiner. Preparation of self-supporting carbon thin films. *Nuclear Instruments and Methods in Physics Research Section A: Accelerators, Spectrometers, Detectors and Associated Equipment*, 480(1):199–203, 2002.

[46] G. Dollinger and P. Maier-Komor. Structure studies of carbon foils with the aim to improve the ability for heavy-ion stripping. *Nuclear Instruments and Methods in Physics Research Section A: Accelerators, Spectrometers, Detectors and Associated Equipment*, 257(1):64–68, 1987.

[47] S. K. Zeisler and V. Jaggi. Production of stripper foils by laser ablation of carbon–boron sputter targets. *Nuclear Instruments and Methods in Physics Research Section A: Accelerators, Spectrometers, Detectors and Associated Equipment*, 613(3):434–435, 2010.

[48] C. S. Jolivet and J. O. Stoner. Mounting stripper foils on forks for maximum lifetime. *Nuclear Instruments and Methods in Physics Research Section A*, 590(1-3):51–56, 2008.

[49] H. Hasebe, H. Okuno, H. Kuboki, H. Imao, N. Fukunishi, M. Kase, and O. Kamigaito. Development of rotating beryllium disk stripper. *Journal of Radioanalytical and Nuclear Chemistry*, 305(3):825–829, 2015.

[50] A. Takagi, I. Sugai, Y. Irie, and Y. Takeda. Temperature measurements of carbon stripper foil by pulsed 650 keV H- ion beam. In *Proceedings of European Particle Accelerator Conference EPAC2008*. 2008.

[51] G. Dollinger and P. Maier-Komor. Heavy-ion irradiation damage in carbon stripper foils. *Nuclear Instruments and Methods in Physics Research Section A: Accelerators, Spectrometers, Detectors and Associated Equipment*, 282(1):223–235, 1989.

[52] G. Frick, V. Chaki, B. Heusch, C. Ricaud, P. Wagner, and E. Baron. Stripping experiments in carbon foils with heavy ions in the energy range of 0.4-0.9 meV/a. *Revue de Physique Appliquée (Paris)*, 12(10):1525–1533, 1977.

[53] R. Auble and D. Galbraith. Lifetime Measurements on Carbon Stripper Foils. *Paper to be presented at the International Target Conference*, Boston, 1979.

[54] P. Maier-Komor, G. Dollinger, and E. Hammann. Thickness calibration of carbon foils. *Nuclear Instruments and Methods in Physics Research Section A: Accelerators, Spectrometers, Detectors and Associated Equipment*, 303(1):88–93, 1991.

[55] J. O. Stoner. Densities of carbon foils. *Nuclear Instruments and Methods in Physics Research Section A: Accelerators, Spectrometers, Detectors and Associated Equipment*, 303(1):94–98, 1991.

[56] U. Sander and H. H. Bukow. Study of crystallo graphic transformation of carbon foils under ion irradiation. *Radiation Effects*, 40(3):143–150, 1979.

[57] E. Ranzinger, P. Maier-Komor, H. Maier, and H. Münzer. Tests of specially treated carbon stripper foils under heavy ion bombardment. *Nuclear Instruments and Methods*, 184(1):211–214, 1981.

[58] P. Maier-Komor, E. Ranzinger, and H. Münzer. Laser treated carbon stripper foils. *Nuclear Instruments and Methods in Physics Research*, 200(1):5–11, 1982.

[59] Ziegler J. F., Biersack J. P. , Littmark U. *The stopping and range of ions in solids*, volume 1. Pergamon Press, New York, 1985.

[60] P. Sigmund. *Stopping of heavy ions: A theoretical approach*, volume 204 of *Springer tracts in modern physics Atomic physics*. Springer, Berlin, 2004.

[61] J. F. Ziegler and J. P. Biersack. SRIM-2013: Stopping and Range in Matter, 2013.

[62] P. Sigmund. Stopping of swift heavy ions: Solved and unsolved problems. In P. Sigmund (ed.), *Ion beam science*, volume 1 of *Matematisk-fysiske meddelelser* 557–593. Det Kongelige Danske Videnskabernes Selskab, Copenhagen, 2006.

[63] N. Bohr. On the constitution of atoms and molecules. *Philosophical Magazine Series 6*, 26(151):1–25, 1913.

[64] H. Bethe. Zur Theorie des Durchgangs schneller Korpuskularstrahlen durch Materie. *Annalen der Physik*, 397(3):325–400, 1930.

[65] F. Bloch. Zur Bremsung rasch bewegter Teilchen beim Durchgang durch Materie. *Annalen der Physik*, 408(3):285–320, 1933.

[66] F. Bloch. Bremsvermögen von Atomen mit mehreren Elektronen. *Z. Physik (Zeitschrift für Physik)*, 81(5-6):363–376, 1933.

[67] R. Spohr. *Ion Tracks and Microtechnology: Principles and Applications*. Vieweg+Teubner Verlag, Wiesbaden, 1990.

[68] P. Sigmund. *Particle penetration and radiation effects: General aspects and stopping of swift point charges*, volume 151 of *Springer series in solid-state sciences*. Springer, Berlin and New York, 2008.

[69] N. Bohr. Scattering and Stopping of Fission Fragments. *Physical Review*, 58(7):654–655, 1940.

[70] N. Bohr. Velocity-Range Relation for Fission Fragments. *Physical Review*, 59(3):270–275, 1941.

[71] J. F. Ziegler. Stopping of energetic light ions in elemental matter. *Journal of Applied Physics*, 85(3):1249, 1999.

[72] J. Lindhard. *Range concepts and heavy ion ranges: (Notes on atomic collisions, II)*, volume 33 of *Det Kgl. Danske videnskabernes selskab, Copenhagen. Matematiskfysiske meddelelser*. Munksgaard, København, 1963.

[73] A. Meftah, F. Brisard, J. M. Costantini, M. Hage-Ali, J. P. Stoquert, F. Studer, and M. Toulemonde. Swift heavy ions in magnetic insulators: A damage-cross-section velocity effect. *Physical Review B*, 48(2):920–925, 1993.

[74] M. P. R. Waligórski, R. N. Hamm, and R. Katz. The radial distribution of dose around the path of a heavy ion in liquid water. *International Journal of Radiation Applications and Instrumentation. Part D. Nuclear Tracks and Radiation Measurements*, 11(6):309–319, 1986.

[75] B. Gervais and S. Bouffard. Simulation of the primary stage of the interaction of swift heavy ions with condensed matter. *Nuclear Instruments and Methods in Physics Research Section B: Beam Interactions with Materials and Atoms*, 88(4):355–364, 1994.

[76] R. L. Fleischer, P. B. Price, and R. M. Walker. Ion Explosion Spike Mechanism for Formation of Charged-Particle Tracks in Solids. *Journal of Applied Physics*, 36(11):3645, 1965.

[77] F. Dessauer. Über einige Wirkungen von Strahlen. I. *Z. Physik (Zeitschrift für Physik)*, 12(1):38–47, 1923.

[78] M. Toulemonde, C. Dufour, and E. Paumier. Transient thermal process after a high-energy heavy-ion irradiation of amorphous metals and semiconductors. *Physical Review B*, 46(22):14362–14369, 1992.

[79] M. Toulemonde, E. Paumier, and C. Dufour. Thermal spike model in the electronic stopping power regime. *Radiation Effects and Defects in Solids*, 126(1):201–206, 1993.

[80] M. Toulemonde, J. M. Costantini, C. Dufour, A. Meftah, E. Paumier, and F. Studer. Track creation in SiO_2 and $BaFe_{12}O_{19}$ by swift heavy ions: a thermal spike description. *Nuclear Instruments and Methods in Physics Research Section B: Beam Interactions with Materials and Atoms*, 116(1-4):37–42, 1996.

[81] A. Meftah, J. M. Costantini, N. Khalfaoui, S. Boudjadar, J. P. Stoquert, F. Studer, and M. Toulemonde. Experimental determination of track cross-section in $Gd_3Ga_5O_{12}$ and comparison to the inelastic thermal spike model applied to several materials. *Nuclear Instruments and Methods in Physics Research Section B: Beam Interactions with Materials and Atoms*, 237(3-4):563–574, 2005.

[82] M. Caron, H. Rothard, M. Toulemonde, B. Gervais, and M. Beuve. Theoretical and experimental study of electronic temperatures in heavy ion tracks from Auger electron spectra and thermal spike calculations. *Nuclear Instruments and Methods in Physics Research Section B: Beam Interactions with Materials and Atoms*, 245(1):36–40, 2006.

[83] C. Rotaru, F. Pawlak, N. Khalfaoui, C. Dufour, J. Perrière, A. Laurent, J. Stoquert, H. Lebius, and M. Toulemonde. Track formation in two amorphous insulators, vitreous silica and diamond like carbon: Experimental observations and description by the inelastic thermal spike model. *Nuclear Instruments and Methods in Physics Research Section B: Beam Interactions with Materials and Atoms*, 272:9–14, 2012.

[84] M. Toulemonde, W. Assmann, C. Dufour, A. Meftah, and C. Trautmann. Nanometric transformation of the matter by short and intense electronic excitation: Experimental data versus inelastic thermal spike model. *Nuclear Instruments and Methods in Physics Research Section B: Beam Interactions with Materials and Atoms*, 277:28–39, 2012.

[85] M. Toulemonde, W. Assmann, C. Dufour, A. Meftah, F. Studer, and C. Trautmann. Experimental phenomena and thermal spike model description of ion tracks in amorphizable inorganic insulators. In P. Sigmund (ed.), *Ion beam science*, Matematisk-fysiske meddelelser. Det Kongelige Danske Videnskabernes Selskab, Copenhagen, 2006.

[86] M. Lang, R. Devanathan, M. Toulemonde, and C. Trautmann. Advances in understanding of swift heavy-ion tracks in complex ceramics. *Current Opinion in Solid State and Materials Science*, 19(1):39–48, 2015.

[87] O. H. Pakarinen, F. Djurabekova, K. Nordlund, P. Kluth, and M. C. Ridgway. Molecular dynamics simulations of the structure of latent tracks in quartz and amorphous SiO_2. *Nuclear Instruments and Methods in Physics Research Section B: Beam Interactions with Materials and Atoms*, 267(8-9):1456–1459, 2009.

[88] M. Nič, J. Jirát, B. Košata, A. Jenkins, and A. McNaught (eds.). *IUPAC Compendium of Chemical Terminology: Amorphous Carbon*. IUPAC, Research Triagle Park, NC, 2009.

[89] J. Robertson. Diamond-like amorphous carbon. *Materials Science and Engineering: R: Reports*, 37(4-6):129–281, 2002.

[90] J. Robertson. Amorphous carbon. *Advances in Physics*, 35(4):317–374, 1986.

[91] D. R. McKenzie. Tetrahedral bonding in amorphous carbon. *Reports on Progress in Physics*, 59(12):1611–1664, 1996.

[92] A. Grill. Diamond-like carbon: State of the art. *Diamond and Related Materials*, 8(2-5):428–434, 1999.

[93] S. Xu, D. Flynn, B. K. Tay, S. Prawer, K. W. Nugent, S. R. P. Silva, Y. Lifshitz, and W. I. Milne. Mechanical properties and Raman spectra of tetrahedral amorphous carbon films with high sp 3 fraction deposited using a filtered cathodic arc. *Philosophical Magazine Part B*, 76(3):351–361, 1997.

[94] S. Xu, B. K. Tay, H. S. Tan, L. Zhong, Y. Q. Tu, S. R. P. Silva, and W. I. Milne. Properties of carbon ion deposited tetrahedral amorphous carbon films as a function of ion energy. *Journal of Applied Physics*, 79(9):7234, 1996.

[95] D. Schneider, C. Meyer, H. Mai, B. Schöneich, H. Ziegele, H. Scheibe, and Y. Lifshitz. Non-destructive characterization of mechanical and structural properties of amorphous diamond-like carbon films. *Diamond and Related Materials*, 7(7):973–980, 1998.

[96] V. M. Elinson, V. V. Sleptsov, A. N. Laymin, V. V. Potraysay, L. N. Kostuychenko, and A. D. Moussina. Barrier properties of carbon films deposited on polymer-based devices in aggressive environments. *Diamond and Related Materials*, 8(12):2103–2109, 1999.

[97] D. Dasgupta, F. Demichelis, and A. Tagliaferro. Electrical conductivity of amorphous carbon and amorphous hydrogenated carbon. *Philosophical Magazine Part B,* 63(6):1255–1266, 1991.

[98] P. J. Fallon, V. S. Veerasamy, C. A. Davis, J. Robertson, G. A. J. Amaratunga, W. I. Milne, and J. Koskinen. Properties of filtered-ion-beam-deposited diamondlike carbon as a function of ion energy. *Physical Review B*, 48(7):4777–4782, 1993.

[99] Y. Lifshitz. Diamond-like carbon — present status. *Diamond and Related Materials*, 8(8-9):1659–1676, 1999.

[100] R. Lossy, D. L. Pappas, R. A. Roy, J. P. Doyle, J. J. Cuomo, and J. Bruley. Properties of amorphous diamond films prepared by a filtered cathodic arc. *Journal of Applied Physics*, 77(9):4750, 1995.

[101] D. G. McCulloch, E. G. Gerstner, D. R. McKenzie, S. Prawer, and R. Kalish. Ion implantation in tetrahedral amorphous carbon. *Physical Review B*, 52(2):850–857, 1995.

[102] D. McKenzie, D. Muller, and B. Pailthorpe. Compressive-stress-induced formation of thin-film tetrahedral amorphous carbon. *Physical Review Letters*, 67(6):773–776, 1991.

[103] K. Honglertkongsakul, P. W. May, and B. Paosawatyanyong. Electrical and optical properties of diamond-like carbon films deposited by pulsed laser ablation. *Diamond and Related Materials*, 19(7-9):999–1002, 2010.

[104] N. H. Cho, D. K. Veirs, J. W. Ager, M. D. Rubin, C. B. Hopper, and D. B. Bogy. Effects of substrate temperature on chemical structure of amorphous carbon films. *Journal of Applied Physics*, 71(5):2243, 1992.

[105] C. Gao, Y. Wang, A. Ritter, and J. Dennison. Nature of Carbon-Carbon Bonding in Evaporated and Ion-Sputtered (Diamondlike) Amorphous Carbon from (e, 2e) Spectroscopy. *Physical Review Letters*, 62(8):945–948, 1989.

[106] P. K. Chu and L. Li. Characterization of amorphous and nanocrystalline carbon films. *Materials Chemistry and Physics*, 96(2-3):253–277, 2006.

[107] J. Robertson and E. O'Reilly. Electronic and atomic structure of amorphous carbon. *Physical Review B*, 35(6):2946–2957, 1987.

[108] C. T. Chen and F. Sette. High Resolution Soft X-Ray Spectroscopies with the Dragon Beamline. *Physica Scripta*, T31:119–126, 1990.

[109] S. Y. Leung, M. S. Dresselhaus, and G. Dresselhaus. Infrared and Raman spectroscopy of graphite intercalation compounds. *Physica B+C*, 105(1-3):375–380, 1981.

[110] A. Ferrari and J. Robertson. Interpretation of Raman spectra of disordered and amorphous carbon. *Physical Review B*, 61(20):14095–14107, 2000.

[111] R. Dillon, J. Woollam, and V. Katkanant. Use of Raman scattering to investigate disorder and crystallite formation in as-deposited and annealed carbon films. *Physical Review B*, 29(6):3482–3489, 1984.

[112] D. McCulloch, J. Peng, D. McKenzie, S. Lau, D. Sheeja, and B. Tay. Mechanisms for the behavior of carbon films during annealing. *Physical Review B*, 70(8), 2004.

[113] O. R. Monteiro, J. W. Ager, D. H. Lee, R. Yu Lo, K. C. Walter, and M. Nastasi. Annealing of nonhydrogenated amorphous carbon films prepared by filtered cathodic arc deposition. *Journal of Applied Physics*, 88(5):2395, 2000.

[114] N. Xu, S. H. Tsang, E. H. T. Teo, X. Wang, C. M. Ng, and B. K. Tay. Effect of initial sp^3 content on bonding structure evolution of amorphous carbon upon pulsed laser annealing. *Diamond and Related Materials*, 30:48–52, 2012.

[115] T. Roch, A. Lasagni, and E. Beyer. Nanosecond UV laser graphitization and delamination of thin tetrahedral amorphous carbon films with different sp^3/sp^2 content. *Thin Solid Films*, 519(11):3756–3761, 2011.

[116] N. Wada, P. J. Gaczi, and S. A. Solin. "Diamond-like" 3-fold coordinated amorphous carbon. *Journal of Non-Crystalline Solids*, 35-36:543–548, 1980.

[117] Q. Wu, L. Yu, Y. Ma, Y. Liao, R. Fang, L. Zhang, X. Chen, and K. Wang. Raman investigation of amorphous carbon in diamond film treated by laser. *Journal of Applied Physics*, 93(1):94, 2003.

[118] D. Wesner, S. Krummacher, R. Carr, T. K. Sham, M. Strongin, W. Eberhardt, S. L. Weng, G. Williams, M. Howells, F. Kampas, S. Heald, and F. W. Smith. Synchrotron-radiation studies of the transition of hydrogenated amorphous carbon to graphitic carbon. *Physical Review B*, 28(4):2152–2156, 1983.

[119] J. Roth, A. Kirschner, W. Bohmeyer, S. Brezinsek, A. Cambe, E. Casarotto, R. Doerner, E. Gauthier, G. Federici, S. Higashijima, J. Hogan, A. Kallenbach, H. Kubo, J. M. Layet, T. Nakano, V. Philipps, A. Pospieszczyk, R. Preuss, R. Pugno, R. Ruggiéri, B. Schweer, G. Sergienko, and M. Stamp. Flux dependence of carbon erosion and implication for ITER. *Journal of Nuclear Materials*, 337-339:970–974, 2005.

[120] F. Pawlak, C. Dufour, A. Laurent, E. Paumier, J. Perriere, J. P. Stoquert, and M. Toulemonde. Amorphous deuterated carbon films irradiated by swift heavy ions: Infrared measurements and ion beam analysis. *Nuclear Instruments and Methods in Physics Research Section B: Beam Interactions with Materials and Atoms*, 131(1-4):135–140, 1997.

[121] F. Pawlak, C. Dufour, A. Laurent, E. Paumier, J. Perrière, J. P. Stoquert, and M. Toulemonde. Carbon sputtering of polymer-like amorphous carbon by swift heavy ions. *Nuclear Instruments and Methods in Physics Research Section B: Beam Interactions with Materials and Atoms*, 151(1-4):140–145, 1999.

[122] M. J. Paterson, K. G. Orrman-Rossiter, S. Bhargava, and A. Hoffman. Physico-chemical changes in a-C: H by MeV He ion irradiation. *Journal of Applied Physics*, 75(2):792, 1994.

[123] M. Waiblinger, C. Sommerhalter, B. Pietzak, J. Krauser, B. Mertesacker, M. Lux-Steiner, S. Klaumünzer, A. Weidinger, C. Ronning, and H. Hofsäß. Electrically conducting ion tracks in diamond-like carbon films for field emission. *Applied Physics A: Materials Science & Processing*, 69(2):239–240, 1999.

[124] J. Krauser, J.-H. Zollondz, A. Weidinger, and C. Trautmann. Conductivity of nanometer-sized ion tracks in diamond-like carbon films. *Journal of Applied Physics*, 94(3):1959, 2003.

[125] J.-H. Zollondz, J. Krauser, A. Weidinger, C. Trautmann, D. Schwen, C. Ronning, H. Hofsaess, and B. Schultrich. Conductivity of ion tracks in diamond-like carbon films. *Diamond and Related Materials*, 12(3-7):938–941, 2003.

[126] J.-H. Zollondz, D. Schwen, A.-K. Nix, C. Trautmann, J. Berthold, J. Krauser, and H. Hofsäss. Conductive nanoscopic ion-tracks in diamond-like-carbon. *Materials Science and Engineering: C*, 26(5-7):1171–1174, 2006.

[127] D. Schwen. *Structural and electronic properties of swift heavy ion tracks in amorphous carbon: PhD Thesis*. Georg-August-Universität zu Göttingen, 2007.

[128] J. Krauser, A.-K. Nix, H.-G. Gehrke, H. Hofsäss, C. Trautmann, and A. Weidinger. Highly conductive ion tracks in tetrahedral amorphous carbon by irradiation with 30 MeV C_{60} projectiles. *New Journal of Physics*, 13(8):83023, 2011.

[129] D. Schwen, E. Bringa, J. Krauser, A. Weidinger, C. Trautmann, and H. Hofsäss. Nano-hillock formation in diamond-like carbon induced by swift heavy projectiles in the electronic stopping regime: Experiments and atomistic simulations. *Applied Physics Letters*, 101(11):113115, 2012.

[130] D. Schwen, C. Ronning, and H. Hofsäss. Field emission studies on swift heavy ion irradiated tetrahedral amorphous carbon. *Diamond and Related Materials*, 13(4-8):1032–1036, 2004.

[131] A.-K. Nix. *Swift heavy ion irradiation of semiconducting materials - defect production, phase transformation and annealing: PhD Thesis*. Georg-August-Universität zu Göttingen, 2010.

[132] Q. Wei, A. Sharma, J. Sankar, and J. Narayan. Mechanical properties of diamond-like carbon composite thin films prepared by pulsed laser deposition. *Composites Part B: Engineering*, 30(7):675–684, 1999.

[133] C. A. Schneider, W. S. Rasband, and K. W. Eliceiri. NIH Image to ImageJ: 25 years of image analysis. *Nature Methods*, 9(7):671–675, 2012.

[134] H. Stöcker (ed.). *Taschenbuch der Physik: Formeln, Tabellen, Übersichten*. Deutsch, Frankfurt am Main, 2005.

[135] F. C. Marques, R. G. Lacerda, A. Champi, V. Stolojan, D. C. Cox, and S. R. P. Silva. Thermal expansion coefficient of hydrogenated amorphous carbon. *Applied Physics Letters*, 83(15):3099, 2003.

[136] J. Díaz, G. Paolicelli, S. Ferrer, and F. Comin. Separation of the sp^3 and sp^2 components in the C 1s photoemission spectra of amorphous carbon films. *Physical Review B*, 54(11):8064–8069, 1996.

[137] J. Morar, F. Himpsel, G. Hollinger, J. Jordon, G. Hughes, and F. McFeely. C 1s excitation studies of diamond (111). II. Unoccupied surface states. *Physical Review B*, 33(2):1346–1349, 1986.

[138] P. Mérel, M. Tabbal, M. Chaker, S. Moisa, and J. Margot. Direct evaluation of the sp^3 content in diamond-like-carbon films by XPS. *Applied Surface Science*, 136(1-2):105–110, 1998.

[139] T. Leung, W. Man, P. Lim, W. Chan, F. Gaspari, and S. Zukotynski. Determination of the sp^3/sp^2 ratio of a-C:H by XPS and XAES. *Journal of Non-Crystalline Solids*, 254(1-3):156–160, 1999.

[140] J. W. Suk, S. Murali, J. An, and R. S. Ruoff. Mechanical measurements of ultra-thin amorphous carbon membranes using scanning atomic force microscopy. *Carbon*, 50(6):2220–2225, 2012.

[141] D. A. Shirley. High-Resolution X-Ray Photoemission Spectrum of the Valence Bands of Gold. *Physical Review B*, 5(12):4709–4714, 1972.

[142] J. M. Walls and R. Smith. *Surface Science Techniques*. Elsevier Science, Burlington, 1994.

[143] R. Haerle, E. Riedo, A. Pasquarello, and A. Baldereschi. sp^2/sp^3 hybridization ratio in amorphous carbon from C 1s core-level shifts: X-ray photoelectron spectroscopy and first-principles calculation. *Physical Review B*, 65(4), 2001.

[144] S. Doniach and M. Sunjic. Many-electron singularity in X-ray photoemission and X-ray line spectra from metals. *Journal of Physics C: Solid State Physics*, 3(2):285–291, 1970.

[145] S. Jackson. Determining hybridization differences for amorphous carbon from the XPS C 1s envelope. *Applied Surface Science*, 90(2):195–203, 1995.

[146] M. Wojdyr. Fityk: A general-purpose peak fitting program. *Journal of Applied Crystallography*, 43(5):1126–1128, 2010.

[147] J. Dubessy. *Applications of Raman Spectroscopy to Earth Sciences and Cultural Heritage: University textbook*, volume 12 of *EMU notes in mineralogy*. EMU, London, 2012.

[148] A. C. Ferrari and J. Robertson. Raman spectroscopy of amorphous, nanostructured, diamond-like carbon, and nanodiamond. *Philosophical Transactions of the Royal Society A: Mathematical, Physical and Engineering Sciences*, 362(1824):2477–2512, 2004.

[149] F. Tuinstra. Raman Spectrum of Graphite. *The Journal of Chemical Physics*, 53(3):1126, 1970.

[150] M. S. Dresselhaus, G. Dresselhaus, R. Saito, and A. Jorio. Raman spectroscopy of carbon nanotubes. *Physics Reports*, 409(2):47–99, 2005.

[151] S. Logothetidis. Hydrogen-free amorphous carbon films approaching diamond prepared by magnetron sputtering. *Applied Physics Letters*, 69(2):158, 1996.

[152] J. Birrell, J. E. Gerbi, O. Auciello, J. M. Gibson, J. Johnson, and J. A. Carlisle. Interpretation of the Raman spectra of ultrananocrystalline diamond. *Diamond and Related Materials*, 14(1):86–92, 2005.

[153] N. P. Ivleva, A. Messerer, X. Yang, R. Niessner, and U. Pöschl. Raman Microspectroscopic Analysis of Changes in the Chemical Structure and Reactivity of Soot in a Diesel Exhaust Aftertreatment Model System. *Environmental Science & Technology*, 41(10):3702–3707, 2007.

[154] J. Filik. Raman Spectroscopy: A Simple, Non-Destructive way to Characterise Diamond and Diamond-Like Materials. *Spectroscopy Europe*, 17(5):10–17, 2005.

[155] F. Piazza, A. Golanski, S. Schulze, and G. Relihan. Transpolyacetylene chains in hydrogenated amorphous carbon films free of nanocrystalline diamond. *Applied Physics Letters*, 82(3):358, 2003.

[156] R. N. Tiwari and L. Chang. Growth, microstructure, and field-emission properties of synthesized diamond film on adamantane-coated silicon substrate by microwave plasma chemical vapor deposition. *Journal of Applied Physics*, 107(10):103305, 2010.

[157] D. McCulloch, S. Prawer, and A. Hoffman. Structural investigation of xenon-ion-beam-irradiated glassy carbon. *Physical Review B*, 50(9):5905–5917, 1994.

[158] D. G. McCulloch and S. Prawer. The effect of annealing and implantation temperature on the structure of C ion-beam-irradiated glassy carbon. *Journal of Applied Physics*, 78(5):3040, 1995.

[159] C. Adelhelm, M. Balden, M. Rinke, and M. Stueber. Influence of doping (Ti, V, Zr, W) and annealing on the sp^2 carbon structure of amorphous carbon films. *Journal of Applied Physics*, 105(3):33522, 2009.

[160] P. Lespade, A. Marchand, M. Couzi, and F. Cruege. Caracterisation de materiaux carbones par microspectrometrie Raman. *Carbon*, 22(4-5):375–385, 1984.

[161] M. Hulman, V. Skákalová, S. Roth, and H. Kuzmany. Raman spectroscopy of single-wall carbon nanotubes and graphite irradiated by gamma rays. *Journal of Applied Physics*, 98(2):24311, 2005.

[162] G. Abrasonis, R. Gago, M. Vinnichenko, U. Kreissig, A. Kolitsch, and W. Möller. Sixfold ring clustering in sp^2-dominated carbon and carbon nitride thin films: A Raman spectroscopy study. *Physical Review B*, 73(12), 2006.

[163] J. F. Gibbons. Ion implantation in semiconductors-Part II: Damage production and annealing. *Proceedings of the IEEE*, 60(9):1062–1096, 1972.

[164] W. J. Weber and N. J. Hess. Ion beam modification of $Gd_2Ti_2O_7$. *Nuclear Instruments and Methods in Physics Research Section B: Beam Interactions with Materials and Atoms*, 80-81:1245–1248, 1993.

[165] G. Kirchhoff. Ueber das Verhältniss zwischen dem Emissionsvermögen und dem Absorptionsvermögen der Körper für Wärme und Licht. *Annalen der Physik und Chemie*, 185(2):275–301, 1860.

[166] R. J. Nemanich, G. Lucovsky, and S. A. Solin. Infrared active optical vibrations of graphite. *Solid State Communications*, 23(2):117–120, 1977.

[167] M. H. Brodsky and M. Cardona. Local order as determined by electronic and vibrational spectroscopy: Amorphous semiconductors. *Journal of Non-Crystalline Solids*, 31(1-2):81–108, 1978.

[168] J. Knoll and J. Geiger. Optical constants of arc-evaporated amorphous carbon in the far-infrared spectral region. *Physical Review B*, 29(10):5651–5655, 1984.

[169] Q. Wei, J. Sankar, A. K. Sharma, S. Oktyabrsky, J. Narayan, and R. J. Narayan. Atomic structure, electrical properties, and infrared range optical properties of diamondlike carbon films containing foreign atoms prepared by pulsed laser deposition. *Journal of Materials Research*, 15(03):633–641, 2000.

[170] O. Baake, T. Seidl, U. H. Hossain, A. O. Delgado, M. Bender, D. Severin, and W. Ensinger. An apparatus for in situ spectroscopy of radiation damage of polymers by bombardment with high-energy heavy ions. *The Review of scientific instruments*, 82(4):45103, 2011.

[171] S. E. Rodil. Infrared spectra of amorphous carbon based materials. *Diamond and Related Materials*, 14(8):1262–1269, 2005.

[172] T. L. Daulton, M. A. Kirk, R. S. Lewis, and L. E. Rehn. Production of nanodiamonds by high-energy ion irradiation of graphite at room temperature. *Nuclear Instruments and Methods in Physics Research Section B: Beam Interactions with Materials and Atoms*, 175-177:12–20, 2001.

[173] Z. Wang, G. Yu, L. Yu, F. Zhu, D. Zhu, H. Xu, and M. Ruan. Nanocrystalline diamond formation during argon ion irradiation of graphite. *Journal of Applied Physics*, 91(5):3480, 2002.

[174] A. Dunlop, G. Jaskierowicz, P. M. Ossi, and S. Della-Negra. Transformation of graphite into nanodiamond following extreme electronic excitations. *Physical Review B*, 76(15), 2007.

[175] O. A. Shenderova and S. A. Ciftan Hens. Nanodiamonds. In R. Vajtai (ed.), *Springer Handbook of Nanomaterials* 263–300. Springer Berlin Heidelberg, Berlin, Heidelberg, 2013.

[176] X. Fan, K. Nose, D. Diao, and T. Yoshida. Nanoindentation behaviors of amorphous carbon films containing nanocrystalline graphite and diamond clusters prepared by radio frequency sputtering. *Applied Surface Science*, 273:816–823, 2013.

[177] J. Narayan and A. Bhaumik. Research Update: Direct conversion of amorphous carbon into diamond at ambient pressures and temperatures in air. *APL Materials*, 3(10):100702, 2015.

[178] P. Németh, L. A. J. Garvie, and P. R. Buseck. Twinning of cubic diamond explains reported nanodiamond polymorphs. *Scientific reports*, 5:18381, 2015.

[179] R. F. Egerton. Electron energy-loss spectroscopy in the TEM. *Reports on Progress in Physics*, 72(1):16502, 2009.

[180] S. R. P. Silva (ed.). *Properties of amorphous carbon*, volume no. 29 of *EMIS datareviews series*. INSPEC, London, 2003.

[181] R. Hovden, P. Cueva, J. A. Mundy, and D. A. Muller. The Open-Source Cornell Spectrum Imager. *Microscopy Today*, 21(01):40–44, 2013.

[182] S. D. Berger, D. R. McKenzie, and P. J. Martin. EELS analysis of vacuum arc-deposited diamond-like films. *Philosophical Magazine Letters*, 57(6):285–290, 1988.

[183] I. Alexandrou, H.-J. Scheibe, C. J. Kiely, A. J. Papworth, G. A. J. Amaratunga, and B. Schultrich. Carbon films with an sp^2 network structure. *Physical Review B*, 60(15):10903–10907, 1999.

[184] N. Bernier, F. Bocquet, A. Allouche, W. Saikaly, C. Brosset, J. Thibault, and A. Charaï. A methodology to optimize the quantification of sp^2 carbon fraction from K edge EELS spectra. *Journal of Electron Spectroscopy and Related Phenomena*, 164(1-3):34–43, 2008.

[185] O. Glatter (ed.). *Small angle X-ray scattering*. Academic Press, London, 2. print edition, 1983.

[186] P. Kluth, C. Schnohr, O. Pakarinen, F. Djurabekova, D. Sprouster, R. Giulian, M. Ridgway, A. Byrne, C. Trautmann, D. Cookson, K. Nordlund, and M. Toulemonde. Fine Structure in Swift Heavy Ion Tracks in Amorphous SiO_2. *Physical Review Letters*, 101(17), 2008.

[187] M. D. Rodríguez, B. Afra, C. Trautmann, M. Toulemonde, T. Bierschenk, J. Leslie, R. Giulian, N. Kirby, and P. Kluth. Morphology of swift heavy ion tracks in metallic glasses. *Journal of Non-Crystalline Solids*, 358(3):571–576, 2012.

[188] M. C. Ridgway, T. Bierschenk, R. Giulian, B. Afra, M. D. Rodriguez, L. L. Araujo, A. P. Byrne, N. Kirby, O. H. Pakarinen, F. Djurabekova, K. Nordlund, M. Schleberger, O. Osmani, N. Medvedev, B. Rethfeld, and P. Kluth. Tracks and Voids in Amorphous Ge Induced by Swift Heavy-Ion Irradiation. *Physical Review Letters*, 110(24), 2013.

[189] D. Schauries, A. A. Leino, B. Afra, M. D. Rodriguez, F. Djurabekova, K. Nordlund, N. Kirby, C. Trautmann, and P. Kluth. Orientation dependent annealing kinetics of ion tracks in c-SiO_2. *Journal of Applied Physics*, 118(22):224305, 2015.

[190] C. Hubert, K. O. Voss, M. Bender, K. Kupka, A. Romanenko, D. Severin, C. Trautmann, and M. Tomut. Swift heavy ion-induced radiation damage in isotropic graphite studied by micro-indentation and in-situ electrical resistivity. *Nuclear Instruments and Methods in Physics Research Section B: Beam Interactions with Materials and Atoms*, 365:509–514, 2015.

[191] C. Hubert. *Characterization of radiation damage induced by swift heavy ions in graphite*. Dissertation, Technische Universität Darmstadt, Darmstadt, Germany, Januar 2016.

[192] W. J. Parker, R. J. Jenkins, C. P. Butler, and G. L. Abbott. Flash Method of Determining Thermal Diffusivity, Heat Capacity, and Thermal Conductivity. *Journal of Applied Physics*, 32(9):1679, 1961.

[193] R. D. Cowan. Pulse Method of Measuring Thermal Diffusivity at High Temperatures. *Journal of Applied Physics*, 34(4):926, 1963.

[194] J. A. Cape and G. W. Lehman. Temperature and Finite Pulse-Time Effects in the Flash Method for Measuring Thermal Diffusivity. *Journal of Applied Physics*, 34(7):1909, 1963.

[195] M. Shamsa, W. L. Liu, A. A. Balandin, C. Casiraghi, W. I. Milne, and A. C. Ferrari. Thermal conductivity of diamond-like carbon films. *Applied Physics Letters*, 89(16):161921, 2006.

[196] A. A. Balandin, M. Shamsa, W. L. Liu, C. Casiraghi, and A. C. Ferrari. Thermal conductivity of ultrathin tetrahedral amorphous carbon films. *Applied Physics Letters*, 93(4):43115, 2008.

[197] B. Cappella and G. Dietler. Force-distance curves by atomic force microscopy. *Surface Science Reports*, 34(1-3):1–104, 1999.

[198] H. Hertz. Über die Berührung fester elastischer Körper. *Journal für die reine und angewandte Mathematik*, 92:156–171, 1882.

[199] M. Nagatsu, N. Takada, T. Tsukishima, and M. Shimada. Reflectivity measurements of graphite in the infrared and submillimeter wave regions. *Journal of Nuclear Materials*, 209(2):204–211, 1994.

[200] R. Danjoux. Window or External Optics Transmittance: A817-T560472. *Technical Publication itc INFRARED TRAINING CENTER*, 60:1–9.

[201] W. Wien. Ueber die Energievertheilung im Emissionsspectrum eines schwarzen Körpers. *Annalen der Physik und Chemie*, 294(8):662–669, 1896.

[202] A. Beer. Bestimmung der Absorption des rothen Lichts in farbigen Flüssigkeiten. *Annalen der Physik und Chemie*, 162(5):78–88, 1852.

[203] J. H. Lambert and E. Anding. *Lamberts Photometrie: [Photometria, sive De mensura et gradibus luminus, colorum et umbrae] (1760)*, volume Nr. 31-33 of *Ostwalds Klassiker der exakten Wissenschaften*. W. Engelmann, Leipzig, 1892.

[204] W. M. Haynes. *CRC Handbook of Chemistry and Physics*. CRC Press, Hoboken, 92th ed. edition, 2011.

[205] D. Schwen and E. Bringa. Atomistic simulations of swift ion tracks in diamond and graphite. *Nuclear Instruments and Methods in Physics Research Section B: Beam Interactions with Materials and Atoms*, 256(1):187–192, 2007.

[206] Z. G. Wang, C. Dufour, E. Paumier, and M. Toulemonde. The S e sensitivity of metals under swift-heavy-ion irradiation: a transient thermal process. *Journal of Physics: Condensed Matter*, 6(34):6733–6750, 1994.

[207] K. Nordlund, M. Ghaly, and R. S. Averback. Mechanisms of ion beam mixing in metals and semiconductors. *Journal of Applied Physics*, 83(3):1238, 1998.

[208] M. Ghaly, K. Nordlund, and R. S. Averback. Molecular dynamics investigations of surface damage produced by kiloelectronvolt self-bombardment of solids. *Philosophical Magazine A*, 79(4):795–820, 1999.

[209] H. J. C. Berendsen, J. P. M. Postma, W. F. van Gunsteren, A. DiNola, and J. R. Haak. Molecular dynamics with coupling to an external bath. *The Journal of Chemical Physics*, 81(8):3684, 1984.

[210] K. Beardmore and R. Smith. Empirical potentials for C-Si-H systems with application to C_{60} interactions with Si crystal surfaces. *Philosophical Magazine A*, 74(6):1439–1466, 1996.

[211] D. W. Brenner. Empirical potential for hydrocarbons for use in simulating the chemical vapor deposition of diamond films. *Physical Review B*, 42(15):9458–9471, 1990.

[212] D. W. Brenner. Erratum: Empirical potential for hydrocarbons for use in simulating the chemical vapor deposition of diamond films. *Physical Review B*, 46(3):1948, 1992.

[213] H. U. Jäger and K. Albe. Molecular-dynamics simulations of steady-state growth of ion-deposited tetrahedral amorphous carbon films. *Journal of Applied Physics*, 88(2):1129, 2000.

[214] K. Nordlund. Molecular dynamics simulation of ion ranges in the l-100 keV energy range. *Computational Materials Science*, 3:448–456, 1995.

[215] A. Stukowski. Visualization and analysis of atomistic simulation data with OVITO–the Open Visualization Tool. *Modelling and Simulation in Materials Science and Engineering*, 18(1):15012, 2010.

[216] C. H. Rycroft. VORO++: a three-dimensional voronoi cell library in C++. *Chaos*, 19(4):41111, 2009.

[217] X. Yuan and A. N. Cormack. Efficient algorithm for primitive ring statistics in topological networks. *Computational Materials Science*, 24(3):343–360, 2002.

[218] L. Colombo and A. Fasolino. *Computer-Based Modeling of Novel Carbon Systems and Their Properties*, volume 3. Springer Netherlands, Dordrecht, 2010.

[219] J. N. Glosli and F. H. Ree. The melting line of diamond determined via atomistic computer simulations. *The Journal of Chemical Physics*, 110(1):441, 1999.

[220] M. Krause, W. Egger, W. Ensinger, C. Hugenschmidt, B. Löwe, L. Ravelli, M. Tomut, and C. Trautmann. Positron annihilation lifetime spectroscopy study of vacancy cluster evolution in swift heavy ion irradiated HOPG. In *GSI SCIENTIFIC REPORT 2010*, volume 2011-1 384. 2010.

Acknowledgements

I would like to thank the numerous people who contributed to this thesis by their support. In particular, I sincerely thank:

- **My doctoral mother Prof. Dr. Christina Trautmann** for always having an open door, her support, her guidance and encouragement during the time of my doctoral thesis. I thank her especially for all the time she invested in reading and correcting my manuscripts and this thesis.
- **Dr. Marilena Tomut** for sharing her experience and knowledge, for providing ideas, her advice and support during the last years and for giving me the freedom to follow my scientific interests.
- **Prof. Dr. Wolfgang Ensinger** for acting as a referee.
- **Prof. Dr. Oliver Kester and Prof. Dr. Karsten Albe** for being members of the examination committee.
- **Dr. Daniel Severin and Dr. Markus Bender** for introducing me to M-branch and the GSI accelerator, the help during beamtimes, discussions, their support and advice.
- **Dr. Bettina Lommel** for the preparation of stripper foils, but also for her support and advice concerning this thesis and for caring.
- **Jutta Steiner** for introducing me into the preparation and handling of the stripper foils and for preparing large amounts of samples in short time.
- **Prof. Dr. Kai Nordlund and Dr. Flyura Djurabekova** for giving me the possibility of a research stay in their group and their endless patience in answering my questions.
- **Arne Siegmund** for all his technical support, help with the installation of new devices and with experiment setups, troubleshooting, and for all the sample orders.
- **Dr. Aleksi Leino** for introducing me to the world of (MD) simulations and his endless patience, help and support during and after my stay in Helsinki.
- **Ruben Precht** for performing the XPS measurements.
- **Dr. Stefan Lauterbach and Dr. Leopoldo Molina-Luna** for TEM and EELS measurements, different trials to optimize the results and for answering all my questions.
- **Dr. Birgit Kindler and the other memebers of GSI target laboratory** for the chromatic aberration measurements and her support.
- **Dr. Marcel Toulemonde** for providing inelastic thermal spike calculations.
- **Henrique Vasquez Muinos** for help with MD simulations.
- **Dr. Patrick Kluth and his group at the Australian Synchotron** for the SAXS measurements and data analysis.
- **Andreas Plog** for the AFM measurements and data analysis.
- **Anthony Dunlap, Pascal Simon, Marcel Urban and Christoph Tropsch** who contributed with their great work and support during beamtimes to this thesis.

- **Dr. Christian Hubert** for his help concerning all issues of everyday business of the "carbon-group" and during beamtimes, for scientific discussions and for a lot of fun.
- **Anton Romanenko** for the help during beamtime and with Raman problems.
- **Dr. Ina Schubert** for interesting discussions, moral support and advice, and for being the best office-mate.
- **Materials research group at GSI** for the great atmosphere, coffee rounds, beamtime support, discussions, all their help and a lot of fun.
- **All members of the accelertor laboratory at Helsinki University** for the warm welcome and the nice coffee breaks.
- **Dr. Raphael Danjoux** for the support and suggestions concerning the thermography experiments.
- **Dr. Hiroo Hasebe** for providing CNT-foils and the friendly welcome to Tokyo at INTDS14.
- **Dr. Isao Sugai** for providing different carbon stripper foils and the warm welcome to Tsukuba.
- **Dr. Vinder Jaggi** for providing DLC foils.
- **Dr. Julia Patzsch and Silvo Heinschke** for performing gasadsorption measurements.
- **Prof. Dr. Johann Krauser** for performing AFM current measurements.
- **Dr. Marton Major** for performing XRR measurements.
- **Dr. Roland Seitz** for performing ellipsometry measurements.
- **Maria Syrigou** for performing the lattice fringe analysis.
- **Michelle Wöllner** for performing Infrasorp measurements.
- **Danubia Nanotech** for trying to produce thin, freestanding SWCNT foils.
- **The BMBF** for project funding.
- **The HGS-HIRe graduate school** for the financial support that gave me the possibility to attend several interesting conferences, the representation of PhD students' interests and the great soft-skill courses.
- **My loved ones** for their limitless support, never questioning my way, for everything.

Wissenschaftlicher Werdegang

Katharina Kupka

06/2006	Abitur an der Ziehenschule, Frankfurt am Main
10/2006 – 05/2012	Studium Materialwissenschaft an der Technischen Universität Darmstadt
09/2009 – 08/2010	Auslandsstudium an der Seoul National University
07/2012 – 07/2016	Promotion an der Technischen Universität Darmstadt, Fachbereich Materialwissenschaft, durchgeführt im Bereich Materialforschung am GSI Helmholtzzentrum für Schwerionenforschung
11/2014, 01/2015	Forschungsaufenthalt an der University of Helsinki, Department of Physics, Division of Materials Physics

Publications

Parts of this thesis are based on the following peer-reviewed publications and reports and have been also described in Bachelor theses and internship reports.

Peer-reviewed publications

K. Kupka, M. Tomut, P. Simon, C. Hubert, A. Romanenko, B. Lommel and C. Trautmann. Intense heavy ion beam-induced temperature effects in carbon-based stripper foils *Journal of Radioanalytical and Nuclear Chemistry* 3 (2015) 305:875-882
doi: 10.1007/s10967-015-4057-x

C. Hubert, K. O. Voss, M. Bender, **K. Kupka**, A. Romanenko, D. Severin, C. Trautmann and M. Tomut. Swift heavy ion-induced radiation damage in isotropic graphite studied by micro-indentation and in-situ electrical resistivity *Nuclear Instruments and Methods in Physics Research B* (2015) 365:509-514
doi:10.1016/j.nimb.2015.08.056

Reports

K. Kupka, C. Hubert, D. Nguyen, M. Tomut and C. Trautmann. Structural changes induced by intense swift heavy-ion beamsin carbon-based materials *Annual Report Faculty of Materials and Geo Sciences 2012* (2013) 134

M. Tomut, C. Hubert, **K. Kupka**, B. Lommel, A. Beusch, D. Severin, C. Trautmann. Beam Monitoring on Graphite Targets by Infrared Thermography *GSI Scientific Report 2012* (2013) 407

C. Hubert, M. Tomut, **K. Kupka**, A. Romanenko, B. Schuster, H-P. Liermann, C. Trautmann. High-Resolution Synchrotron X-Ray Diffraction of Swift Heavy Ion Irradiated Graphite *GSI Scientific Report 2012* (2013) 408

K. Kupka, M. Tomut, C. Hubert, R. Danjoux, B. Lommel, J. Steiner, C. Trautmann. Measurements of Carbon Stripper Foils Emissivity for Quantitative On-line Infrared Thermography *GSI Scientific Report 2012* (2013) 409

Duy C. Nguyen, M. Tomut, C. Hubert, **K. Kupka**, B. Xu, C. Trautmann. Simulation of Stress Waves Induced by Pulsed Heavy Ion Beams in Thin Graphite Targets *GSI Scientific Report 2012* (2013) 410

M. Urban, **K. Kupka**, M. Tomut, C. Hubert, A. Romanenko, B. Lommel, C. Trautmann. Laser flash analysis of irradiated amorphous carbon stripper foils *GSI Scientific Report 2014* (2015) 265
doi:10.15120/GR-2015-1-APPA-MML-MR-13